Flow Instability Study of a Natural Circulation Loop with Supercritical Fluids

By

Lei Zhang

A Thesis submitted to the Faculty of Graduate Studies of

The University of Manitoba

in partial fulfillment of the requirements of the degree of

MASTER OF SCIENCE

Department of Mechanical and Manufacturing Engineering

University of Manitoba

Winnipeg

ABSTRACT

Supercritical flow instability in a natural circulation loop with a single horizontal heated channel was experimentally and numerically studied.

The experiment was conducted at pressures from 7.6 to 8.6 MPa and inlet temperatures from 10 to 22 °C with supercritical CO_2. A total of 13 flow instability cases were obtained. Parametric effects such as system pressure, inlet temperature, and heated channel outlet local loss were concluded from steady-state flow-power curve. The effect of different loop configurations, as well as the valve on the connecting line on flow instability, was also investigated.

The CATHENA code was used to model the current experimental loop with supercritical water. Flow instabilities were numerically studied with an open loop and a loop connected with accumulator (reservoir) models. Factors that may affect the predictions of steady state results with CATHENA code were discussed and the effect of accumulator as well as the valve on the connecting line was also tested.

ACKNOWLEDGEMENTS

I would like to express my appreciation and thanks to my advisors, Dr. V. Chatoorgoon and Dr. R. Derksen, for their invaluable guidance. I would also like to thank my committee members, Dr. M. Birouk and Dr. A. Rajapakse for their helpful comments and suggestions. I'm grateful to Sviatoslaw Karnaoukh for technical support of the experiment as well as Dr. Aleksandar Vasic at Canadian Nuclear Laboratories who provided invaluable guidance and support about the CATHENA code. I am also grateful to AECL for the financial support of this project. Last but not least, I would like to thank my wife, Sujuan Li and my family for their wonderful support, guidance, and patience.

TABLE OF CONTENTS

ABSTRACT i

ACKNOWLEDGEMENTS ii

TABLE OF CONTENTS iii

LIST OF TABLES vii

LIST OF FIGURES x

NOMENCLATURE xiv

CHAPTER 1 1

1.1 Nuclear Energy 1

1.2 Supercritical Water Cooled Reactors (SCWRs) 3

1.3 Natural Circulation Systems 5

1.4 Supercritical Fluids 8

1.4.1 Supercritical Water 8

1.4.2 Supercritical CO_2 11

1.5 Flow Instabilities of Thermo-hydraulic Systems 13

1.5.1 Ledinnegg Instability 14

1.5.2 Pressure Drop Oscillations 15

1.5.3 Density Wave Oscillations 15

1.5.4 Flow Instability of Natural Circulation Systems 17

1.5.5 Supercritical Flow Instabilities 18

1.6 Research Objective 19

1.7 Outline of Thesis 20

CHAPTER 2 22

2.1 Review of Supercritical Flow Instabilities 22

2.1.1 Supercritical Flow Instability of Single Heated Channels 22

2.1.2 Supercritical Flow Instability of Parallel Heated Channels 28

2.1.3 Supercritical Flow Instability of Natural Circulation Systems 31

2.2 Summary of Literature Review 40

CHAPTER 3 47

3.1 Introduction 47
3.2 Experimental Set-up and Components 47
3.2.1 Pressure Control System 48
3.2.2 Purging System 50
3.2.3 Power Supply System 50
3.2.4 Vacuum and Evacuation System 52
3.2.5 Cooling System 52
3.2.6 Data Acquisition System 53
3.2.7 Piping, Joints and Valves 54
3.3 Instrumentation 55
3.3.1 Temperature Measurement 57
3.3.2 Pressure Measurement 58
3.3.3 Flow Measurement 58
3.3.4 Heating Power 60
3.3.5 Instrumental Uncertainty 60
3.4 Test Preparation and Procedures 62
3.4.1 Calibration 62
3.4.2 Leakage Test 62
3.4.3 Evacuation and Vacuum 63
3.4.4 Pressurization 63
3.4.5 Before Adding Power 64
3.4.6 Test Procedures 66
CHAPTER 4 69
4.1 Introduction 69
4.2 Steady State Characteristic and Repeatability of the Experimental Case 70
4.3 Determination of Flow Instability Boundary 72
4.4 Experimental Flow Instability Cases 75
4.5 Parameter Study 88
4.5.1 Parametric Effects Study 88

4.5.2 Accumulator Effect Study 90
4.6 Effects of Different Loop Configurations on Flow Oscillations 92
4.6.1 Close Loop Condition (C1) 92
4.6.2 Rectangular Loop with Accumulator Only (C2) 94
4.6.3 Rectangular Loop with Settling Chamber (C3) 96
4.6.4 Rectangular Loop with Both Settling Chamber and Accumulator (C4) 102
4.6.5 Comparison of Steady State Results with Different Loop Boundary Conditions 106
4.7 Summary 109
CHAPTER 5 111
5.1 Introduction 111
5.2 Numerical Modeling 112
5.2.1 Introduction of the CATEHNA Code 112
5.2.2 Physical Model 114
5.2.3 Governing Equations 114
5.2.4 Assumptions 120
5.2.5 Boundary and Initial Conditions 120
5.2.6 Sensitivity Test of Numerical Discretization Parameters 121
5.3 Validation of Numerical Code against Water 123
5.4 Modeling of Our Experimental Natural Circulation Loop with Supercritical Water 128
5.4.1 Open Loop Model 129
5.4.2 Rectangular Loop with Accumulator 137
CHAPTER 6 143
6.1 Summary 143
6.2 Conclusions 144
6.2.1 Experimental Study 144
6.2.2 Numerical Modeling 146
6.3 Recommendations for Future Work 146
6.3.1 Experimental Study 146

6.3.2 Numerical Modeling 147
REFERENCE 148
APPENDIX I 158
APPENDIX II 159
APPENDIX III 162

LIST OF TABLES

Table 2-1 Summary of analytical and numerical studies on flow instabilities of SNCLs 43
Table 2-2 Summary of experimental investigations on supercritical flow instabilities based on rectangular NCLs 45
Table 3-1 Specifications of instruments 56
Table 4-1 Experimental cases and instability boundary (with accumulator connected) 75
Table 5-1 Local K factors used for numerical simulation 118
Table 5-2 Dimensions of simplified model and node number for each section 118
Table A III. 1 Averaged values of measured signals during experiment for each data point (Case 1) 162
Table A III. 2 Averaged values of measured wall surface temperature during experiment for each data point (Case1) 163
Table A III. 3 Averaged values of measured signals during experiment for each data point (Case 2) 164
Table A III. 4 Averaged values of measured wall surface temperature during experiment for each data point (Case2) 165
Table A III. 5 Averaged values of measured signals during experiment for each data point (Case 3) 166
Table A III. 6 Averaged values of measured wall surface temperature during experiment for each data point (Case3) 167
Table A III. 7 Averaged values of measured signals during experiment for each data point (Case 4) 168
Table A III. 8 Averaged values of measured wall surface temperature during experiment for each data point (Case4) 169
Table A III. 9 Averaged values of measured signals during experiment for each data point (Case 5) 170
Table A III. 10 Averaged values of measured wall surface temperature during experiment for each data point (Case5) 171
Table A III. 11 Averaged values of measured signals during experiment for each data point

(Case 6) 172
Table A III. 12 Averaged values of measured wall surface temperature during experiment for each data point (Case6) 173
Table A III. 13 Averaged values of measured signals during experiment for each data point (Case 7) 174
Table A III. 14 Averaged values of measured wall surface temperature during experiment for each data point (Case7) 175
Table A III. 15 Averaged values of measured signals during experiment for each data point (Case 8) 176
Table A III. 16 Averaged values of measured wall surface temperature during experiment for each data point (Case8) 177
Table A III. 17 Averaged values of measured signals during experiment for each data point (Case 9) 178
Table A III. 18 Averaged values of measured wall surface temperature during experiment for each data point (Case9) 179
Table A III. 19 Averaged values of measured signals during experiment for each data point (Case 10) 180
Table A III. 20 Averaged values of measured wall surface temperature during experiment for each data point (Case10) 181
Table A III. 21 Averaged values of measured signals during experiment for each data point (Case 11) 182
Table A III. 22 Averaged values of measured wall surface temperature during experiment for each data point (Case11) 183
Table A III. 23 Averaged values of measured signals during experiment for each data point (Case 12) 184
Table A III. 24 Averaged values of measured wall surface temperature during experiment for each data point (Case12) 185
Table A III. 25 Averaged values of measured signals during experiment for each data point (Case 13) 186

Table A III. 26 Averaged values of measured wall surface temperature during experiment for each data point (Case13) 187

LIST OF FIGURES

Figure 1.1 Comparative primary energy consumption at year 2015 (Data from IAEA [3]) 2
Figure 1.2 Age distribution of operating reactors in the world at year 2017 (Data from IAEA [3]) 2
Figure 1.3 Layout of Canadian SCWR thermal cycles (Data from Duffey, 2016 [8]) 5
Figure 1.4 Schematic of natural circulation loop.....6
Figure 1.5 Schematic diagram of the passive moderator cooling system.....7
Figure 1.6 Scheme of the phase diagram for water 8
Figure 1.7 Thermo-physical property variations of water at a supercritical pressure of 25 MPa [15].....9
Figure 1.8 Water density vs. Temperature at different pressures [15] 10
Figure 1.9 Supercritical CO_2 properties at 8 MPa [15].....11
Figure 1.10 Dimensionless density trends as a function of dimensionless enthalpy for water and CO_2 [15] 12
Figure 1.11 Types of thermos-hydraulic instabilities of two phase flow.....14
Figure 1.12 Pressure drop across a heated channel vs. the mass flow rate.....15
Figure 1.13 A simplified system for density wave oscillations 16
Figure 1.14 Stability regions of type I and type II for both forced (A) and natural (B) circulation loop (reproduced based on [20]).....17
Figure 2.1 Schematic diagram of the experimental loop in Lomperski et al. [55] 32
Figure 2.2 Schematic diagram of the experimental loop in Sharma et al. [61] 34
Figure 2.3 Schematic diagram of the experimental loop in Sharma et al. [62] 35
Figure 2.4 Schematic diagram of the experimental loop in Chen, L et al. [65].....36
Figure 2.5 Schematic diagram of the experimental loop in T'Joen, C. and M. Rohde [66]....37
Figure 2.6 Schematic diagram of the experimental loop in Chen, Y.Z et al. [67, 68] 38
Figure 3.1 Schematic of natural circulation loop with horizontal single channel 49
Figure 3.2 Emergency shut down switch.....51
Figure 3.3 Power supply interlock.....51
Figure 3.4 Secondary side cooling system.....53

Figure 3.5 Front view of the heated channel with thermocouple arrangement 55
Figure 3.6 Top view of the heated channel with differential pressure sensors arrangement ...55
Figure 3.7 Pneumatic supply.....64
Figure 3.8 Swegelok fitting on high pressure side of booster pump 64
Figure 3.9 Main power supply.....65
Figure 3.10 Rectifier.....66
Figure 3.11 Circuit breaker.....66
Figure 4.1 Steady state flow-power curve of natural circulation loop.....71
Figure 4.2 Comparison of heated channel outlet temperature.....71
Figure 4.3 Determination of boundary heating power (Case 12) 73
Figure 4.4 Determination of boundary heating power (Case 3) 74
Figure 4.5 Variation of mass flow rate with heating power (Case2) 76
Figure 4.6 Flow oscillations with various changes of key parameters versus time (Case2) ...77
Figure 4.7 Evolution of segmental pressure drops with flow time (Case 2).....78
Figure 4.8 Variation of mass flow rate with heating power (Case 6) 79
Figure 4.9 Flow oscillations with various changes of key parameters versus time (Case6) ...80
Figure 4.10 Evolution of segmental pressure drops with flow time (Case 6).....81
Figure 4.11 Variation of mass flow rate with heating power (Case 13).....82
Figure 4.12 Flow oscillations with various changes of key parameters versus time (Case13)83
Figure 4.13 Evolution of segmental pressure drops with flow time (Case 13).....84
Figure 4.14 Evolution of top wall temperatures with flow time (Case 13) 85
Figure 4.15 Evolution of bottom wall temperatures with flow time (Case 13) 86
Figure 4.16 Effect of system pressure on power-flow curve and instability boundary 89
Figure 4.17 Effect of inlet temperature on power-flow curve and instability boundary 89
Figure 4.18 Effect of outlet local loss coefficient on power-flow curve and instability boundary 90
Figure 4.19 Accumulator effect (Case1).....91
Figure 4.20 Accumulator effect(Case3).....91
Figure 4.21 Accumulator effect (Case4).....91

Figure 4.22 Flow behaviours evolve with time (based on Case 12) 93
Figure 4.23 Evolution of mass flow rate as well as system pressure with flow time 95
Figure 4.24 Oscillations of various parameters with time (Valve V-4 partially closed) 96
Figure 4.25 Evolution of mass flow rate as well as system pressure with flow time (Case 12) 97
Figure 4.26 Parameters change with flow time (cut-off frequency of 1.4 Hz for pressure drop) 98
Figure 4.27 Evolution of mass flow rate as well as system pressure with flow time 100
Figure 4.28 Parameters change with flow time (valve V- 2 almost closed) 101
Figure 4.29 Evolution of mass flow rate as well as system pressure with flow time 102
Figure 4.30 Parameters change with flow time (valve V-2 fully open) 103
Figure 4.31 Flow characteristics with valve V-2 half closed 104
Figure 4.32 Evolution of flow characteristics with valve V-2 almost closed 105
Figure 4.33 Parameters change with time (with heating power of 11.85kW) 105
Figure 4.34 Comparison of steady state flow-power curves with different loop configurations 106
Figure 4.35 Boundary heating power with various CO_2 inlet temperatures 108
Figure 4.36 Loop hot side CO2 temperatures when instability occurs 109
Figure 5.1 Simplified model of the experimental natural circulation loop 117
Figure 5.2 Test of time steps on flow oscillations (H_2O simulated) 121
Figure 5.3 Grid sensitivity test for steady state flow (H_2O simulated) 122
Figure 5.4 Grid independence study on flow instability boundary (H_2O simulated) 123
Figure 5.5 Schematic of the CIAE loop [67] 124
Figure 5.6 Variation of flow rate with power [67] 124
Figure 5.7 Increase of power with time [67] 125
Figure 5.8 Physical model of the CIAE loop for the CATHENA code 126
Figure 5.9 Mass flow rate versus power 127
Figure 5.10 Variation of the inlet and outlet water temperatures with increase of heating power 128

Figure 5.11 Local K factors distribution effect on steady state H_2O results.....130
Figure 5.12 Local K factors distribution effect on steady state H_2O results.....131
Figure 5.13 Pipe roughness effect on steady state simulation with H_2O.....131
Figure 5.14 Properties of fluid inside the heated channel at steady state 133
Figure 5.15 Evolution of mass flow rate with time (open loop model).....133
Figure 5.16 Evolution of pressure drops (P=25MPa, Tin=349.482°C, Kout=13.1).....134
Figure 5.17 Fluid temperature along the heated section at 1471.24 s and1476.23 s 135
Figure 5.18 Fluid specific heat along the heated section at 1471.24 s and1476.23 s 135
Figure 5.19 Fluid density along the heated section at 1471.24 s and1476.23 s.....136
Figure 5.20 Fluid enthalpy along the heated section at 1471.24 s and1476.23 s.....136
Figure 5.21 Determination of flow instability boundary with reservoir.....138
Figure 5.22 Evolution of mass flow rate with time (rectangular loop with reservoir) 139
Figure 5.23 Valve effect test with V-4 close from restart.....140
Figure 5.24 Valve effect test with V-4 close when flow oscillation occurs 140
Figure 5.25 Valve effect on flow instability behaviour.....141
Figure 5.26 Valve effect on flow instability boundary.....142
Figure A I. 1 Experimental test facility.....158
Figure A II. 1 Horizontal bottom part of the experimental loop 159
Figure A II. 2 Area enlargement of tubes.....159
Figure A II. 3 Area contraction of tubes.....160
Figure A II. 4 Annular chamber 161

NOMENCLATURE

A	cross-section area of the conduit (m^2)
C	flow profile coefficient
C_p	specific heat at constant pressure (J/(kg•ºC))
De	hydraulic diameter (m)
DP	pressure drop (Pa)
Fr	Froude number
H	loop height (m)
K	local loss coefficient
K_f	fluid thermal conductivity ($W \cdot m^{-1} \cdot K^{-1}$)
L	pipe length (m)
M	mass flow rate (kg/s)
N_{spc}	sub-pseudocritical number
N_{tpc}	trans-pseudocritical number
P	system pressure (MPa)
Pr	Prandtle number
Q	heating power at heated channel (kW)
Re	Reynolds number
S	cross section area at the inlet of settling chamber
T	temperature (℃)
TS	test section
V	volume of settling chamber(m^3)
W	loop width (m)
c	speed of sound (m/s)
f	wall friction factor
f_0	resonance frequency (Hz)

g	gravitational acceleration(m2/s)
h	fluid specific enthalpy (J/kg)
h_f	fluid heat transfer coefficient ($W \cdot m^{-2} \cdot K^{-1}$)
l	pipe length (m)
l_0	neck length of the connecting line (m)
m	interface mass transfer rate
p	local pressure (Pa)
q_w	power added to fluid (kW)
t	time (s)
v_k	velocity of phase k (m/s)
w	fluid velocity (m/s)

Greek letters

Γ_k	source of non-condensable
α_k	fraction of the cross-section occupied by phase k
β	isobaric thermal expansion coefficient (K^{-1})
β_k	phase-to-interface pressure difference
ε	wall roughness (m)
μ	viscosity (Pa s)
ν	kinetic viscosity (m^2/s)
ρ	density (kg/m^3)
τ	shear stress (N/m^2)
ζ_k	wall shear fraction for phase k

Subscripts

channel	heated channel
cr	critical
HX-in	inlet of heat exchanger

HX-out	outlet of heat exchanger
f	fluid
in	inlet of heated channel
k	phase k
out	outlet of heated channel
p	constant pressure
pc	pseudo-critical

CHAPTER 1

INTRODUCTION

1.1 Nuclear Energy

Climate change has become a well-known phenomenon worldwide. According to Intergovernmental Panel on Climate Change (IPCC), in the past century, the average temperature of the earth increased between 0.4 °C and 0.8 ℃ and it will continue to rise about 1.4 to 5.8 °C over the next century [1]. Global warming has irreversible impacts on the earth's ecosystem. It speeds the melting of glaciers, affects the agriculture and water supply, and causes acidification of the ocean. The probability of occurrence of extreme weather conditions such as heat waves, droughts, floods, cyclones and wildfires increases with the continuing rise of global temperatures. Scientific research has shown that the causes of climate change are most likely due to the emission of greenhouse gases (GHG), including mainly carbon dioxide (CO_2). And the emission of CO_2 from burning fossil fuel and industrial processes is believed to be the main sources (78%) of total GHG emissions increased in the past years from 1970 to 2010 [1]. The Paris Agreement, signed in December 2015, marked a turning point for the world as a whole to fight climate change. It aimed to hold the increase in the global average temperature to well below 2 ℃ above pre-industrial levels and to pursue efforts to limit the temperature increase to 1.5 °C above pre-industrial levels [2].

Considering the global GHG emissions are highly related with energy, the use of energy technologies that emit small amounts of CO_2 per unit of energy service is crucial to meet the demand for increased energy consumption while still reducing GHG emissions. As can be seen in Figure 1.1, the non-renewable energy consumption of coal, gas, and oil still consist of about 86% of the total energy sources and are the main sources of GHG emissions. According to the latest database of International Atomic Energy Agency (IAEA) [3], currently there are 449 commercial nuclear power reactors under operation. The total nuclear

capacity now is over 390,000 MW, which only provides about 11% of the world's electricity as a continuous, reliable, climate friendly energy source. To achieve the ambitious goal of the Paris Agreement as well as to meet the growing demand for energy due to the global population increase, the composition of nuclear power and other low carbon technologies must be increased. More generating capacity of nuclear power utilizing advanced technologies should be added to replace the role of fossil power plant and gas-fired or oil-fired stations.

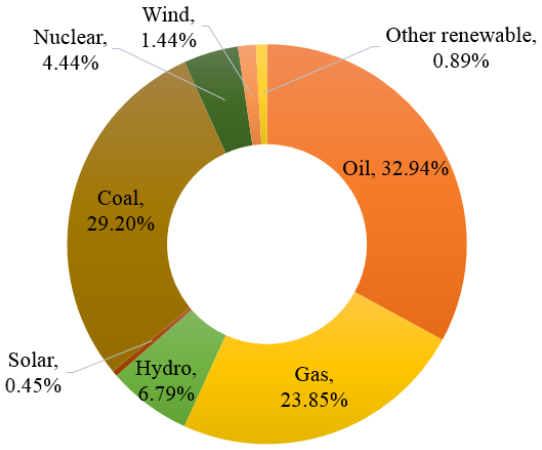

Figure 1.1 Comparative primary energy consumption at year 2015 (Data from IAEA [3])

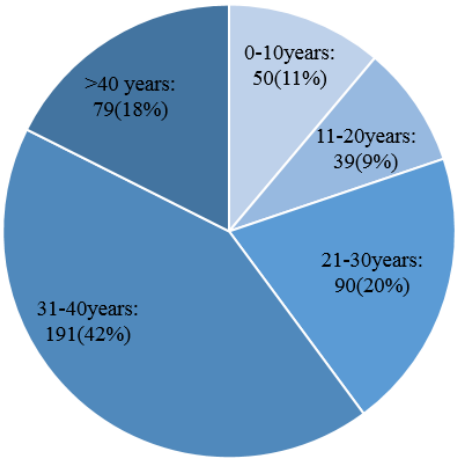

Figure 1.2 Age distribution of operating reactors in the world at year 2017 (Data from IAEA [3])

Nuclear reactors are classified into Generation I, II, III, III+, and IV, based on their designs. The Generation I reactor refers to the early prototype of power reactors from the 1950s and 1960s. Generation II reactors are designed to be reliable and economical commercial reactors,

which has a typical operation lifetime of 40 years and were built from late 1960s to the end of 1990s [4]. The age structure of the 449 nuclear power units in operation is shown in Figure 1.2. Most of these reactors are the Generation II reactors. In total, 60% of these units have been operated for more than 30 years, and 79 reactors of them have even been operated for more than 40 years and more. These units' operational lifetime can be extended to be 50 or 60 years before they are slowly shutdown. Generation III reactors (since year 1996) are essentially Generation II reactors but with improved fuel technology, thermal efficiency, modularized construction and safety systems and standardized design. Generation III$_+$ reactors further improved the safety features based on Generation III reactors and have the state-of-art technology in application now. Generation IV reactors, new and innovative reactor designs, are currently being studied by the Generation IV International Forum (GIF) [5] and are not expected to be commercially available until 2030 - 2040.

1.2 Supercritical Water Cooled Reactors (SCWRs)

The purpose of GIF is to stimulate innovative research and development on next generation reactors, providing new designs and implements of sustainable, economical, safe and reliable Generation IV reactors to meet the increasing demand of economic, environmental and social requirements of 21st century. According to the technology roadmap for Generation IV nuclear reactor designs [6], there are six most promising nuclear energy systems, which include the Gas-cooled Fast Reactor (GFR), Lead-cooled Fast Reactor (LFR), Molten Salt Reactor (MSR), Sodium-cooled Fast Reactor (SFR), Very High Temperature Reactor (VHTR), and Supercritical Water-cooled Reactor (SCWR).

Amongst these reactor designs, SCWR is the only one that utilizes light water as the coolant and evolves directly from the current Generation III and Generation III$_+$ water-cooled reactors. It can be operated at high temperature, high pressure conditions above the thermodynamic critical point of water (373.946 °C, 22.064 MPa). The high pressure, high temperature working conditions of SCWR help increase the thermal efficiency to be over 45%, a significant increase compared to the traditional Generation III and III$_+$ water cooled

reactors of ~ 35%. Another main advantage for SCWR is that the working fluid supercritical water undergoes no phase change above the thermodynamic critical point so the SCWRs can adopt a once through coolant system and operate at a high temperature level without encountering the Departure of Nuclear Boiling (DNB) problem. Steam water separation and recirculation pumps are also not necessary. This would result in considerable plant simplicities and a compact design. Furthermore, the supercritical gas turbine is a proven technology which has been widely used in over 400 supercritical fossil-fired power plants worldwide. The current SCWR designs can match the working condition and utilize the existing supercritical water turbine technology directly without any further development. In sum, the SCWR combines the technologies of Generation III and III$_+$ Light Water Reactors (LWRs) and supercritical-water fossil plants, and is economically competitive because of the reduction of capital cost from plant simplification and high thermal efficiency.

Generally, there are two types of SCWR designs; one is the European SCWR design (also known as High Performance Light Water Reactor, HPLWR) that uses a pressure vessel, whereas the Canadian SCWR design uses pressure tubes to contain the high pressure coolant and fuel in the reactor core [7]. For both designs, the working system pressure is 25 MPa. Feedwater coolant inlet temperature and outlet temperature are 280 °C and 500 °C for the European HPLWR design and for the Canadian SCWR design they are 315 °C and 625 °C, respectively.

A schematic diagram of the direct thermal cycle of Canadian SCWR as well as the temperature and pressure at various stages in the cycle is shown in Figure 1.3. To take full advantage of the supercritical turbine technology, the Canadian SCWR thermodynamic cycle design [8] will eventually adopt the steam reheat option used in fossil power plants. In general, the supercritical water (25 MPa, 625 °C) at the exit of the reactor core flows directly to the high pressure turbines (HPT). After it does the work in the HPT, coolant water (7 MPa, 420 °C) at the back end is divided into two parts; one part flows into the high pressure (HP) heaters as a heating source for the feedwater at the inlet of the reactor core, the other part is sent back through the second pass of reactor core to be reheated to the desired exit

temperature of 625 °C range at a lower pressure of 6.2 MPa before entering the intermediate pressure turbine (IPT). Similarly at the back end of IPT, the steam is divided again; part of it flows into the low pressure turbine (LPT) to do more work; the rest of it is sent to low pressure (LP) heaters as a heating source for the feedwater. The low pressure, low temperature at the exit of LPT is further cooled by a condenser. The condensed water is then pumped into the reactor as feedwater for the next circulation.

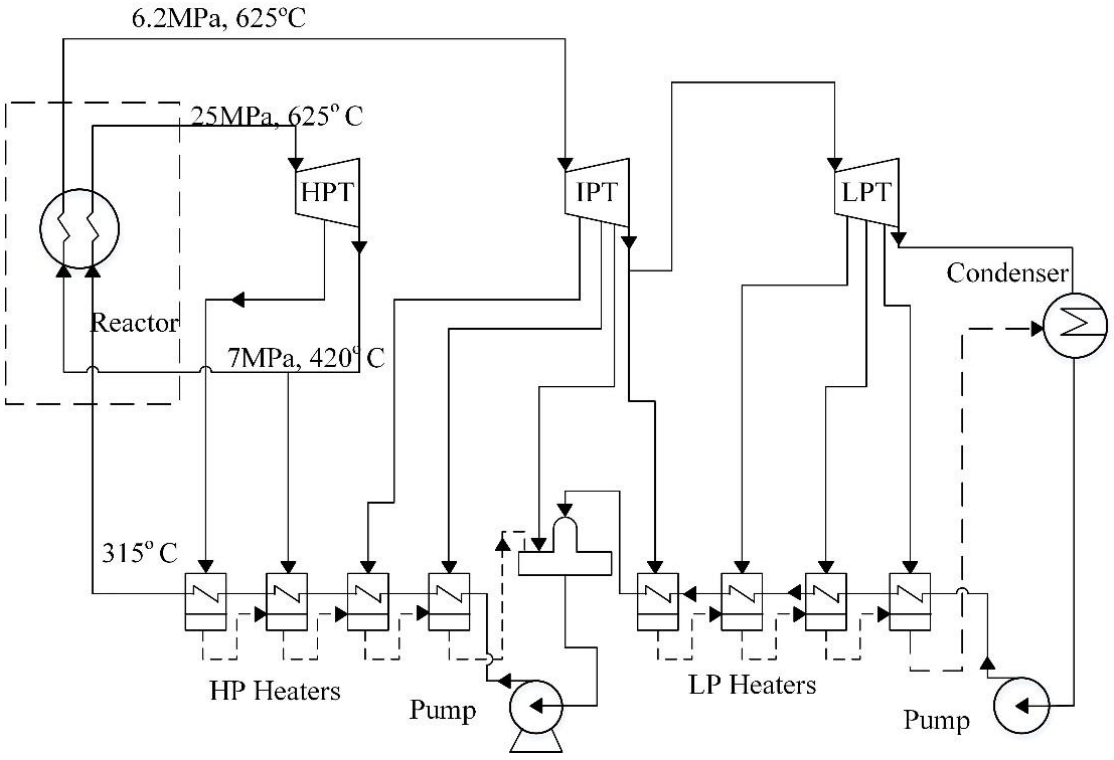

Figure 1.3 Layout of Canadian SCWR thermal cycles (Data from Duffey, 2016 [8])

1.3 Natural Circulation Systems

Natural circulation loops (NCLs) are flow systems utilizing a heat sink located higher than the heat source to generate a density gradient which works as the driving force for fluid to flow in the system, as is shown in Figure 1.4. The simplicity of NCLs makes it appealing for various thermal energy conversion systems, such as solar heaters [9], absorption refrigerators [10], re-boilers in chemical industries and cooling of various engines [11].

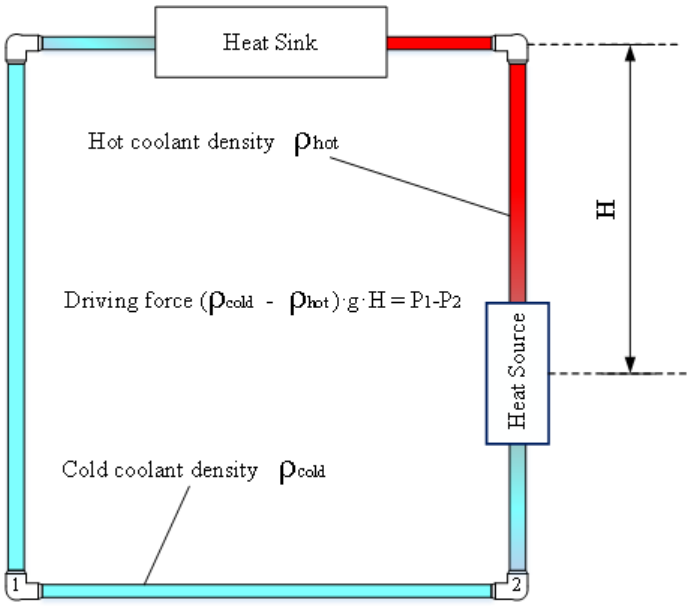

Figure 1.4 Schematic of natural circulation loop

One of the most important applications of NCLs is in water-cooled nuclear reactors. Without the installation, maintenance and operation of pumps, natural circulation systems are more economical and have enhanced passive reliabilities because there's no need for electric power supplies to operate the circulation pumps under emergency conditions. Therefore, the NCLs, either as a primary cooling system or a reserved cooling system to remove decay heat, are a must in modern water reactor design including the newly proposed supercritical water reactors (SCWRs) [12, 13]. Supercritical natural circulation systems are passive cooling systems. Take the Canadian SCWR designs as an example, the key feature of the Canadian SCWR design is known as the "no-core-melt" concept. As a tube type design, the primary coolant is separated from the heavy-water moderator. Both the primary coolant side and the moderator side are equipped with a passive cooling system show in Figure 1.5.

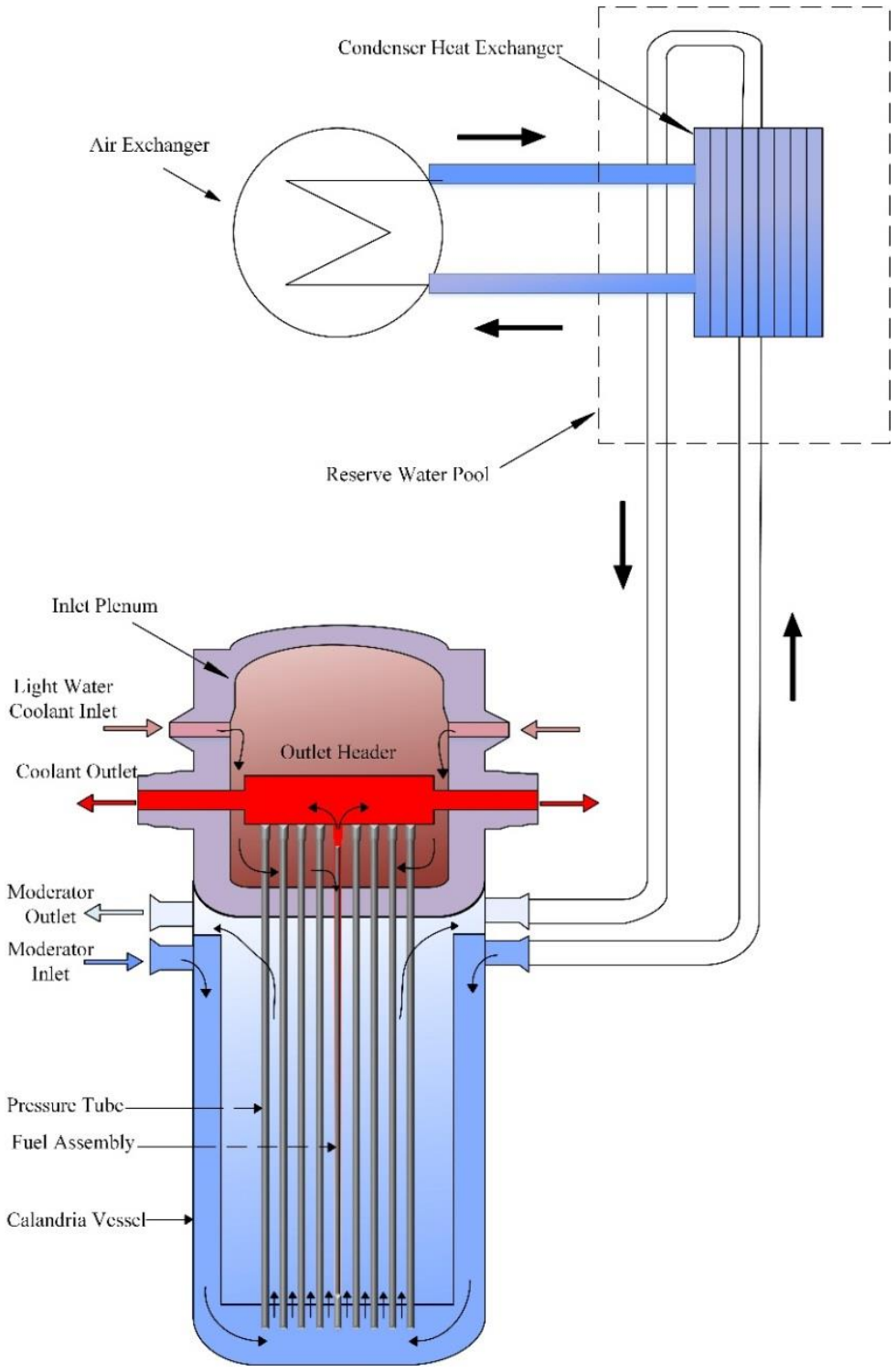

Figure 1.5 Schematic diagram of the passive moderator cooling system.

The system consists of a condenser heat exchanger immersed in the reserve water pool and air heat exchangers. This system could use the moderator to remove heat from the inner tube through conduction-convection heat transfer and, therefore, keeping the fuel cladding below

its melting point for both normal operating and accident conditions. The decay core heat is then dumped into the reserve water pool by the isolation condenser heat exchanger, and air heat exchangers are used to remove the reserve water pool heat. These are all done passively with natural circulation systems, which therefore greatly improves the reliability of the cooling systems and eliminate the possibility of a Fukushima-type core melt accident [14].

1.4 Supercritical Fluids

Literally Supercritical fluid is a fluid that works with both pressure and temperature above its critical point. The critical point of a fluid is thermodynamically denoted as a point of the maximum pressure and temperature at which both liquid and vapor form of the fluid can exist in equilibrium at the same time. In this section, the properties of supercritical fluids, supercritical water and supercritical carbon dioxide, will be introduced.

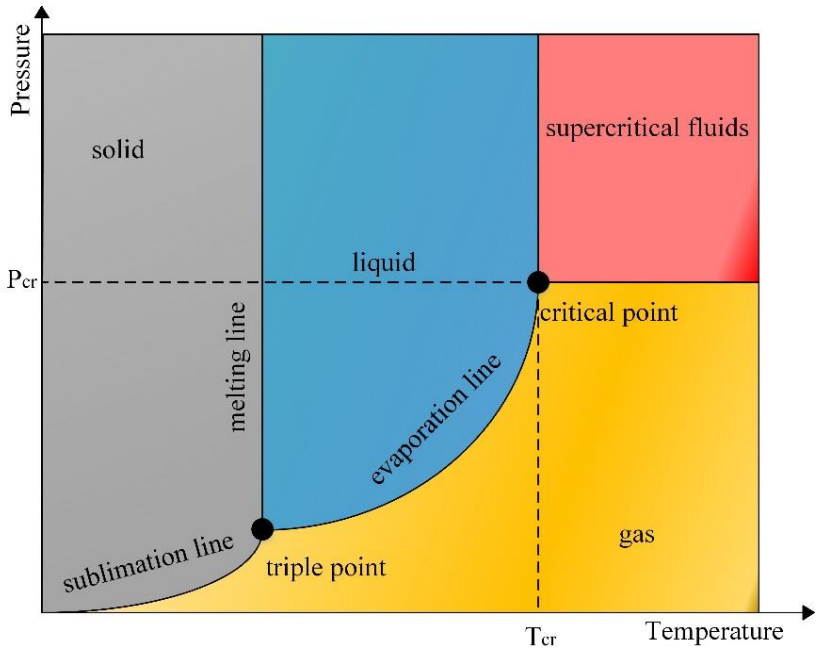

Figure 1.6 Scheme of the phase diagram for water

1.4.1 Supercritical Water

Figure 1.6 shows a schematic of the phase diagram of water. As can be seen, there are two important points in the diagram; one is the triple point where the solid phase, liquid phase,

and vapour phase coexist, the other one is the critical point. The triple point is the intersection of three important lines, respectively the sublimation line, melting line and evaporation line. The sublimation line represents the equilibrium between solid and gas, and the substance changes directly from solid to gas when it is crossed. The melting line separates the solid phase and liquid phase of water, whereas the evaporation line separates the liquid phase and the gaseous phase. The critical point locates at the upper end of the boiling line, which is the highest pressure and temperature can be reached for water with both liquid and vapour phases. The critical point of water is 22.06 MPa for pressure and 373.9 °C for temperature, respectively. The distinctive feature of a supercritical fluid compared to a subcritical fluid is that if a fluid is under supercritical pressures, it will convert from liquid to a vapour-like state smoothly without the appearance of vapour and liquid interface when it is heated continuously.

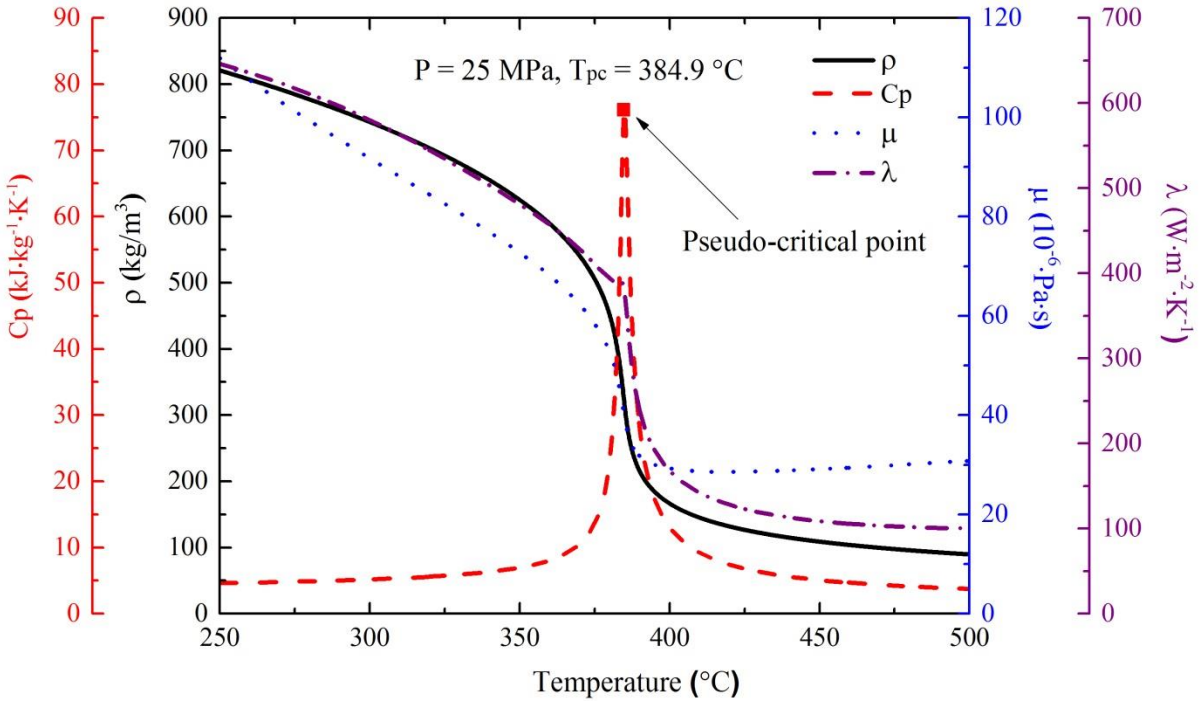

Figure 1.7 Thermo-physical property variations of water at a supercritical pressure of 25 MPa [15]

For each given supercritical pressure, there's a corresponding pseudo-critical point, at which the fluid specific heat capacity (C_p) attains its maximum value. Figure 1.7 shows the properties change of water around the pseudo-critical point (Tpc = 384.9 °C) at 25 MPa. It

can be seen that the properties such as specific heat (C_p), density (ρ), viscosity (μ), and thermal conductivity (λ) will experience a drastic change in the pseudo-critical region. With the increase of temperature, the specific heat goes through a spike while the derivatives of properties such as density, viscosity, and thermal conductivity also experience spikes when passing the pseudo-critical point. For example, at a pressure of 25 MPa, when the water is heated from 377 °C to 393 °C (~ +2.5%), the density reduces radically from 488.85 to 194.89 kg/m^3 (~ -60%).

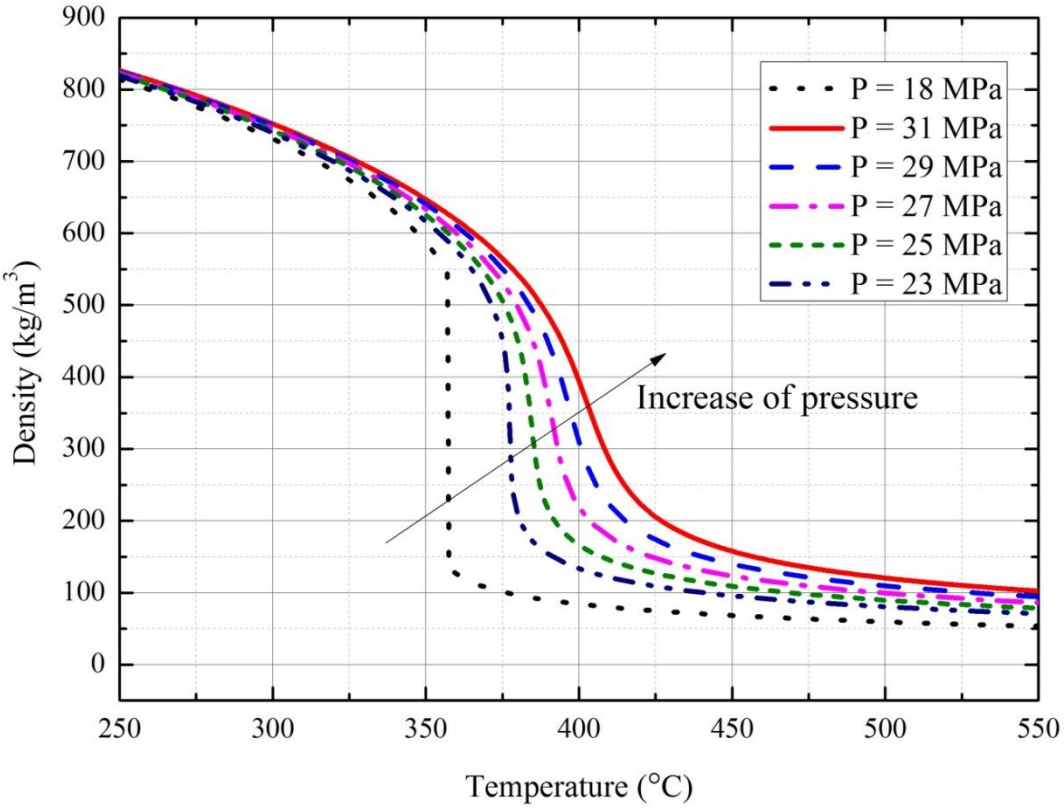

Figure 1.8 Water density vs. Temperature at different pressures [15]

The density change of water at both subcritical and supercritical pressure are also compared and shown in Figure 1.8. It can be observed that density at subcritical pressure of 18 MPa will decrease abruptly with a steep drop at the boiling point. The liquid water becomes liquid and vapour mixture as it is heated through the boiling point. In comparison, the density change at supercritical pressures (larger than P_{cr} = 22.064 MPa) is more smooth when the temperature surpasses the pseudo-critical point. With more heat, the supercritical water will turn into a vapour-like state liquid and the phase interface completely disappears. Another

feature can be observed from Figure 1.8 is that with the increase of system pressure, the change of water properties like density (not limited to density) is less drastic. This will actually induce a smaller perturbation to the system when it is heated across the pseudo-critical point.

1.4.2 Supercritical CO_2

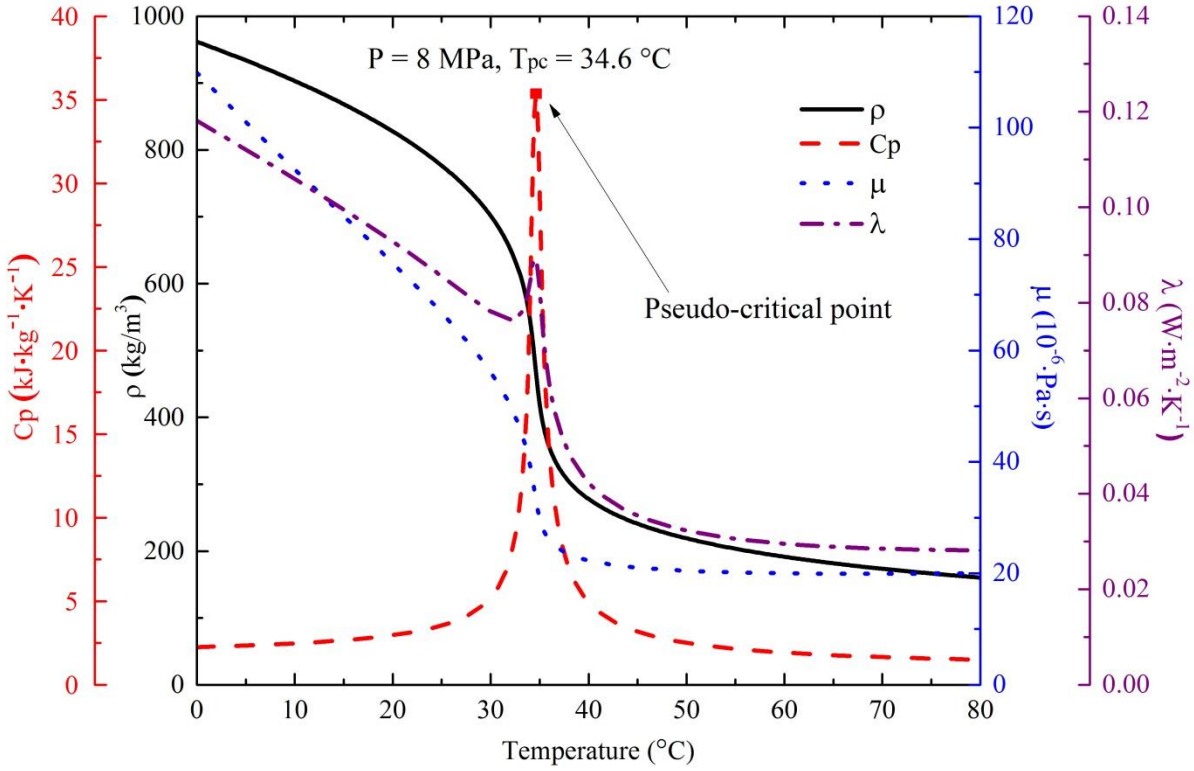

Figure 1.9 Supercritical CO_2 properties at 8 MPa [15]

As one of the supercritical fluids, supercritical CO_2 has already been widely used as a solvent in CO_2 extraction; potential applications include power generation, chemical reactions, polymer production and processing, semiconductor processing, powder production, environmental and soil remediation and dry cleaning [16]. It can be seen from Figure 1.9 that thermo-physical property variations of carbon-dioxide at supercritical pressure of 8MPa are very similar to those of supercritical water. The main properties such as specific heat (C_p), density (ρ), viscosity (μ), and thermal conductivity (λ) also experience a drastic change at the vicinity of pseudo-critical point. Compared with water, CO_2 has a much lower critical point of P_{cr} = 7.39 MPa and T_{cr} = 32.1 °C.

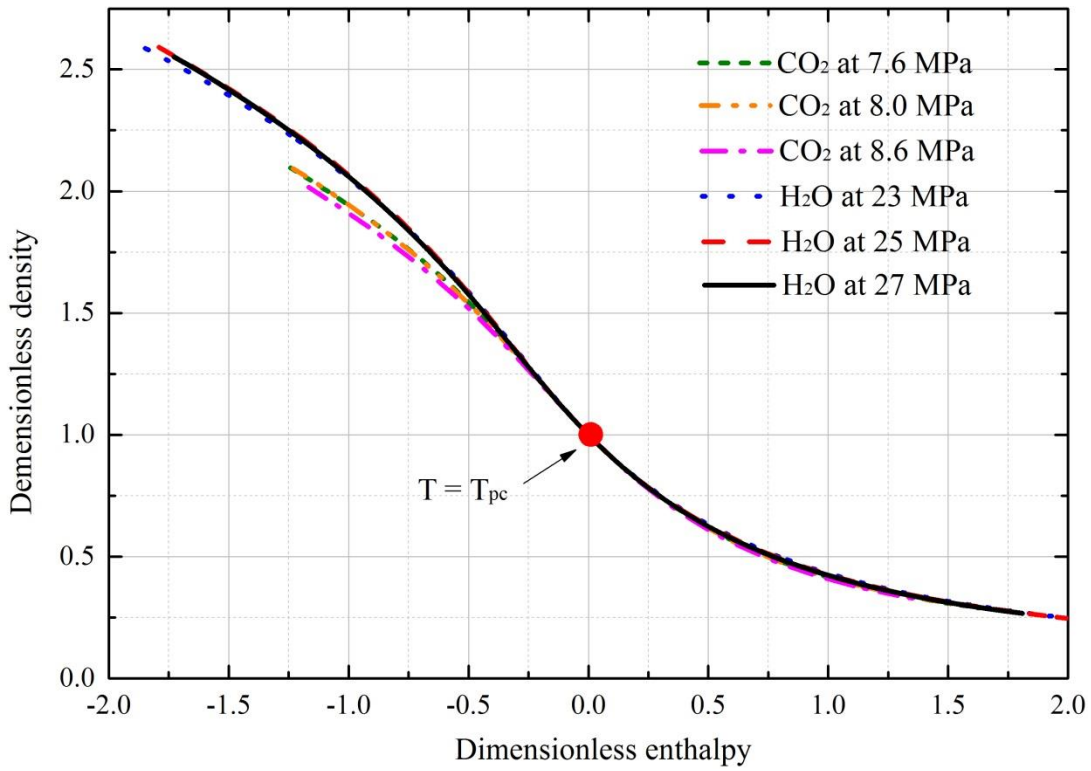

Figure 1.10 Dimensionless density trends as a function of dimensionless enthalpy for water and CO_2 [15]

Further analysis done by Ambrosini [17] shows that the thermophysical properties of density and enthalpy of water and CO_2 agree very well under various supercritical pressures in the dimensionless form, as shown in Figure 1.10. The dimensionless enthalpy and density are defined as follows [17]:

$$h^* = \frac{\beta_{pc}}{C_{p,pc}}(h - h_{pc}) \qquad \text{Equation (1-1)}$$

$$\rho^* = \frac{\rho}{\rho_{pc}} \qquad \text{Equation (1-2)}$$

Although there's a slight discrepancy at the heavy fluid part ($T < T_{pc}$), the dimensionless curves match strikingly well starting from the pseudo-critical point to the light fluid region ($T > T_{pc}$). Non-flammable, non-toxic, relatively lower cost, ambient critical temperature, and most importantly the similar thermodynamic state compared with water; all these advantages make supercritical CO_2 a good substitute for experimental study about thermodynamic

behaviour of supercritical water. In the present thesis, supercritical CO_2 is selected as the working fluid for experimental investigation.

1.5 Flow Instabilities of Thermo-hydraulic Systems

Before the classification of flow instability occurring in thermo-hydraulic systems, it is important to define the flow instability first. A system is considered stable if the key parameter such as mass flow rate returns to its original state after either external perturbations (fluctuations in mass flow rate, inlet temperature, heat input, etc.) or internal perturbations (flow pattern transitions). The system is assumed to be unstable if it stabilizes to a new steady state (static instability) or oscillates with increasing amplitude (dynamic instability). It should be noted that the unstable oscillation of all thermo-hydraulic systems will finally fluctuate with limited amplitude because of the nonlinearities of the system (Hopf bifurcation). Usually amplitudes more than 10% of the mean value is considered as an indication of instability, otherwise the system is assumed to be neutrally stable [18].

Based on the analysis method, the thermo-hydraulic instabilities are mainly classified as static instabilities and dynamic instabilities. The static instability of a system may have multiple steady-state solutions. As for dynamic instability, it involves multiple regenerative feedbacks between the flow rate, pressure drop, void fraction, etc. The dynamic behaviour is time dependent and fully transient governing equations are required to explain the phenomenon as well as predict the threshold [19]. Figure 1.11 is a summary of the classification of two phase flow thermo-hydraulic instabilities discussed by Boure et al. [19] and Fukuda et al. [20]. Amongst these two phase flow instabilities, Ledinegg static instability, density wave oscillations and pressure drop oscillations are the most commonly observed and studied thermo-hydraulic flow instabilities of boiling systems. Follow the extensive review of Boure et al. [19], these three types of flow instabilities are discussed as follows. Flow instabilities occur with natural circulation systems are also briefly introduced.

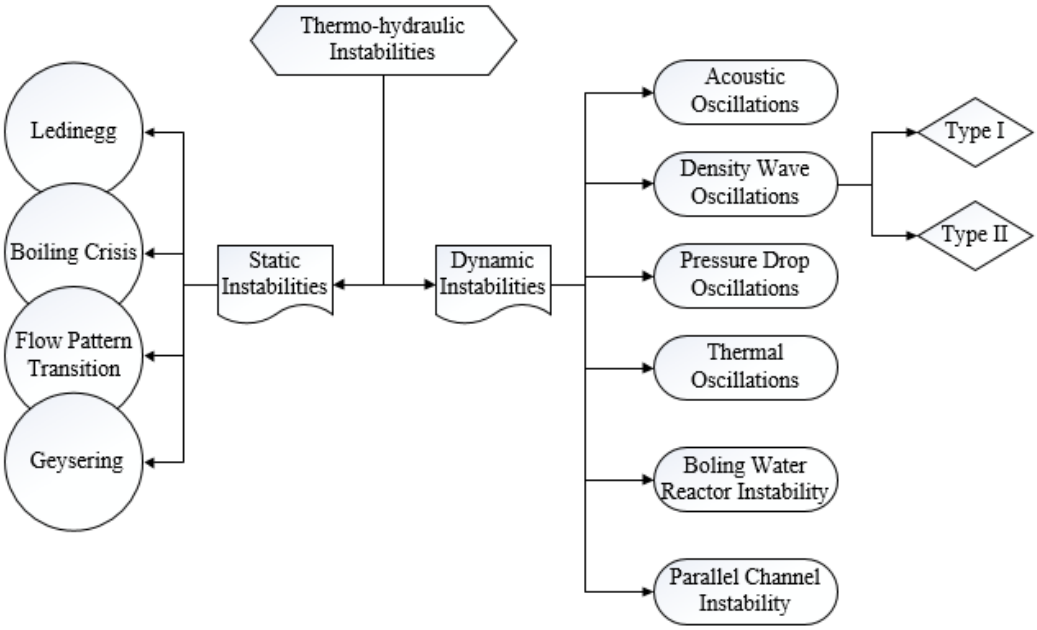

Figure 1.11 Types of thermos-hydraulic instabilities of two phase flow

1.5.1 Ledinnegg Instability

Ledinnegg static instability is also known as flow excursion. Flow will undergo a sudden, large amplitude drift from its initial state in an excursive way, and finally stabilizes at a lower or higher value than the initial without returning to the initial state. This occurs when the loop supply pressure drop – flow rate curve (external characteristic) is larger than the channel demand pressure drop – flow rate curve (internal characteristic) [19]. The mathematical model of the pressure drop – flow rate curve of two phase flow in a heated channel is a cubic equation and a typical curve is shown in Figure 1.12. If the nominal operation point is *a*, a slight decrease in mass flow rate will make the demand pressure drop larger than the supply pressure drop and the mass flow rate will decrease further until it reaches a new balance at point *b*. This spontaneous shift of operation point will cause a significant drop of mass flow rate. With the same heating input, the occurrence of Ledinegg instability may cause a dryout of the channel wall. Ledinegg instability can be delayed by installing an inlet throttle valve to make the external characteristic steeper than that of internal characteristic [19].

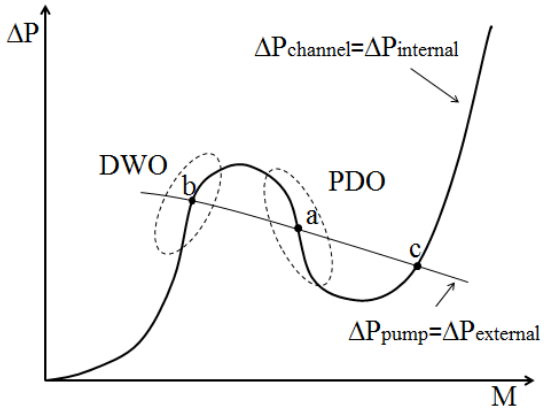

Figure 1.12 Pressure drop across a heated channel vs. the mass flow rate

1.5.2 Pressure Drop Oscillations

Pressure drop oscillations (PDOs) are classified as a compound dynamic flow instability, which is triggered by a static instability phenomenon. Pressure drop oscillations are always found to be on the negative slope of the pressure drop – flow rate curve when there's a compressible volume such as a surge tank upstream of the heated channel or considerable "large" compressible volume at a very long heated section [19]. Pressure drop oscillations usually occur with large fluctuation amplitudes of key parameters and the frequency is less than 1 Hz depending mainly on the compressibility of the surge tank. An explanation of mechanism of pressure drop oscillations was given by S. Kakac and B. Bon [21] and will not be repeated here. It should be noted that the pressure drop oscillations could be eliminated by adding a throttling device between the surge tank and heated section.

1.5.3 Density Wave Oscillations

Density wave oscillations (DWOs) are one of the most commonly seen dynamic instabilities and usually occur on the positive slope of the pressure drop – mass flow rate curve [19], as shown in Figure 1.13. A boiling channel with sub-cooled inlet conditions usually consists of three regions with heat input of the channel: the single-phase liquid region, two-phase liquid-vapour mixture region, and the single-phase vapour region. Any internal or external disturbances may cause variations in local heat transfer processes and the distribution of each

phase. Under certain circumstances, when the feedbacks of mass flow rate, pressure drop, and void fraction become 180 ° out of phase, self-sustained density wave oscillations occur. Following is a simple explanation of the mechanism of density wave oscillations.

As is shown in Figure 1.13, a simple model consisting of a water supply tank, a heated channel with exit flow restriction is adopted for analysis of density wave oscillations. For steady-state flow, the pressure at the heated channel inlet (P_{in}) and outlet (P_{out}) as well as the vapour generation rate are constant.

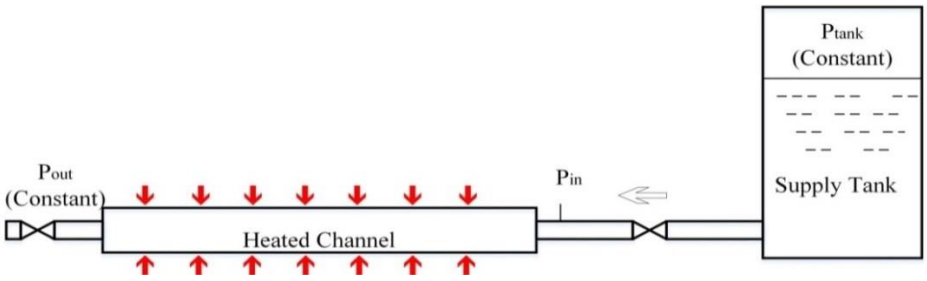

Figure 1.13 A simplified system for density wave oscillations

With the increase of heat input, liquid-vapour mixture will appear at the exit of the heater. At a specific given heat input, suppose the liquid-vapour mixture restricts at the channel exit and cause a sudden infinitesimal increase of pressure P_{out}. This pressure perturbation will transmit spontaneously to the channel inlet and cause an increase in pressure P_{in}. Since the total pressure drop (P_{tank} - P_{out}) is constant, the pressure drop (P_{tank} - P_{in}) will increase, resulting in an increase of mass flow rate at the channel inlet. It can be seen from Figure 1.12 that on the positive slope of the curve, the pressure drop (P_{in} - P_{out}) will go up with increase of mass flow rate. As the fluid particle travels to the channel exit, the pressure drop (P_{tank} - P_{in}) will decrease because the total pressure drop (P_{tank} - P_{out}) is constant. This will further cause a decrease in mass flow rate at the channel inlet. With the same heating input, a smaller mass flow rate means more liquid-vapour mixture generating at the heated channel exit, which causes a pressure perturbation at the restriction and the whole process starts over again. The whole cycle will become self-sustained once a specific phase lag between the pressure drop and mass flow rate is met. From the analysis, it is found that for a typical density wave

oscillation, the period is about two times the residence time of a fluid particle in the heated channel [21].

Fukuda and Kobori [20] conducted both experimental and numerical studies on forced and natural circulation loops with two-phase flow and further classified the density wave oscillations into type I and type II from the phenomenological point of view. The unstable regions for type I and type II instabilities with both forced (curve A) and natural circulation (curve B) loops are shown in Figure 1.14. Type I instability occurs at very low steam quality conditions ($x_{out} \cong 0 \sim 10\%$) with low power and high inlet sub-cooling, of which the gravitational pressure drop in the unheated riser plays a dominant role. Type II instability occurs at relatively high power and steam quality ($x_{out} \geq 30\%$), of which the frictional pressure drop in the heated section as well as in the riser section plays a dominant role.

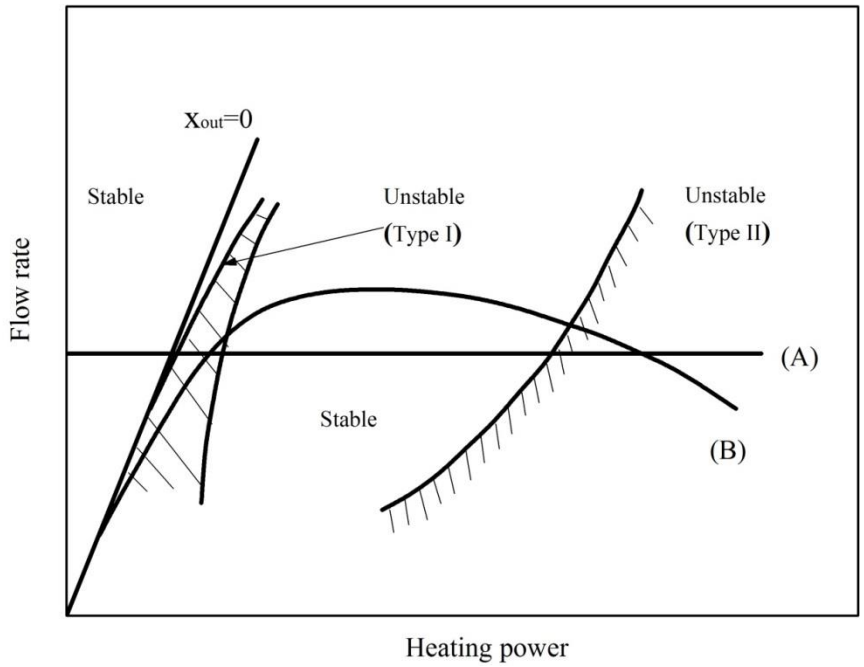

Figure 1.14 Stability regions of type I and type II for both forced (A) and natural (B) circulation loop (reproduced based on [20])

1.5.4 Flow Instability of Natural Circulation Systems

Flow instabilities occur in boiling heated channels can also exist in natural circulation systems. And natural circulation systems are inherently less stable compared with forced circulations of boiling heated channels due to the nonlinear nature of the natural circulation

phenomenon. The fluid behaviors in natural circulation systems are very complex due to combined effects of buoyancy and flow acceleration. It is known that the change of heating power will affect the driving force, causing a change in flow rate which in turn affects the driving force. For example, the change of heating power will affect the vapor generating rate. As the vapor state fluid (light fluid) moves along the riser section, it enhances the driving force and, therefore, increases the flow rate. If the flow rate increases, with the same heat input, the vapor generation rate will decrease, more heavy fluid moves along the riser section, causing the decrease of driving buoyancy force and, hence, the flow. Oscillatory behaviors can occur when special conditions of feedbacks are met between the driving force and flow rate. As a result, natural circulation systems are more susceptible to flow instabilities than boiling channels with forced circulation. Usually flow instabilities occur with boiling channels also happen with natural circulation systems, but flow instability with subcritical single phase was only found with natural circulation systems [18].

1.5.5 Supercritical Flow Instabilities

In spite of the benefits of SCWRs listed in section 1.2, sharp changes of water physical properties (mainly the large change of density) similar to two-phase flow happen when the water temperature transitions through the pseudo-critical point, as shown in Figure 1.8. As was mentioned in previous section 1.5.3, a boiling channel with sub-cooled inlet conditions usually consists of three regions with heat input of the channel under subcritical conditions: the single-phase liquid region, two-phase liquid-vapour mixture region, and the single-phase vapour region. Similarly, a heated channel with supercritical fluids can also be divided with three regions: the “heavy fluid region”, “heavy and light fluid mixture”, and the “light fluid region” [22]. This analogy between the two suggests that thermal hydraulic instabilities that occur under subcritical conditions are highly likely to occur under supercritical conditions. It was already found that density wave oscillations similar to two-phase flow also occurred under supercritical conditions, whereas Ledinegg instability and pressure drop oscillations

were uncommon because the pressure drop – mass flow rate curve shown in Figure 1.12 doesn't have a negative slope under normal supercritical conditions [23].

Flow oscillations are highly undesirable as they may lead to mechanical vibrations, problems in system control, and in extreme circumstances, the heat transfer surface may burn-out and heat transfer deterioration can occur. Thermal fatigue is another potential cause of damage which a thermal reactor may experience during continual cycling of wall surface temperature in a closed loop. Thermal stresses in the wall and cladding material may cause mechanical breakdown and in the worst case scenario, release radioactive materials [21]. Hence, the study of flow characteristics in supercritical natural circulation systems (SNCLs), especially their different performances with varied loop geometries and boundary conditions, becomes essential in system design and operation.

The main methods used in most of the reported works are theoretical in nature, with 1D codes being frequently adopted. Experimental studies of NCLs with supercritical water available in open literature are rare in number compared to subcritical flow instability studies [24]. One of the main reasons is the high pressure, high temperature working conditions of water. Thus, some substitute fluids with similar properties change like CO_2 become appealing because they can be safely operated at relatively lower pressures and temperatures with lower costs [25]. In the present study, supercritical CO_2 was used as the working fluid for the experimental work (as explained in section 1.4.2), and supercritical water was used for the numerical studies.

1.6 Research Objective

Present study focuses on supercritical flow instabilities in NCLs. A supercritical natural circulation loop with horizontal channels [26] and one vertical loop with two parallel channels were constructed at University of Manitoba for the purpose of gaining insights into flow characteristics of SNCLs and providing good and plenteous experimental flow instability data. A licensed non-linear CATHENA (version3.5.4.4) code [27] was also adopted to model and interpret the experimental results presented.

To be specific, objectives of present study are:

1) Develop a generic understanding of flow stability in natural circulation loops with supercritical fluids.

2) Enrich the data bank of supercritical flow instability experiment.

3) Conduct effect study such as different loop configurations and parameters to see how it affects the flow instability boundary.

4) Numerically analyze the same experimental loop with supercritical water to gain more insights into the flow instability phenomenon with SNCLs and find plausible measures for suppressing or even diminishing the flow instability.

1.7 Outline of Thesis

Chapter 1 introduces the background of present work, which mainly includes the nuclear energy, supercritical water reactor, natural circulation system, supercritical fluids, and flow instabilities of thermal hydraulic systems. The research objectives as well as outline of thesis are also proposed.

Chapter 2 reviews the supercritical flow instabilities in single heated channels, parallel channel systems, and natural circulation loops. A summary of the supercritical flow instability study on NCLs is also made.

Chapter 3 describes the experimental set-up, components, instrumentation, test procedures and methods used in obtaining the flow instability data.

Chapter 4 presents the experimental flow instability results of a natural circulation loop with single horizontal channel. Totally 13 flow instability cases are collected and summarized. Then a base experimental case is selected and flow instability study with four different loop configurations are tested and compared. Valves on the connecting line of the rectangular loop and the accumulator or settling tank are also throttled and studied about its effect on flow instability behaviour. The parameter effects such as pressure, outlet valve local K factor, and inlet temperatures are also presented.

In Chapter 5, the non-linear CATHENA code is introduced and used to model supercritical water flow instability of the natural circulation loop. Physical model and governing equations are introduced. Mesh sensitivity test is conducted and the code is validated with available steady-state experimental water data. The numerical work is first conducted with a simplified open loop model without wall heat structures and the accumulator. Parameters that affect the steady-state results are studied. The accumulator is then represented by a reservoir with constant pressure and temperature. The valve effect on the connecting line is also investigated.

Chapter 6 summarizes the main findings and also presents some recommendations for future work.

CHAPTER 2

LITERATURE REVIEW

2.1 Review of Supercritical Flow Instabilities

Since flow instability is a well-known phenomenon in power-engineering systems, plenty of work has been performed under both subcritical and supercritical pressures with various systems. Single channel, parallel channels and natural circulation loops could all be considered and studied in this area. The present literature review is mainly focused on the supercritical flow stability analyses.

2.1.1 Supercritical Flow Instability of Single Heated Channels

Zuber [28] carried out one of the earliest analytical flow instability study on supercritical heated channels. A two-region model with “liquid like region” and “gas like region” of a heated channel was proposed and analyzed. Similarities of thermodynamic state under subcritical, near critical and supercritical conditions were pointed out. Mechanisms of flow oscillations at both low and high inlet sub-cooling conditions were discussed, stability map for defining the areas of stable and unstable was constructed and some suggestions were made to eliminate the onset of flow oscillation.

Fukuda et al. [20] experimentally studied flow instabilities of a forced circulation system with supercritical helium as the working fluid. Three types of flow oscillations were identified, namely type A, B, and C. Type A oscillation was confirmed to be a Helmholtz type, which was caused by acoustic resonance. When type A oscillation occurred, pressure at both inlet and outlet were oscillating but the fluid temperature did not oscillate. Type B and C oscillations were density wave oscillations and occurred at high heating power or low flow rate conditions when the inlet temperature was lower than the pseudo-critical temperature and the fluid at the test section exit crossed the pseudo-critical temperature. Based on the transit time and oscillation period, type B oscillation was found to be mainly caused by the pressure

drop in the tubing from the inlet plenum to the flow-regulating valve, whereas type C oscillation was caused by pressure-drop characteristics in the test section. The feature of type B oscillation was that both pressure and temperature oscillated with long periods and large amplitudes and for type C oscillation it was similar but with a shorter period.

Yi et al. [29] performed a linear thermal-hydraulic stability analysis of the supercritical light water cooled reactor design SCLWR-H with the frequency domain method at both full power and partial-power operating conditions. The stability analysis code was developed by using a linearized one-dimensional, single-channel, single-phase model. Results revealed that with proper orifice pressure drop coefficient, the SCLWR-H design could be operated safely at normal condition as well as during partial power operations. Parametric effects study also suggested that increasing the orifice pressure drop coefficient, decreasing the power to flow ratio, or decreasing the inlet temperature could stabilize the system.

Zhao et al. [22] developed a three-region model by dividing the heated channel with supercritical water into three regions such as “light fluid region”, “heavy and light fluid mixture region”, and “heavy fluid region”. Stability maps defining the onset of density wave oscillations were presented with the newly developed pseudo sub-cooling number and expansion number. Both Ledinegg static instability and density wave oscillations were analyzed with the frequency domain method. According to the stability maps, increase of the inlet orifice, inlet flow, or system pressure would make the single channel more stable. At low pseudo sub-cooling numbers, increasing the inlet temperature would destabilize the channel, whereas increasing the inlet temperature would stabilize the channel at high pseudo sub-cooling numbers.

Ortega Gómez et al. [30] performed stability analysis of a uniformly heated channel with supercritical water. Following the work of Zhao et al. [22], new non-dimensional parameters, namely pseudo-phase-change number and pseudo-sub-cooling number, were proposed for supercritical water for the neutral stability plane. A typical pressure drop – mass flux curve for the uniformed heated channel with supercritical water showed that Ledinegg excusive

instabilities and pressure drop oscillations would not occur because there was no negative sloping region of the curve. Linear stability results showed that using an approximate equation of state with two-region or three-region model predicted an overly conservative neutral stability boundary.

Ambrosini [23] presented an analogy of instability analyses of water flowing in heated channels under both boiling and supercritical conditions. A uniformly heated channel was utilized and modeled with the RELAP5/MOD3.3 code for both conditions. It was confirmed that density wave oscillations occurred at both conditions were very similar, whereas the Ledinegg instability, which was commonly observed with boiling heated channels, only occurred with very low inlet temperatures under supercritical conditions and was far from the normal operation of a SCWR channel.

Ambrosini et al. [17] proposed novel non-dimensional parameters and analyzed the stability of a heated channel with supercritical fluids. With the pseudo-critical condition as the only reference state, the new dimensionless parameters, trans-pseudo-critical number and sub-pseudo-critical number actually represent the counterparts of the classic sub-cooling and phase change numbers of two-phase boiling channels. One of the advantages by adopting the pseudo-critical point as the reference state was that a single dimensionless density – dimensionless enthalpy curve could be generated regardless of the supercritical pressure, which make it possible to use these non-dimensional parameters to scale the system from one fluid to another.

$$N_{tpc} = \frac{Q_{channel}}{M_{channel}} \frac{\beta_{pc}}{C_{p,pc}} \qquad \text{Equation (2-1)}$$

$$N_{spc} = \frac{\beta_{pc}}{C_{p,pc}} (h_{pc} - h_{in}) \qquad \text{Equation (2-2)}$$

The effectiveness and generality of these non-dimensional groups were further assessed by Ambrosini et al. [31, 32] with different supercritical fluids. However, the dimensionless groups were not thoroughly assessed for stability boundary predictions. It was found that

these new non-dimensional parameters were not limited to supercritical water stability analyses; they could also be applied for a variety of supercritical fluids such as supercritical CO_2, R23 and Ammonia.

C. T'joen [33] conducted a sensitivity linear stability analysis of a vertical heated supercritical channel with the Comsol® software package. It was found that property uncertainty had a very small effect on the threshold of flow instability, whereas the friction factor and heat flux distribution had a significant effect of about 1.7 ~ 3%. The most significant propagating uncertainty was found to be the geometry, a tolerance of as high as 10% could be caused by a given ±25 um uncertainty of the hydraulic diameter of the physical model selected in the study.

Tian et al. [34] developed a code named FREDO-CSR1000 and analyzed the flow instability of a SCWR design CSR1000 with the frequency-domain method. Both an average power channel and a hot channel were investigated and a stability map was constructed. It was concluded that the onset of the flow instabilities was when the fluid temperature approached the pseudo-critical temperature. The stability map showed that the channel with average power was more stable than the hot channel.

Chatoorgoon [35] proposed and assessed new non-dimensional parameters for static instability of supercritical fluids in heated channels. Unlike the non-dimensional parameters developed by previous researchers (Zhao et al. [22]; Ortega Gómez et al. [30]; Ambrosini and Sharabi [17]), these new dimensionless parameters were specially derived for predicting flow instability boundary of a heated channel and therefore might be useful for engineers as a design tool. The results of the flow instability analysis showed that there was a cut-off temperature above which there would be no static instability. It was also found that vertical down-flow was the orientation most susceptible to have static instability and vertical up-flow was the orientation least likely to exert static instability compared to horizontal flow. Non-dimensional parameters for oscillatory flow were also developed.

Zhang et al. [36] proposed a new three-region model and conducted an analysis of density wave oscillation inside heated tubes with the frequency domain method. This three-region model adopted a regional partition method to divide the large variations of physical properties of supercritical water in tubes by using two newly defined parameters, pseudo-critical water temperature and pseudo-critical steam temperature. These two temperatures were determined by the optimal value of volume expansion coefficient. Results showed that the predicted instability threshold were within ± 26% relative error range of the compared experimental results, whereas all the previous models (Zuber [28]; Zhao et al. [22]) were greater than 30%.

With the development of hardware for computations, computational fluid dynamics (CFD) has become an economic and powerful tool in analyzing the fluid hydraulics in supercritical systems. More and more work is reported in the supercritical flow instability area.

Sharabi, M. B et al. [37] was probably one of the earliest in open literature who had presented a prediction of flow instability in a supercritical heated channel with the CFD FLUENT code. The addressed physical model was a 2-D tube which had the same dimensions as those used in Ambrosini et al. [23, 31] for comparison of the results. Heating power was slowly increased until the occurrence of flow rate oscillations while keeping the pressure drop across the heated channel constant. It was found that both the standard k-ε model and the more detailed low-Reynolds model could predict the onset of density wave oscillations at relatively large power-to-flow ratio in the supercritical heated channel.

Sharabi, M.B et al. [38] performed a follow-up CFD study with a 3-D stability analysis of SCWR rod bundle sub-channels. Transient analysis was also reported with the 1-D RELAP5 code. It was found that the characteristics of the density wave oscillations in triangular and square pitch rod bundles were similar as those in circular channels. Moreover, the density wave mechanism was nearly the same.

With the help of a 3-D CFD code STARCCM+ and 1-D RELAP5 code, Ampomah-Amoako et al. [39-41] carried out a series of flow instability studies on 3-D nuclear reactor

sub-channels and 1-D heated channels with supercritical water. The first part of the research was mainly focused on pure thermo-hydraulic flow instabilities. A CFD methodology was first developed, relatively coherent results of the periods of the oscillations and the stability thresholds for different physical models confirmed the capabilities of the considered CFD code and suggested that the instability phenomenon of heated channels was mainly characterised by 1D behaviour. For the second part, the coupled neutronic–thermal hydraulic instabilities in a sub-channel slice belonging to a square lattice assembly were analyzed with a point kinetic neutronic model. Vertical upward flow, vertical down flow, horizontal flow were all studied with both STAR-CCM+ and RELAP5 code. Decay ratio and period of oscillations generally agreed well with different flow directions between the results of the two codes except the different behaviours predicted for the bottom peaked power distribution with vertical upward flow, which could be considered as a good starting point for further utilization of CFD codes in supercritical flow instability analysis of heated channels.

Dutta et al. [42] developed a 1-D nonlinear thermal-hydraulic code (THRUST) for analyzing the density wave oscillations in the CANDU SCWR. The THRUST code was first validated with the numerical results of Ambrosini et al. [17] and T'Joen et al. [33] and then a simplified U-shape single heated channel was adopted for flow instability analysis. Parametric studies showed that high power to mass flow ratio would make the CANDU SCWR more unstable, an increase in flow rate or inlet orifice pressure drop coefficient would always stabilize the system, increasing the outlet orifice will always destabilize the system, and sinusoidal heat flux made the system more unstable compared with uniform heat flux with higher pseudo-phase-change number.

Ebrahimnia et al. [43] studied the supercritical flow instability of a single heated channel with the numerical ANYSYS CFX code. Supercritical water was the working fluid. Two different turbulent models, k-ε and SST were tested on the predictions of both excusive and oscillatory flow instabilities and compared with the in house 1-D SPORTS code [44]. Results showed that thresholds of the instability predicted by the two turbulent models as well as the 1-D

code agreed well. In addition, turbulent Prandtl number variation was found to have negligible effects on the flow instability boundary.

2.1.2 Supercritical Flow Instability of Parallel Heated Channels

Supercritical flow instability in parallel channels includes the two-parallel system and multi-channel system. The former usually consists of two parallel tubes; the latter is focused on all the parallel sub-channels of a reactor core.

Chatoorgoon [45] conducted a flow instability study of two horizontal parallel tubes with supercritical water. A point heat source model was used to analytically derive the non-dimensional parameters that defined the instability boundaries. Results show that supercritical flow instability in horizontal channels is driven by the state property variation of density with enthalpy and the second derivative of density with enthalpy is a dominant term for the onset of flow oscillations in horizontal flow.

Hou [46] investigated the flow stability of multi-parallel channels of a newly designed mixed-spectrum SCWR (SCWR-M) which had a fast spectrum zone; both the linear frequency domain method and non-linear time-domain method were used. The linear stability results showed that the fast zone of SCWR-M design had a wide range of stable operating conditions; the non-linear results showed that a transitional stability region existed. In addition, the power distribution effect was also analyzed and it was found that a uniformly axial power distribution was more susceptible to flow instability than those with cosine-shaped or fork-shaped distributions.

A follow-up study on flow instability in parallel channels of the mixed-spectrum SCWR (SCWR-M) with a thermal spectrum zone was carried out by Liu [47] with frequency-domain and time-domain methods. It was concluded that the linear results and non-linear results agreed well with each other and this design also had a large safety margin. In addition, the heat transfer effect on flow instability phenomena showed that decreasing the wall thermal conductivity could improve the system stability and unlike the fast spectrum zone design, the system was not very sensitive to the distributions of axial power.

Xiong et al. [48] conducted an experimental study of flow instability in two vertical parallel channels with supercritical water flowing upward. The test section was made of two circular INCONEL 625 tubes with inner diameter of 6mm and outer diameter of 11 mm. Investigations showed that the evolution of the flow rates could be divided into four stages, quasi-symmetrical flow, asymmetrical flow caused by redistribution, irregular fluctuation, and the parallel flow instability. Totally nine oscillatory flow instability boundary points were obtained at various flow conditions. Parametric effects study indicated that increasing the system pressure and decreasing the inlet temperature made the system more stable.

Xiong et al. [49] developed a 1-D non-linear in-house code and conducted an analysis of supercritical flow instability in a simplified parallel channel system, which was proposed based on the experimental parallel-channel system [48]. The comparison between the numerical results and experimental results showed good agreement on the predictions of the flow instability boundary. A study of the inlet temperature revealed that the inlet temperature had a non-monotonic effect on the flow instability threshold.

Following the line of research done by Xiong et al. [48, 49], Xi et al. [50] used the 3-D CFD CFX code and investigated the flow instability of the parallel channel system. The numerical results were compared with previous experimental data and 1-D code results; it was found that the CFX code was able to capture the onset of the flow oscillations and the flow instability boundary predicted was better than the 1-D code used by Xiong et al. [49]. However, this conclusion was not borne out by the study of Li et al. [51].

Li et al. [51] performed a further numerical study of Xiong's experiments with the 3-D ANSYS CFX code and 1-D non-linear SPORTS code. Their results were not only compared with the experiment but also with the previous 1-D and 3-D predictions of Xiong's [49] and Xi's [50]. The drawbacks of both Xiong's 1-D and Xi's CFX results were pointed out. For Xiong's 1-D predictions, wrong boundary conditions imposed at the inlet and outlet of the channels were found. Improperly temporally converged results were found in Xi's CFX predictions. As a result, the conclusion stated by Xi et al that 3-D CFX predictions of the

actual experiments were better than 1- D predictions were not supported by Li's study. As their 1-D SPORTS predictions had a smaller RMS error than the CFX results, it appears that the 1-D results are better than the 3-D CFX results. However, they also suggested that further comparison between 1-D and 3-D CFX predictions should be made when the outlet total pressure can be specified in CFX. Furthermore, the order of transient scheme was examined by Li et al. The first order transient scheme was suggested for use due to its consistence and reliance.

Xi et al. [52] further conducted another similar experiment of supercritical water flowing upward in vertical parallel channels. The experimental loop configuration was the same as that of Xiong's [48], except that a larger wall thickness in the heated parallel channels was adopted. The effect of axial power shape on the flow instability was studied by dividing each heated channel into two sections so heating power could be controlled separately. Results showed that instability occurred even with a thick INCONEL 625 tube (Inner diameter of 6mm and outer diameter of 19mm) when axially deceased power shape was added at the outlet section. One of the oscillatory instability was found when the outlet temperature was close to pseudo-critical temperature and another one occurred when the exit temperature was larger than 500 °C. In addition, compared with axially deceased power shape, the system with uniform axial power shape is a more stable system and that parallel channel flow instability was not found in cases with axially increased power shape.

Following the previous stability analysis of a single heated channel [42], Dutta et al. [53] modified the 1-D nonlinear code THRUST and performed a stability analysis of multi-parallel channels in a CANDU SCWR design. Both in-phase and out-of-phase density wave oscillations were investigated without considering the neutronic reactivity feedback. Results indicated that asymmetric heating power would make the CANDU SCWR much more unstable. The CANDU SCWR had a larger stable zone for the in-phase mode than the out-of-phase mode.

Zhang et al. [54] experimentally investigated supercritical flow instability of two vertical parallel channels with supercritical water. Similar to Fukuda's [20] classification of two-phase density wave oscillations, two types of flow oscillations, namely type I (in-phase) and type II (out-of-phase), were identified during the experiment. Type I instability had long period and occurred at lower heating power region when the channel exit temperature approached the pseudo-critical temperature, which was similar to the type I two-phase flow instability occurring at low steam quality. Type II instability had a much smaller period and occurred at relatively higher heating power with a much larger enthalpy at the exit.

2.1.3 Supercritical Flow Instability of Natural Circulation Systems

Chatoorgoon [55] analytically and numerically studied a rectangular natural circulation loop with supercritical water. The instability boundary of the SNCLs was postulated to be at the peak point of the steady state flow-power curve and corresponding non-dimensional parameters were analytically derived based on an idealized point heat source and sink model. The dimensionless parameters were then verified with numerical results of the non-linear SPORTS code and good agreement (6% difference) of the flow instability prediction was achieved.

Chatoorgoon et al. [25, 56] further conducted an extensive numerical analysis of 94 H_2O cases and 145 CO_2 and H_2 cases with both non-linear SPORTS code and an in-house linear code. Various parameters like inlet temperature, channel inlet and outlet local loss K factors, and loop heights and lengths were tested for the validation of the previous derived dimensionless parameters [55]. Results showed that the flow instability boundaries were around the peak steady state flow rate with 95% accuracy, the non-dimensional parameters originally proposed based on a point heat source and sink model with supercritical water appeared to be valid parameters defining the stability boundary of supercritical system with distributed heating and cooling. In addition, other supercritical fluids like CO_2 and H_2 were also studied and it was found that flow instability characteristics of supercritical CO_2 was very similar to that of supercritical water with a natural circulation system, so CO_2 was

suggested as an experimental supercritical fluid because of lower cost and safer operational conditions.

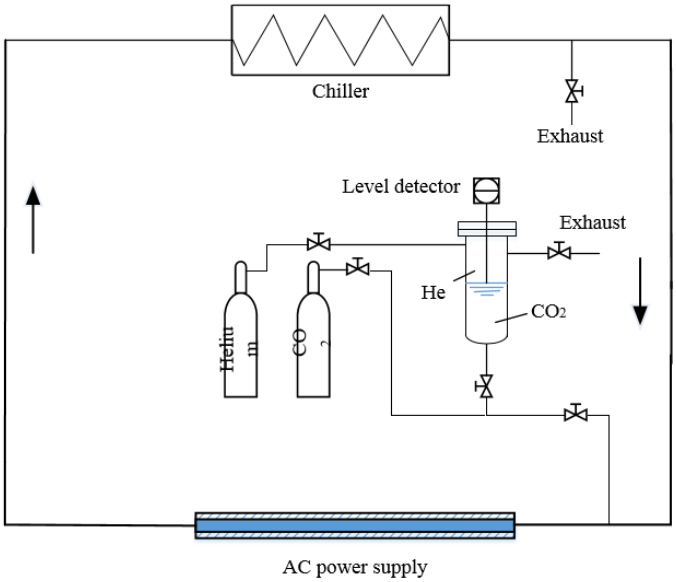

Figure 2.1 Schematic diagram of the experimental loop in Lomperski et al. [55]

Lomperski et al. [57] at the Argonne National Laboratory experimentally studied the flow instability of a supercritical natural circulation loop with CO_2 as the working fluid. The experiment was operated in the neighboring region of pseudo-critical point with inlet temperature of 20 – 30 °C, outlet temperature of 40 – 85 °C, and system pressure of 75 - 95 bar, but no flow instability was found.

Jain, R and Corradini, M.L., [58] performed a 1-D linear stability analysis of the experimental system used by Lomperski et al. [57]. Interestingly, the numerical results showed a clear flow oscillation behavior and it was found that the flow instability boundary of natural-convection systems were not restricted to the peak region of steady state flow-power curve; it was actually a complex function of fluid properties and loop geometries.

Jain, P.K. and Rizwan-uddin [59] developed a 1-D non-linear code FIASCO and numerically investigated the flow instability of the supercritical natural circulation loop adopted by Chatoorgoon [55]. It was found that the stability threshold was sensitive to the time step and grid size used for numerical analysis. Parametric effects were also conducted and all the

instability boundaries were identified on the positive slope of the steady state flow-power curve.

An extensive steady state and instability analysis of a supercritical natural circulation loop with water was performed by Sharma et al. [60] with the linear SUCLIN code. Various parameters such as loop diameter, loop height, local loss coefficient, and heater inlet temperatures were studied to check their effects on flow instability boundary as well as the relationship between the peak point of steady state flow-power curve and when the pseudo-critical temperature was reached at the heater exit. It was concluded that the stability threshold of the supercritical natural circulation systems was not restricted to the peak of the steady state flow-power curve. Increasing the loop diameter and loop height destabilized the system but it didn't significantly affect the heater outlet temperature at which peak steady state flow rate was achieved. Increasing the local loss coefficient on cold side of the loop or the system pressure stabilized the system. And the increase of local loss coefficient shifted the outlet temperature beyond the pseudo-critical temperature at which peak flow rate was achieved.

Sharma et al. [61] reported a numerical and experimental study of a supercritical loop with CO_2. The experiment was conducted with system pressure of 8 – 9 Mpa, and four different orientations of heater and cooler were tested; namely, the horizontal heater horizontal cooler (HHHC), horizontal heater vertical cooler (HHVC), vertical heater horizontal cooler (VHHC), and vertical heater vertical cooler (VHVC). Flow instability was only observed with the HHHC orientation during experiments while the loop was operated in the pseudo-critical temperature range. The developed NOLSTA code was able to predict the steady state behavior of the loop but the instability boundary predictions only matched qualitatively with the experimental results. In addition, the pipe wall effect was investigated and it was found that the thermal capacitance of pipe walls had a strong damping effect on flow instability.

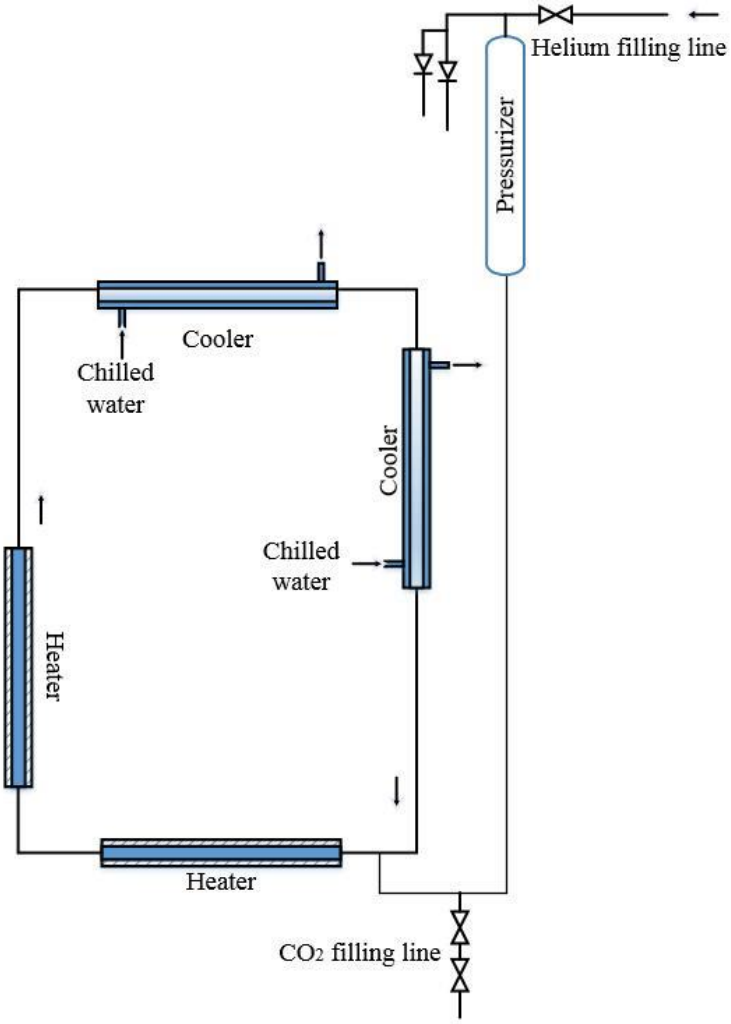

Figure 2.2 Schematic diagram of the experimental loop in Sharma et al. [61]

An experiment with supercritical water was also conducted by Sharma et al. [62] with the same loop design of Sharma et al. [61]. Similar to the CO_2 experiment, instability had been observed within a very narrow range of power near the pseudo-critical temperature for HHHC orientation only.

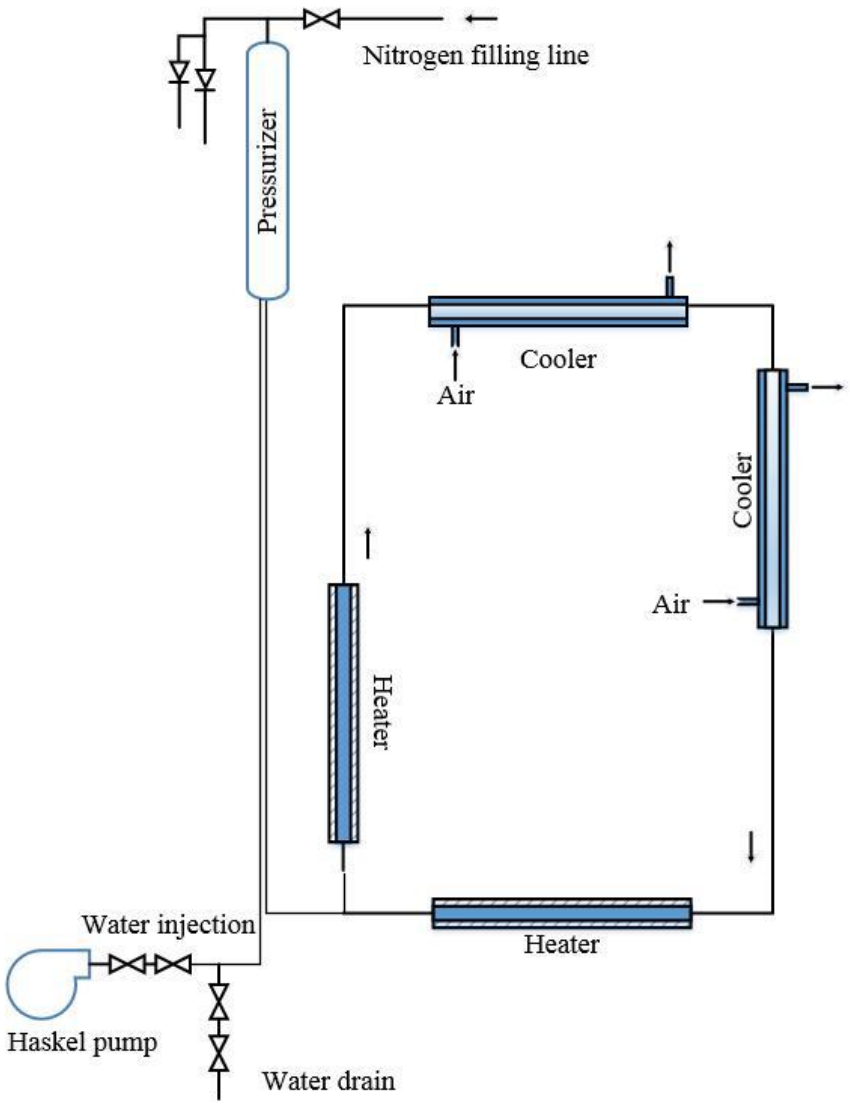

Figure 2.3 Schematic diagram of the experimental loop in Sharma et al. [62]

Chen, L., et al. [63] utilized a 2-D non-linear code and studied a closed supercritical CO_2 natural circulation loop with constant heater and cooler wall temperatures as the boundary conditions. A transition point based on the fluid average temperature was identified, below this transition temperature, the supercritical CO_2 flow was repetitive-reversal flow, whereas higher than this transition temperature it was stable single-direction flow. In addition, an average fluid temperature of 102 °C was defined as the second "critical temperature" above which no flow instability was observed.

A further analysis conducted by Chen, L., et al. [64] with the same model showed that with a larger pipe diameter of 15 mm (with 6mm for previous studies), the results were all stable

regardless of heater wall temperatures. Parametric effects such as loop aspect ratio, unsteady heat input, heater/cooler orientation, and loop inclination were also included. Results indicated that the loop with an aspect ratio of 1 was most unstable and it could be more stable with more asymmetric arrangements.

An experimental study of supercritical CO_2 in a rectangular close loop was also performed by Chen, L., et al. [65]. The experimental loop had a horizontal heater at the bottom and horizontal cooler on the top. Experimental cases were conducted both at near-critical region and supercritical region. It was found that the two-phase flow or single-phase gas flow at sub-critical might lead to instability but no supercritical flow instability was observed during experiments.

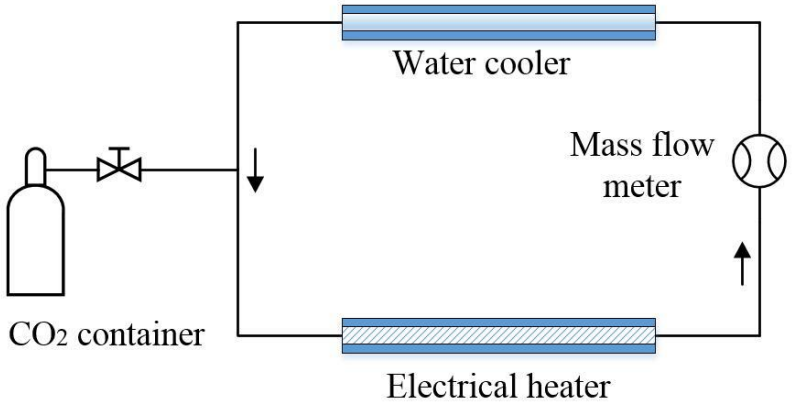

Figure 2.4 Schematic diagram of the experimental loop in Chen, L et al. [65]

T'Joen, C. and M. Rohde [66] experimentally studied a supercritical natural circulation loop with supercritical Freon R23 as the working fluid. The experimental loop was a scaled natural circulation driven model of HPLWR, which has a moderator and three heating sections. A clear zone of coupled thermo-hydarulic-neutronic flow instability was presented. The obtained stability map showed that for a single core inlet temperature there existed a low and high power stability boundary, below which no instability was observed. In addition pure thermo-hydraulic instability was not found in the operated power range.

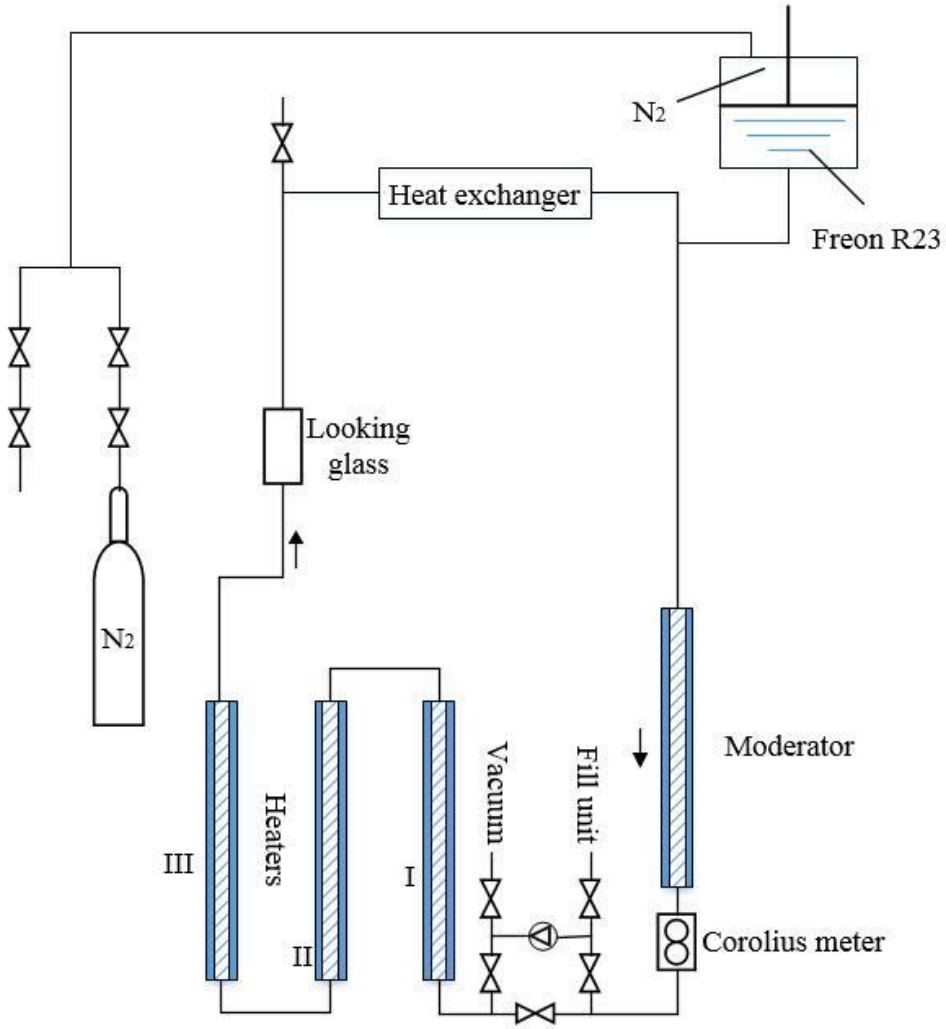

Figure 2.5 Schematic diagram of the experimental loop in T'Joen, C. and M. Rohde [66]

Chen, Y.Z., et al. [67, 68] conducted experiments of supercritical water in a natural circulation loop with different heater diameters. Flow instability was clearly identified to be near the peak region of flow-power curve when the heating power was given at 11.6 kW and the heated channel outlet temperature is 370 °C. The flow instability disappeared with further input of heating power. The measured heat transfer coefficient was also compared with classical heat transfer correlations. And it was found that the existing heat transfer correlations over-predicted the heat transfer performance and could describe the complex heat transfer characteristics due to the combined effects of buoyance force, non-uniformity of fluid properties and flow instability.

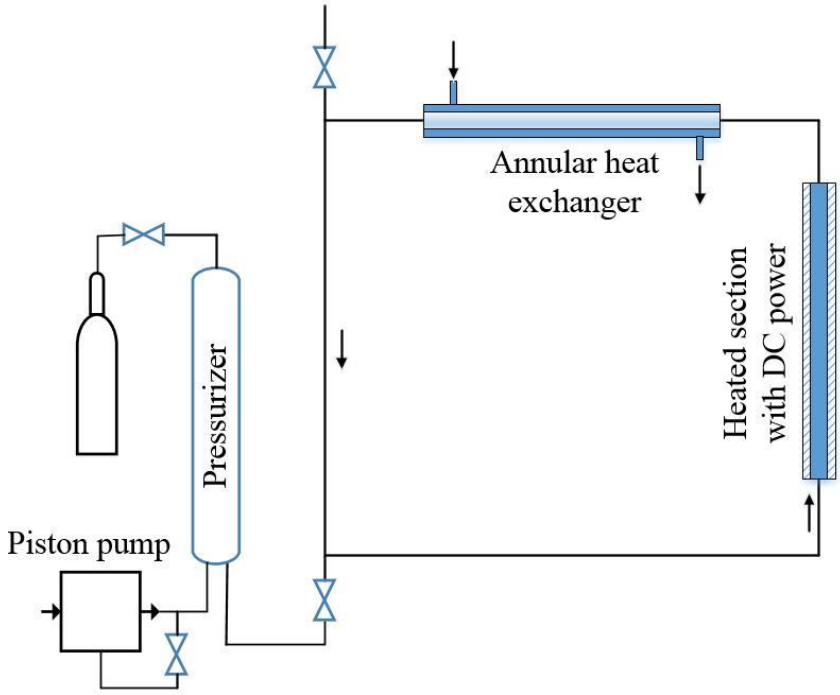

Figure 2.6 Schematic diagram of the experimental loop in Chen, Y.Z et al. [67, 68]

With the application of dimensionless relationship proposed by Ambrosini and Sharabi [17], B.T. Swapnalee [69] developed a general correlation for predicting steady state flow of supercritical natural circulation loop. The correlation was tested and found to be in good agreement with available experimental water and CO_2 data for all four orientations of heater and cooler. Static instability analysis was also conducted with both fluids but was only found with supercritical water.

Debrah, S.K., et al. [70] made an attempt to extend the non-dimensional parameters derived by Ambrosini and Sharabi [17] from heated channels to a supercritical natural circulation loop. It was pointed out that the steady state characteristic of a natural circulation loop could be expressed in dimensionless form by using the trans-pseudo-critical number, sub-pseudo-critical number and Froude number. It was also mentioned that the adopted methodology for extending these dimensionless parameters was limited to natural circulation loops with constant cross section and without heating structures. In addition, the RELAP5 code was used with an idealized loop simplified from the CIAE loop [67] and a numerical study was conducted to verify the derived dimensionless parameters.

Debrah, S.K., et al. [71] carried out a further study with the RELAP5 code, NCLoop-Tran non-linear code, and Ncloop-line linear code for modeling the real CIAE loop [67]. Although good agreement was achieved between different code results, there was still a large discrepancy between the predicted flow instability boundary and the experimental one; the predicted flow instability was at a high power-flow rate ratio, whereas the experimental flow instability boundary occurred near the peak region of the flow-power curve. Efforts were made to find the cause of the discrepancy and it was pointed out that the heat structures had a strong damping effect on the flow instability boundary of supercritical natural circulation loops. The reason for the discrepancy between numerical results and experimental data was still not very clear.

J. Mahmoudi [72] experimentally studied the thermal-hydraulic behaviors of a supercritical CO_2 natural rectangular loop under both steady state and unstable conditions. Friction factors were produced and compared with the available friction-factor correlation in open literature. Results showed that the obtained frictional pressure drop data fell with 1 – 1.2 times of the Blasius formula. In addition, flow oscillations were observed when the CO_2 outlet temperature was higher than the pseudo-critical temperature on the negative slope part of the mass flow rate versus power curve.

Sarkar et al. [24] reviewed the recent advances in supercritical natural circulation systems mainly focusing on the heat transfer aspects as well as the flow instabilities.

Tilak, A.K. and D.N. Basu [73] proposed an in house 1-D non-linear code and investigated the dynamic responses of a supercritical water natural circulation loop with aperiodic and periodic power excitations. Compared with ramp, exponential, and sinusoidal excitations, stepwise power destabilized the system most.

Archana, V., et al. [74] developed a 2-D-axi-symmetric CFD code and compared with an in house 1-D non-linear code, simulation results showed better agreement of the 2-D CFD code with the experimental results [62] at higher power region.

2.2 Summary of Literature Review

Table 2.1 and Table 2.2 summarize the numerical and experimental supercritical flow instability studies mentioned above.

From Table 2.1, it can be noticed that most of the studies on flow instabilities of SNCLs focused on rectangular loops with supercritical H_2O or CO_2 as the working fluids. Both the steady state and flow unstable characteristics have been widely studied numerically and effects of the parameters as well as loop geometries on steady state performances of SNCLs are well established. It can be concluded that flow characteristics of SNCLs are mainly affected by operating parameters and loop geometries, which include the loop length, loop diameter and heat structures.

Table 2.2 shows that only limited literatures reported experimental instability study. Amongst these experimental investigations, results with flow instabilities are even rarer. Chen, Y.Z., et al. [67] reported flow instabilities with supercritical water when the power reached about 11.6kW and the heated channel outlet temperature was 370°C. Sharma et al. [61, 62] presented supercritical flow instability results over a narrow window of power in the pseudo-critical temperature region with both CO_2 and H_2O, respectively.

A further close check of both the numerical and experimental flow instability results in the tables arouse more concerns as follows:

Firstly, flow instability cases reported by Chen, Y.Z., et al. [67] and Sharma et al. [61, 62] were obtained with a changing inlet temperature which is different from most of the numerical work presented in Table 2.1 and makes it more complicated for numerical simulation. In fact, the corresponding numerical work done by Debrah, S.K., et al. [71] and Sharma et al. [60, 61] could only match qualitatively with the experimental flow instability results. More experimental work must be conducted with a constant fluid inlet temperature and corresponding numerical work also should be performed to further explain the discrepancy between the numerical predictions about the locations of instability boundary point on steady state flow-power curve and the experimental results.

Secondly, the experimental flow instability results of the natural circulation loops were all found to occur within the pseudo-critical region and disappeared with further increase of heating power. This contradicts the numerical findings that the flow instability will become larger with more power input. The experimental flow instability results seem to be the type I flow instability reported by Zhang, L., et al. [54] where the outlet temperature is close to the pseudo-critical line. Type II flow instability occurs when the heated channel outlet temperature is much higher than the pseudo-critical temperature, which means the instability boundary points will be located on the negative slope of flow-power curve of a natural circulation system. This has been found with numerical studies, but only J. Mahmoudi [72] reported three related experimental flow instability cases. The search of this kind of flow instability is important because in real applications it is always critical to determine the maximum heating power that can be added so a stability margin can be designed to guarantee the safe running of a system.

Moreover, very few people mentioned the important role of the accumulator (referred as pressurizer or expansion tank by other researchers) played on the fluid dynamics of SNCLs. In most of the experimental investigations, accumulators were used as an auxiliary pressure control system for the SNCLs, but no detailed information was provided. And in most of the numerical studies, open loop boundary condition with equal pressures at inlet and outlet and constant inlet temperature were used which eliminated the accumulator and its connecting line. However, it must be pointed out that the accumulator is an indispensable part of SNCLs which serves as surge tanks that can damp out pressure oscillations, accumulate fluid and return it when necessary. It may affect the flow instability boundary and must be studied. Literature of single phase NCLs studies reveals that the accumulator not only has mass and momentum exchange but also energy exchange with the loop and should be considered for flow instability studies [75, 76].

Lomperski et al. [57] were probably the only one in open literatures who performed a test of the accumulator effect in their experimental investigations on supercritical flow instability studies. Artificial loop instability was produced by rapid injection of helium in the pressurizer.

Then the isolation valve was closed and reopened to observe the flow characteristics. Interestingly the flow oscillations disappeared after the accumulator was isolated and occurred again when the accumulator was reconnected, which contradicts the expectation that the accumulator has a stabilizing effect on the system. This is a very important finding; however, no detailed information was reported and the dimension of the surge line and the operating parameters were also not strictly controlled. Hence, further systematic investigations on the effect of accumulator are necessary.

Table 2-1 Summary of analytical and numerical studies on flow instabilities of SNCLs

Author(s)	Fluid(s)	Loop details	Boundary conditions	Methodology	Flow characteristics
Chatoorgoon [55]	H_2O	Rectangular loop H = 14 m, W = 6 m, L = 40 m, I. D. = 0.0785 m, HHHC orientation.	$P_{in} = P_{out}$ = 25MPa, T_{in} = constant, open loop	Analytical and SPORTS 1-D non-linear code	Flow-power curve, non-dimensional parameters, effect of inlet temperature, flow area, and friction Instability occurred at peak region of flow-power curve
Chatoorgoon et al. [25, 56]	H_2O, CO_2, H_2	Rectangular loop H = 10, 14, and 17 m, W = 6 m, L = 40 m, I. D. = 0.0785 m, HHHC	$P_{in} = P_{out}$ = 25MPa, T_{in} = constant, open loop	Analytical and SPORTS 1-D non-linear code	Flow-power curve and non-dimensional parameters Instability occurs at peak region of flow-power curve
Jain, R., et al. [58]	H_2O, CO_2	Chatoorgoon's loop UW-Madison loop with H = 3 m, W = 2 m and L = 10 m Lomperski's ANL loop, HHHC	$P_{in} = P_{out}$, T_{in} = constant, open loop	Linear 1-D code	Flow –power curve, instability is found to be on positive slope of the flow-power curve
Jain P.K., et al. [59]	CO_2	Rectangular loop with H = 10 m and W = 6 m, L heater = 2 m and L_{cooler} =1 m, HHHC	$P_{in} = P_{out}$, T_{in} = constant, open loop	Non-linear 1-D FIASCO code	Flow-power curve and parametric effects study, instability is found to be on positive slope of flow-power curve
Chen, L., et al. [63]	CO_2	Rectangular loop with H = 2 m and W = 5 m, I. D. = 0.006 m, L_{heater} = L_{cooler} = 3 m, HHHC	Close loop, T_{heater} = constant, T_{cooler} = constant	2-D non-linear CFD code	No flow-power curve. Instability occurs when average fluid temperature is smaller than 375K.
Sharma et al. [60]	H_2O	Rectangular loop with H = 4.1 m and W = 3.01 m. L_{heater} = 1.3 m and L_{cooler} = 1.2 m, HHHC	$P_{in} = P_{out}$, T_{in} = constant, open loop	1-D linear SUCLIN code	Flow-power curve, parameters effects study as well as pipe diameter and local loss K study. Instability deviates as much as -40% to +60% from peak flow rate.
Chen, L., et al. [64]	CO_2	Rectangular loop with H = 2.0 m, W = 5 m, L_{heater} = L_{cooler} = 3.0 m (base study), HHHC	Close loop, T_{heater} = constant, T_{cooler} = constant	2-D planar code	Various parameters study. No flow-power curve. Instability occurs with smaller diameter loops when heating temperature is below 523K

Table 2-1 continued

Debrah, S.K., et al. [70]	H_2O	Rectangular loop with H = 1.8 m, W = 2.4 m and L_{heater} = 1.4 m, L_{cooler} = 1.7 m and also the CIAE loop [67], VHHC	Close loop with changing power input	Analytical study and RELAP5 code	Mass flow rate evolution with time, comparison of calculation results with CIAE experimental results, test of heat structures. Instability occurs at negative slope of flow-power curve
Debrah, S.K., et al. [71]	H_2O	Rectangular loop with H = 1.8 m, W = 2.4 m and L_{heater} = 1.4 m, L_{cooler} = 1.7 m and also the CIAE loop [67], VHHC and HHHC orientation	Reservoir with P = constant	RELAP5 code, non-linear NCLoop-Tran and Linear NCLoop-line code	Instability occurs at negative slope of flow power curve, instability was postpone with introduce of heat structures
Archana, V., et al. [74]	CO_2	Rectangular loop H = 4.1 m and W = 3.01 m. L_{heater} = 1.22 m, L_{cooler} = 1.2 m, VHVC orientation	Close loop Change of water temperature on secondary side	1-D code, 2-D axi-symmetric code	Flow-power curve, Heat transfer coefficient and velocity and temperature fields in the heater and cooler sections
Abhilash K. Tilak et al. [73]	H_2O	Chatoorgoon's loop [55] HHHC orientation	$P_{in} = P_{out}$, T_{in} = constant, open loop	1-D code	Flow-power curve, test of power excitations.

Table 2-2 Summary of experimental investigations on supercritical flow instabilities based on rectangular NCLs

Author(s)	Fluid(s)	Loop details	Accumulators	Operating range	Flow characteristics
Lomperski, S., et al. [57]	CO_2	Rectangular loop with H = 2.0 m, W = 2.5 m, L = 15.06 m, L_{heater} = 1.0 m, L_{cooler} = 6.0 m. I. D. = 0.0139 m for heater and riser. I. D. = 0.0094 m for heat exchanger. HHHC orientation	Yes	P = 75 – 95 bar, T_{in} = 20 – 30 °C, T_{in} is kept constant for each case	Flow-power curve No flow instability found
Swapnalee, B.T., et al. [69]	CO_2, H_2O	Rectangular loop with H = 4.1 m, W = 3.01 m, I. D. = 13.88 mm, O. D. = 21.34 mm, tube in tube heat exchanger with outer tube I. D. = 0.0779 m, HHHC, HHVC, VHHV, VHVC orientation	Yes	P_{CO2} = 8.5 - 9.0 MPa, P_{H2O} = 22.5 - 24.1 MPa, T_{in} = 264.9 - 396.5 °C	Correlations for calculating steady state data of supercritical natural circulation loops No instability data presented
T'Joen, C and Rohde, M [66]	R23	Non-rectangular loop, H = 10.6 m, L = 28.6 m, $L_{preheater}$ = 1.1 m, L_{cooler} = 0.5 m, L_{core} = 0.8 m, Vahterus plate shell heat exchanger, VHHC orientation	Yes	P = 5.7 MPa, T_{in} = -29.7 - 19.3 °C, Tin is kept constant for each case	Flow-power curve No pure thermos-hydraulic instability
Chen, Y.Z., et al.[67, 68]	H_2O	Rectangular loop, H = 1.77 m, W = 2.1 m, I. D. = 0.01 m, annular heat exchanger with inner tube I. D. = 0.01 m and O. D. = 0.013 m and outer tube I. D. = 0.016 m and O. D. = 0.02 m, L_{cooler} = 1.7 m, VHHC orientation	Yes	P = 24.9 - 25.9 MPa, T_{in} changes with input of power	Flow-power curve, comparison of experimental results with existing heat transfer correlations. Instability was found to be near the peak region of the flow-power curve
Chen, L., et al. [65]	CO_2	Rectangular loop, H = 0.8 m, W = 0.6 m, I. D. = 0.008 m, O. D. = 0.01 m. Tube in tube cooler, constant heater wall temperatures and constant cooler temperatures, HHHC orientation	No	P = 6.0 - 9.0 MPa, constant heater and cooler wall temperatures	Steady state parameters such as mass flow rate, pressure, temperature change with time. Instability occurred at sub-critical pressures, no supercritical instability

Table 2-2 continued

Sharma et al. [61]	CO_2	Rectangular loop with H = 4.1 m, W = 3.01 m, I. D. = 13.88 mm, O.D. = 21.34 mm, tube in tube heat exchanger with outer tube I.D. = 0.0779 m, HHHC, HHVC, VHHV, VHVC orientation	Yes	P = 7.7 - 9.0 MPa, T_{in} changes from 27 to 31°C, secondary side coolant parameters was kept constant	Flow-power curve and different heat transfer correlations tested with NOLSTA code. Instability only occurred with HHHC orientation. All of the instability was observed when the loop was operated in the pseudo-critical temperature range
Sharma et al. [62]	H_2O	Rectangular loop with H = 4.1 m, W = 3.01 m, I. D. = 13.88 mm, O. D. = 21.34 mm, tube in tube heat exchanger with outer tube I. D. = 0.0779 m, HHHC, HHVC, VHHV, VHVC orientation	Yes	P = 22.1 – 24 MPa, T_{in} changes from 75 °C to 400 °C, secondary side coolant parameters was kept constant	Flow-power curve and steady state parameters change with time, compare of experimental data with NOLSTA code utilizing different heat transfer correlations. Instability only occurred with HHHC orientation. All of the instability was observed when the loop was operated in the pseudo-critical temperature range

CHAPTER 3

EXPERIMENTAL SET-UP AND TEST PROCEDURES

3.1 Introduction

The previous literature review shows that the experimental data of supercritical flow instability in natural circulation loops is very limited in the open literature compared to the extensive work on subcritical two-phase flow instability of natural circulation systems. To gain a better understanding of flow instability characteristics of natural circulation loops with supercritical fluids, a supercritical natural circulation loop was built at University of Manitoba. The experimental loop was originally designed by Dr. Vijay Chatoorgoon and fabricated by Stern Laboratories. It consists of three parallel channels ganged together with inlet and outlet headers. It was designed to study the thermal hydraulics of supercritical water, but during the process some components of the loop were replaced with parts for carbon dioxide due to cost and safety concerns. Tummalapalli [26] assembled the loop and performed pre-experimental tests such as chemical cleaning, leak tests and a pressure test of 10 MPa. J. Mahmoudi [72] modified the experimental loop by removing the headers and two parallel channels and conducted a detailed pressure drop analysis of a horizontal single channel. Flow instability study was also performed, but only three flow instability cases were reported. For the present work, more efforts are made to acquire flow instability data as well as study the effect of various loop configurations on the flow instability behaviours.

3.2 Experimental Set-up and Components

Figure 3.1 is a schematic of the experimental loop and its main components; a more detailed drawing with dimensions is given in Appendix I. The experimental set-up is a rectangular loop with a horizontal single test channel located at the bottom tier. The right

hot leg is wrapped by a heating tape to generate a density difference which works as a driven force for initializing the flow in a counter clockwise direction. The hot fluid is cooled down by a shell & tube heat exchanger to a desired value for circulation. To be specific, the experimental loop mainly consists of the following components which corresponds to the numbers in order in Figure 3.1: pressure control system, purging system, power supply system, vacuum and evacuation system, cooling system, data acquisition system (not shown in Figure 3.1) and miscellaneous components such as settling chamber, heating tape, piping, joints and valves.

3.2.1 Pressure Control System

A pressure control system (region 1 of Figure 3.1) was implemented to regulate the loop pressure to a nominal value when operating the loop. It mainly includes a Nitrogen gas cylinder (Praxair® industrial Nitrogen with 2200 psi), check valve, single stage pressure regulator (PR-50 series, GO regulator®), bladder type accumulator (Hydac®), and a high pressure back pressure regulator (BP-60 series, Go regulator®). The bladder inside the accumulator acts as a gas-proof screen and separates the accumulator into a liquid CO_2 section (outside the bladder) and a Nitrogen gas section (inside the bladder).

Before running the loop, the back pressure regulator is pre-determined to a desired operating pressure (e.g. 8 MPa). With the increase of heating input, the loop pressure will also increase with expansion of CO_2. Once the loop pressure is higher than the set limit (e.g. 8 MPa), the bladder will be compressed and some liquid CO_2 will be stored in the accumulator. Meanwhile, some of the compressed Nitrogen gas will be automatically released to the atmosphere through the back pressure regulator. Then balance will be achieved again inside the accumulator and loop pressure is maintained at the pre-determined value.

Practically, there's a problem about this system that should be noted. With the increase of

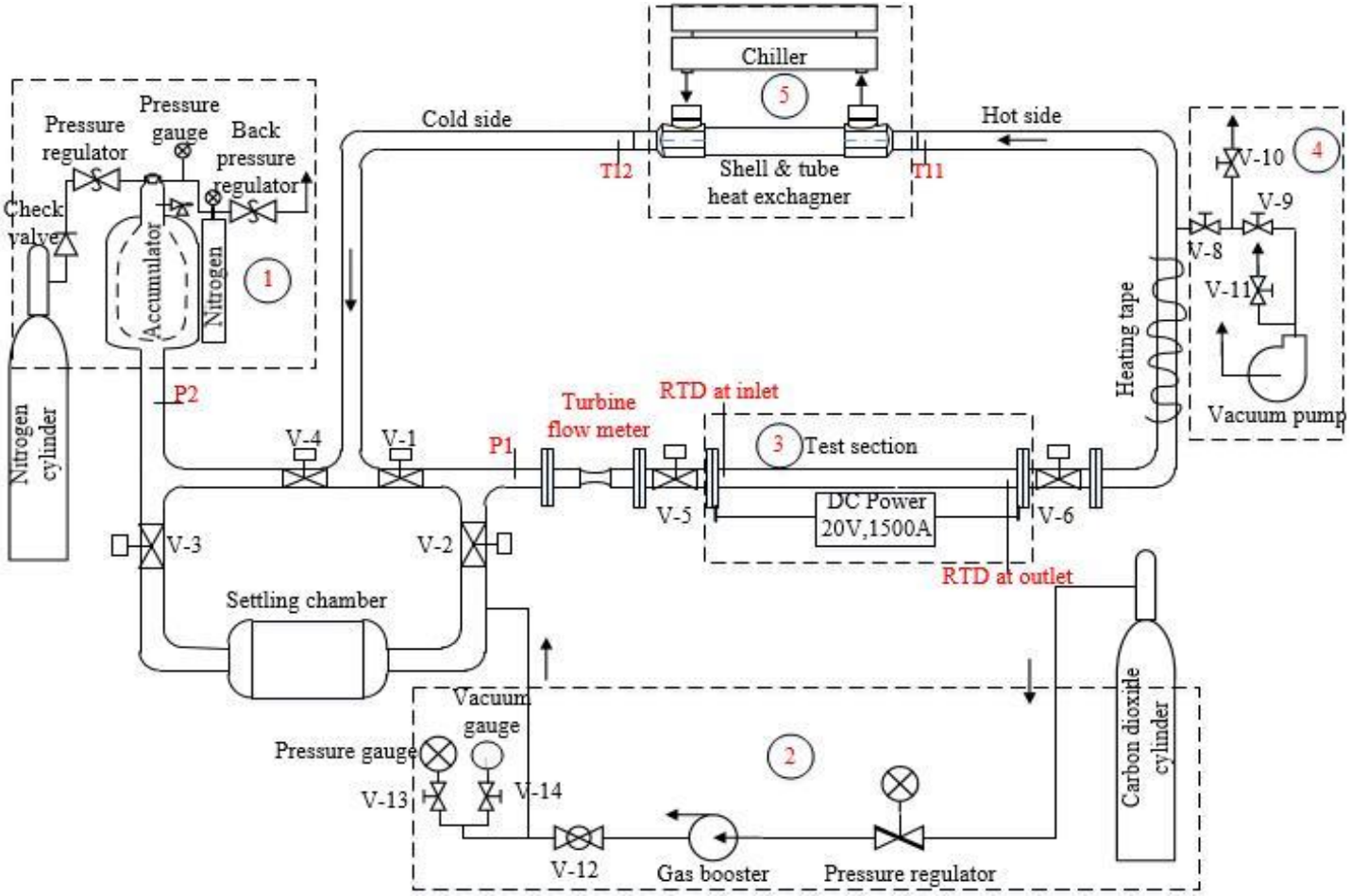

Figure 3.1 Schematic of natural circulation loop with horizontal single channel

heat input, the system pressure of CO_2 increases continuously and the bladder inside the accumulator is pressed more and more, to an extent that the bladder may be compressed and rub against the outer shell of the accumulator. This may cause the damage of the bladder inside the accumulator. So another method was used later to control the system pressure in the experiment study, which was to control the valves V-8, V-9 and V-10 to directly release some CO_2 into the atmosphere. This method will not damage the bladder of the accumulator. A back pressure regulator is suggested to replace valve V-8 for more accurate operation for future experimental studies.

3.2.2 Purging System

A purging system (region 2 of Figure 3.1) is necessary for pressurizing the loop to desired supercritical pressures. Once the entire loop is vacuumed, valve V-14 is closed and valves V-12, V-13 are opened. Then a pressure regulator with standard CGA connections are used to regulate the flow of CO_2 from the CO_2 cylinder (Praxair® CO_2 of 99.99% purity). The CO_2 cylinders are supplied with a pressure of 5.8 MPa, so the loop can be directly pressurized until a balance between the loop pressure and CO_2 cylinder pressure is reached. A Maxpro® gas booster with a compression ratio of 20:1, which is capable of generating up to a maximum pressure of 31.30 MPa, is then used to suck more CO_2 from cylinder to boost the loop pressure to a desired operating pressure (e.g. 8 MPa).

3.2.3 Power Supply System

An EMHP 20-1500 rectifier (EMHP Power Supply®), donated by Atomic Energy of Canada, is used to supply DC power on the test section of the loop. A circuit breaker rated at 1500 Amps is installed between the rectifier and test section. The test channel works as a resistor and heat is generated when current passes through the test channel. With LabVIEW programming, done by a previous summer student, the output of the rectifier (0~1500 A, 0~20 V) can be controlled precisely (minimum increment of 0.001

kW) and continuously during experiments by a mouse. The resistance of the heated channel is about 0.026 Ω, and the maximum ideal voltage output of the rectifier is 20 V, though the ideal output of the rectifier is 30 kW, the actual maximum heating load generated by the test section is about 15.4 kW.

Figure 3.2 Emergency shut down switch

Figure 3.3 Power supply interlock

To prevent electrical shock, the test section is electrically isolated from the rest of the test facility by using glass filled teflon glass gaskets between the stainless steel flanges and insulating sleeves to the flange bolts. The rectifier output current and voltage will jump to zero when either the maximum wall temperature pre-set value (450 °C) of test section or the maximum output voltage (20 V) or maximum pressure (10 MPa) is reached. There are also other measures for personal safety. For example, power can also become zero when the door of the shield is open. Under emergency conditions the power supply can be manually shut off by pushing a red knob (Figure 3.2) fitting on the loop shield front panel or using a mechanical key to deactivate the power supply interlock (Figure 3.3) on the back panel of shield. More safety features of the experimental set-up including rupture disk assembly, safety shield, CO_2 detection system can be found in Tummalapalli

[26]. It should also be noted that with the increase of power output, the rectifier will gradually become hot and may stop working at high power, so cooling is necessary to keep it working. The door of the room where the rectifier is placed must be always left open and fans inside and outside the room must be turned on during the experiment.

3.2.4 Vacuum and Evacuation System

As can be seen from region 4 in Figure 3.1, the vacuum and evacuation system includes a vacuum pump (R5-PB0003 A, Busch®), ball valves V-8, V-9, V-10, and V-11. This system can work in two stages. The first one is vacuuming air from the loop before pressurizing it with CO_2. This can be done by opening valves V-8, V-9, closing V-10, V-11 and turning on the vacuum pump. The second one is releasing CO_2 into atmosphere by opening valves V-8, V-10 and closing V-9, V-11. Valve V-11 is a bypass and used to test if the vacuum system is working or not. For maintenance of the vacuum pump, pump oil should be regularly checked and replenished if it drops below the ¼ mark on the oil sight glass.

3.2.5 Cooling System

The cooling system is designed and installed by three M. Eng students, the technician Sviatoslaw Karnaoukh and present author for the purpose of cooling the supercritical CO_2 down to a specific inlet temperature. As is shown in Figure 3.4, the cooling system includes two different cooling systems, one for summer and another for winter. The two circulation cooling systems share the same insulated tank, circulation pump (US MOTORS®), shell & tube heat exchanger (EXERGY LLC®), turbine flow meter (Seametrics® SPX series), strainers and ball vavles. The main difference is that an air cooled chiller (International Cooling Company) is used as a heat sink in summer time, whereas the winter system utilizes a big blower (LEESON®) and the cold outside environmental temperature as the heat sink.

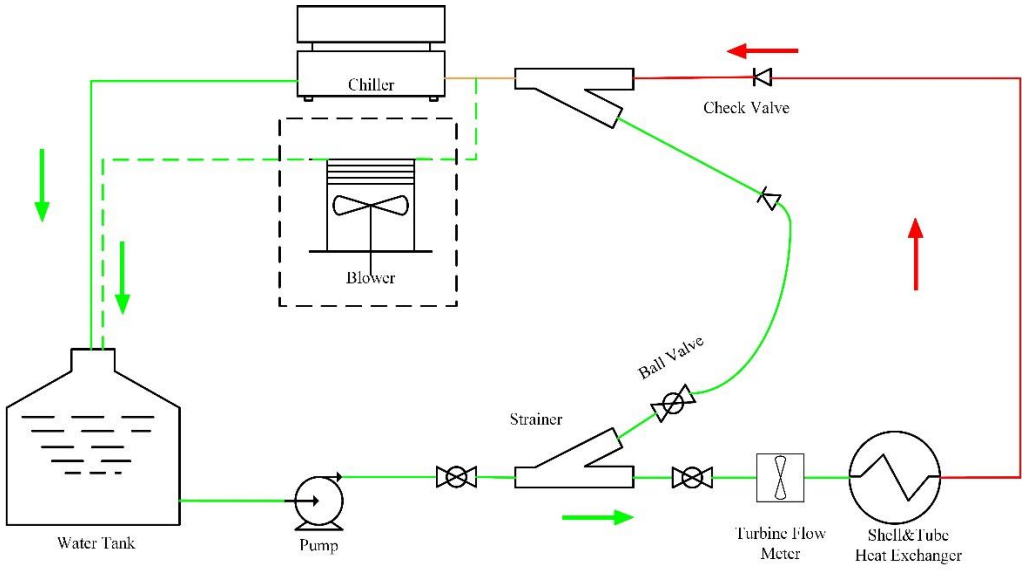

Figure 3.4 Secondary side cooling system

Antifreeze water is used as the working fluid in winter whose purpose is to prevent icing inside the system. Tap water is used as the coolant for summer time. Cold coolant is pumped from the tank directly to the heat exchanger. The water tank and piping connected are insulated to prevent heat exchange with room temperature. Hot coolant will be cooled down either by chiller or the roof-top blower and sent to the tank for circulation. For the summer cooling system, a desired coolant temperature can be set on the front panel of the chiller. The chiller will automatically start working when the coolant temperature is 1 ˚C higher than the pre-set value and stop working when the coolant temperature is 1 ˚C lower than the pre-set value. For the winter cooling system, the desired cooling effect is mainly achieved by adjusting the mass flow rate of the coolant.

3.2.6 Data Acquisition System

A data acquisition (DAQ) system was designed and installed by a summer student and further modified by J. Mahmoudi [72] and present author for monitoring and recording all the measured signals. It mainly includes sensors or transducers that measure the target

signals, wires, signal conditioning hardware, a personal computer (PC) with National Instrument LabVIEW software. The measured sample signals such as temperature, pressure, volume flow rate, heating voltage are transmitted to the DAQ module (USB 2416) through wires, the DAQ module then converts the sample signals into typical output of 4-20 mA or 0-5 V which can be manipulated by the PC. The NI LabVIEW interface developed can show all the parameters collected on the PC monitor. The experiment conductor can also control some parameters on the LabVIEW interface, generate an output signal with the USB3104 DAQ module to remote control some devices such as the electro-pneumatic valves and rectifier of the power supply system. As mentioned in previous section 3.2.3, safety feature of emergency shut off of power supply is also embedded in the interface by programming.

3.2.7 Piping, Joints and Valves

The test section is an Inconel 625 seamless tube (19.05 mm O. D. and 12.95 mm I. D.) with a length of 2640 mm for its good electrical and thermal conducting properties. The test section is connected with rest of the loop by means of Swagelok® fittings (1/8’’couplings) and flange joints (1’’ Class 2500, WN XXS), as shown in Figure 3.5 and 3.6. The total heating length between the two conductors is 2988mm. Two conductors are welded to the flanges for DC power from the rectifier.

Most of the loop (see Appendix I) is made of XXH stainless steel 316 L pipe (42.16 mm O. D. and 22.75 mm I. D.) which is connected by various socket welded joints, flanges and valves. These joints include 90 ºelbow joints (31.75 mm 6000# 316SS stainless steel, S.W.), tee joints (31.75 mm 316 SS stainless steel, S.W.) and couplings (31.75 mm 6000# 316SS stainless steel, S.W.). Those flanges are stainless steel flanges (31.75 mm and 25.4 mm WN, Class 2500 B16 XXH SA 182 F316/316L). Electro-pneumatic valves of 19.05 mm size were installed at both inlet and outlet of test sections, see Figure 3.1. These Electro-Pneumatic valves include a valve (Jareki®), an actuator (Habonim®) and a

position controlling transducer (Flowserve®). Other flow control valves (H27 series Habonim® ball valves) like V-1, V-2, V-3 and V-4 were welded to the loop, see Figure 3.1. The entire loop is insulated with M Board insulation sheets and the settling chamber is insulated with Superwool® Fibre to reduce heat loss.

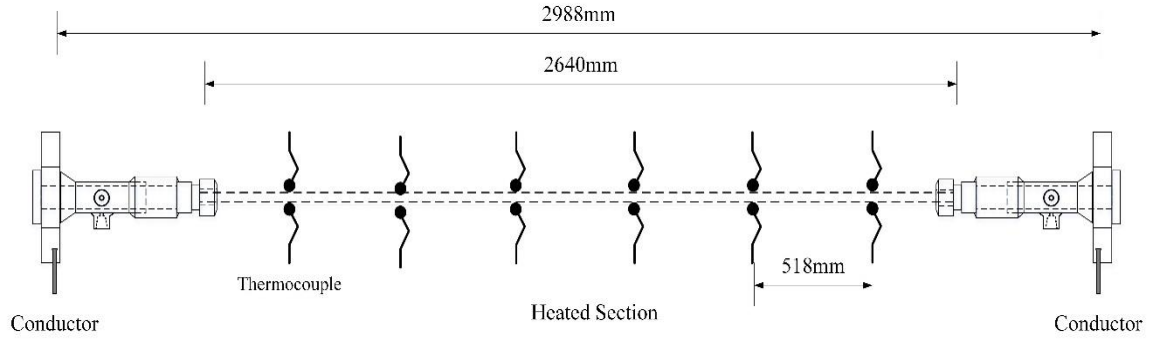

Figure 3.5 Front view of the heated channel with thermocouple arrangement

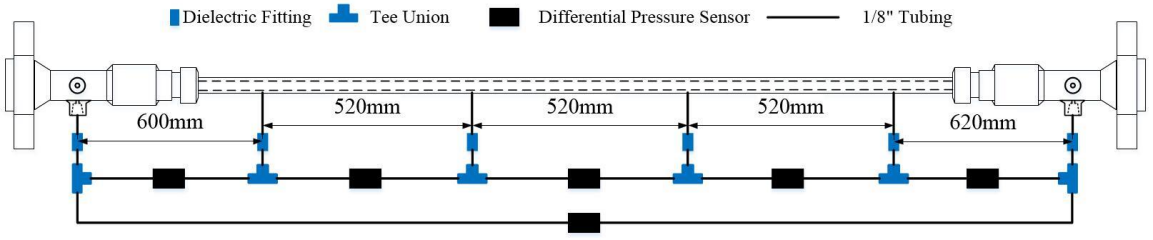

Figure 3.6 Top view of the heated channel with differential pressure sensors arrangement

3.3 Instrumentation

The parameters measured during the experiments are: system pressure, pressure drops, CO_2 volume flow rate, coolant flow rate of secondary side cooling system, inlet and outlet water or antifreeze water temperature, heat exchanger inlet and outlet CO_2 temperature, wall temperature of the test section, voltage drop across test section, and voltage drop across shunt resistor located at back part of the rectifier. Information of instruments is summarized in Table 3.1.

Table 3-1 Specifications of instruments

Instrument	Specification	
Absolute Pressure Transducer	GP:50 Industrial Pressure Transducer Model: 311-C-RO-3-CJ, Range: 0 ~ 1500 psi	System pressure
Differential Pressure Transducer	Validyne Engineering Corporation Model: DP303 Range: 0 ~ 0.3 psi	Segment pressure drop along test section; Pressure drop across heat exchanger
Differential Pressure Transducer	Validyne Engineering Corporation Model: DP303 Range: 0 ~ 0.5 psi	Total pressure drop along test section
Differential Pressure Transducer	Validyne Engineering Corporation Model: DP360 Range: 0 ~ 8 psi	Pressure drop across electro-pneumatic valves
Multichannel Carrier Demodulator	Validyne Engineering Corporation Model: CD280	Signal conditioning for pressure transducers; Calibration of pressure transducers
Hand-held Pressure Calibrator	Martel Corporation Model: T140-200” H_2O Range: ±200” H_2O	Calibration of pressure transducers
Pneumatic Hand Pump	Martel Corporation Model: MECP 100 Range: -12~100 psi	Calibration of pressure transducers
Turbine Flow Meter	OMEGA Engineering Model: FTB-1421 Range: 0.6~3 GPM	CO_2 flow rate
Turbine Flow Meter	Seametrics Model: SPX-050 Range: 0.6 ~ 40 GPM, 0.4 ~ 20 GPM, 0.1~10 GPM	Coolant flow rate
Digital Rate Meter/ Tantalization	OMEGA Engineering Model: DPF701-A3 Range: 0.5 Hz ~ 30 kHz	Frequency indicator Signal conditioning
Rate/Total Indicator	Seametrics Model: FT420 Range: 1.0 ~ 1500 pulses/second	Flow rate indicator Signal conditioning

Table 3-1 continued

Resistance Temperature Detector (RTD)	OMEGA Engineering Model: P-M-A-1/8-6-1/8-P-3 Range: 0 ~ 60 º	Fluid temperature at inlet of test section (read-out included)
Resistance Temperature Detector (RTD)	OMEGA Engineering Model: P-M-A-1/8-6-1/8-P-3 Range: 0 ~ 150 º	Fluid temperature at outlet of test section (read-out included)
Thermocouple	OMEGA Engineering Model: K-type, 1/8" sheath diameter	Fluid temperature at inlet and outlet of shell & tube heat exchanger
Thermocouple	OMEGA Engineering Model: K-type, 1/16" sheath diameter	Fluid temperature at inlet and outlet of shell & tube heat exchanger
Isolated DC Voltmeter	Wilkerson Instrument Corporation Model: SR2101 Range: 0 ~ 20 V	Voltage drop across test section
Bridge/Strain Gage Signal Conditioner	OMEGA Engineering Model: DMD4059 Range: From 0 ~ 5mV to 0 ~ 400 mV	Signal conditioning
Rectifier	TDK-Lambda Inc. Model: EMHP 20 - 1500 Range: 0 ~ 20 V, 0 ~ 1500 A	Power supply

3.3.1 Temperature Measurement

Fluid temperatures at the inlet and outlet of the test sections are measured by two ultra-precise RTD sensors (OMEGA®). These RTDs have a class A accuracy. Class A= ± (0.15+0.002*T) where T varies from -30 to 300 ℃. The response time of the RTDs is about 0.6s for liquid water. Flow temperatures of CO_2 and coolant water or antifreeze water at the inlet and outlet of the heat exchanger were measured with T-type thermocouples (1/8" sheath diameter, ±0.5 °C accuracy, response time of about 0.3s for liquid water), obtained from the OMEGA Company. Twelve K-type thermocouples (±1 °C accuracy) with 1/16" sheath diameter are spot welded with equal intervals on the top and bottom of heated test section surface to measure wall temperatures, as shown in

Figure 3.5 a. The output of the thermocouples is directly connected with a USB-2416 module. Once the thermocouple mode is configured, the USB-2416 module has a built-in cold-junction compensation and open thermocouple detection.

3.3.2 Pressure Measurement

Two absolute pressure transducers are mounted on the experimental loop. One is located just below the accumulator to measure the absolute pressure inside the loop, see Figure 3.1. The other is installed on the inlet of the loop, which can be used to measure system total pressure of the loop when the accumulator is isolated. These pressure transducers can measure up to a frequency of 20Hz, which is sufficient for measuring pressure fluctuations.

Totally nine differential pressure transducers (Validyne®) are installed to measure pressure drops at different parts of loop. It includes total pressure drop and segment pressure drops along the heated section (see Figure 3.5 b), pressure drop across inlet and outlet electro-pneumatic valves, and pressure drop across heat exchanger. With a 0.5% F.S. accuracy and a fast response time of 0.05 s, these differential pressure transducers are excellent for measuring dynamic signals.

The output voltage signals of pressure sensors were transmitted to the CD280 carrier demodulator and amplified to a ±10 Vdc full-scale output. Then the voltage signals were transmitted to a USB-1616HS DAQ module (Measurement Computing®).

3.3.3 Flow Measurement

After a comprehensive search on venturi, coriolis, and turbine flow meters by J. Mahmoudi [72], a FTB-1421 turbine flow meter (OMEGA®) was chosen and installed at upstream (see Figure 3.1) of the heated channel for measurement (meter accuracy of ±1% reading) of supercritical CO_2 volume flow rate. An advantage of a turbine flow meter is its low pressure drop across the meter compared with a Coriolis flow meter. It is already

known that a smaller local friction loss at heater inlet will make the system more unstable. Since the experiment is to study the flow instability of the system, it's better to have relatively low friction loss at the heater inlet. Unlike the venturi flow meter which needs pressure sensors to measure the pressure drop across the venturi flow meter to further determine the flow rate, the turbine flow meter can directly measure the output frequency that is proportional to volumetric flow of the liquid fluid.

The turbine flow meter is calibrated by the manufacture with water and a 5-Point NIST traceable calibration certificate is provided. According to the turbine flow meter theory it can be applied directly in measuring liquid CO_2 because the kinematic viscosity of supercritical CO_2 (~0.07 centistokes) is much smaller than the kinematic viscosity of water (~ 1 centistokes). A DPF701-A3 rate meter (OMEGA®) is used to indicate the transient frequencies of turbine flow meter and also convert the electrical signal to a typical 4~20mA analog output. Combined with a 250 Ω resistor, the 4 ~ 20 mA current signal is converted to a typical 1 ~ 5 V voltage signal and then be transmitted to the USB-1616HS DAQ module. Then the volume flow rate can be calculated by the following equation

$$\dot{V}_{CO_2} = \frac{f_{CO_2}}{K_{CO_2}} \qquad \text{Equation (3-1)}$$

where $\dot{V}_{CO_2}$ is the volume flow rate of liquid CO_2, f_{CO_2} is the output frequency from the flow meter, K_{CO_2} is manufacture calibrated flow coefficient.

The flow rate of coolant water or antifreeze water on secondary side is also measured by turbine flow meters (Seametrics® SPX-050 series). A read-out device (to be specified) is also installed for converting the pulse frequencies from the turbine flow meter to a typical 1~5V voltage signal and then be transmitted to the USB-1616HS DAQ module. Similar

to the CO_2 turbine flow meter, the volume flow rate can also be calculated with equation 3-1.

3.3.4 Heating Power

The heating power is calculated based on the voltage drop across the heated test section and current output from the rectifier. A DC input two-wire transmitter (SR2101, accuracy ±0.1% of span) is used to measure the voltage drop and convert it to a typical output signal of 4 ~ 20 mA. A resistor of 250 Ω is connected to further convert the current signal to typical 1 ~ 5 V, which can be accepted by the DAQ module. A shunt resistor is located on the back panel of the rectifier, the voltage drop across the shunt resistor ranges from 0 to 100 mV, which corresponds the output from zero to full rated current (0 ~ 1500 A). A Bridge/Strain Gage Signal Conditioner (OMEGA®, DMD4059) is installed to convert the 0 ~ 100 mV to a typical output voltage signal of 1 ~ 5 V, then the current passing through the shunt resistor can be calculated, which is also the current passing through the heated section.

A linear correlation for calculating current with voltage drop is developed based on voltage drop across the heated channel and current (I= (voltage drop)*43.524+14.369). The heating power can be calculated simply with the measured voltage drop across the channel with a maximum uncertainty of ±2.2%.

3.3.5 Instrumental Uncertainty

There's no such a thing as a perfect measurement. All measurements of a variable contain inaccuracies. The measurement actually equals best estimate ± uncertainty. Uncertainties of measurement include instrumental uncertainty, random uncertainty, and the uncertainty caused by assumptions. Random uncertainty is usually caused by the experimenter. Take the present experiment as an example, there is a desire to measure a fluid flow rate or system pressure in the natural circulation system at a steady-state

condition. After making changes, it still takes a few minutes for the loop to stabilize. Although the system might be in “steady” operation after some time, there inevitably will be some time variations of flow rate or system pressure that will appear as random errors of the measurements during a period of time. The random uncertainty can be reduced by recording the data for a longer time (2.5 ~ 5 minutes) for current time-wise experiment. There are also some uncertainty induced by assumptions in the present experiment. For instance, the thermocouples for measuring fluid temperature are always tried and assumed to be placed at the center of the pipeline and the fluid temperature at the center is assumed to be equal to the averaged bulk temperature of the cross section of the pipe or tube. Last, but not least, every measuring instrument has an inherent uncertainty that is determined by the precision of the instrument. The following is a list of instrumental uncertainties of present experiment.

For temperature measurement, the RTDs for measuring liquid CO_2 temperature have a class A accuracy. Class A= ± (0.15+0.002*T) where T varies from -30 to 300℃. The T-type thermocouples have an accuracy of ±0.5 °C, whereas the K type thermocouples for tube wall temperature measurement have an accuracy of ±1 °C.

For pressure drop measurement, the differential pressure transducer VALIDYNE® DP363 and DP303 has an accuracy of ±0.5% of full span. The GP:50 industrial grade pressure transducer for measuring system pressure has an accuracy of ±0.2% of full scale, which is ±0.016 MPa for an nominal pressure of 8 MPa.

For volume flow rate measurement of liquid CO_2, the meter accuracy is ±0.98% for the upper 70% range of the FTB 1421 turbine flow meter. Unfortunately, almost all of the data points collected in the current experiment are in the lower 30% range of the meter, a meter accuracy of as large as -2.92% is calculated based on the calibration report provided by the manufacture, which means all the experimental results of CO_2 flow rate is underestimated by 2.92%. For the secondary side cooling system, the turbine flow

meter (SEAMETRICS® SPX series) for measuring water volume flow rate has an accuracy of ±1% of span.

For heating power, the EMPH® rectifier is rated to hold current fluctuations to within 0.1% of the full load current, for the line voltage variations of 0.1%. The SR2101 transmitter for voltage drop has an accuracy of ±0.1% of span and the temperature stability is ±0.015% of span per °C. The DMD4059 bridge/strain gage signal conditioner has better than ±0.1% of span and ±0.01% per °C.

3.4 Test Preparation and Procedures

Test preparation is mainly focused on calibration of differential pressure transducers, calibration of thermocouples, leakage test, evacuation and pressurization of test loop.

3.4.1 Calibration

DP cells (Validyne®) are initially calibrated by the manufacture and should be regularly calibrated before pressurizing the loop. With a Martel T-140-200" WC pressure calibrator and a Martel hand pump, the calibration is done by adjusting the ZERO and SPAN on the CD280 demodulator (Validyne®). Screw terminals ZERO and SPAN correspond the minimum and maximum values on the calibrator. DP cells are firstly disconnected and connected with a pressure calibrator. With zero stimulus to the DP cell, terminal ZERO is adjusted to ensure a LabVIEW interface reading of 0 psi. Hand pump is used to exert a maximum differential pressure on the DP cell. Terminals SPAN is adjusted until the differential pressure value on LabVIEW interface match the value on the pressure calibrator. With an ice bath and a boiling water bath of distilled water, a double-point calibration method is adopted for calibration of the thermocouples. Detailed information of the procedures can be found in [77].

3.4.2 Leakage Test

Leakage test is conducted after calibration is done. Praxair® industrial Nitrogen gas with 2200psi is used as a test gas because of its lower price and better performance compared to carbon dioxide. The experimental loop is pressurized with 400 - 500 psi for checking big leakages. After one day, if a pressure drop is identified, soapy water is used to detect the leakage. If there's no pressure drop or the pressure drop is very little, the experimental loop is pressurized further to check for leaks. Leakages usually exist at fittings and joints.

3.4.3 Evacuation and Vacuum

Once the leakage test is finished, the loop is flushed three times with CO_2. Then the whole loop is evacuated and vacuumed to eliminate air and moisture. For evacuation, valves V-3, V-4, V-5, V-6, V-8, and V-10 are opened. Valves V-1, V-2, V-9, V-11, and V-12 remain closed. For vacuum, V-13 is closed and V-14 is opened. The vacuum pump is turned on for about 20 hours. It is turned off to cool down after 3 hours' continuously operating. Valves V-8 and V-10 is closed when vacuum pump is turned off.

3.4.4 Pressurization

To pressurize the loop, the accumulator is pre-charged with a pressure of 450 psi. Valves V-1, V-2, V-8, V-9, V-10, and V-14 are closed. Valves V-3, V-4, and V-13 are open. Carbon-dioxide cylinder is then connected and opened. Ball valve V-12 is then opened and the pressure regulator is adjusted to slowly release some carbon dioxide into the loop. Once a balance of pressure is achieved between the loop and carbon dioxide cylinder, the booster pump is turned on to further pressurize the loop. To turn on the booster pump, the pneumatic supply system is turned on first, see Figure 3.7.

It must be noted that the connecting hose and high pressure part of the booster pump (red rectangular in Figure 3.8) becomes very hot after continuous operation. And the high pressure O-rings and plastic gaskets may be damaged, so cooling methods such as

spraying water on the hot part to cool it down or the booster pump has to be stopped after 15minutes' operation. Meanwhile, the accumulator is also pressurized slowly with Nitrogen gas by adjusting the pressure regulator. Once the pressure meets the desired working pressure, the loop is kept for a day to stabilize.

Figure 3.7 Pneumatic supply

Figure 3.8 Swegelok fitting on high pressure side of booster pump

3.4.5 Before Adding Power

Valves are checked to make sure they are at the right position. Experiments are done with or without accumulator and settling chamber.

·Close loop configuration (C1)

In this configuration, valves V-4, V-2 are in the closed position and V-1 is in open position, thus eliminating both the accumulator and settling chamber from the experiment.

·Non-close loop configuration with bladder type accumulator (C2)

In this configuration, valves V-1 and V-4 is in open condition and valves V-2, V-3 are in close position.

·Non-close loop configuration with settling chamber only (C3)

In this configuration, valves V-1, V-2 are in open position and valves V-3, V-4 are in the closed position.

·Non-close loop configuration with both bladder type accumulator and settling chamber (C4)

In this configuration, valves V-1, V-2, and V-3 are in open position and valves V-4 are in the closed position.

Electro-pneumatic valves V-5 and V-6 should always be kept open. All the instruments especially the absolute pressure sensors and thermocouples are double checked. If everything is working properly, access doors of the safety shield are closed and locked. The emergency shutdown switches are checked to keep deactivated. Now the power system is switched on step by step. First, the main power supply (Figure 3.9) is switched on. Second, the rectifier (Figure 3.10) is switched on. Third, the circuit breaker (Figure 3.11) is turned on. Now the power supply is ready for use.

Figure 3.9 Main power supply

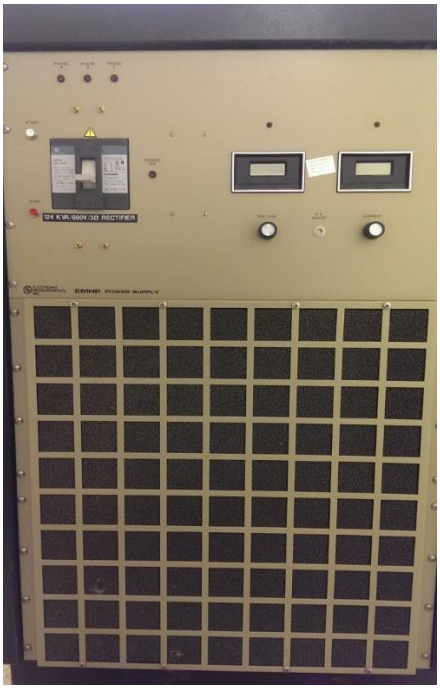

Figure 3.10 Rectifier

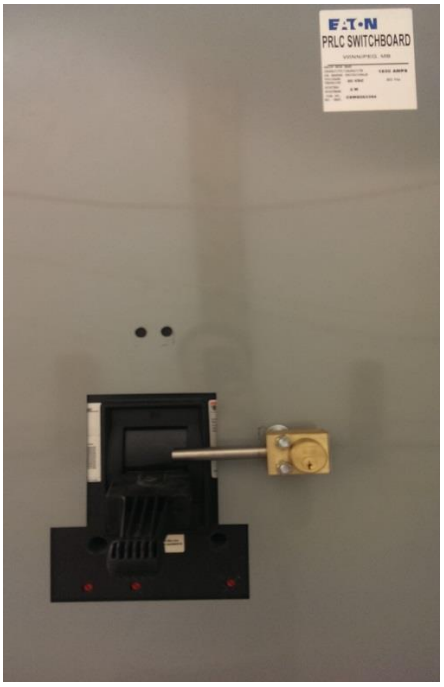

Figure 3.11 Circuit breaker

3.4.6 Test Procedures

The experimental loop is first run in steady state conditions. Then the inlet temperature and system pressure are kept constant while the heating power is increased to search for flow instability. The test procedures are as follows:

1) All signals of room temperature are recorded for 2 minutes.

2) The chiller and pre-set the output temperature (usually based on experience) of coolant are turned on.

3) The heating tape to add a small amount of power (0.5 kW), is turned on.

4) The power is increased to 1 kW over 10 minutes.

5) Observing the rate meter, if the value on rate meter is larger than180Hz, the heating tape is unplugged. This means the flow has already been initialized.

6) The power is increased to 4 kW over another 30 minutes and freeze power by clicking the freeze button on interface.

7) The electro-pneumatic valves V-5 and V-6 are adjusted to a desired position to hold the power for 15 minutes until the flow is steady again.

8) Steady state results are recorded for 5 minutes.

9) Heating power is added slowly. Meanwhile, output temperatures of coolant are adjusted on front panel of chiller to cool down the CO_2 to a desired value. The back pressure regulator of the accumulator is adjusted to keep the loop pressure at the desired value.

10) Once the power is increased, all the parameters are kept constant for 5 minutes to observe the wave chart of CO_2 flow rate on LabVIEW interface to see if there's an instability or not.

11) When instability is found, the power is reduced a little bit until the instability disappears. Data recording starts. At the same time the power is increased to observe the onset of instability.

12) After instability data is recorded, the power is reduced and parameters like inlet temperature are changed for another case.

13) When all cases are done, the power is decreased step by step until power becomes zero. Circuit breakers, rectifier, and main power supply are switched off. The mechanical key from power supply interlock is put it away.

14) The electro-pneumatic valves are fully opened. When the wall temperatures are close to room temperature, the chiller is turned off.

CHAPTER 4

EXPERIMENTAL RESULTS AND DISCUSSION

4.1 Introduction

Due to the strong coupling of the flow and driving force, natural circulation loops are always more susceptible to flow oscillations than forced circulation systems with pumps. Although it is already numerically found that the flow characteristics of supercritical natural circulation loops rely on the loop geometry, input power, system pressure, and inlet fluid temperature, direct experimental observations are still rare compared with the numerous experimental findings in sub-critical systems. In this chapter, the steady state characteristics of a natural circulation loop with single horizontal heated channel are studied. To study both steady state characteristics and flow oscillations, the power was gradually increased to search for flow oscillations while keeping the system pressure, inlet fluid temperature and outlet valve position constant during the test. During this process, both the steady state points and flow instabilities were recorded for numerical validations. Totally 13 loop flow instability cases were collected and assessed. Parametric effects such as system pressure, inlet temperature, and heated channel outlet local loss were studied based on the obtained instability cases. The accumulator effect, as well as various loop configurations on flow instability behaviours was also systematically studied for the first time. The local loss coefficients due to area changes around the experimental loop were calculated and shown in Appendix II. The working fluid of the present experiment was CO_2. To study the flow instability of supercritical CO_2, the operating condition must pass through the critical point of CO_2 (P_{cr} = 7.38 MPa, T_{cr} = 31.0 °C). Besides, with the increase of system pressure, the system will be more stable and flow

instability is harder to obtain. Therefore, the operating pressure for all the experimental cases was 7.6 – 8.6 MPa and the inlet CO_2 temperature range was 10 – 26 °C.

4.2 Steady State Characteristic and Repeatability of the Experimental Case

An experimental case of system pressure of 7.6 MPa, inlet temperature of 20 °C and no inlet and outlet local loss coefficient was conducted and the steady state flow-power curve was presented in Figure 4.1. As was expected, the mass flow rate of the system first increases with heating power input then decreases with further increase of heating power. On the positive slope portion of the flow-power curve the driven buoyancy force due to density difference dominates. The friction loss in hot leg (right leg of the experimental loop) increases gradually with the increase of flow rate and counterbalances the driven force in the peak region. After the peak region, the friction loss in the hot leg quickly increases and outweighs the driven force so the mass flow rate decreases with further input of heating power, though the negative slope of this case was not available due to the limitation of heating power input.

So any disturbance in the driving force affects the flow and will, in turn, affect the driving force. The drastic decrease of properties such as density when the fluid temperature surpasses the pseudo-critical point causes an increase in the driven buoyance force and therefore increases the flow rate, see Figures 4.1 and 4.2. With the increase of the flow rate, the increase of fluid enthalpy will be smaller with the same heat input, which means more ‘denser’ fluid is contained in the hot leg of the loop and the driven buoyance force decreases accordingly. A regenerative feedback is established under specific working conditions and damped or undamped flow oscillations may occur.

Before the study of flow instability behaviours, the same experimental case was duplicated and compared with the results of J. Mahmoudi [72] as a repeatability test. As

we can see from Figures 4.1 and 4.2, the two cases with the same working conditions agree very well (within uncertainties), which shows the repeatability of the experiments.

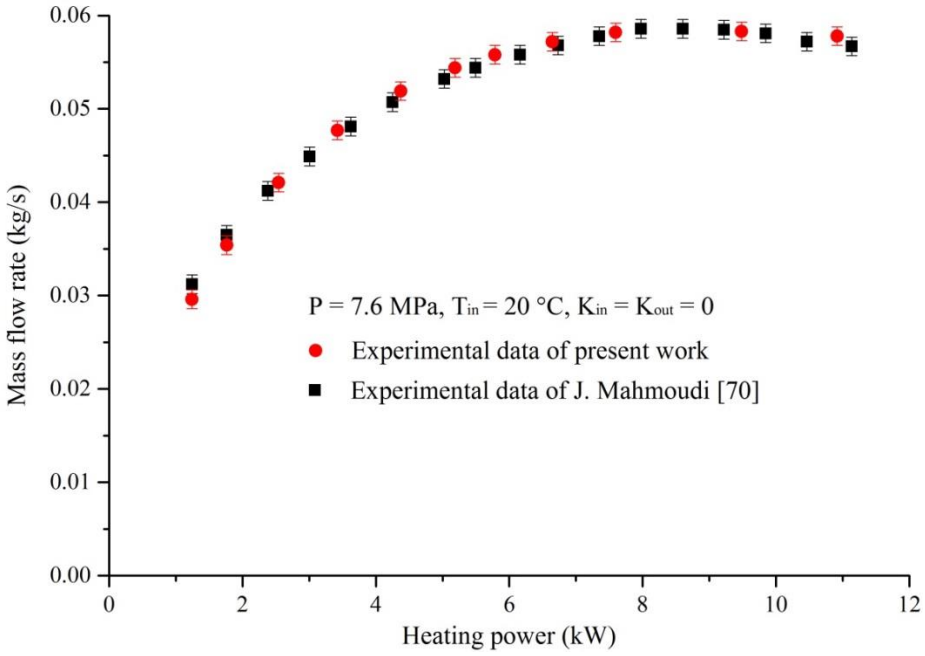

Figure 4.1 Steady state flow-power curve of natural circulation loop

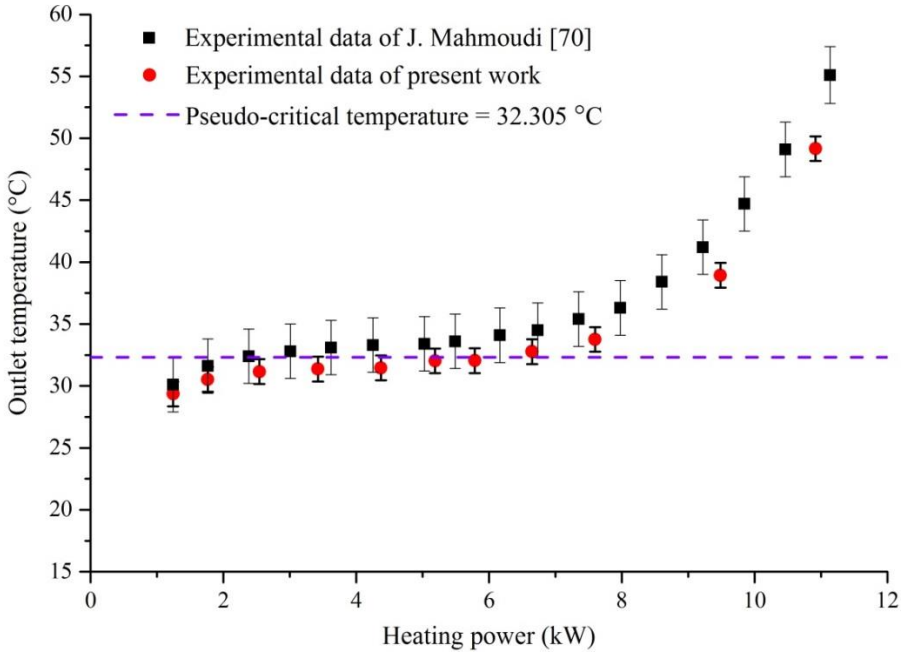

Figure 4.2 Comparison of heated channel outlet temperature

It can be seen from Figure 4.2 that with the increase of heating power from 2 kW to 7 kW, the heated channel outlet temperature actually doesn't increase much (~ 2.5 °C). This is because the fluid undergoes the pseudo-critical region, which is also called 'large specific region', see Figures 1.7 and 1.9. Interestingly, it can be noted that the pseudo-critical region of the fluid at the heated test section outlet doesn't correspond to the peak region of the flow-power curve, which actually occurs on the positive slope of the steady state flow-power curve.

4.3 Determination of Flow Instability Boundary

It is always important to know the stability boundary to safely run a natural circulation loop. As mentioned before, when parameters such as inlet temperature, system pressure and outlet and inlet valve throttling are fixed for a specific loop, heating power becomes the only changing parameter that affects the flow behaviour. In the present study, power was increased by intervals of 0.2 ~ 0.5 kW to search for heating power at the onset of flow instability.

For a winter cooling system, the cooling water temperature remains almost constant in an hour because of the constant outdoor temperatures; the CO_2 inlet temperature can be controlled by adjusting the coolant water flow rate. Take the case with system pressure of 7.6 MPa, inlet temperature of 16 °C, and outlet local loss coefficient of 13.1 as an example. As shown in Figure 4.3, with a small increase from 10.3 kW to 10.66 kW in about 5 seconds, the key parameters of flow rate, system pressure, CO_2 temperature at the heated channel outlet, pressure drop across shell & tube heat exchanger starts oscillating in a periodic behavior. So the boundary heating power for this flow instability case is between 10.3 kW and 10.66 kW. Unlike numerical simulations, it is very difficult to find the 'exact' boundary heating power while keeping other parameters constant during experiments. So an average value of 10.48 kW was assumed to be the boundary heating power.

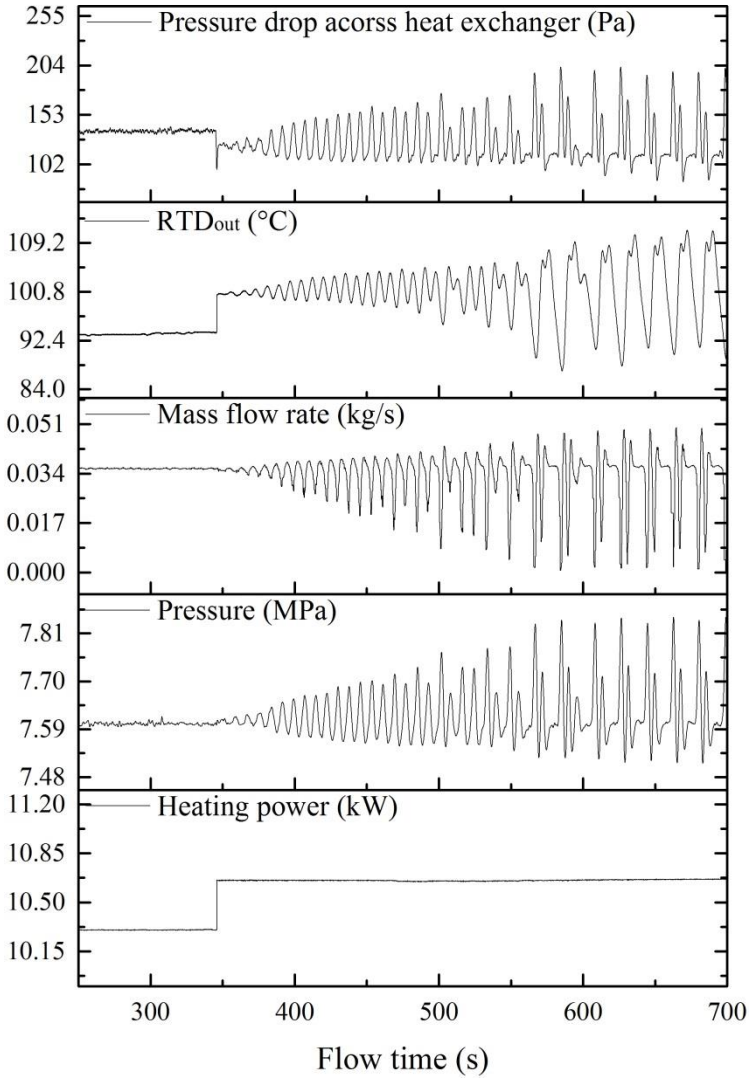

Figure 4.3 Determination of boundary heating power (Case 12)

For the summer cooling system with chiller as the heat sink, the flow rate of the secondary side cooling system is always kept constant. The CO_2 inlet temperature can be adjusted by controlling the coolant water temperature. With a preset coolant water temperature, the chiller will start working when the coolant water is 1 °F below the preset temperature and stop working when it is 1 °F higher. Take Case 3 (P = 8 MPa, T_{in} = 20 °C, K_{out} = 16.7) as an example, instability was found when the heating power was increased from 10.39kW to 10.75kW. And the loop pressure increased to 8.1 MPa and

the inlet temperature was about 20.5 °C if the secondary side cooling system was kept unchanged.

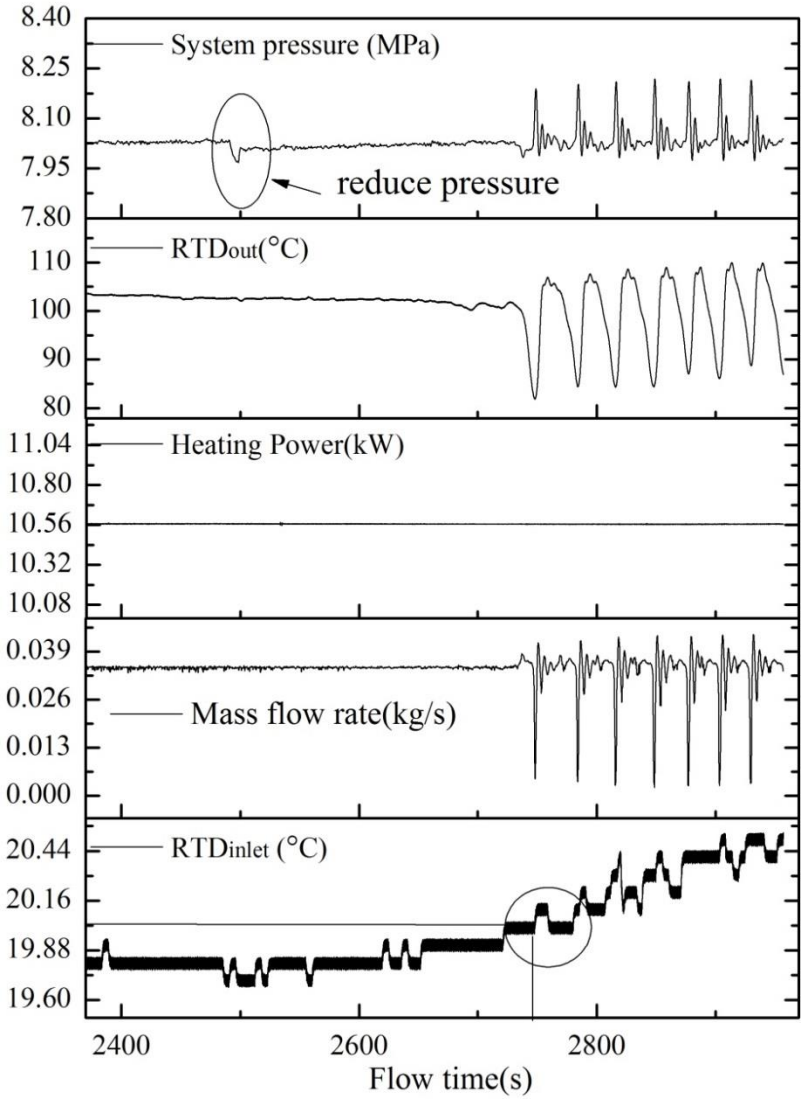

Figure 4.4 Determination of boundary heating power (Case 3)

To search for the instability boundary, the heating power was decreased with an interval of 0.1 kW and then kept constant. Meanwhile, the chiller was turned on to cool the inlet temperature slightly below 20 °C and the chiller was turned off to let the loop settle down. The circulation coolant temperature would slightly increase which resulted in an increase of CO_2 inlet temperature. Mass flow rate was monitored to check if there was flow

instability or not when the inlet temperature reached 20 °C. If the monitored CO_2 inlet temperature was about 20 ± 0.2 °C (values showing on LabVIEW interface) when flow instability occurred, the corresponding power input was considered the boundary power (Figure 4.4). Usually this process was repeated until the instability boundary power was found.

Based on this method, totally 13 flow instability cases under various operating conditions were conducted and their corresponding boundaries are summarized in Table 4-1.

Table 4-1 Experimental cases and instability boundary (with accumulator connected)

Cases	P (MPa)	T_{in} (°C)	K_{out}	Boundary heating power (kW)	Boundary mass flow rate (kg/s)
1	7.6	20	9.7	11.503	0.0385
2	8.0	20	12.7	11.509	0.0369
3	8.0	20	16.7	10.566	0.0344
4	7.6	20	21.0	9.345	0.0300
5	8.6	20	11.3	13.482	0.0383
6	8.0	20	30.0	8.525	0.0270
7	8.0	18	17.8	10.657	0.0350
8	8.0	23	18.0	10.377	0.0310
9	8.0	23	19.9	9.904	0.0288
10	7.6	10	11.6	12.25	0.0352
11	7.6	13	13.2	10.627	0.0363
12	7.6	16	13.1	10.48	0.0337
13	7.6	19	11.9	9.885	0.0306

4.4 Experimental Flow Instability Cases

The flow characteristics of the 13 flow instability cases were similar to each other, so three typical flow instability cases (Case 2, Case 6, and Case 13) of both steady state and oscillation behaviours are randomly selected and discussed. The steady state points of all 13 cases are presented in Appendix IV. It should be noted that all the 13 cases are loop flow instability cases with only the bladder type accumulator connected.

Example 1 (Case 2)**:** System pressure of 8 MPa, CO_2 inlet temperature of 20 °C, and outlet local loss coefficient of 12.7.

The similar steady state trend as explained in section 4.2, was obtained for Case 2 and plotted in Figure 4.5. Totally 15 steady state points were obtained for this case. The bigger blank dot represents the flow instability boundary. It can be seen clearly from Figure 4.5 that the flow instability occurred on the negative slope of the steady state flow-power curve.

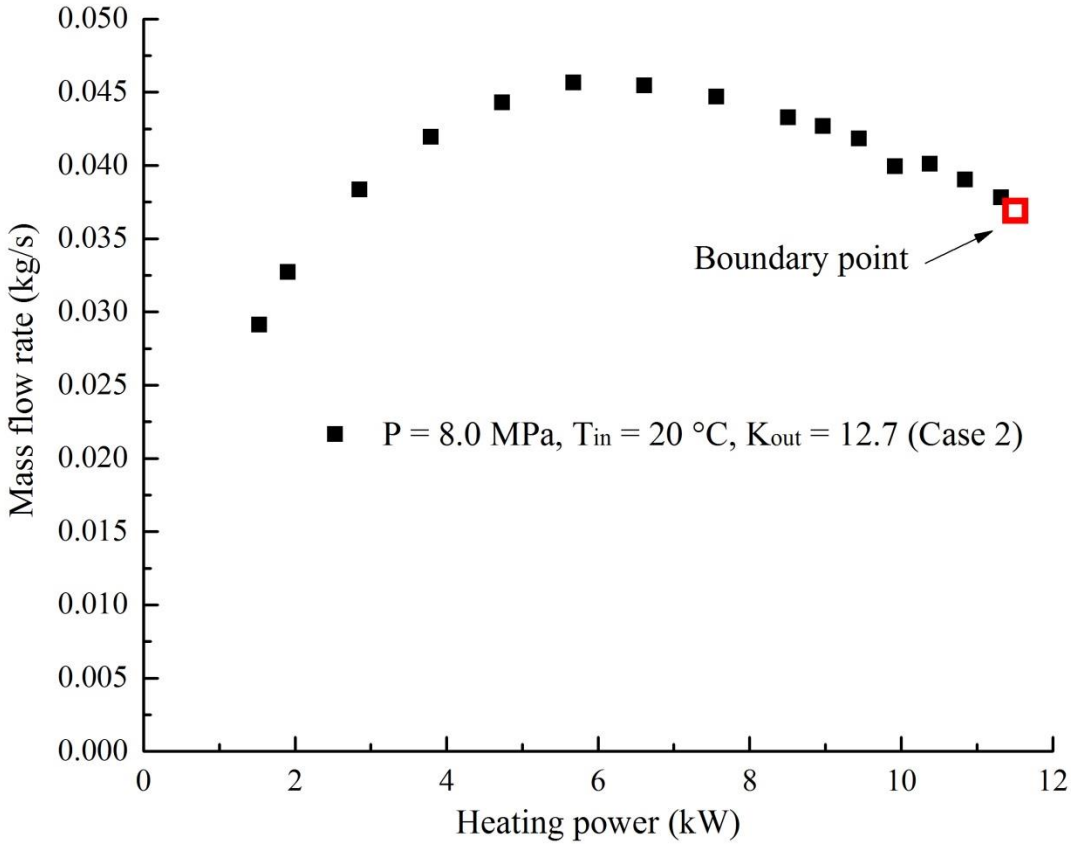

Figure 4.5 Variation of mass flow rate with heating power (Case2)

Figure 4.6 and 4.7 illustrates the dynamic behaviours of key parameters monitored when flow oscillation occurred. For a given constant power 12.25 kW, the fluctuations (larger than ±20% around the averaged value) of the fluid flow rate gradually increased with

time until a limit cycle oscillation was met. The maximum peak to peak fluctuation amplitude of system pressure was about 0.4 MPa for the limit cycles.

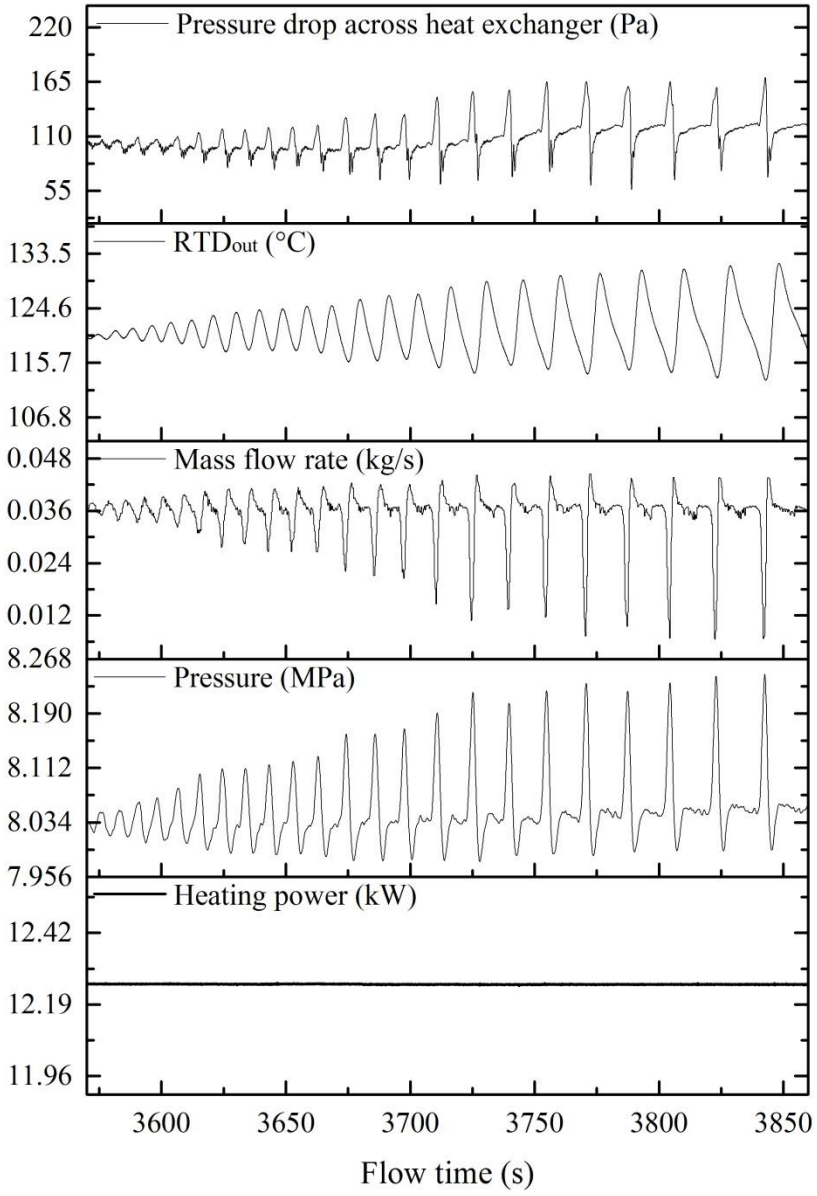

Figure 4.6 Flow oscillations with various changes of key parameters versus time (Case2)

Figure 4.6 shows that the system pressure oscillates exactly 180° out of phase with the mass flow rate and in phase with the heated channel outlet temperature. The heated channel outlet temperature was much larger than the pseudo-critical temperature (T_{pc} = 34.6 °C for P = 8 MPa of CO_2) and the peak to peak amplitude of the heated channel

outlet temperature was 18.5 °C. The pressure drop across the heat exchanger also oscillated periodically, but with a small phase lag with other parameters. All these phenomena show the flow instability is typical loop flow instability. The period of the limit cycle oscillations, however, was only 18.2 s, which was about 1/4 of the transit time (about 80 s) around the whole loop.

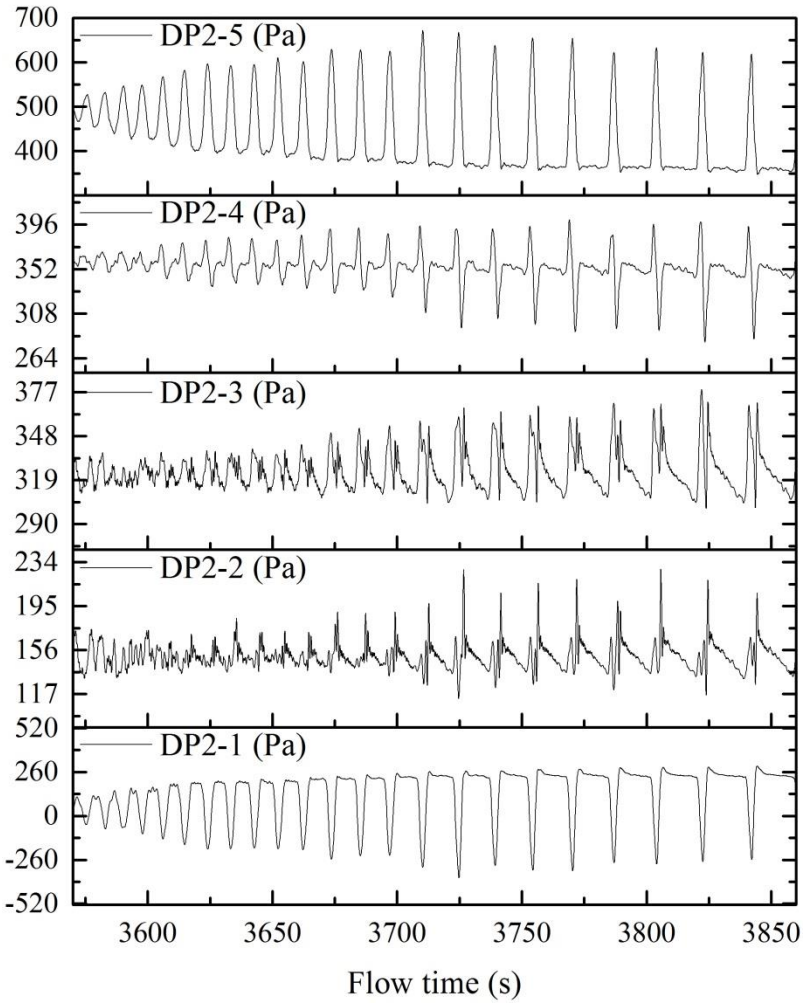

Figure 4.7 Evolution of segmental pressure drops with flow time (Case 2)

Figure 4.7 illustrates the change of segmental pressure drop along the heated channels when flow oscillations occurred. Considering the flow oscillation period was about 18.2 s, a second order Butterworth low pass filter with cut-off frequency of 0.5 Hz was used for

filtering the high frequency noises of differential pressure sensors (DPs). It can be seen that along the heated channel, the pressure drop for each segment increased. This was because with the input of heating power, the fluid temperature along the heated section increased and the density of the fluid along the heated section decreased, which resulted in the increase of the frictional pressure drop and acceleration pressure drop. It is interesting to find that the first segment of pressure drop (DP2-1) oscillated 180° out of phase with the last segment of the pressure drop (DP2-5), whereas the three segments of pressure drop (DP2-2 – DP2-5) at the middle of the heated channel fluctuated with different flow behaviours. The dynamic behaviours of the differential pressure drops was possibly a combination of the pressure waves moving forward and the pressure waves bounced back at the heated channel outlet valve.

Example 2 (Case 6)**:** Pressure of 8 MPa, CO_2 inlet temperature of 20 °C, and outlet local loss coefficient of 30.

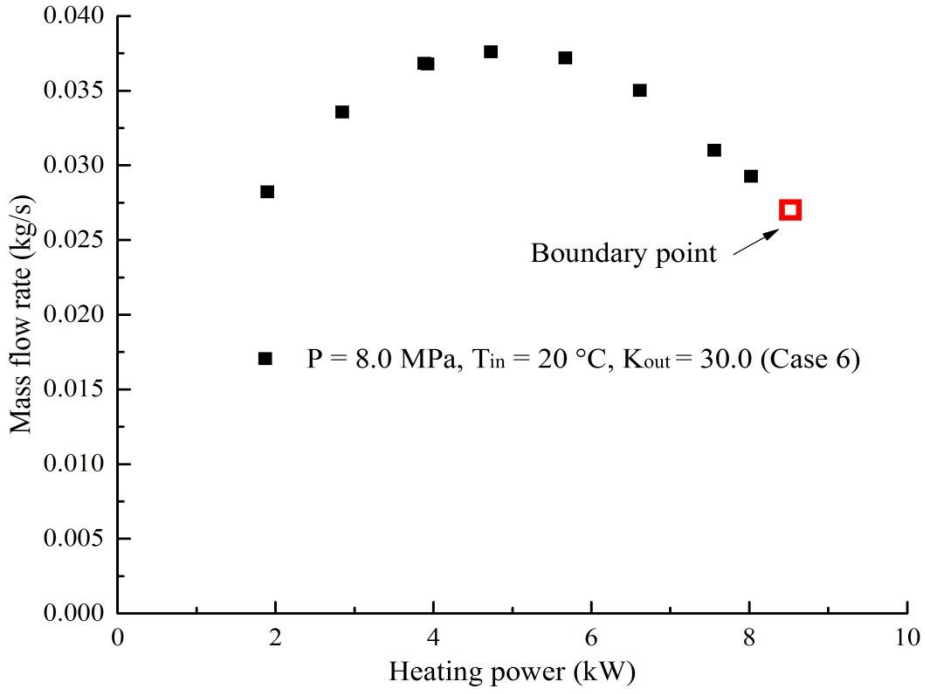

Figure 4.8 Variation of mass flow rate with heating power (Case 6)

Compared with Case 2, the heated channel outlet valve was throttled more while the system pressure and CO_2 inlet temperature were kept the same. As expected, a similar trend of flow-power curve was obtained but with a smaller peak mass flow rate because of the higher resistance in the loop. The flow instability boundary was again found to be on the negative slope of the steady state flow-power curve, shown in Figure 4.8.

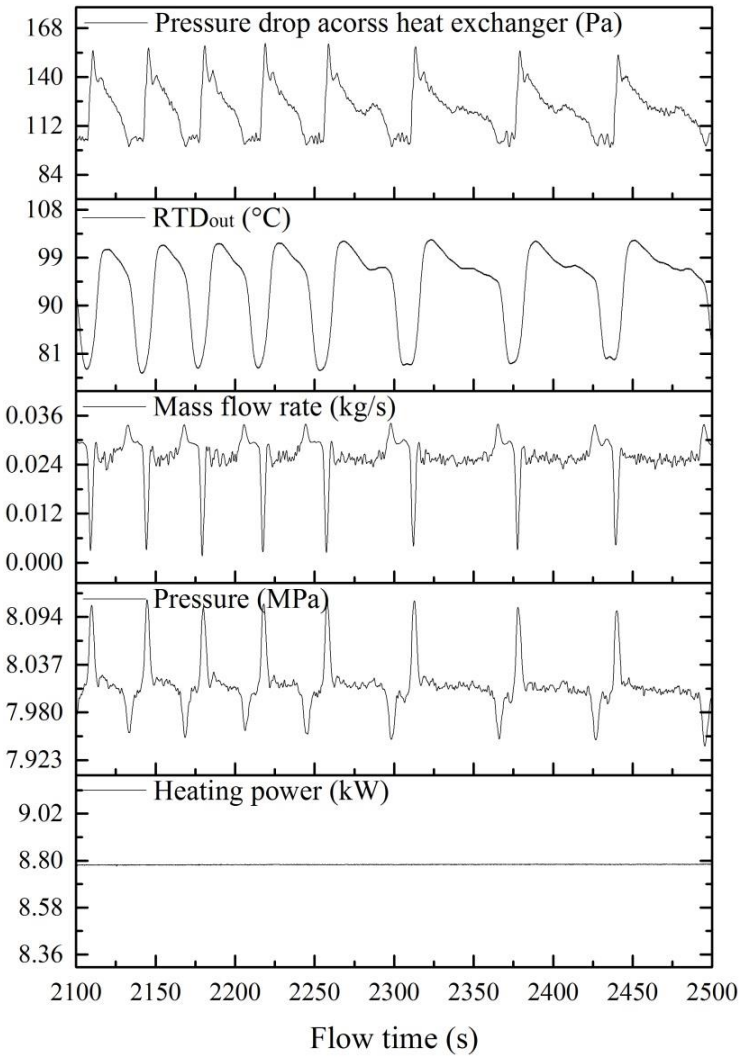

Figure 4.9 Flow oscillations with various changes of key parameters versus time (Case6)

A sample of flow oscillation behaviours were shown in Figures 4.9 and 4.10 at 8.78 kW. Similar to Case 2, the flow instability was self-sustained limit cycle flow oscillations. The mass flow rate oscillated largely out of phase with system pressure and almost in phase

with the heated channel outlet temperature. The heat exchanger at the upper tier of the loop also showed periodical oscillation behaviour. The period of oscillation in this case was about 34.9 ~ 70.2 s and the transit time of the loop for the steady state condition just before the occurrence of the oscillation was about 110s.

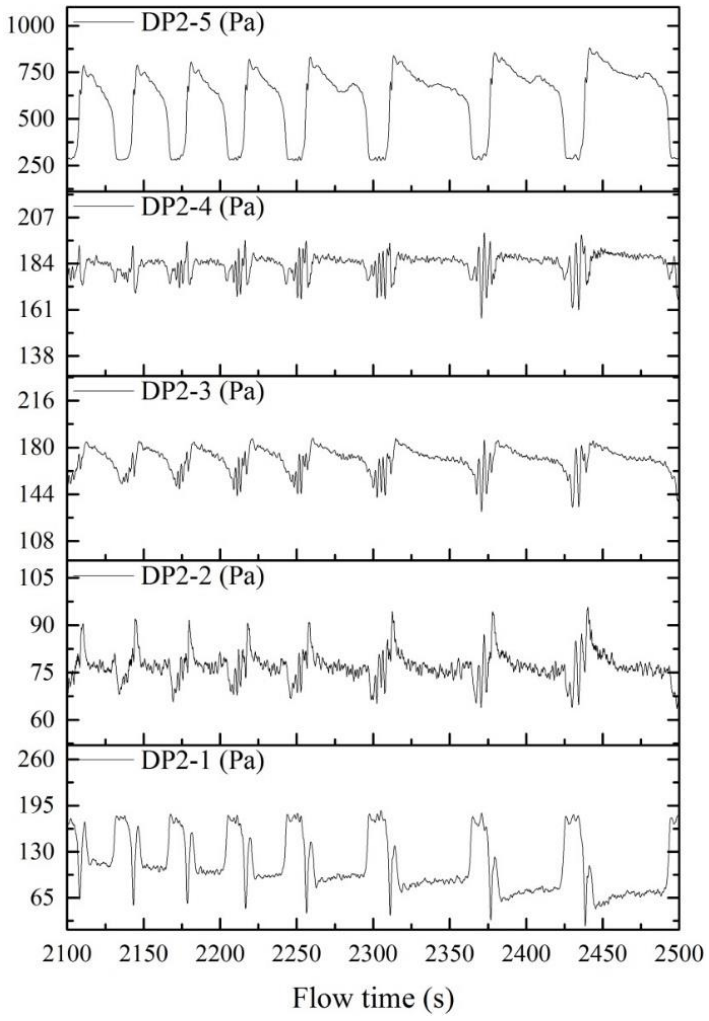

Figure 4.10 Evolution of segmental pressure drops with flow time (Case 6)

The plots of segmental pressure drops along the heated channel showed various oscillation behaviours similar to Case 2. This time the first segment of pressure drop was not 180 ° out of phase with the last segment of pressure drops. The transit time from the inlet of the loop to the heated channel outlet valve was calculated to be 32.6 s for this

case, which was close to the initial oscillation period of 34.9 s. Similar to Case 2, the inconsistent oscillations of different segmental pressure drop seemed to be caused by the feedback pressure waves and the pressure waves moving forward. Because if not, all the segmental pressure drops would oscillate with a similar behaviour except a phase lag between each other like the following Case 13.

Example 3 (Case13)**:** Pressure of 7.6 MPa, CO_2 inlet temperature of 19 °C, and outlet local loss coefficient of 11.9.

Similar to Case 2 and Case 6, the steady state mass flow rate first increased with the increase of power input and then decreased after the peak value was reached, as shown in Figure 4.11. The flow instability boundary was also found to be on the negative slope of the flow-power curve. In fact, the flow instability boundaries of all 13 cases identified were located on the negative slope and the heated channel outlet temperatures when flow oscillations occurred were much higher than the corresponding pseudo-critical temperatures.

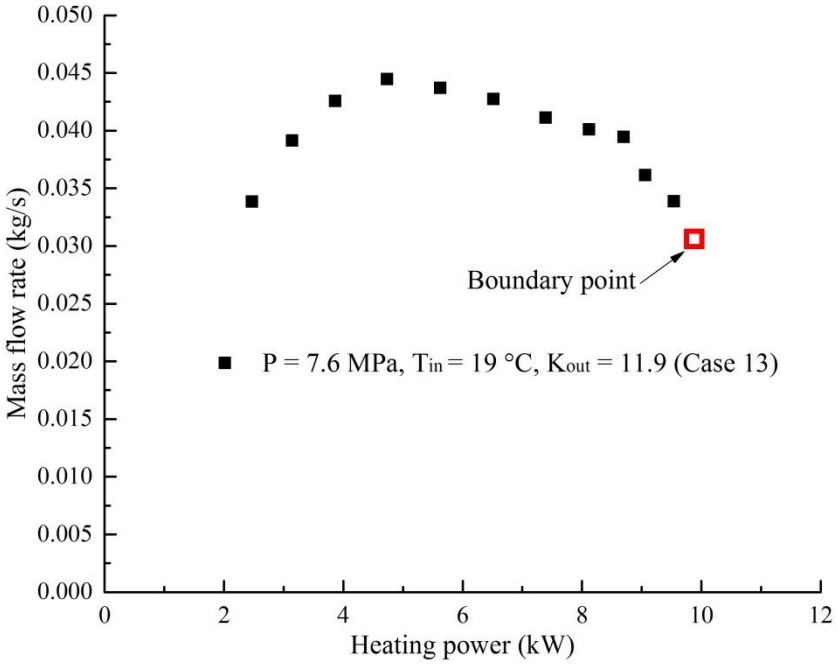

Figure 4.11 Variation of mass flow rate with heating power (Case 13)

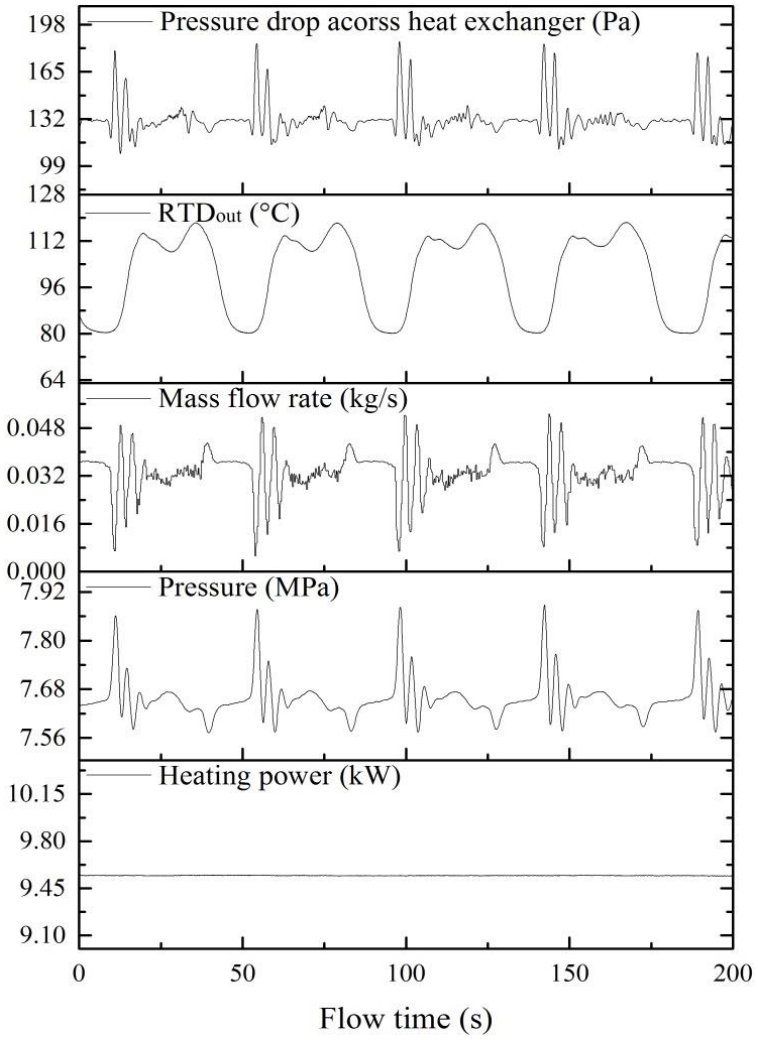

Figure 4.12 Flow oscillations with various changes of key parameters versus time (Case13)

Figures 4.12, 4.13, 4.14 and 4.15 show a set of representative time traces of oscillation behaviours for Case 13 at 9.54 kW. The similarities between Case 13 and the previous mentioned two cases were that the mass flow rate oscillated out of phase with system pressure, but there were also differences in the flow characteristics. From Figure 4.12, it can be observed that the mass flow rate oscillations with longer period (43.3 s) accompanied with shorter periods (3.7 s) of damping fluctuations. This was possibly due the interaction between bladder type accumulator and the hot, 'light' fluid at the heated channel outlet; both of them were compressible and could 'press' each other when the big oscillations started. The bladder type accumulator absorbed energy and damped waves,

but the periodical flow oscillation of the loop was in the dominant position and was still transmitted along the loop. Figure 4.13 plots the segmental pressure drop changes along the heated section. Unlike the previous two instability cases which had different dynamic behaviours, the oscillation behaviours are very similar (except DP 2-3 at the middle of test section) but with slightly different phases.

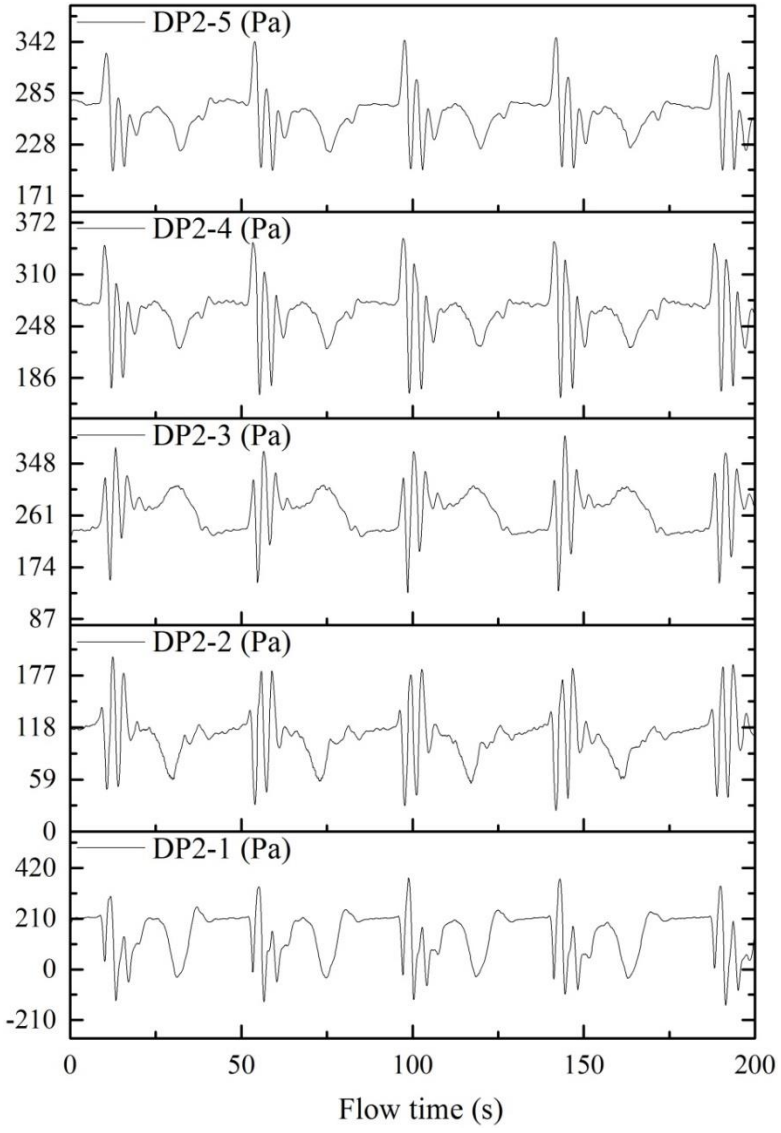

Figure 4.13 Evolution of segmental pressure drops with flow time (Case 13)

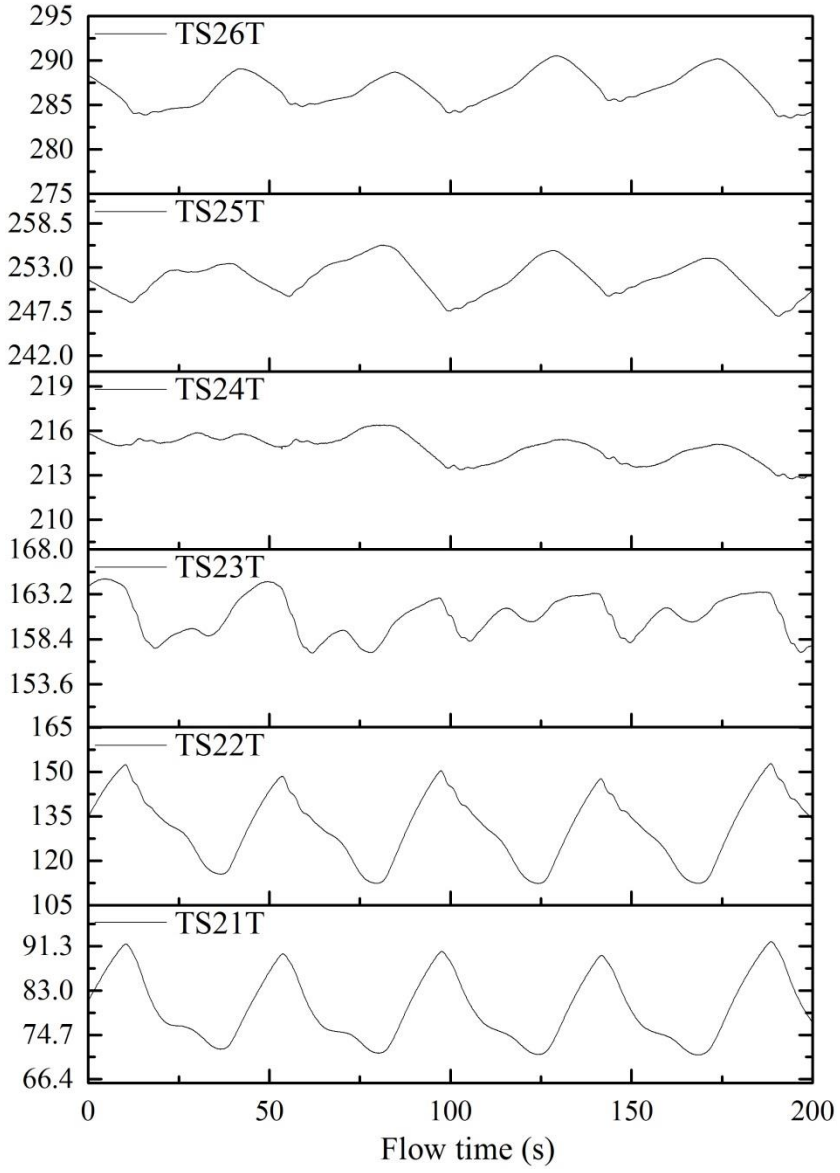

Figure 4.14 Evolution of top wall temperatures with flow time (Case 13)

Figures 4.14 and 4.15 show temperature oscillations of both top and bottom outer wall surface at various locations (section 1 to 6) along the heated channel. As can be seen, the bottom tube wall temperatures were all relatively smaller than the top ones. The reason is obvious. For a horizontal heated channel, the fluid inside the channel would gradually have a thermal stratification with increasing heat input, the top of which was hot fluid with a smaller density and at the bottom was cooler fluid with higher density. The

average difference between the top and bottom temperatures for each cross section increased along the heated channel until a maximum (137 °C for Case 13) was reached at the 'heavy & light' fluid mixture region where the fluid surpassed the pseudo-critical point and had the most drastic change of properties. Then the temperature difference decreased in the pure 'light' fluid region which is usually the last section of the heated channel.

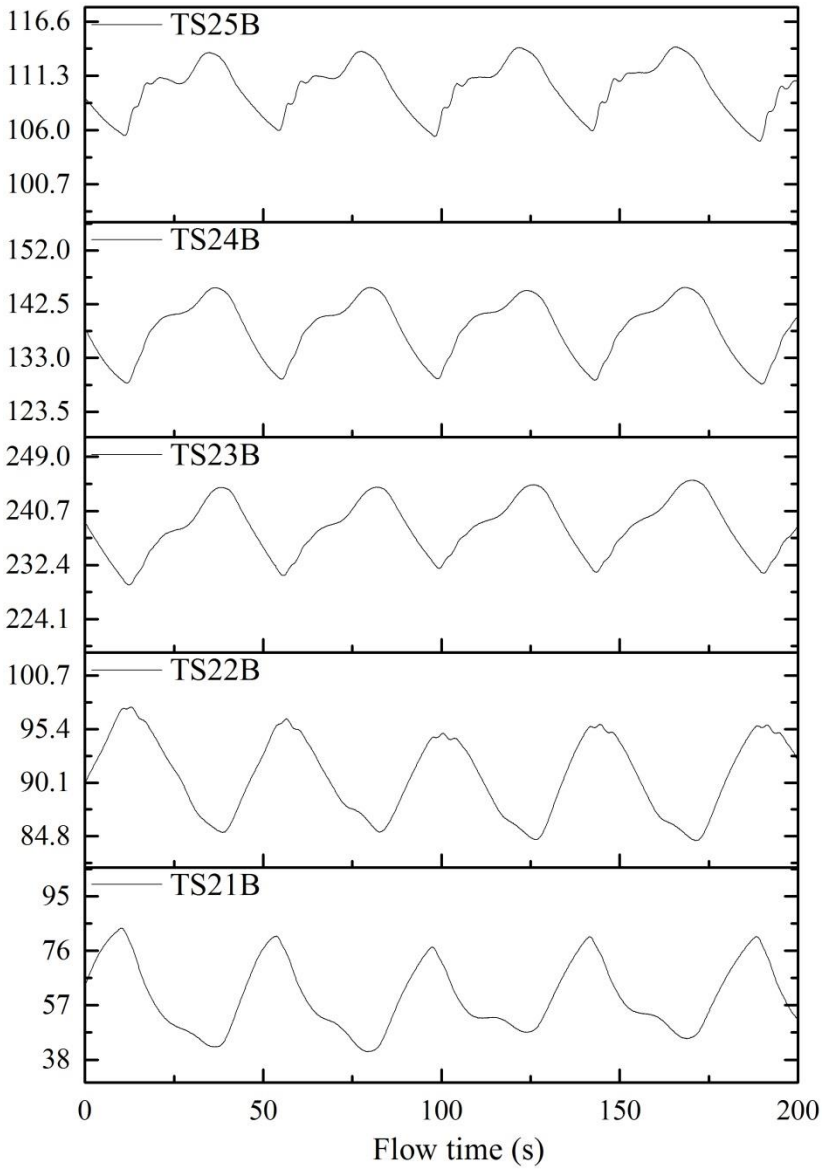

Figure 4.15 Evolution of bottom wall temperatures with flow time (Case 13)

Another apparent characteristic was that the peak to peak oscillation amplitudes of bottom wall surface temperatures at 'heavy' fluid region (about 40 °C) were much larger than that of 'light' fluid region (about 15 °C), which was the same for top wall surface temperatures. Even for the same cross section the oscillations of wall surface temperatures on the bottom was larger than the ones at the top. Take section 1 as an example, the peak to peak oscillation of temperature at the bottom was about 40 °C, whereas the peak to peak oscillation amplitude of temperature at the top was only about 17.5 °C. It was because with the same heat input the 'heavier' fluid always had a better cooling effect than the 'lighter' ones and was more sensitive to the variations of mass flow rate. This phenomenon of tube wall surface temperatures was also observed in all the other flow instability cases.

To sum up, for all the typical loop flow instabilities found with accumulator connected, the oscillation of mass flow rate was 180° out of phase with system pressure and almost in phase with heated channel outlet fluid temperature. The various dynamic behaviours of pressure drops as well as other important parameters like wall surface temperatures showed that the existence of interaction between the accumulator and the hot, 'light' CO_2. Besides, different from previous studies [61, 62], which reported, that the flow oscillation mainly occurred near the peak region, all instability cases found in the present studies were on the negative slope of the flow-power curve with outlet temperatures exceeding the pseudo-critical temperature. This finding is very similar to the type II instability under two-phase flow conditions proposed by Fukuda et al. [20] and Zhang et al. [54].

4.5 Parameter Study

4.5.1 Parametric Effects Study

Steady state flow-power maps of obtained experimental cases are illustrated in Figures 4.16 ~ 4.18. The instability boundary points, presented by red blank dots with blank interiors, are also included in flow-power plots.

Parameter effects of pressure, inlet temperature and local K factor of outlet valve on steady state characteristics and instability boundary of the loop can also be found in Figures 4.16 ~ 4.18. Due to the sensitivity of electro-pneumatic valves, outlet local loss coefficients K_{out} may not be kept exactly the same for different cases. Nevertheless, the general conclusions drawn still hold true to some extent and are consistent with previous numerical and analytical findings:

1) Increase of system pressure raises pseudo-critical point temperature resulting in a shift of peak mass flow rate to the right and stabilizes the system.

2) The increase of outlet K factors decreases mass flow rate significantly and moves the peak point to the left. The stability boundaries indicate a more unstable system.

3) Lower inlet temperature causes a larger density difference between the hot and cold legs also leading to a shift of peak mass flow rate to the right. In the present test range, an increase in inlet temperature will make the system more unstable, but the instability boundary is not dramatically influenced by inlet temperature change.

Interestingly, no instability was identified in the tested power range when the inlet CO_2 temperature was fixed at 22 °C of which the reason is still unknown. Due to the limitation of tube wall alarming temperature (425 °C), test cases for inlet temperature larger than 22 °C were conducted, but not finished. It can also be observed from Figure 4.17 that the mass flow rate quickly decreases to a small value as the power increases, which

correspondingly cause a large increase of tube wall temperatures. Considering the safety issue, the test had to be stopped.

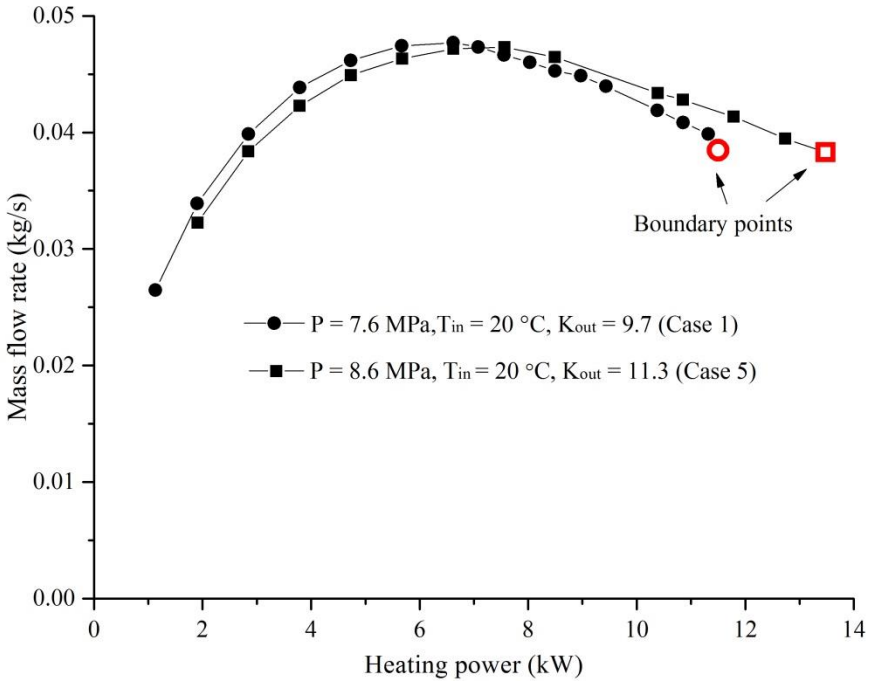

Figure 4.16 Effect of system pressure on power-flow curve and instability boundary

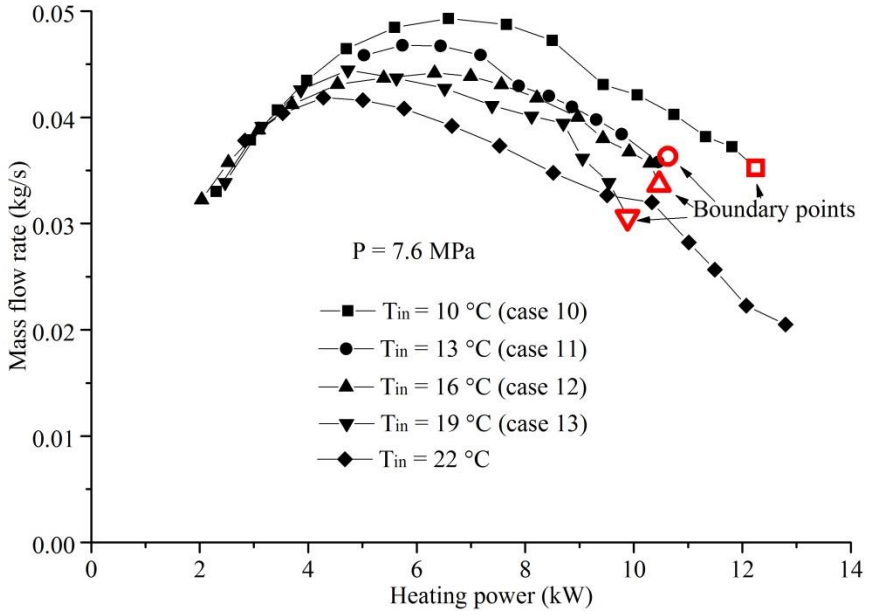

Figure 4.17 Effect of inlet temperature on power-flow curve and instability boundary

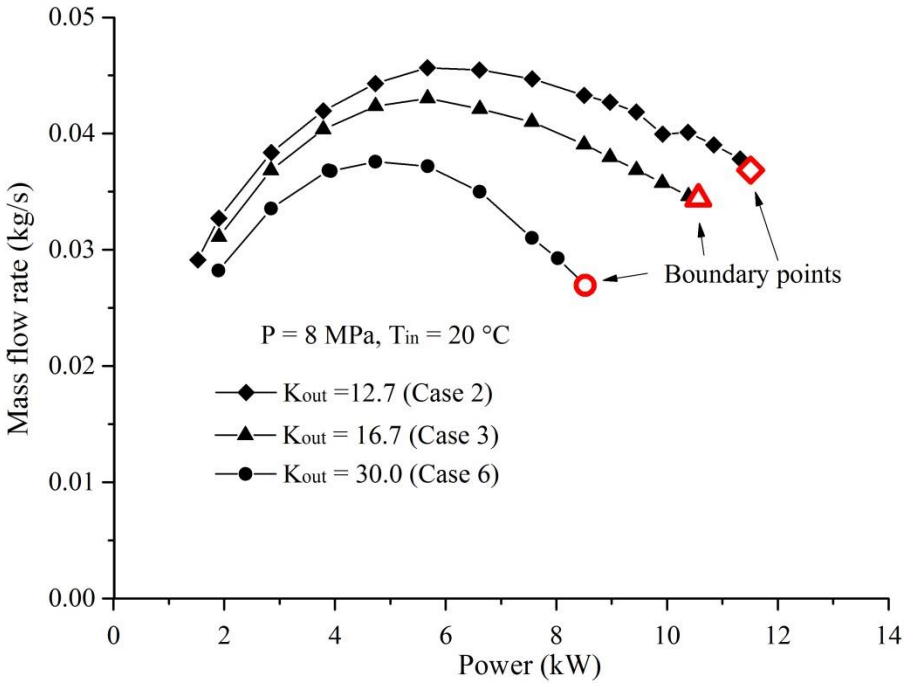

Figure 4.18 Effect of outlet local loss coefficient on power-flow curve and instability boundary

4.5.2 Accumulator Effect Study

The accumulator effect on flow instability was also tested by closing valve V1-4 to isolate the accumulator when instability occurred and a more systematic study is shown in section 4.6. As is shown in Figures 4.19, with the elimination of accumulator, the periodic oscillation of several parameters including system pressure, mass flow rate, and RTD outlet temperature immediately disappeared and the whole system became stable. When the valve was open to get the accumulator involved at a later time, the system became unstable again. This indicates that the accumulator plays an important role in flow instability of a natural circulation loop. It works as a compressible volume and interacts with the hot leg of the loop which is also compressible when the fluid temperature is beyond the pseudo-critical temperature. The accumulator effects had been repeatedly tested in all instability cases to make sure the phenomenon was not accidental. Another two typical examples are given in Figures 4.20 and 4.21. The results were the same in all cases tested.

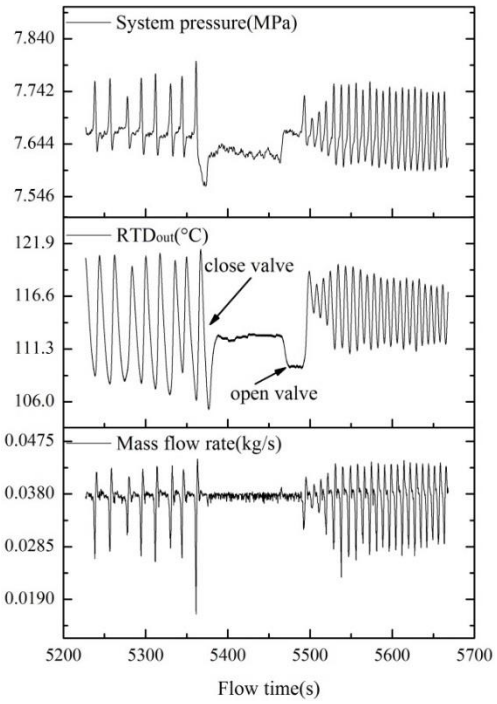

Figure 4.19 Accumulator effect (Case1)

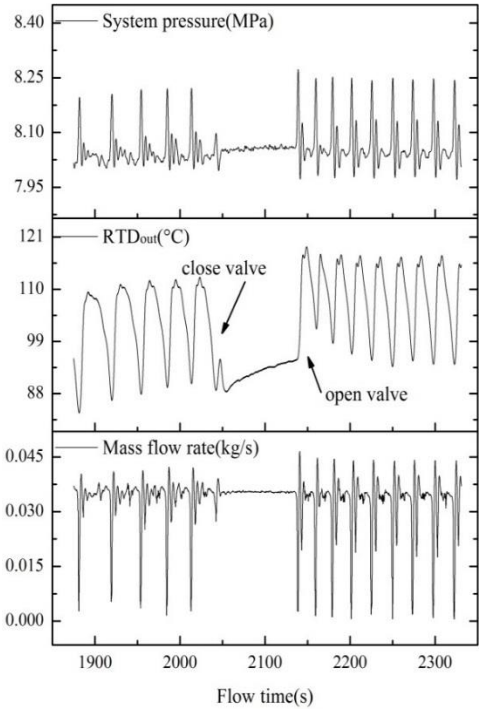

Figure 4.20 Accumulator effect(Case3)

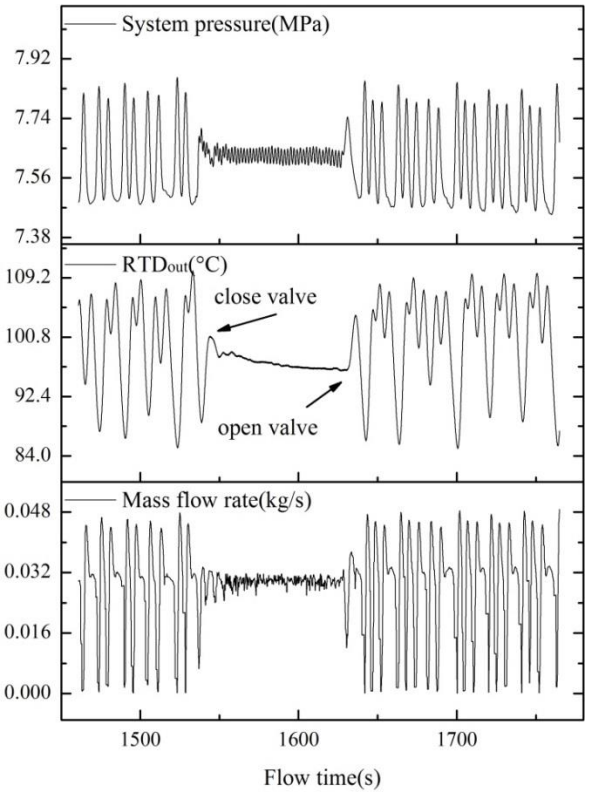

Figure 4.21 Accumulator effect (Case4)

4.6 Effects of Different Loop Configurations on Flow Oscillations

As was mentioned in the literature review, very few people mentioned the important role the accumulator (also referred as pressurizer or expansion tank) played on the fluid dynamics of supercritical natural circulation loops. In this section, an experimental case (Case 12) of system pressure 7.6MPa, inlet temperature 16°C, and outlet valve K_{out} =13.1 was selected as the base case; various loop configurations such as close loop condition (C1), rectangular loop connect with accumulator only (C2), loop connect with settling chamber only (C3), loop connect with both accumulator and settling chamber (C4) were studied systematically. The valve effect on the connecting line was also tested.

4.6.1 Close Loop Condition (C1)

The flow instability boundary power of Case 12 was 10.48 kW with the accumulator connected. For present case, valve V-4 and valve V-2 were closed so the loop was conducted with a close condition. And the heating power was increased gradually to search for flow instability; the case was stopped when the maximum wall surface temperature was close to the pre-set temperature. Figure 4.22 shows the key parameters change with time when the heating power was increased to about 12.2 kW, CO_2 temperature at heated channel outlet was not plotted because the temperature had exceeded the upper limit (150 °C) of the RTD. Although the mass flow rate showed some fluctuations, it was not typical loop oscillations like the ones shown in section 4.4 and concluded to be noise because the other key parameters like system pressure and pressure drop across heat exchanger all showed almost stable behaviours. This finding agrees with the experimental investigations done by Chen, L., et al. [65]. With their natural circulation loop, no flow instabilities were observed when the loop was operated under closed loop conditions with supercritical CO_2, but flow instability was found under subcritical conditions with the same loop.

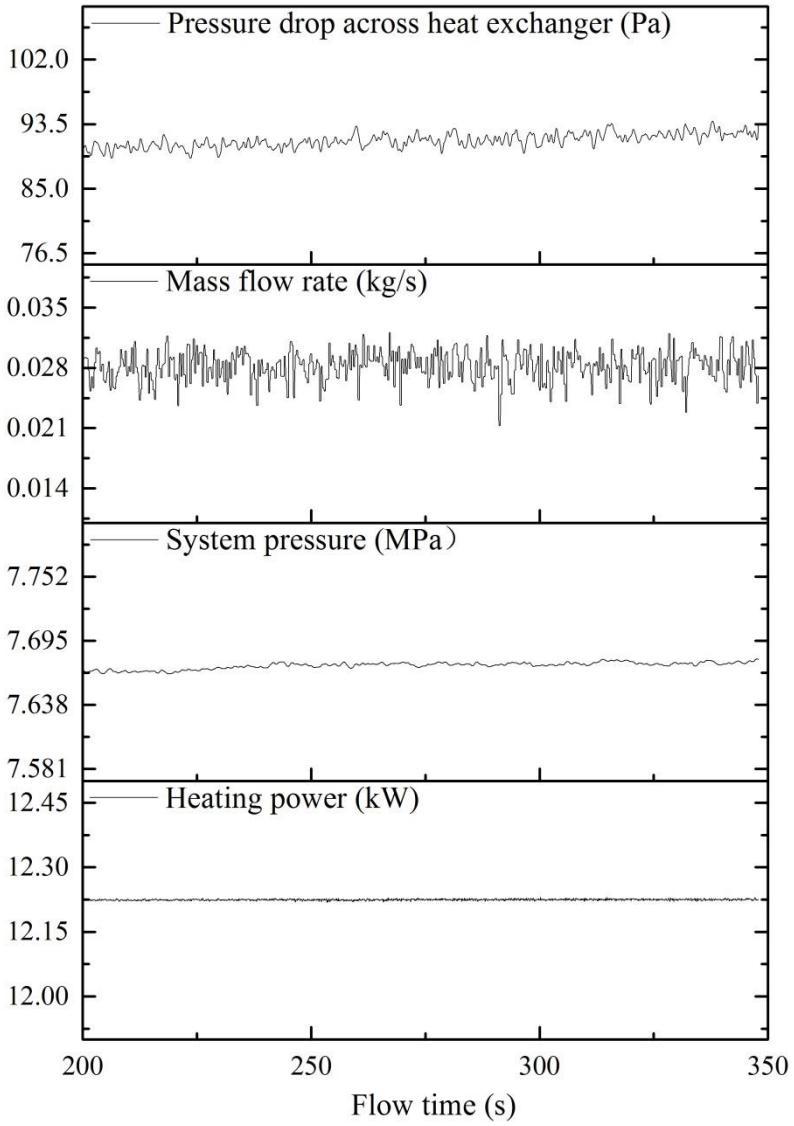

Figure 4.22 Flow behaviours evolve with time (based on Case 12)

The difference between the Chen, L., et al. [65] experiment and current experiment is that the heating power of the former experiment was added on the outer surface of the heated section with curved resistance wires, and an almost constant (less than 0.2 °C) coolant water temperature at inlet and outlet of the tube in tube heat exchanger was kept, whereas the current experiment used the test section as a resistance and heated it directly with uniform power and the coolant water inlet and outlet temperatures varied with increase of heating input to the loop. Despite these differences in heating and cooling methods, it

reveals that for closed loop boundary condition, it's difficult to find typical loop instability behaviour when the CO_2 inlet temperature is kept constant, because the compressible volume of the experimental loop is limited and the heated section wall structure has a strong damping effect on the flow instability.

4.6.2 Rectangular Loop with Accumulator Only (C2)

The experimental loop was tested with the same working condition, but connected the loop to the bladder type accumulator by opening the valve V-4. This set-up was the same as the cases shown in section 4.4. The throttling effect of valve V-4 was further tested by partially closing it.

a) With V-4 fully open

For this working condition, a sample of the signals was already presented in Figure 4.3. The main observations were the same as the typical loop instability cases presented in section 4.4. The mass flow rate fluctuated periodically out of phase with the system pressure and the period of the limit cycle oscillations was about 18 s. The CO_2 temperature on the hot side of the loop as well as the pressure drop across the heat exchanger also illustrated typical natural circulation loop instabilities that were not observed with the closed loop condition. This shows that the accumulator is an indispensable part of supercritical flow instabilities in natural circulation loop, without which no typical loop flow instability was observed during all the experimental tests. The bladder type accumulator acts as a compressible volume and interacts with the hot CO_2 fluid inside the loop which is also compressible when heated above pseudo-critical temperature.

b) With V-4 partially open

Experimental results presented in previous sections with close loop condition and Lomperski's ad hoc test [57] already showed that by closing valve V-4 to isolate the

accumulator (pressurizer) the flow instability would be eliminated inside a supercritical natural circulation loop. But it was still unknown what would happen if valve V-4 was partially closed. So in this section, the experimental case was repeated with stepwise increase of heating power until flow instability occurred, except that the valve V-4 was partially open. During the process, CO_2 was bled from the loop to keep the loop pressure around 7.6 MPa.

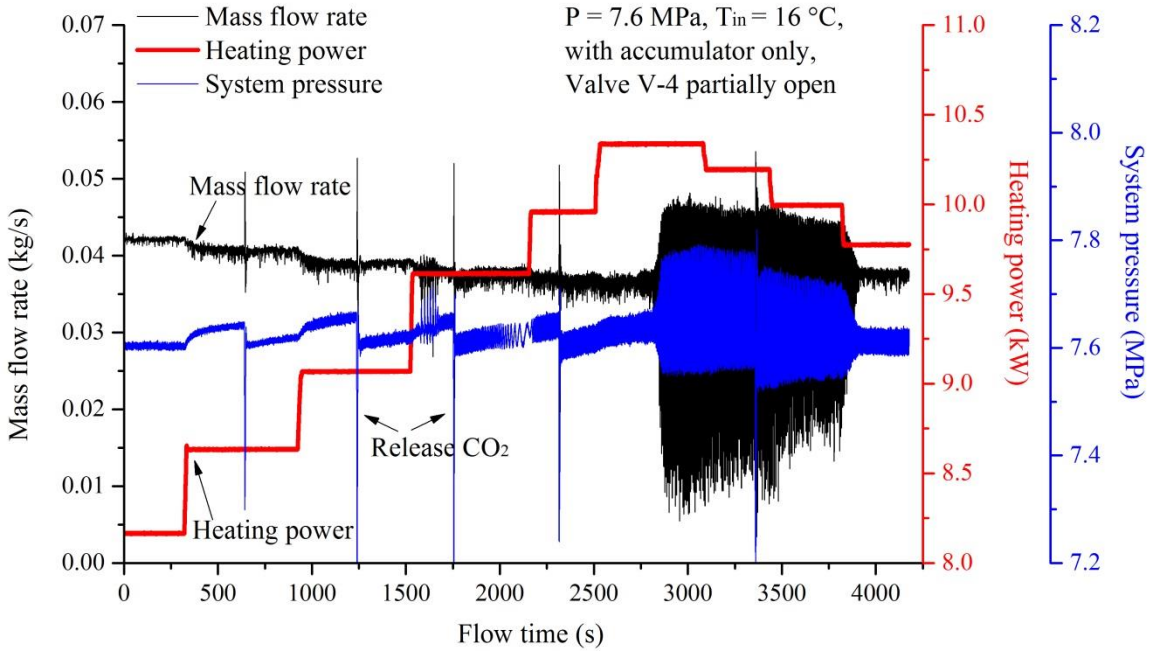

Figure 4.23 Evolution of mass flow rate as well as system pressure with flow time

It can be seen from Figures 4.23 and 4.24 that, instability still appeared when the heating power was increased from 9.96 kW to 10.34 kW. It can also be observed that with the increase of power the flow rate gradually decreased which meant the flow oscillations actually occurred on the negative slope of the flow-power curve. Compared with the characteristics of two spikes in one oscillation period with valve V-4 fully open, the dynamic behaviours of the oscillations showed only one spike in a single period of about 6 s with valve V-4 partially open, which meant the throttling of the valve V-4 on the

connecting line had an effect on the flow oscillation behaviours. Nevertheless, the flow instability boundary doesn't change much.

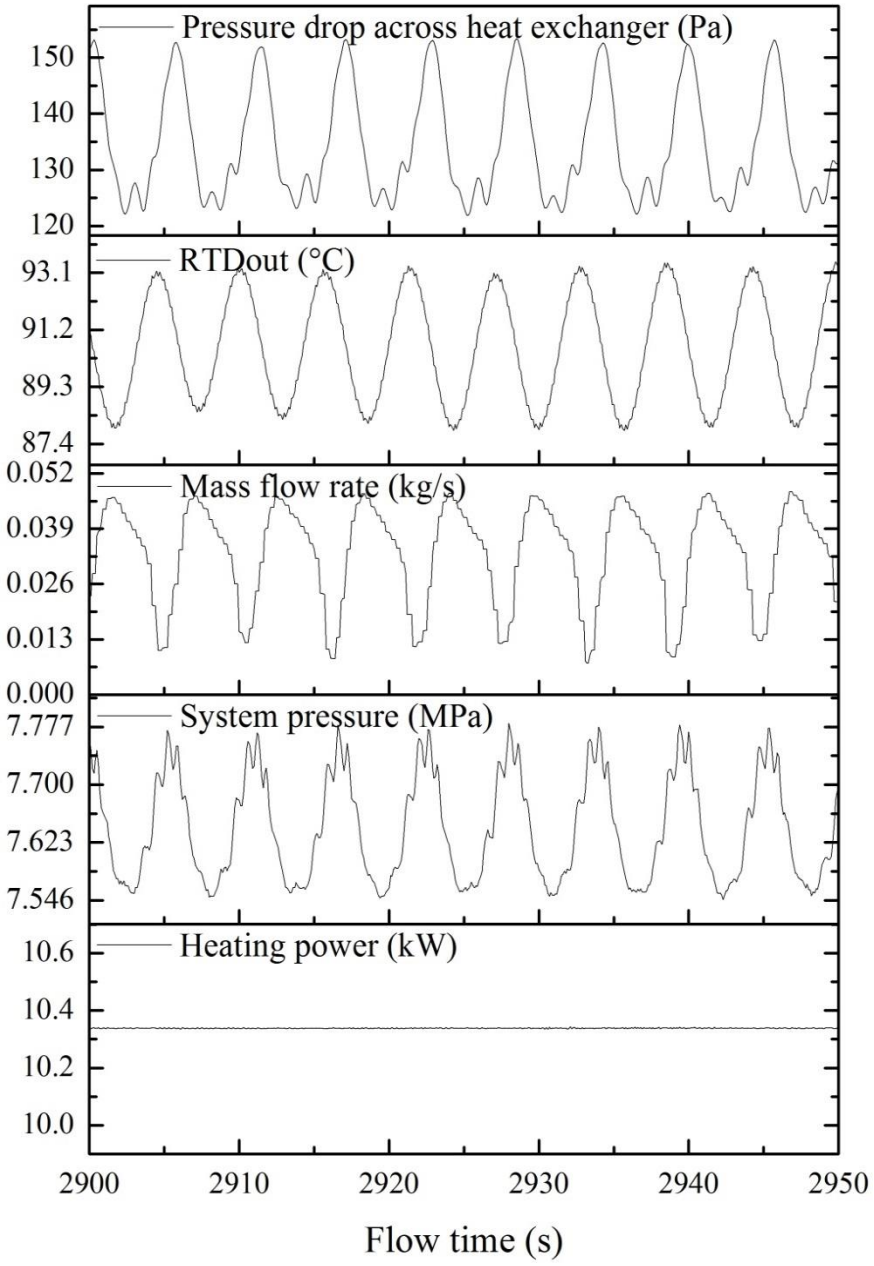

Figure 4.24 Oscillations of various parameters with time (Valve V-4 partially closed)

4.6.3 Rectangular Loop with Settling Chamber (C3)

a) With Valve V-2 Fully Open

In numerical analysis of supercritical flow instabilities, a large reservoir with constant pressure and temperature was usually used as the boundary condition of the natural circulation loop. This can be physically realized by connecting a large container with the experimental loop. To test if this condition can have an effect on the occurrence of flow instability or not, a large settling chamber was connected with the present loop, instead of using the bladder type accumulator. The difference between the settling tank and the bladder type accumulator is that the settling tank is a large rigid cylinder without any bladder or piston inside. Its volume is about five times that of the accumulator and the distance between the loop and settling tank is also shorter than the connecting length of the accumulator. The experimental case with the same working condition was conducted except valves V-3 and V-4 were closed to isolate the accumulator and valves V-1 and V-2 were open.

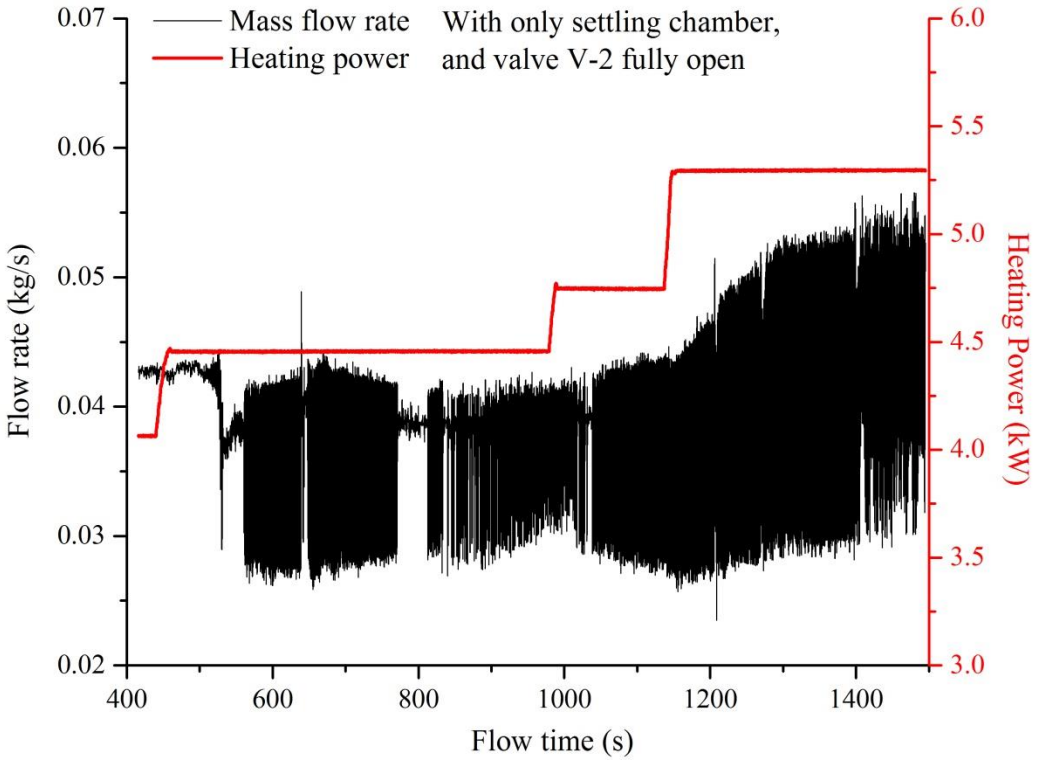

Figure 4.25 Evolution of mass flow rate as well as system pressure with flow time (Case 12)

As is shown in Figure 4.25, when the power was increased from 4.06 kW to 4.46 kW, flow fluctuations occurred. At the same time the system pressure was increased with the increase of power. So some CO_2 was released to keep the system pressure around 7.6 MPa. With further increase of power, the amplitude of the fluctuation became larger and the average mass flow rate also increased. This means the flow fluctuations occurred on the positive slope of flow-power curve.

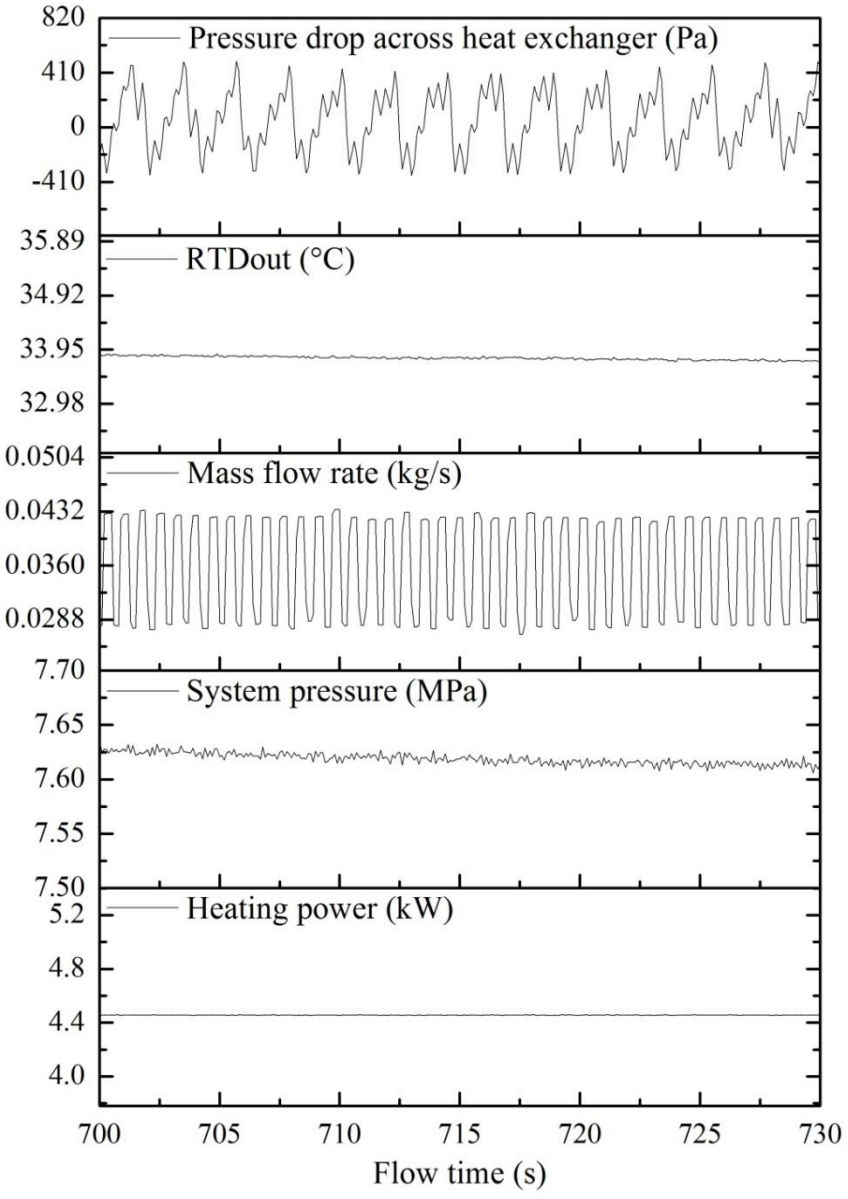

Figure 4.26 Parameters change with flow time (cut-off frequency of 1.45 Hz for pressure drop)

The parameters change with flow time is also presented in figure 4.26. It should be mentioned that a Butterworth filter with a cut-off frequency of 1.45 Hz was used to filter the electrical noises of the pressure drop signal. It can be observed that the flow oscillations are very different from the typical loop oscillations with bladder type accumulator connected. Only the turbine flow meter and differential pressure sensors showed oscillation behaviours. One of the main features is that the period is much shorter with only a 0.8 s period. Another difference found by comparing with the typical loop instability mentioned in previous section was that the pressure drop across heat exchanger oscillated with periodic flow reversals. When this phenomenon occurred, the whole loop was visible to be swinging. Whereas the RTD placed at the outlet of the heated section didn't show any flow oscillation behaviour. This may be due to the fact that the response time of the RTD is about 0.6 s, which is too close to the 0.8 s period such that this short period fluctuation may not be captured. More effort was made to get over this short period oscillation and search for the real loop instability. It was found that this short period oscillation didn't die out with further increase of power. The interesting phenomenon was that this short period oscillation occurred when the CO_2 temperature of the loop hot leg was within the pseudo-critical region (pseudo-critical temperature 32.3 °C at 7.6 MPa), where the volumetric thermal expansion coefficient for the fluid is the largest. The reason for the occurrence of the short period oscillations is unclear. It seems very likely that this short period oscillations are thermal acoustic waves generated when the inside wall temperature over a large part of the test section exceeded the pseudo-critical temperature [78]. Whereas the frequency of oscillations found in the current study is much smaller than the typical thermal acoustic waves of 10-100 Hz. Further analysis showed that this short period oscillation may be a phenomenon of a Helmholtz resonator. Considering that the short period oscillations only occurred with the rigid settling chamber, it is likely that the large settling chamber acts as a resonator and

resonates periodically with the rectangular loop. The resonance frequency can be calculated based on the resonance frequency equation [79],

$$f_0 = \frac{c}{2\pi}\sqrt{\frac{S}{l_0 \cdot V}} \qquad \text{Equation (4-1)}$$

where f_0 is the resonance frequency, c is the sound velocity in liquid CO_2 (839 m/s), S is the cross section area at the inlet of opening area, l is the neck length (total length of the loop with the connecting line), and V is the volume of settling chamber (0.056 m^3). The calculated resonance frequency is 2.69 s which is close to the period (about 2 s) of the oscillations across the heat exchanger. The difference is due to the fact that there are lots of small area changes and elbows along the experimental loop and the length used in the frequency equation is an ideal condition with constant loop area. The effective length is actually longer so the resonance frequency will be closer to the experimental frequency.

b) With valve V-2 partially open

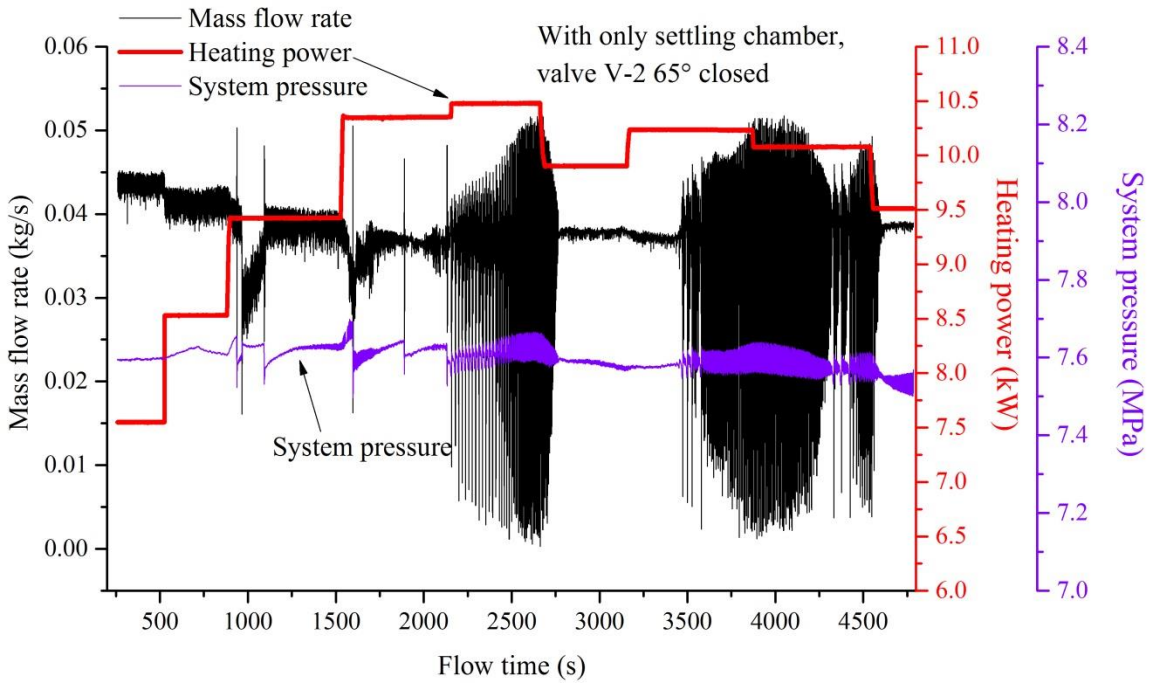

Figure 4.27 Evolution of mass flow rate as well as system pressure with flow time

The valve V-2 was also throttled to test its effect on flow oscillations, see Figure 4.27. Interestingly, with the same operating conditions except that V-2 was 65 ° closed, flow instability with longer period was observed when the heating power was larger than 10.48 kW. An enlargement of the mass flow oscillations (Figure 4.11) show that the flow oscillation period was larger (about 20 s). The measured RTD temperature at heater outlet showed a typical limit cycle oscillation with the same period of about 20 s.

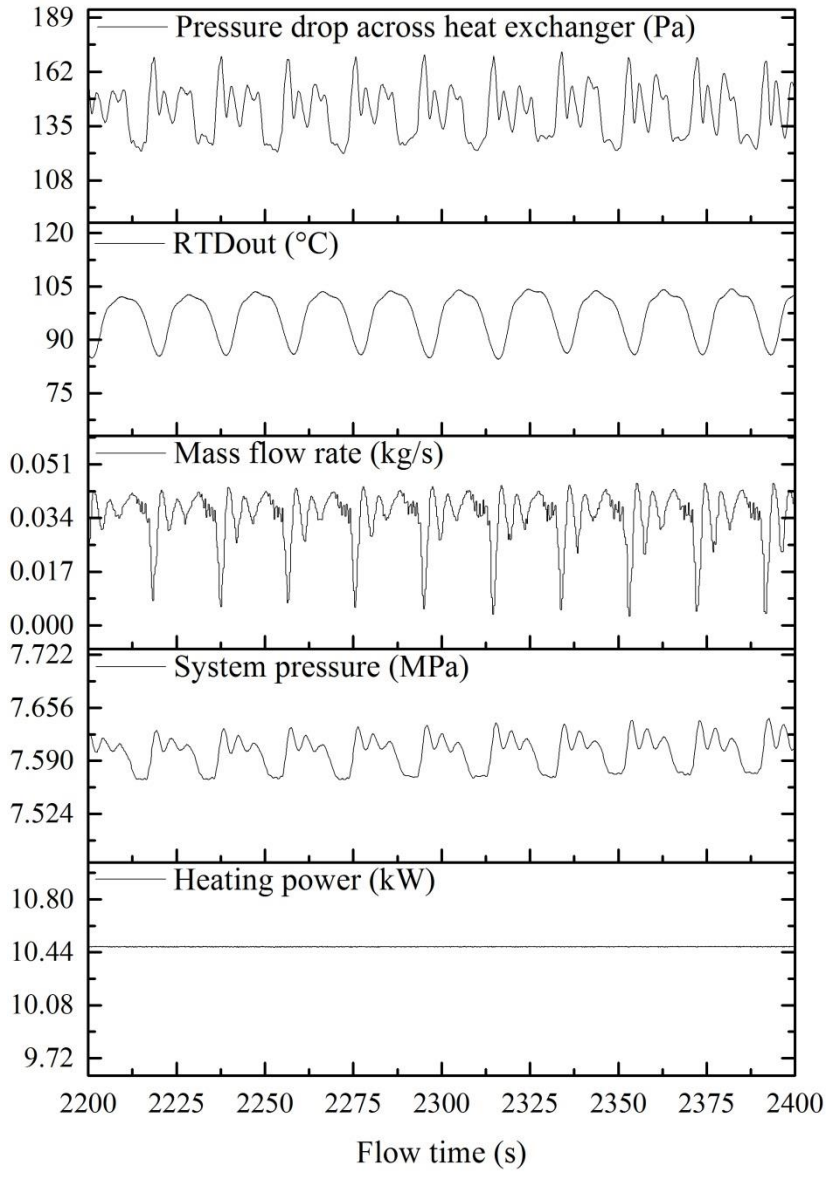

Figure 4.28 Parameters change with flow time (valve V- 2 almost closed)

The hot fluid temperature was much higher than the pseudo-critical temperature of 32.3 °C while the short period oscillation shown in the previous section was around the pseudo-critical temperature at 7.6 MPa. The pressure drop across heat exchanger further indicated that this was a typical loop instability which was similar to the one connected with bladder type accumulator. So it means that by adding more resistance in the connecting line between the settling chamber and rectangular loop, the short period flow fluctuations can be suppressed and eliminated.

4.6.4 Rectangular Loop with Both Settling Chamber and Accumulator (C4)

a) With V-2 fully open

More efforts were made to attenuate the short period oscillations and search for loop instability by connecting both the settling chamber and bladder type accumulator together to see if the accumulator can absorb the short period fluctuations or not. From Figures 4.29 and 4.30, short period oscillation similar to the oscillations found in the previous section occurred.

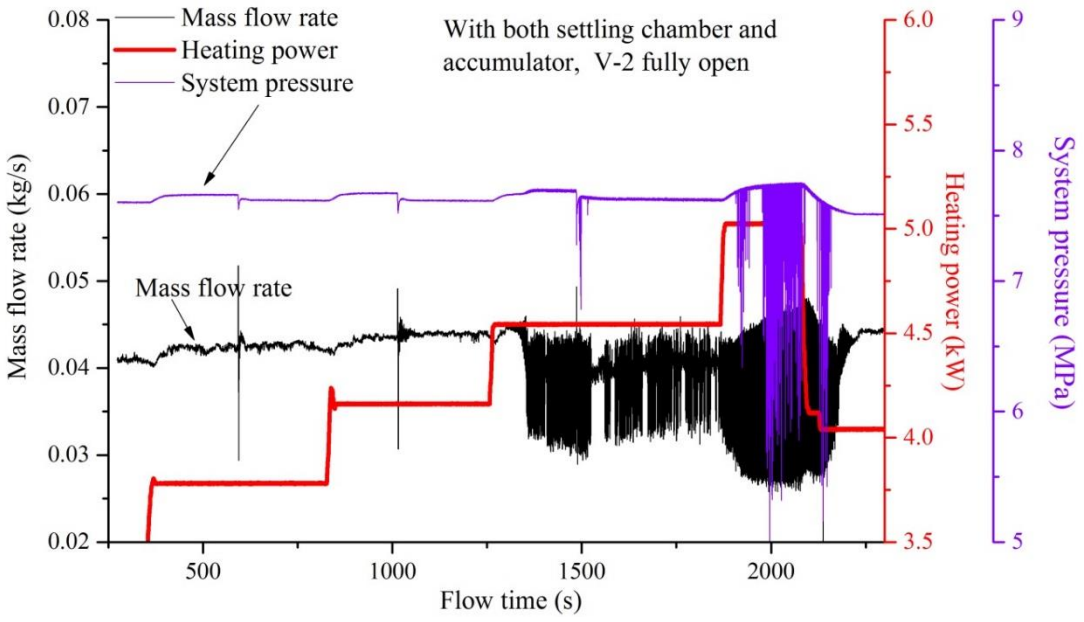

Figure 4.29 Evolution of mass flow rate as well as system pressure with flow time

It meant the bladder accumulator couldn't absorb it. Even the oscillation boundary heating power was close to be 4.5 kW in the two conditions which meant the Helmholtz resonator (settling chamber) effect was dominant. The heated channel outlet temperature was also in the pseudo-critical region. The main difference was found when the mass flow rate was filtered with the same cut-off frequency of 1.45 Hz. In Figure 4.30, it can be seen that a larger oscillation period of about 9s still exist (although the amplitude is small) for pressure drop across the heat exchanger which was different from the one in Figure 4.26. It indicated that the oscillations in this condition were a combination of Helmholtz resonance and loop instability.

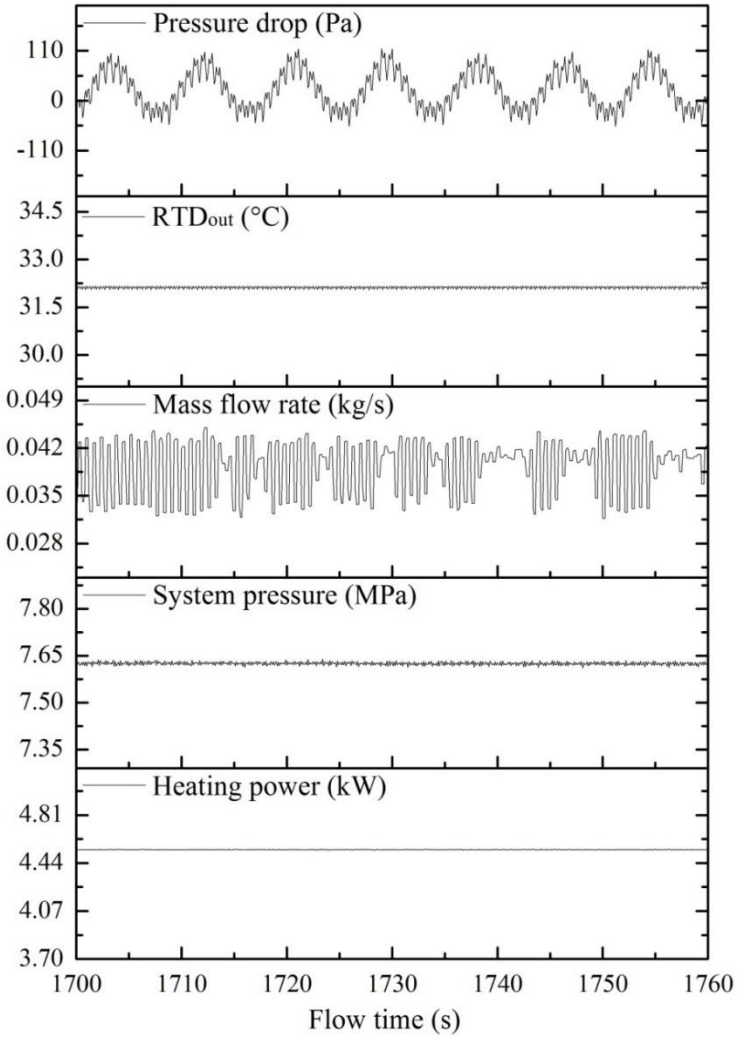

Figure 4.30 Parameters change with flow time (valve V-2 fully open)

b) With V-2 partially open

It was further proved that by throttling valve V-2 the short period oscillation can be postponed and attenuated. In Figure 4.31, with the valve V-2 half closed, it shows that with a heating power of 5.67 kW the short period oscillations started with smaller amplitude.

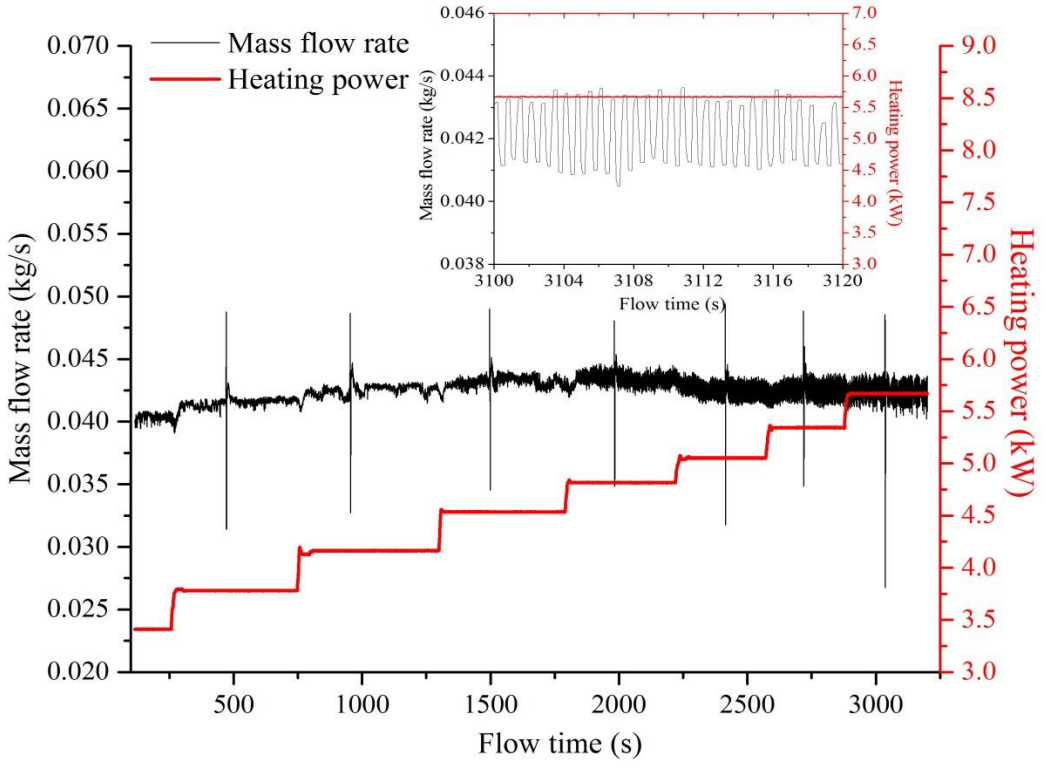

Figure 4.31 Flow characteristics with valve V-2 half closed

By further throttling the valve V-2 to almost close (>75°), the short period oscillations completely disappear. More power was added and finally loop instability with typical oscillation period of 10s appeared; see Figures 4.32 and 4.33. Similar to the ones shown in section 4.4, the instability occurred on the negative slope of the flow-power curve when heated channel outlet temperature is far surpassing the pseudo-critical point temperature. But the boundary heating power was larger to be between 10.83 kW and 11.86 kW.

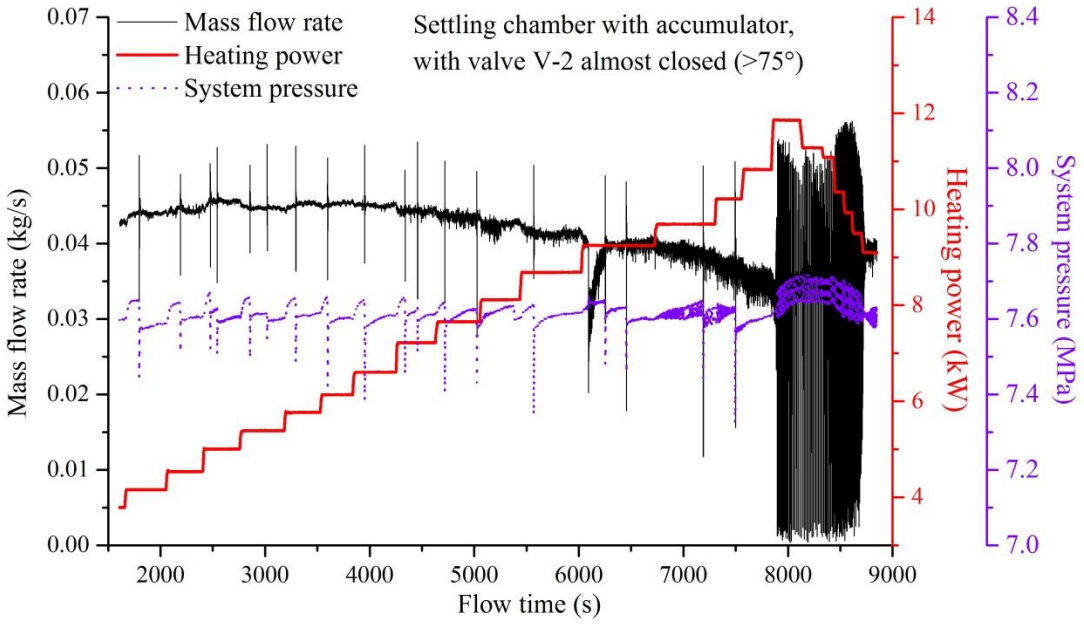

Figure 4.32 Evolution of flow characteristics with valve V-2 almost closed

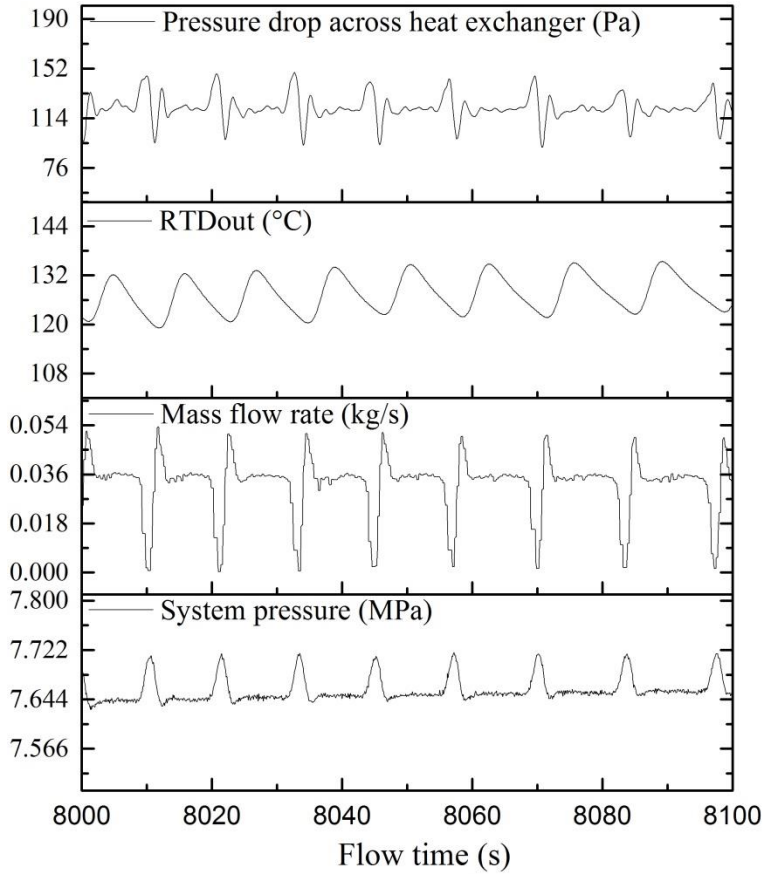

Figure 4.33 Parameters change with time (with heating power of 11.85kW)

4.6.5 Comparison of Steady State Results with Different Loop Boundary Conditions

The agreement of steady state is a primary requirement for further comparison of instability boundary. Thus, in order to perform a stability comparison, it is necessary to present the steady state flow-power curve accurately and clearly. As was expected, the steady state results (Figure 4.34) under different physical boundary conditions agree well with each other. It can be found that the instability boundaries vary with physically different loop boundary conditions.

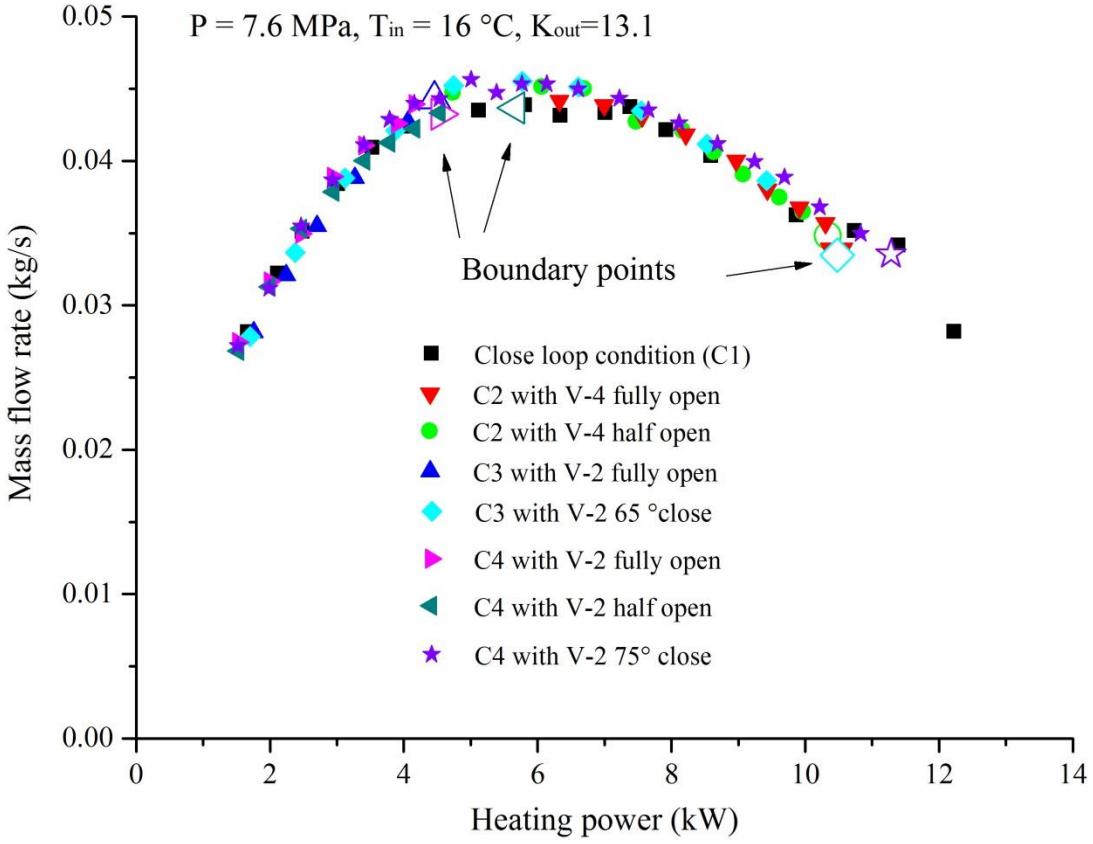

Figure 4.34 Comparison of steady state flow-power curves with different loop configurations

For a closed loop configuration, flow instability did not occur even when the electrical power was increased to 13 kW. For an accumulator condition, typical loop instability was observed and the instability boundary (10.47 kW) was found on the negative slope of the flow-power curve. The valve V-4 was then throttled to more than half of its full position,

but the instability boundary (10.34kW) didn't change much. With the settling chamber condition, short period oscillations occurred in the positive slope of the flow-power curve, which was near the peak mass flow region. With a throttling effect of valve V-2, the short period oscillation disappeared and the boundary power was postponed to the negative slope of steady state curve. The instability boundary (10.48 kW) was closed to the one that occurred with only the accumulator connected. The boundary of the short period oscillation found with both accumulator and settling chamber was almost the same as the one with only the settling chamber connected. By throttling valve V-2 the instability boundary was postponed to the peak of the steady state curve. With further throttling of valve V-2, the short period oscillation totally disappeared and the instability boundary (11.28 kW) of typical loop instability was found to be on the negative slope of the flow-power.

These experimental findings show that the closed loop boundary configuration is the most stable one. The typical loop instability boundaries don't change much by throttling the valve to be around half of its fully open position. Interestingly, the valve throttling effect with both accumulator and settling chamber connected showed a larger instability boundary when the valve was almost closed, which indicates that the resistance along the connecting line may have an effect on the flow instability boundary when it is extremely large. This needs to be validated with numerical investigations.

From previous sections, it was already found that the instability boundary of short period oscillation didn't change much between only accumulator connected and the condition when both accumulator and settling chamber were connected if valve V-2 was fully open. For this part, the effect of loop inlet temperatures on short period oscillation boundary was tested with both accumulator and settling chamber connected at the same time.

As was already shown previously, typical loop instability occurred when the fluid temperature at the heated channel outlet was far exceeding the pseudo-critical

temperature. But this was not the same with the shot period oscillations. Figure 4.35 shows that the boundary heating power decreased with increase of loop inlet CO_2 temperatures. It is observed from Figure 4.36 that all the short period oscillations occurred when the outlet CO_2 temperature was near the pseudo-critical temperatures. So with a larger inlet CO_2 temperature, less power was needed to heat the CO_2 to the pseudo-critical temperature. When the CO_2 at the heater outlet was close to the pseudo-critical temperature, the change of fluid properties caused a pressure perturbation in the whole system. This perturbation was absorbed if the loop was only connected with the bladder type accumulator and the system would show steady state behaviour, whereas if the large rigid settling chamber got involved, the perturbation became amplified and resonated inside the whole system.

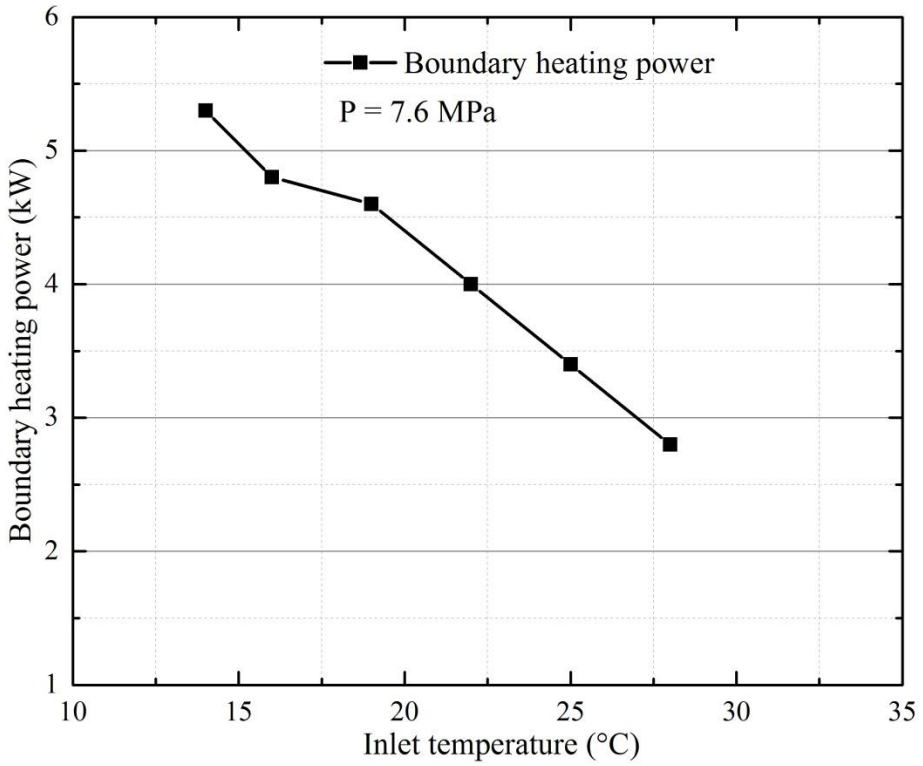

Figure 4.35 Boundary heating power with various CO_2 inlet temperatures

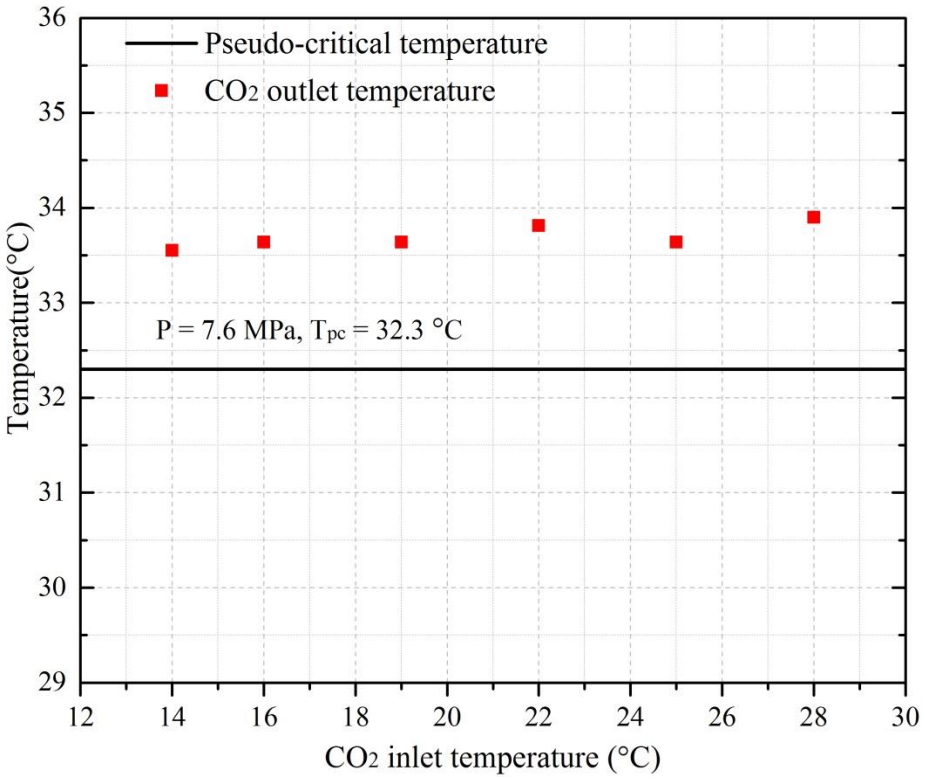

Figure 4.36 Loop hot side CO2 temperatures when instability occurs

4.7 Summary

Flow instability cases were identified during experiments and recorded. The effects of various system parameters as well as different loop configurations on natural circulation loop instabilities were investigated experimentally and systematically under supercritical conditions. The main conclusions can be drawn as follows:

1) Instability was not found with the closed loop condition at the given power range which means the accumulator (pressurizer) is an indispensable part in supercritical natural circulation flow instability studies.

2) Two different flow oscillations were identified with distinct difference in periods during experiments. The short period flow fluctuation was found when the loop was connected with the rigid settling tank and may be due to the Helmholtz

resonator effects between the settling tank and the loop. The second flow oscillation occurred with the accumulator connected and was typical loop instability with the important parameters oscillating periodically in a similar manner.

3) By throttling the valve in the connecting line between the bladder type accumulator and loop, the loop instability boundary didn't change much. Whereas the short period oscillations can be postponed or even eliminated if more local resistance was added in the pipeline between the settling tank and loop. And the introduction of accumulator together with the settling tank could not absorb the short period fluctuations.

4) Comparison of the steady state flow-power curve showed that the typical loop instabilities with various loop configurations were found to be on the negative slope while the short period oscillations were observed to occur on the positive slope which was near the peak region.

5) The short period oscillations occurred when the heated channel outlet temperature was around the pseudo-critical temperature. Increase in inlet temperature caused the system to be more unstable. For the typical loop instability, the increase of inlet temperature (10 ~ 22 °C) also destabilizes the system.

6) Steady state flow-power curve with flow instability boundary points clearly shows that all the instabilities found in the experiment are on the negative slope. As was expected, the experimental results show that increase of system pressure makes the system more stable. Increase of outlet K factors will always destabilize the system.

CHAPTER 5

NUMERICAL RESULTS AND DISCUSSION

5.1 Introduction

Literature shows that the numerical flow instability analysis of supercritical natural circulation systems mainly involves both linear and non-linear codes, which are based on frequency domain method and time domain methods, respectively. For the linear stability analysis, an infinitesimally small perturbation is added to the linearized governing equations of mass, momentum and energy equations, and the solution is used to predict the flow instability boundary and generate a flow instability map. The non-linear study deals with the governing equations in time domain and can provide more detailed information of the fluid characteristics such as the typical loop instability of limit cycle oscillations. To get a better understanding of the flow behaviours observed in experiments and gain an insight into the mechanisms of flow instability in a natural circulation loop, a licensed non-linear code, CATHENA, was applied and a numerical analysis of the mentioned experimental loop in previous chapter was conducted.

Since the current version of CATHENA code can only model supercritical water, numerical modeling with water flowing in the rectangular loop of the energy lab, University of Manitoba, was conducted. Considering the property similarities between the two supercritical fluids (CO_2 and H_2O) as mentioned in section 1.4, it is interesting to know if similar flow oscillation behaviours can occur, or not, with the same loop. It should be noted that the input file created for modeling supercritical water inside the natural circulation loop can be easily modified for supercritical CO_2 simulation once the CATHENA code is updated to a new version. The current numerical study aims to test

the capability of CATHENA code in modeling supercritical flow instability in a natural circulation loop as well as understanding the mechanisms of supercritical flow instability.

The CATHENA code had only been benchmarked with supercritical heat transfer experiment in a tube [80], its application in flow instability studies of supercritical natural circulation systems has not been reported though. As mentioned, the current version of CATHENA code can only model water, so a supercritical water experiment in a natural circulation loop [67] was firstly chosen to directly test its capability in flow instability study of supercritical natural circulation systems. After the validation, flow instability of the current experimental loop was numerically studied with an open loop condition and also a loop connected with accumulator (reservoir). For both conditions, wall structure effects were eliminated from this numerical study and supercritical water was used as the working fluid. The reasons for the complicated flow oscillation behaviour observed during experiment were analyzed qualitatively and the effect of the valve on the connecting line was also tested numerically. Parameters that affect the numerical steady state results were also conducted and discussed.

5.2 Numerical Modeling

5.2.1 Introduction of the CATEHNA Code

The acronym CATHENA stands for Canadian Algorithm for THErmalhydraulic Network Analysis, which is a licensed code developed by Atomic Energy of Canada Limited (AECL). It has been applied to a wide range of thermal hydraulic problems, in particular for the design and safety analysis of CANDU reactors [81]. The code uses a one-dimensional, two-fluid, non-equilibrium representation of two-phase flow in piping networks. The modeling of experimental thermal hydraulic test facilities can be realized by connecting a series of components such as pipe, T-junction, reservoir, volume and tank component. System models such as discharge model, accumulator model, heat

exchanger, junction resistance, pump, and valve are also available. The CATHENA code also has a GENeralized Heat Transfer Package (GENHTP), which allows one dimensional or two dimensional heat conduction modeling for heat transfer of pipes, fuel pins or other solid conduction materials in contact with the fluid. The basic hydraulic model consists of six partial differential equations for mass, momentum, and energy conservation - three for each phase, as shown in section 5.2.4. To solve these equations, staggered mesh, one-step semi-implicit first-order, donor-cell upwind differencing over control volumes or nodes are adopted. The detailed information on the numerical scheme is not presented here but can be found in [27].

For the current code version (CATHENA 3.5.4.4), a HLWP-VERSION (1) numerical option is used, which makes it possible to perform thermal hydraulic simulations at supercritical pressure conditions [82]. Fluids operating at supercritical pressures can only exist in one state that is either a liquid or a vapour. As a result, a constant void fraction of 0.0 is set automatically so the conservation equations for only one state are being used. The wall friction factors used are still the ones adopted at subcritical pressures. It should also be mentioned that when the system pressure is supercritical, the heat transfer correlation is automatically the Dittus-Boelter correlation [83] regardless of the options selected in the GENHTP model.

$$h_f = 0.023 \frac{K_f}{D_e} \mathrm{Re}_f^{0.8} \mathrm{Pr}_f^{0.4} \qquad \text{Equation (5-1)}$$

where h_f is the heat transfer coefficient ($W \cdot m^{-2} \cdot K^{-1}$), K_f is the fluid thermal conductivity ($W \cdot m^{-1} \cdot K^{-1}$), Re_f is the fluid Reynolds number, Pr_f is the fluid Prandtl number.

As for the water properties, the latest international water property standards (IAPWS-95) is adopted which extends from P_{min} = 611.657 Pa to P_{max} = 100 MPa and critical point occurs at the pressure of P_{cr} = 22.0703 MPa and a temperature of T_{cr} = 373.936 ℃.

5.2.2 Physical Model

As is shown in Figure 5.1, the physical model used is a simplified model of the experimental loop, which mainly focuses on the primary CO_2 side. The tested loop is a rectangular one with horizontal heater and horizontal cooler. Starting from the inlet boundary condition to the outlet boundary, it is divided into 24 pipe components if included the pipeline connecting the accumulator. There are also a volume component representing the T junction and a reservoir mimicking the accumulator. Heat is directly added to the fluid domain and no heat transfer package with correlations are adopted for current numerical study. The local pressure loss coefficients for various area changes are calculated in Appendix II. Nine equivalent local K factors are summarized and shown in Table 5-1. The dimensions and discretization nodes of the rectangular loops are shown in Table 5-2. The shell & tube heat exchanger consists of 127 small tubes (Φ3.175×0.3175 mm) and the CO_2 flows in the tube side. The heat exchanger inlet also has a diverging section and a converging section at the outlet, but in the numerical model they are replaced with appropriate local loss coefficients K_5 and K_6, respectively.

5.2.3 Governing Equations

The two-fluid model conservation equations solved in CATHENA can be written as [27]:

Mass conservation (for phase k);

$$\frac{\partial}{\partial t}(\alpha_k \rho_k) + \frac{1}{A}\frac{\partial}{\partial z}(A\alpha_k \rho_k C_{0k} v_k) = m_{ki} - \Gamma_k \qquad \text{Equation (5-2)}$$

Momentum conservation (for phase k);

$$\begin{aligned} &\frac{\partial}{\partial t}(\alpha_k \rho_k C_{0k} v_k) + \frac{1}{A}\frac{\partial}{\partial z}(A\alpha_k \rho_k C_{1k} v_k^2) + \frac{1}{A}\alpha_k \frac{\partial}{\partial z}(A p_k) \\ &+ \frac{1}{A}\beta_k \frac{\partial}{\partial z}(A\alpha_k) = \tau_{kw} + \tau_{ki} + m_{ki} v_{ki} + p_{ki}^{'} - \alpha_k \rho_k g_z \end{aligned} \qquad \text{Equation (5-3)}$$

Energy conservation (for phase k);

$$\frac{\partial}{\partial t}\left\{\alpha_k \rho_k \left[h_k + \frac{v_k^2}{2}\right]\right\} + \frac{1}{A}\frac{\partial}{\partial z}\left\{A\alpha_k \rho_k C_{0k} v_k \left[h_k + \frac{v_k^2}{2}\right]\right\} - \alpha_k \frac{\partial p_k}{\partial t}$$
$$-\alpha_k \beta_k \frac{\partial \alpha_k}{\partial t} = q_{kw} + q_{ki} + \tau_{ki} v_{ki} + v_{ki} p_{ki}^{'} + m_{ki}\left(h_{ki} + \frac{v_{ki}^2}{2}\right) - \alpha_k \rho_k v_k g_z \qquad \text{Equation (5-4)}$$

In addition, an equation of thermodynamic state is required for the density and is given by

$$\rho_k = \rho_k(p_k, h_k) \qquad \text{Equation (5-5)}$$

Where: α_k is the fraction of the cross-section occupied by phase k; ρ_k is the density of phase k; A is the cross-section area of the conduit; C_{0k} and C_{1k} represent the flow profile coefficients for mass flux and momentum flux, respectively; v_k is the velocity of phase k; m_{ki} is the interface mass transfer rate for the phase k; Γ_k represents a source of non-condensable; p is the local pressure; β_k is the phase-to-interface pressure difference $(p_k - p_i)$; τ_{kw} is the wall shear component for phase k; τ_{ki} is the interface shear for phase k; v_{ki} is the intrinsic interface velocity; $p_{ki}^{'}$ is the apparent mass term; g_z is the acceleration due to gravity in the z direction; h_k is the enthalpy of phase k; q_{kw} is the wall heat transfer to phase k; q_{ki} is the heat transfer from phase k to the interphase; h_{ki} is the enthalpy of phase k at the interface [27].

Since supercritical fluid undergoes no phase change when the fluid is heated to exceed the pseudo-critical point, there's no interface exist like the two phase flow. So all the terms related with interface between phases can be cancelled in the governing equations.

The corresponding coefficients are also summarized as follows.

$\alpha_k = 1,\ \beta_k = 0,\ C_{0k} = C_{1k} = 1,\ \Gamma_k = 0$

So the governing continuity, momentum, and energy equations for one-dimensional supercritical flow can be simplified and written as:

Continuity:

$$\frac{\partial \rho}{\partial t} + \frac{1}{A}\frac{\partial}{\partial z}(A\rho v) = 0 \qquad \text{Equation (5-6)}$$

Momentum:

$$\frac{\partial}{\partial t}(\rho v) + \frac{1}{A}\frac{\partial}{\partial z}(A\rho v^2) + \frac{1}{A}\frac{\partial}{\partial z}(Ap) = \tau_w - \rho g_z \qquad \text{Equation (5-7)}$$

Energy:

$$\frac{\partial}{\partial t}\left\{\rho\left[h + \frac{v^2}{2}\right]\right\} + \frac{1}{A}\frac{\partial}{\partial z}\left\{A\rho v\left[h + \frac{v^2}{2}\right]\right\} - \frac{\partial p}{\partial t} + \rho v g_z = q_w \qquad \text{Equation (5-8)}$$

Equation of state:

$$\rho = \rho(p, h) \qquad \text{Equation (5-9)}$$

It should be noted that in the conservation equations presented here all the quantities represent cross-sectional area and time average values.

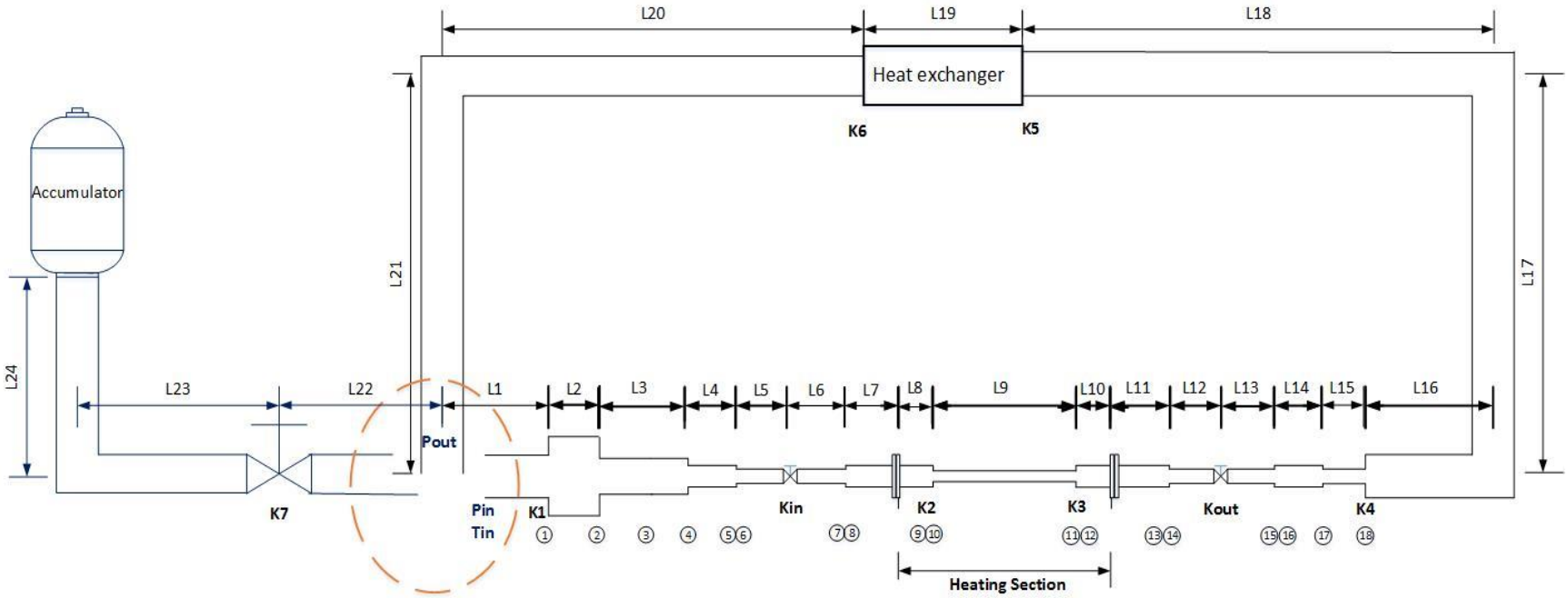

Figure 5.1 Simplified model of the experimental natural circulation loop

Table 5-1 Local K factors used for numerical simulation

Cases	K_1	K_2	K_3	K_4	K_{in}	K_{out}	K_{elbow}	K_5	K_6
1	11.82	1.34	1.77	2.51	0	13.1	0.22	2.0	2.7

Table 5-2 Dimensions of simplified model and node number for each section

Label	Length	I.D.	Node number				
	(m)	(mm)	100mm per node	60mm per node	20mm per node	10mm per node	40mm per node
L1	0.6	22.7584	6	10	30	60	15
L2	0.448	25.4	5	8	23	46	12
L3	0.49	21.1836	5	9	25	50	13
L4	0.248	14.224	3	5	13	26	7
L5	0.134	12.7	2	3	7	14	4
L6	0.15	12.7	2	3	8	16	4
L7	0.223	14.224	3	4	12	24	6
L8	0.174	14.224	2	3	9	18	5
L9	2.64	12.945	27	44	132	264	70
L10	0.174	14.224	2	3	9	18	5
L11	0.213	14.224	3	4	11	22	6
L12	0.14	12.7	2	3	7	14	4
L13	0.17	12.7	2	3	9	18	5
L14	0.29	14.224	3	5	15	30	8
L15	0.36	12.7	4	6	18	36	9
L16	1.03	22.7584	10	18	52	104	26
L17	1.02	22.7584	10	17	51	102	26
L18	3.535	22.7584	35	59	177	354	89
L19	0.414	2.54 / small tube	6	7	21	42	11
L20	3.535	22.7584	35	59	177	354	89
L21	1.02	22.7584	10	17	51	102	26

The default wall shear force per unit pipe component length for mixed flow regime in CATHENA code is the HTFS correlation [84] and given by,

$$\tau_{kw} = -\zeta_k \left[\frac{\tau^* f_{kw}}{D_e} \rho_k |v_k| \frac{v_k}{2} + \left(\frac{k}{l} \right) \rho_m |v_m| \frac{v_m}{2} \right] \qquad \text{Equation (5-10)}$$

Where: ζ_k is the wall shear fraction for phase k, τ^* is the two-phase friction-factor multiplier, f_{kw} represents the phase k wall-friction factor, D_e is the conduit hydraulic diameter (m), $\frac{k}{l}$ is the minor loss per unit pipe length, ρ_m and v_m are the averaged fluid density (kg/mm^3) and velocity (m/s), respectively.

For supercritical flow, the wall shear stress force per unit pipe component length can be simplified to,

$$\tau_w = \left[\frac{f}{D_e} + \frac{k}{l} \right] \rho |v| \frac{v}{2} \qquad \text{Equation (5-11)}$$

For rough conduits, the wall-friction factor is determined from the Colebrook-White formula as follows [85]:

$$\frac{1}{\sqrt{f}} + 2\log_{10}\left(\frac{\varepsilon}{D_e} \right) = 1.14 - 2\log_{10}(1 + 9.35 \frac{D_e / \varepsilon}{\mathrm{Re}\sqrt{f}}) \qquad \text{Equation (5-12)}$$

where f is the wall-friction factor, Re is the Reynolds number, D_e is the hydraulic diameter (m), ε is the conduits wall roughness (m).

The Reynolds number is defined as:

$$\mathrm{Re} = \frac{\rho v D_e}{\mu} \qquad \text{Equation (5-13)}$$

where μ is the viscosity (Pa s).

The conduits wall roughness used is 1.5×10^{-5} m. The effect of wall roughness on numerical results is discussed in section 5.7.

5.2.4 Assumptions

The following assumptions are made with regards to the governing equations of mass, momentum, and energy conservations:

(a) The flow in a supercritical natural circulation loop is one dimensional.

(b) Heat conduction in the axial direction is negligible and neglected.

(c) Heating power with uniform wall heat flux is directly absorbed by the fluid in the heated section and extracted in the heat exchanger. And, there's no heat loss for rest of the loop because it's insulated.

5.2.5 Boundary and Initial Conditions

The inlet of the loop is defined as the left end of the bottom horizontal pipe and the outlet of the loop is the exit of the pipe connected with outlet of the heat exchanger, as shown in Figure 5.1. For an open loop, the boundary conditions can be summarized as follows:

(a) H_2O inlet and outlet pressure are constant to be the system pressure.

(b) H_2O inlet temperature is kept constant

(c) Heat is added directly at the heated section and the same amount of heat is removed directly at the heat exchanger. The rest of the loop is considered adiabatic on the outer surface of the pipe wall.

For a loop connected with an accumulator, the corresponding conditions are as follows:

(a) The pressure and temperature are kept constant at the accumulator or reservoir.

(b) Heat is added directly at the heated section and the same amount of heat is removed at the heat exchanger. The rest of the loop is considered adiabatic on the outer surface of the pipe wall.

For both working conditions, the initial condition of the loop is constant temperature equal to the inlet temperature and constant pressure equal to the system pressure around the loop.

5.2.6 Sensitivity Test of Numerical Discretization Parameters

Accurate prediction of flow instability boundary is one of the major concerns in natural circulation loop flow instability studies. It has already been found that the stability threshold is sensitive to the time step and grid size used for numerical analysis [59]. Hence, to ensure that the results are both temporal and spatial grid independent, a time step as well as grid refinement study is performed and presented in subsections below. An optimal time step and grid size is chosen and used for the rest of the analysis.

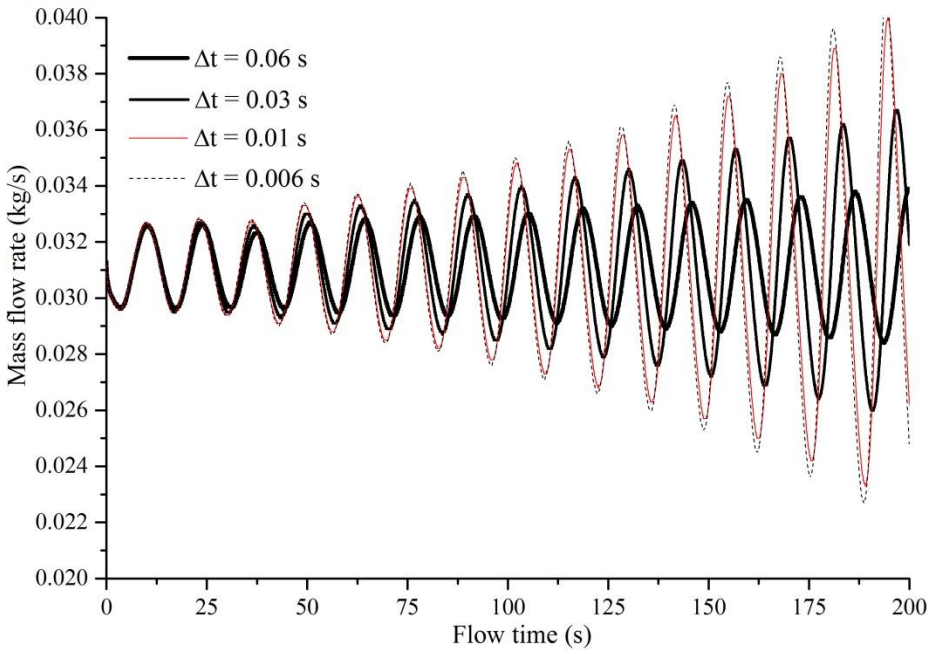

Figure 5.2 Test of time steps on flow oscillations (H_2O simulated)

a) Effect of Temporal Grid Refinement

To begin with, a base Supercritical H_2O case with system pressure 25 MPa, inlet temperature of 349.482 °C and K_{out} = 13.1 is selected and modeled with CATHENA code. A power of 28.5 kW slightly larger than the stability threshold value of 28 kW is chosen, and various time step sizes of 0.006 ~ 0.06 s are tested to show its effects on the flow oscillation. In all these cases the spatial grid size is kept constant at 0.04 m. As is shown in Figure 5.2, with reduction of time step values, the period and amplitude of the growing flow oscillations gradually match, which shows that Δt = 0.01 s and 0.006 s are adequate time steps for accurate stability analysis. In present study, Δt = 0.01 s is used for all thermal hydraulic cases.

b) Effect of Spatial Grid Refinement

To ensure the convergence of the numerical solution, a spatial grid independence study is also performed. To search for the flow instability threshold, an increment of 0.25 kW was used. Effects of various grid sizes on both the steady state numerical result and flow instability boundary are shown in Figures 5.3 and 5.4, respectively. It can be seen that there's no visible difference between the three meshes selected, which means even for the coarsest mesh (node length of 0.1 m), the calculated steady state result is reasonably accurate. But the spatial grid size does have an effect on the flow instability boundary. With the refinement of the grid, the flow instability boundary gradually becomes spatially converged at 28 kW for the present test case. Considering the computational time and resources, the grid size with 0.04 m per node was selected for all the numerical cases.

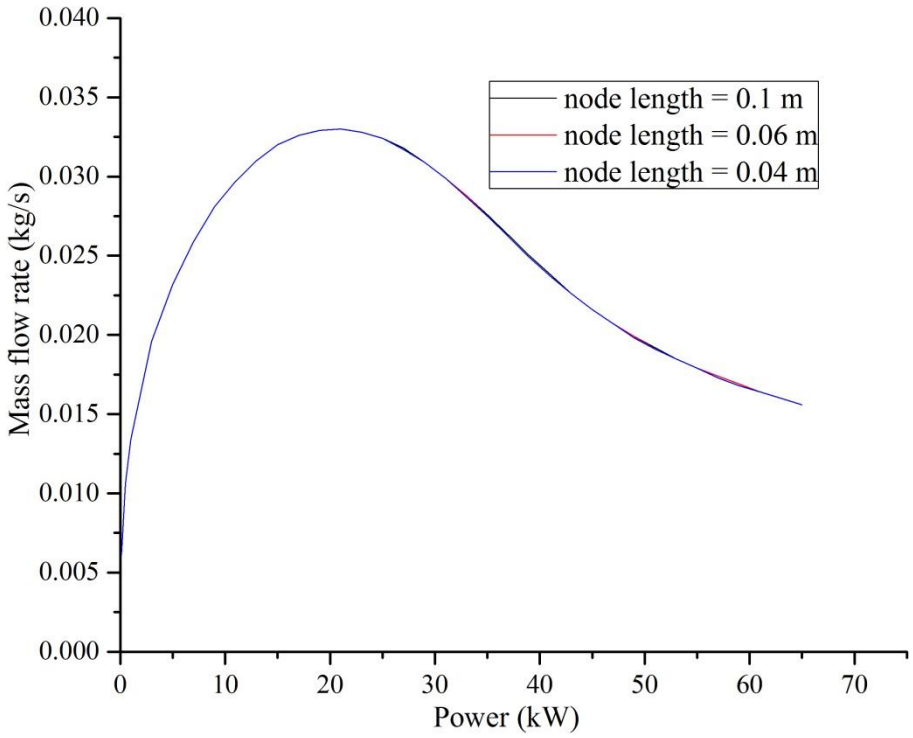

Figure 5.3 Grid sensitivity test for steady state flow (H_2O simulated)

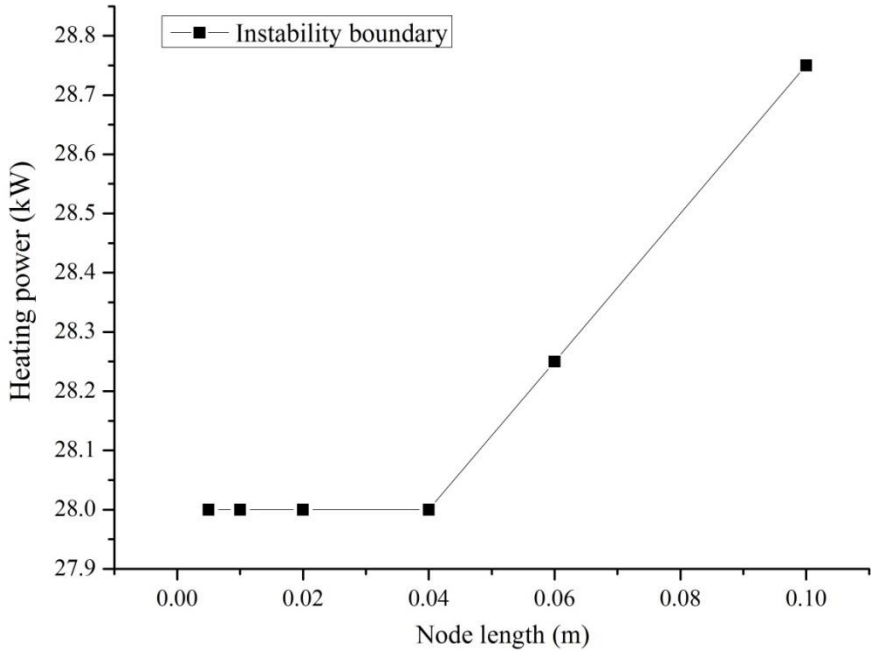

Figure 5.4 Grid independence study on flow instability boundary (H_2O simulated)

5.3 Validation of Numerical Code against Water

As mentioned in section 5.1, the capability of CATHEN code in simulating supercritical water flow instability in natural circulation systems should first be tested. Y.Z. Chen et al. [67] reported flow instability behaviour when doing an experimental study of a natural circulation loop with supercritical water at the China Institute of Atomic Energy (CIAE). So their experiment was selected to validate the CATHENA code results, and the CIAE experimental loop was illustrated in Figure 5.5.

The CIAE loop is also a rectangular loop but with a vertical heater on the right and an upper horizontal tube in tube heat exchanger. A three-head piston pump is used to establish a system pressure of about 25 MPa for the pressurizer. DC power supply with capacity of 70V×6750 A is used as a heating source for the test section. The coolant water on the primary side is deionized water and tap water is used on the secondary side. The whole loop was insulated with glass-fiber. The flow rate of the loop was calculated based on heat balance equation with the power and water temperature difference between the inlet and outlet of the heated section. Flow oscillations were observed under some operating conditions, as shown in Figure 5.6. Figure 5.7 shows the stepwise increase of heating power with time.

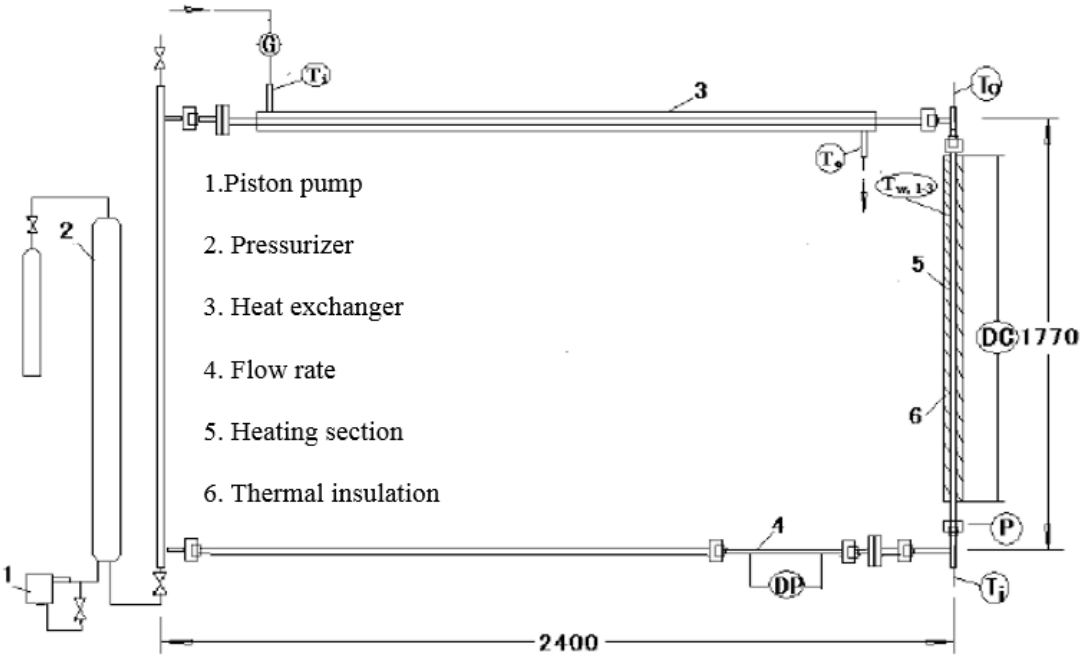

Figure 5.5 Schematic of the CIAE loop [67]

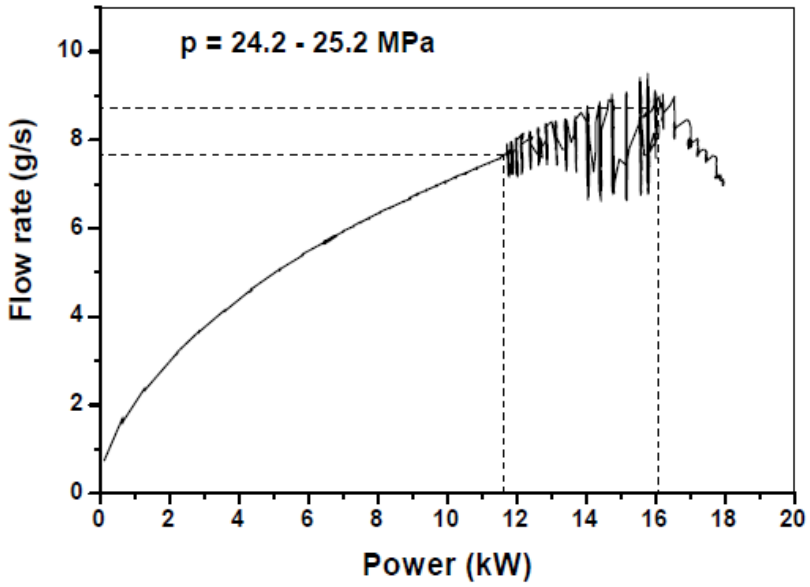

Figure 5.6 Variation of flow rate with power [67]

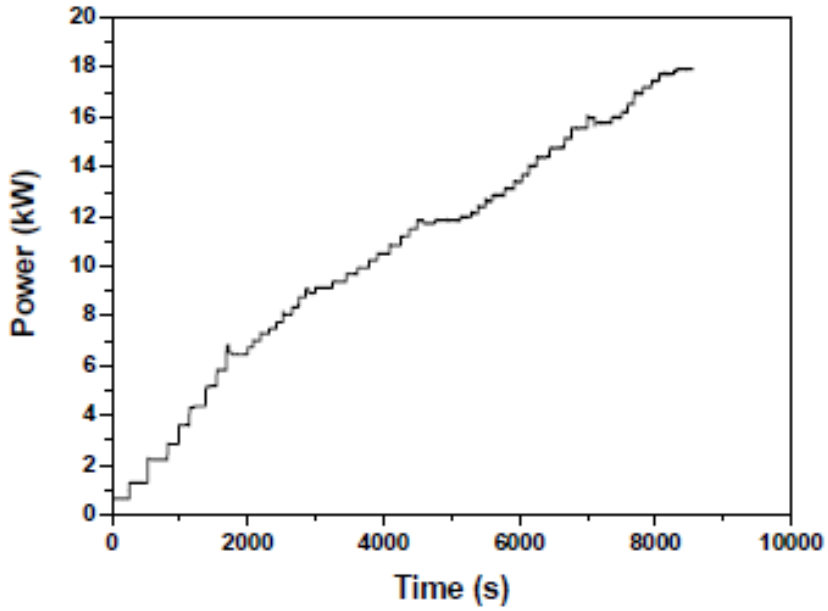

Figure 5.7 Increase of power with time [67]

For numerical simulation, the CIAE loop is divided into 16 pipe components. The detailed information of the dimensions as well as node numbers used is shown in Figure 5.8. The inner diameter for the loop is 0.01 m, except that the inner diameter of pipe 4 is 0.004 m and pipe 7 is 0.00462 m. The local loss coefficient due to pipe area changes are calculated and listed based on reference [86].

According to the linear stability analysis based on classical control theory, the characteristic equation of the flow is highly related with its steady state, accurate prediction of the steady state results are a prerequisite for a successful stability analysis. So the purpose of the validation study is to obtain an assessment of the CATHENA code in predicting the steady state flow rate of a natural circulation with supercritical water. An open loop model with constant inlet and outlet pressures was used and no wall structure effects of heater and cooler were considered for the sake of simplicity since they have negligible effects on the steady state performance of the experimental loop. Inlet temperatures used were the measured ones during the experimental process at various heating powers. The system pressure used for the numerical work was 24.7 Mpa, an average value of the experiment.

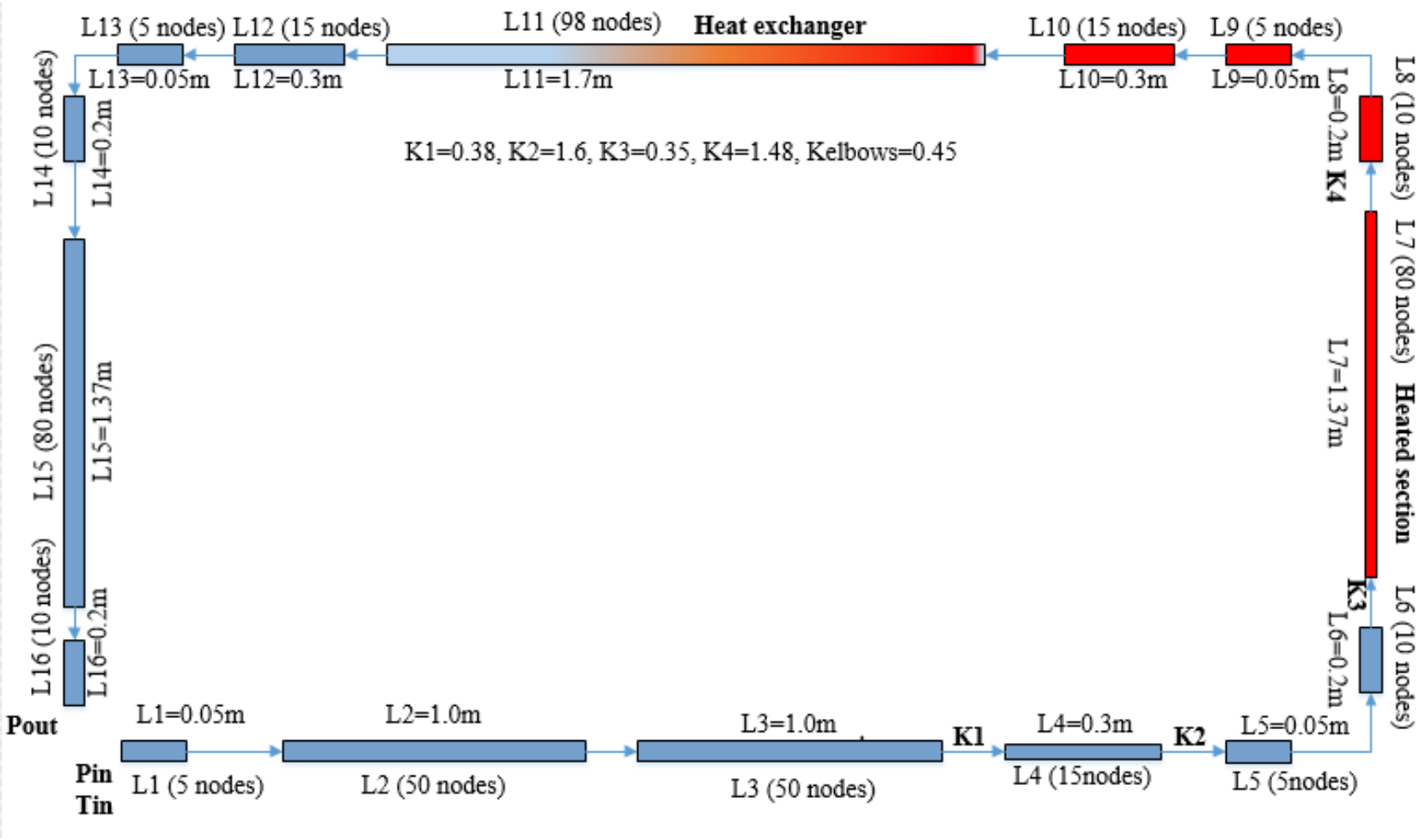

Figure 5.8 Physical model of the CIAE loop for the CATHENA code

Totally two numerical cases with different pipe roughness were conducted. For hard-drawn pipes, the roughness is 1.5×10^{-6} m. Based on the work performed by Debrah et al. [71] who also simulated the CIAE loop, the calculation with pipe roughness of 4.6×10^{-5} m appeared to have the best prediction. So this pipe roughness was also used in the present study and results are shown in Figures 5.9 and 5.10.

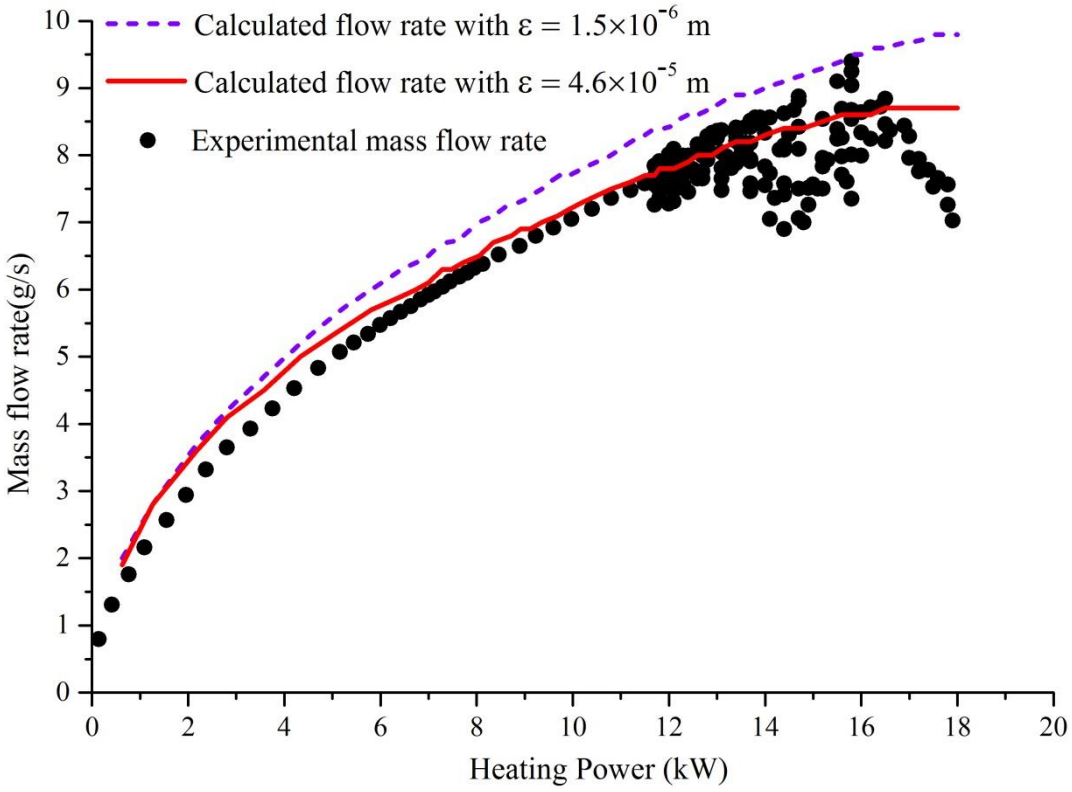

Figure 5.9 Mass flow rate versus power

From the steady state flow-power curve it can be seen that better agreement with experimental results are achieved with larger pipe roughness, especially in the higher power region (8 – 16 kW). But both cases over predict the mass flow rate lower power region (2 – 6 kW). As for the predictions of heated channel outlet temperature, the two numerical cases with different pipe roughness underestimated the fluid outlet temperature at lower power region (2 – 6 kW) because of the larger mass flow rate calculated. At higher power region (8 – 16 kW), the numerical results match the experimental results very well with the larger pipe roughness (4.6×10^{-5} m). The difference of the calculated outlet temperatures between the two cases becomes

smaller when the power is larger than 16 kW. This is clearly because of the large specific heat at the pseudo-critical region (T_{pc} = 384.05 °C at 24.7 MPa). The results between the reference experimental case and the numerical cases show that the CATHENA code can predict the supercritical water flow rate of a natural circulation loop very closely with appropriate local friction loss coefficients and pipe roughness.

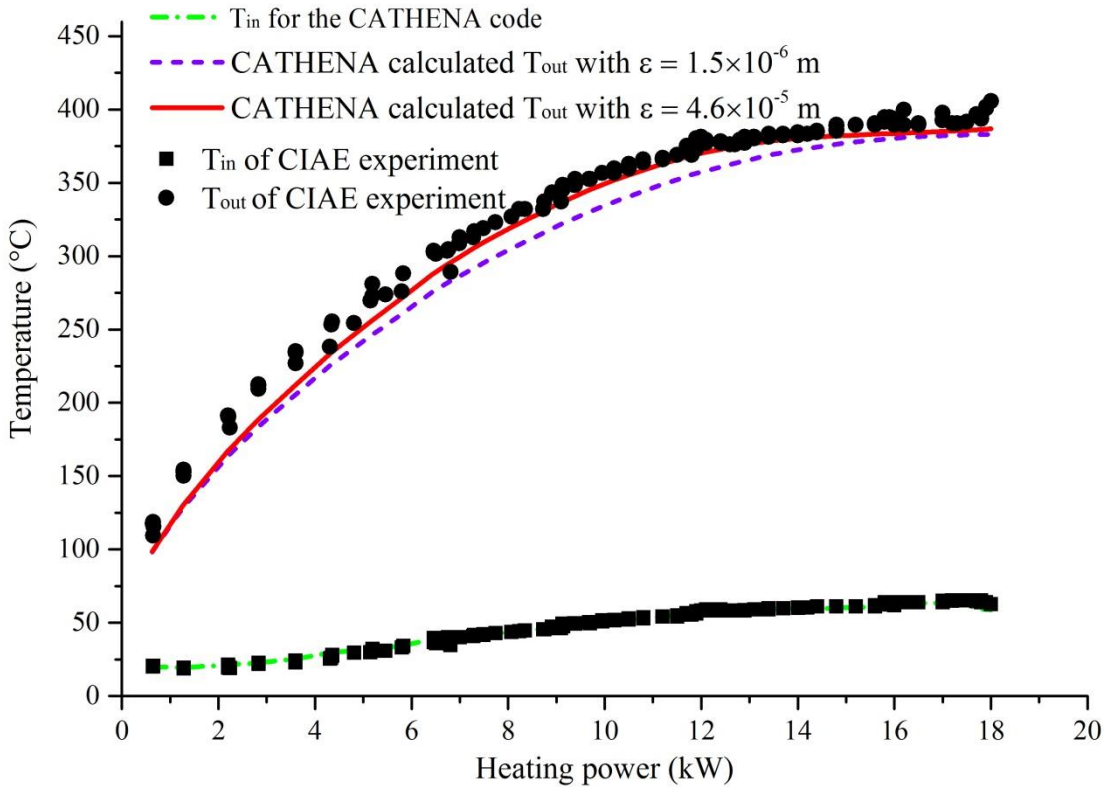

Figure 5.10 Variation of the inlet and outlet water temperatures with increase of heating power

5.4 Modeling of Our Experimental Natural Circulation Loop with Supercritical Water

Based on the purpose mentioned in the introduction, a simple open loop model widely used by other researchers was established and calculated first. Then an accumulator (reservoir) model was used for comparison to see if it has an effect on the flow instability boundary. The valve effects (valve V-4) on flow instability were also tested numerically in this section with the accumulator (reservoir) model.

5.4.1 Open Loop Model

The open loop model only considers the rectangular loop and the boundary condition is constant inlet temperature and pressure and a constant outlet pressure equal to the inlet pressure. The outlet temperature is left untouched and can change with the overall energy balance of the loop. Since heat added and removed were kept equal, the outlet temperature is always expected to be constant with the inlet temperature. So this boundary condition is theoretically possible when both ends of the loop are connecting to an infinite large reservoir, similar to the condition of connecting with settling chamber during experiment. The existence of a steady state is a prerequisite for the study of flow instability, so factors that may affect the steady state results were discussed first.

1) Considerations for the Steady State Prediction

The main factor that affects the prediction of mass flow rate at various heating power is the friction distribution of the loop being modeled. It includes the local losses pipe area changes along the loop and also the friction loss due to pipe roughness.

As can be seen from Figure 5.1, there are a lot of area changes for the bottom pipes of the loop. The local loss coefficients used for current simulation were calculated based on the reference [86] and listed in Appendix II. The accurate calculation of the local loss coefficients due to the area changes actually plays a very important role in the prediction of the steady state results. To test its effect, a sample case with system pressure of 25 MPa, inlet temperature of 349.482 °C, and outlet local loss of 13.1 was chosen and various distribution of local loss K factors on both the cold side (from the loop inlet to the heated channel inlet and heat exchanger outlet to the loop outlet) and the hot side of the loop were tested and shown in Figures 5.11 – 5.13. At first, the calculated local loss coefficients K of 18 area changes at the bottom tire of the loop (see Appendix II) were applied directly to the 16 piping connections shown in Figure 5.1. Then the model of the loop was simplified more by combining the local loss K

factors into four bigger local loss K factors (K_1, K_2, K_3, and K_4, see Table 5-1) on the bottom tire of the loop. In this way the local loss coefficients were combined and divided into two groups, the cold side of the loop (K_1, K_2, K_6) and the hot side of the loop (K_3, K_4, and K_5).

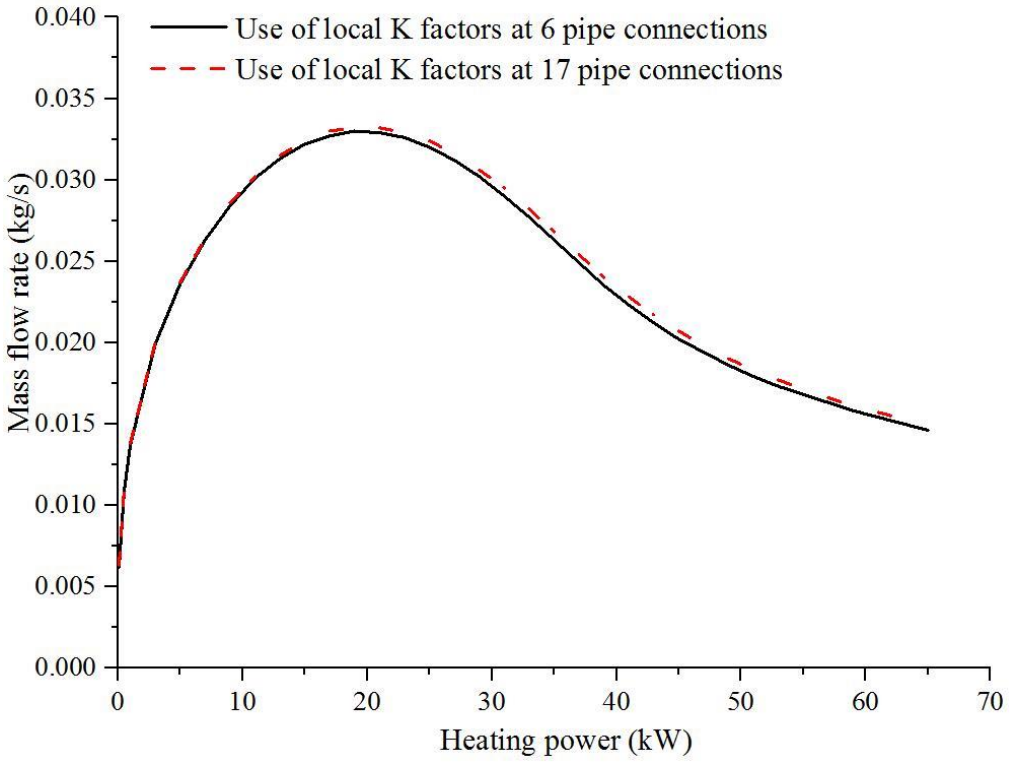

Figure 5.11 Local K factors distribution effect on steady state H_2O results

Figure 5.11 shows that the steady state results predicted by the CATHENA code doesn't change much (maximum difference less than 2%) with the two different conditions, which makes it more convenient to test the local K factors distribution effect on both sides. The calculated local K factors are $K_1 = 4.82$, $K_2 = 1.34$, $K_3 = 1.77$, and $K_4 = 4.51$. To test the effect of the local K on cold side, K_1 was increased to 11.82 and others were kept unchanged. K_4 was decreased to be 2.51 to test the effect of local K on the hot side while keeping the rest of the local K factors constant. Figure 5.12 shows that on either side of the loop, an increase in the local loss coefficients will decrease the mass flow rate. Increase the local K factor on the cold side will shift the steady state curve to the right and decrease the local K factor on the hot side will also

shift the steady state curve to the right. It also can be seen that the local loss K factor on the hot side has a more evident effect on the mass flow rate than the local loss K factor on the cold side.

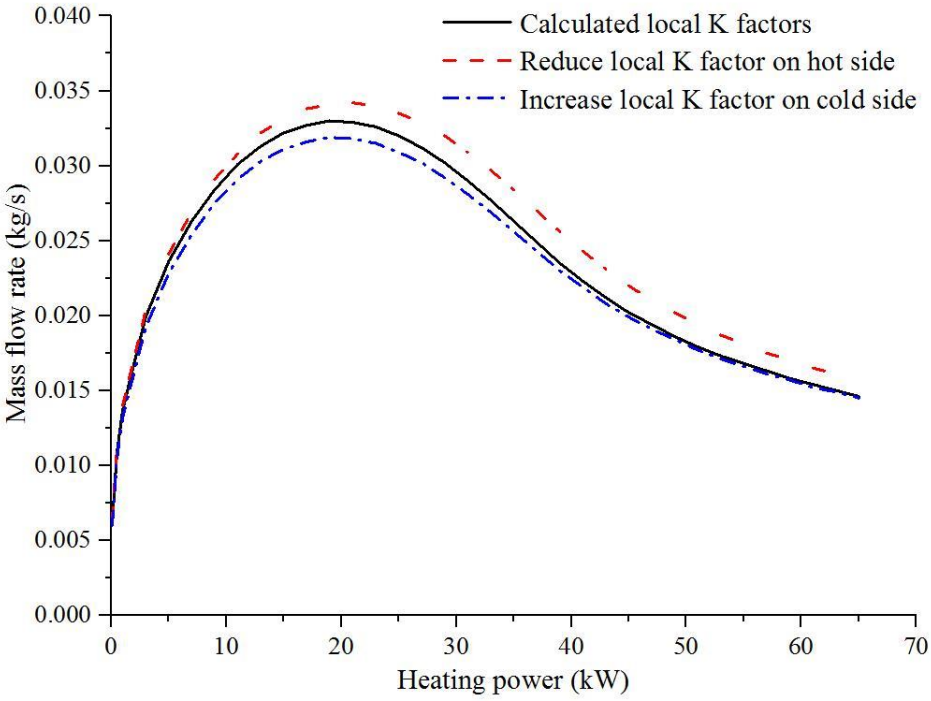

Figure 5.12 Local K factors distribution effect on steady state H_2O results

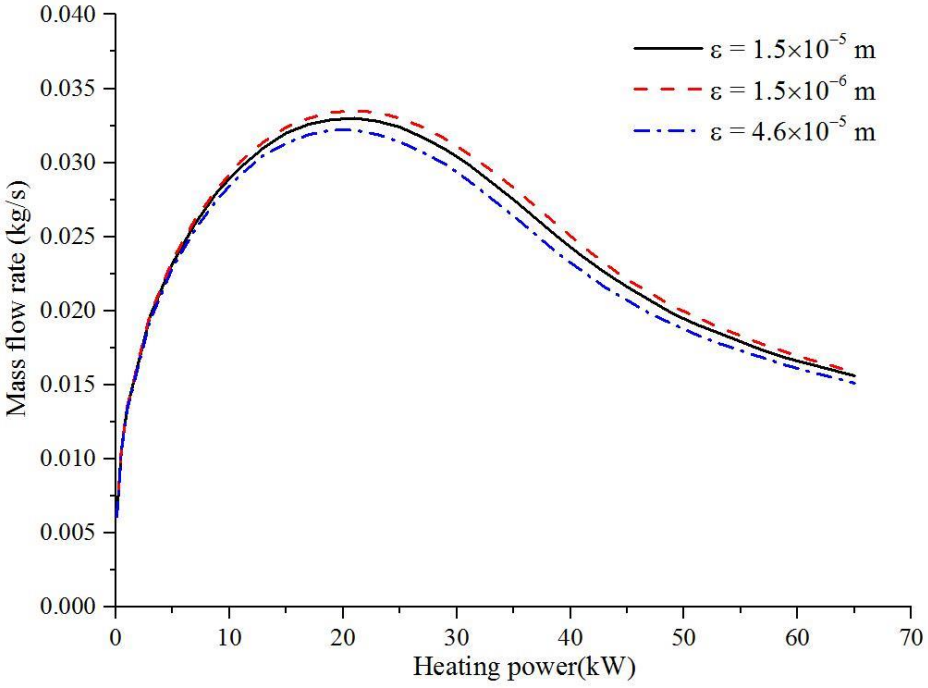

Figure 5.13 Pipe roughness effect on steady state simulation with H_2O

One of the parameters that affect the frictional loss of the loop is the pipe roughness. Three pipe roughness was tested and shown in Figure 5.13. The local K factors used for these three cases were the ones in Table 5-1. The results show that increase of pipe roughness will decrease the predicted mass flow rate and shift the peak of the flow rate a little bit to the left. The friction loss coefficient, f, chosen also has an effect on the prediction of steady state results with different codes. The default correlation used by the CATHENA code is the Colebrook-White correlation, as presented in section 5.2.3. This correlation is proposed for fully developed sub-critical flow based on the bulk properties of the fluid flow, which may not be accurate enough for prediction of supercritical flow in natural circulation loop.

2) Flow Oscillations

The sample case with system pressure of 25 MPa, inlet temperature of 349.482 °C, and outlet local loss of 13.1 was selected and analysed at 29 kW. The geometry information for this case is presented in Table 5-1 and 5-2. The flow instability boundary power for this case is 28 kW without considerting the wall heat structure effect. The spatial distribution of various fluid properties along the heated channel before the flow instability occurred is plotted in Figure 5.14. It is apparent that for this flow instability case, the fluid temperature at the heated channel outlet had surpassed the pseudo-critical temperature (T_{pc} = 385.72 °C at P = 25 MPa) and the location (red square) where the fluid exceeds the pseudo-critical temperature is almost at the middle section of the heated channel. As expected, the fluid temperature increases along the heated channel and has a flat region around the pseudo-critical temperature because of the large peak of the specific heat. The fluid enthalpy increases almost linearly with distance along the heated section. The fluid density transits smoothly from about 600 kg/m^3 at the heated channel inlet to less than 200 kg/m^3 at the heated channel outlet. The distribution of the fluid properties plays a very important role in the intense interaction between buoyancy and frictional forces when flow instability occurs. This will be discussed in more detail in the following section.

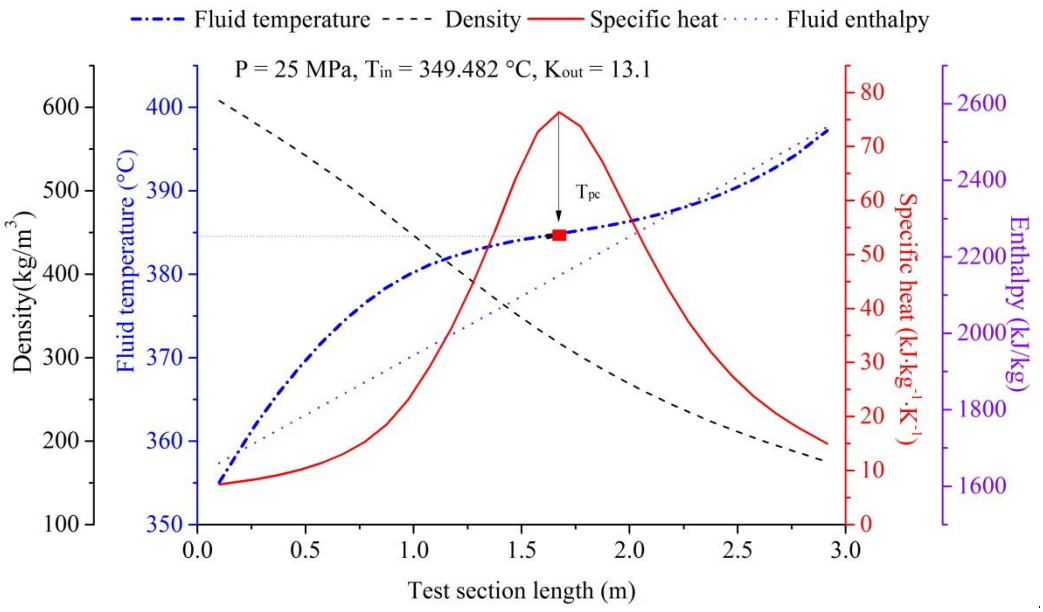

Figure 5.14 Properties of fluid inside the heated channel at steady state

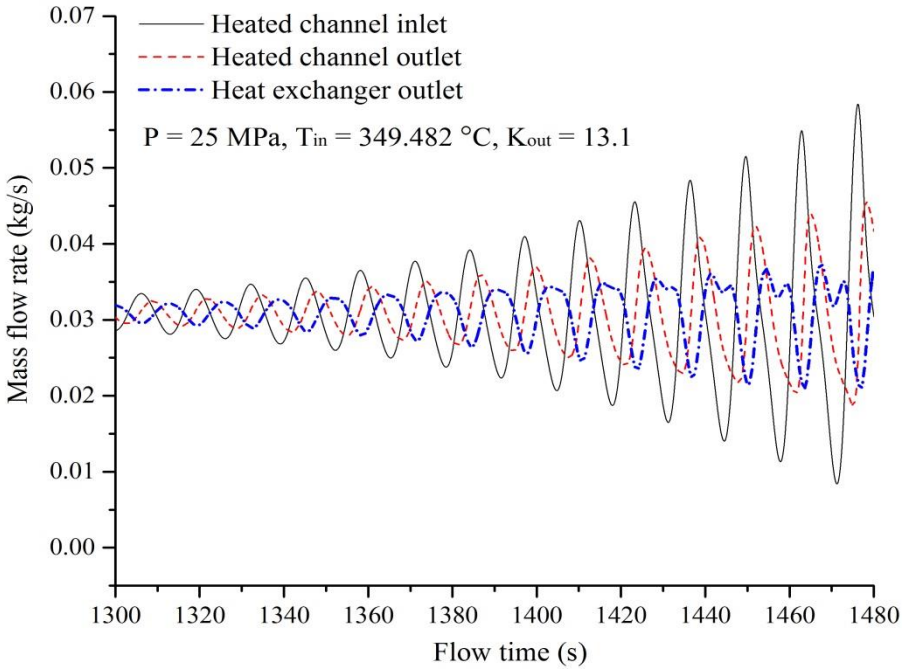

Figure 5.15 Evolution of mass flow rate with time (open loop model)

For the same case, a smaller time step of 0.01 s was used for stability analysis. As can be seen from Figure 5.15, after some calculation time, the mass flow rate of the loop gradually develops into a periodical oscillation similar to two-phase flow instability of natural circulation loop at sub-critical conditions. Mass flow rate of different locations

(heated channel inlet and outlet, outlet of heat exchanger) of the loop was monitored and Figure 5.15 clearly shows that the flow oscillations have phase lags from the inlet of loop to the loop outlet, indicating the delay of flow perturbation propagations inside the loop. The flow oscillation at the heated channel inlet is larger than the one at the channel outlet, which agrees with the experimental findings that the wall surface temperature oscillations larger at the inlet section of the heated channel (section 4.4, example 3). Another interesting feature of the transient results is that the flow oscillation at the heat exchanger has double peaks as the oscillation grows

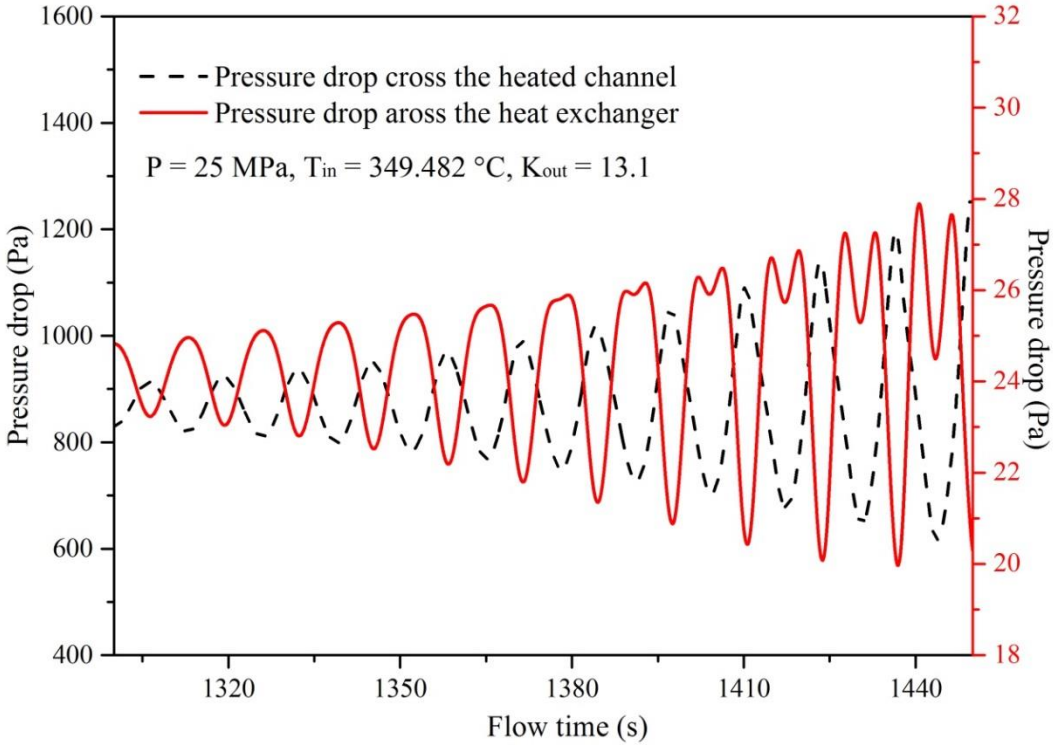

Figure 5.16 Evolution of pressure drops (P=25MPa, Tin=349.482°C, Kout=13.1)

The pressure drops across the heated channel and the heat exchanger were also calculated and presented in Figure 5.16. It shows clearly that the flow oscillation is a loopwise flow instability. The pressure drops across the heated channel at the bottom of the loop and heat exchanger on the top of the loop are exactly out of phase. As the oscillation develops, the pressure drop across the heat exchanger also shows double peaks, behaviour similar to the flow rate fluctuations across the heat exchanger, but with 180 ° out of phase.

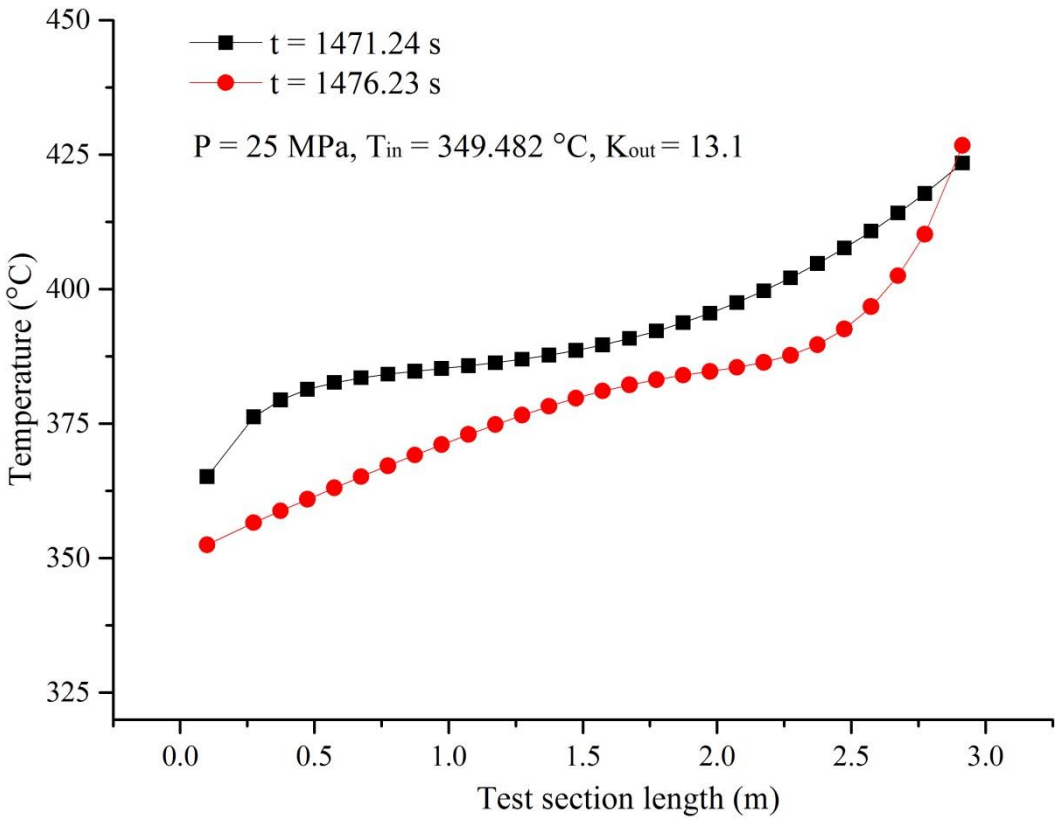

Figure 5.17 Fluid temperature along the heated section at 1471.24 s and1476.23 s

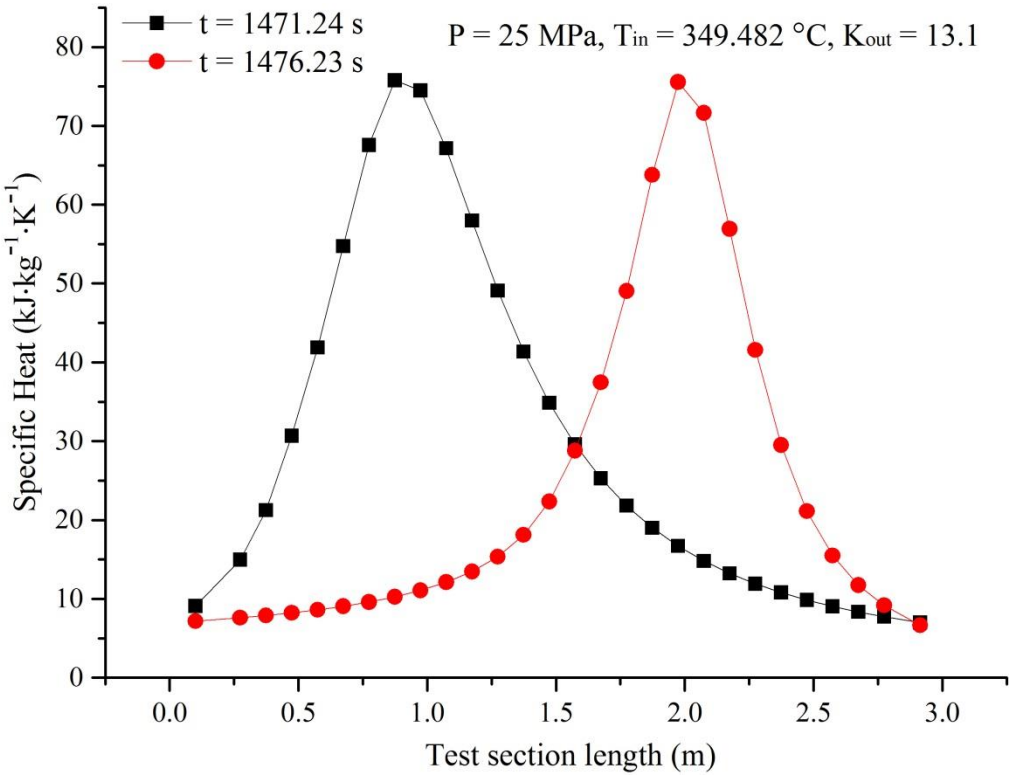

Figure 5.18 Fluid specific heat along the heated section at 1471.24 s and1476.23 s

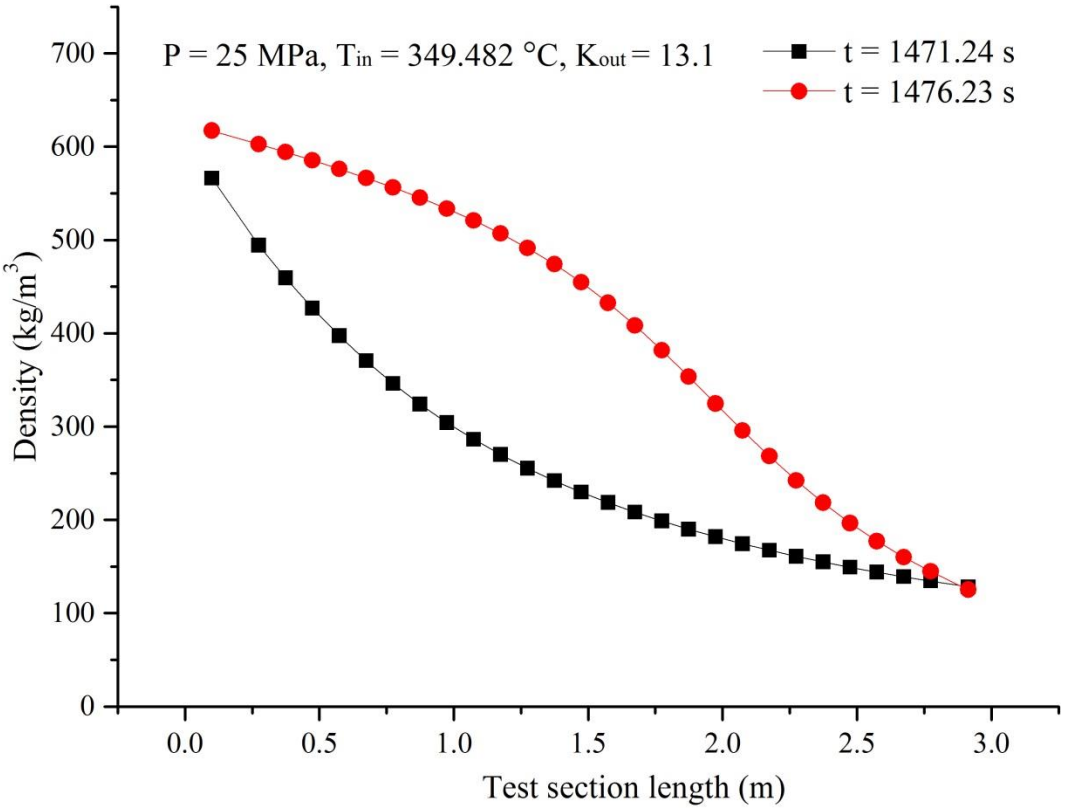

Figure 5.19 Fluid density along the heated section at 1471.24 s and1476.23 s

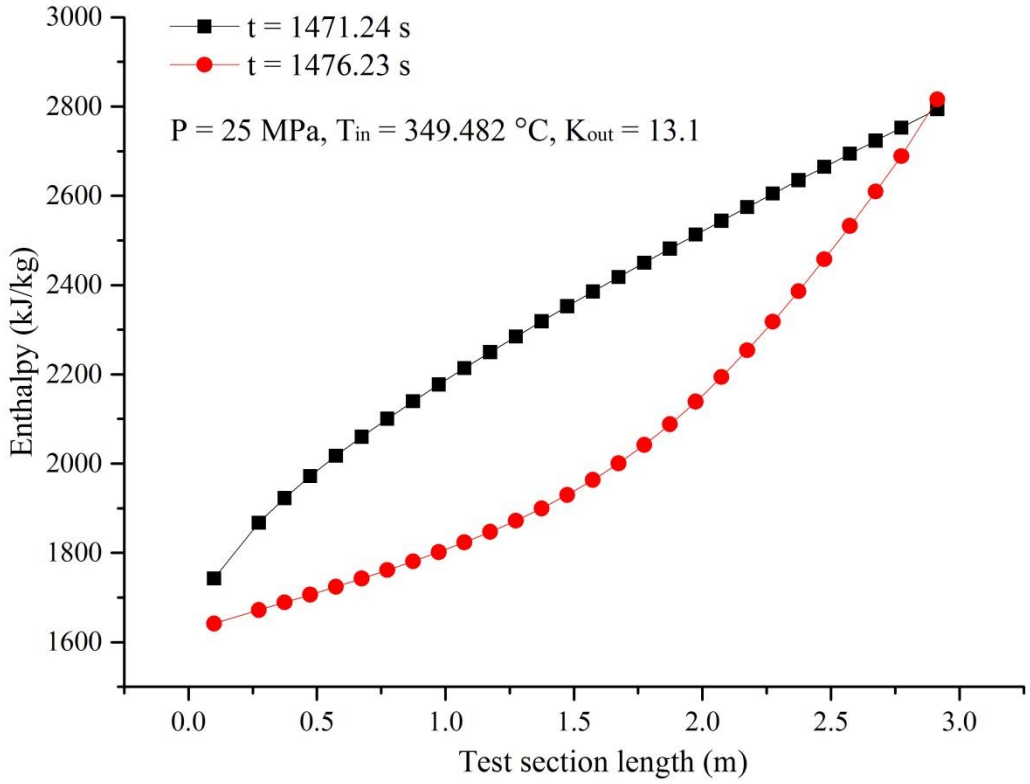

Figure 5.20 Fluid enthalpy along the heated section at 1471.24 s and1476.23 s

Figure 5.18 clearly shows the location (the peak of specific heat) inside the heated channel, at which the fluid surpasses the pseudo-critical temperature. This indicates that the flow oscillation causes a move of the pseudo-critical point, which results in the change of fluid properties such as density and enthalpy, as shown in Figure 5.19 and 5.20. These further causes the distribution of the liquid-like 'heavier' fluid and gas-like 'lighter' fluid and, therefore, ends up with a redistribution of pressure drops along the heated channel and the rest of the loop. As mentioned before, the pressure drop will affect the flow rate of the loop, which in turn influences the driving force. A regenerative feedback will be established under certain conditions and the flow instability will become self-oscillatory.

5.4.2 Rectangular Loop with Accumulator

For a real experimental loop, an accumulator or pressurizer will be connected with the test facility to help control the system pressure. The boundary condition for the real case is actually periodic. So to model this condition, a generic accumulator tank model of the CATHENA code was adopted and tested. After several trial runs, it was found that for a closed system (fixed volume of accumulator without mass loss), the code would stop working when the channel outlet temperature approached the pseudo-critical point temperature. The reason for this is still unclear, but it is possibly due to the large thermal expansion of supercritical fluid near the pseudo-critical point. Because a further debug of the code showed that if the volume of the accumulator was increased, the code would work again. To continue the analysis, an extreme working condition was selected by using a reservoir with infinite volume to represent the accumulator instead of using the generic accumulator tank model. This made the case similar to the open loop condition. The main difference was that a time - dependent volume was used for the T-junction part and a connecting surge line was present, which made it available to test the effects of the connecting line as well as the valve on the connecting line. The same case used for modeling the open loop case is re-calculated in this section.

It is shown in Figure 5.21 that the flow instability boundary predicted is about the same (28 kW) as before, which means the accumulator and the connecting line don't have any effect on shifting the flow instability boundary. The heating power was increased to 29 kW for further comparison of the flow oscillation behaviour with that of the open loop model. As is shown in Figure 5.22, the flow rates at heated channel inlet and outlet, and outlet of heat exchanger show similar phase lags as the open loop model. But the flow rate oscillation behaviours are more irregular, showing a clear change with the involvement of the infinite reservoir. The oscillation period is about 15 seconds, 1.6 s larger than the period of the open loop model. This is due to the connecting line between the accumulator and the rectangular loop. To sum up, similar to the findings of the experimental results, the connection of the accumulator does not affect the flow instability boundary, but it does affect the flow oscillation behaviours. The next section is a further study of the valve on the connecting line between the accumulator and rectangular loop and its effect on flow instabilities.

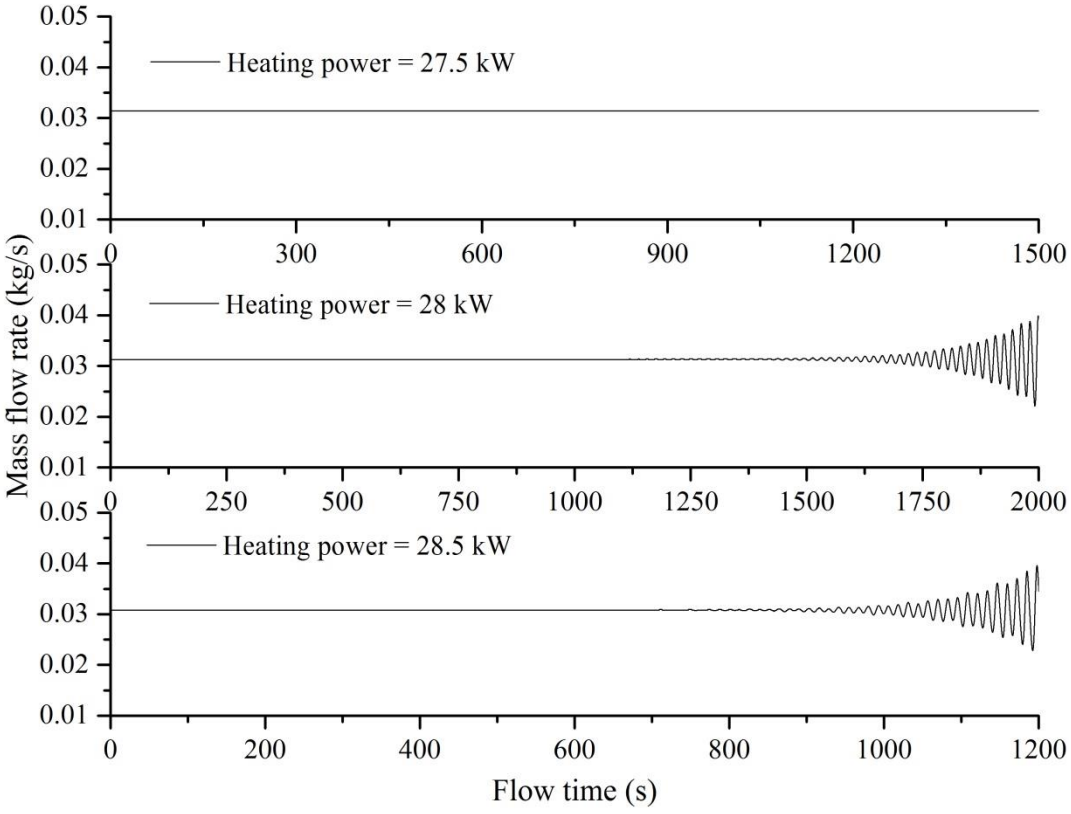

Figure 5.21 Determination of flow instability boundary with reservoir

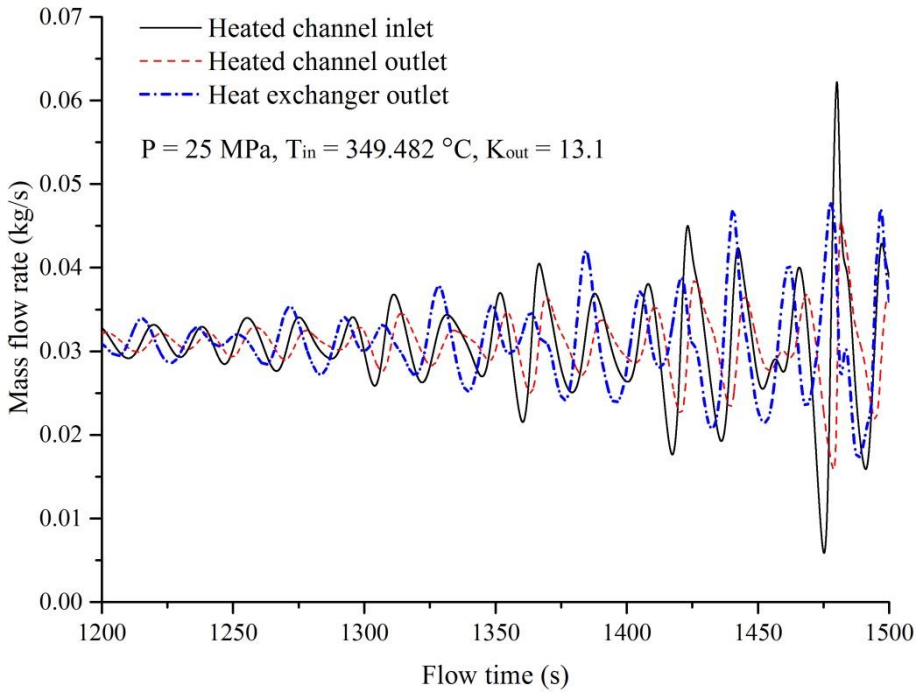

Figure 5.22 Evolution of mass flow rate with time (rectangular loop with reservoir)

During the experiment, the accumulator effect on flow instability was tested by closing valve V1-4 to isolate the accumulator when instability occurred. It was experimentally verified that the periodic oscillation of mass flow rate would disappear after the valve was closed. When the valve was re-opened to activate the accumulator, the system became unstable again. Here the same test is conducted numerically with the reservoir connected. A local junction resistance is defined on the pipeline connecting the reservoir and rectangular loop. The open and close of the physical valve is mimicked by changing the local loss K factor (K_7 in Figure 5.1). Setting the K factor as zero means the valve is fully open and setting the K factor as 1.0×10^{10} or greater means the valve is shut off and the accumulator has been isolated from the loop. Any other values of the local K means the valve is partially open.

Figure 5.23 shows a numerical simulation of flow instability behaviour for the same sample case mentioned previously. As can be seen, with an input power (31 kW) higher than the instability boundary power (28 kW), mass flow rate of the loop starts oscillating at the given condition of 25 MPa and 349.482 °C at the inlet. The same case is re-calculated by closing valve V-4 from restart. It shows a stable behaviour of

flow rate after the reservoir is isolated which means the shut-off of valve V-4 has a stabilizing effect on flow instability.

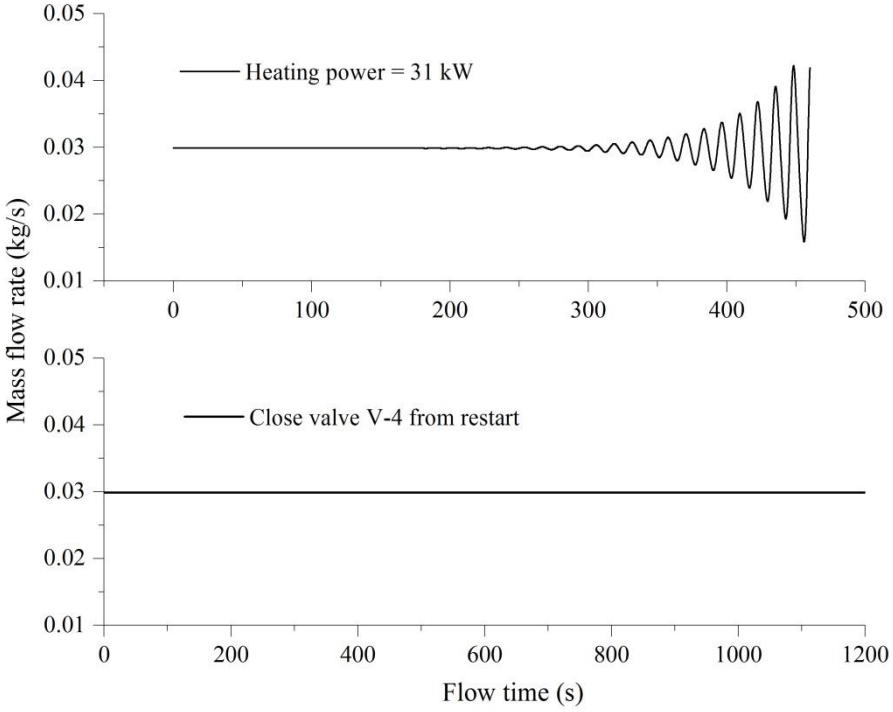

Figure 5.23 Valve effect test with V-4 close from restart

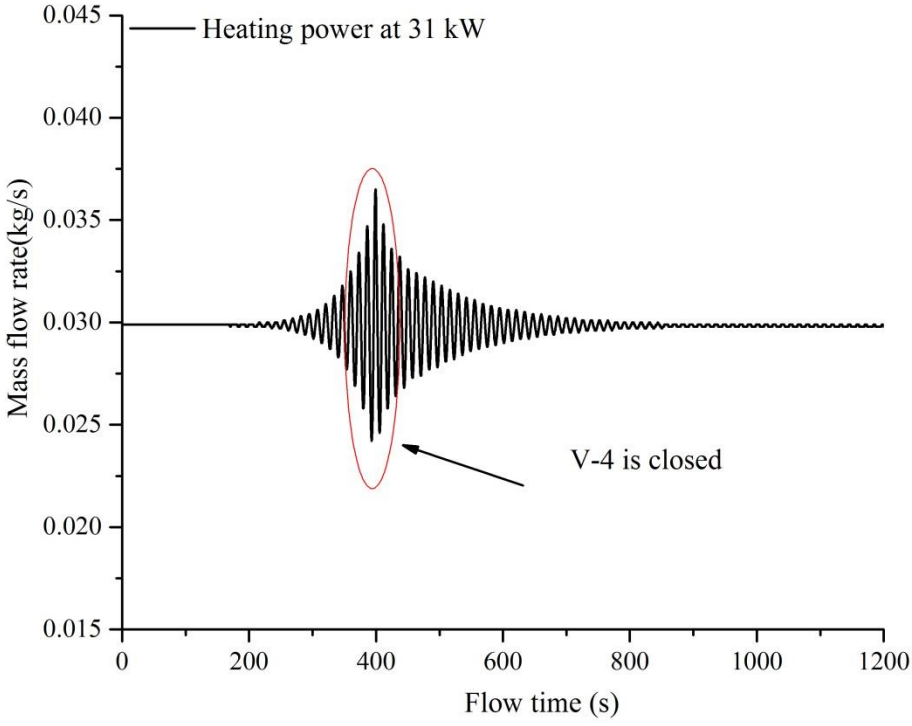

Figure 5.24 Valve effect test with V-4 close when flow oscillation occurs

During the experiment, when instability occurred, if the valve V-4 was closed the flow instability would die out right away. In present section, it is also tested numerically with a restart from a flow rate oscillation (at 400 s) by setting the K factor as 1.0×10^{10} (Close V-4). As is shown in Figure 5.24, unlike the experiment where the flow oscillation immediately diminished, the calculated amplitude of loop mass flow rate gradually decreases and restores to its steady state after some time.

The effect of the valve V-4 is further tested by using various local K values to see if the instability boundary can be affected or not. The same numerical case is performed with heating power of 31kW and local K values of 10^2, 10^4, 10^6, 10^8 and 10^9 are tested. It can be seen from Figure 5.25 that the flow instability behaviour hasn't changed much at lower K values. It is apparently suppressed when the local K factor is around or larger than 1.0×10^8, which means valve V-4 can only have an effect on the flow instability when it is almost closed.

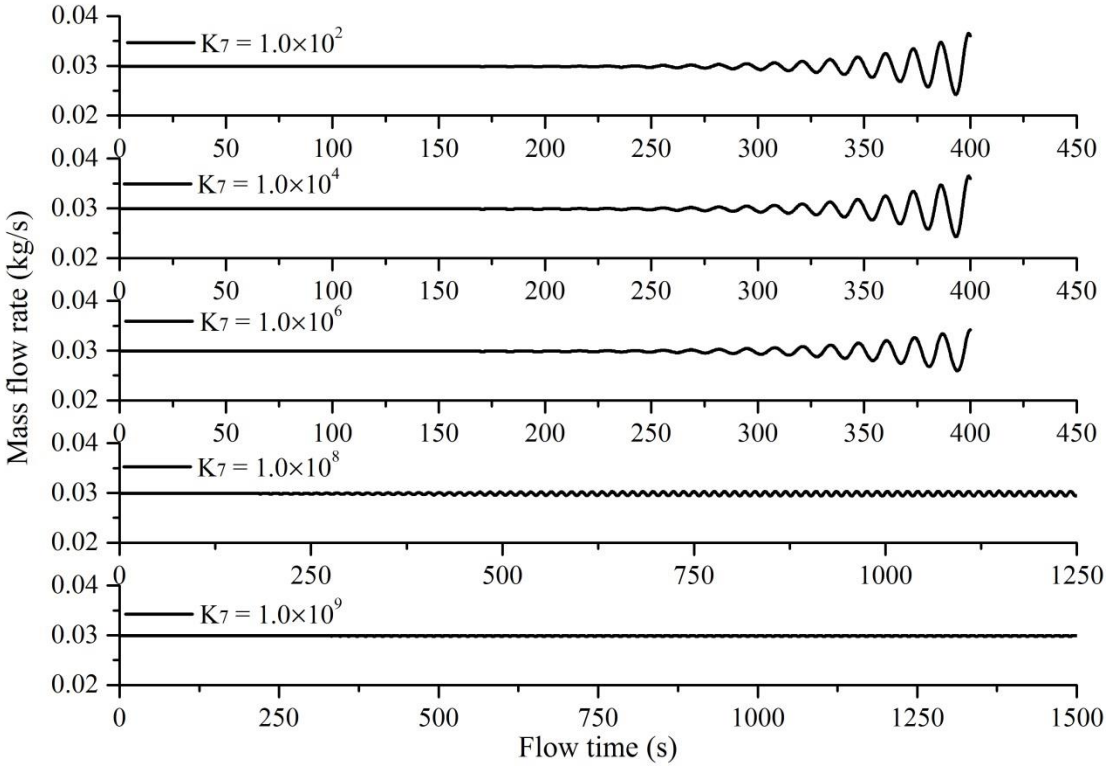

Figure 5.25 Valve effect on flow instability behaviour

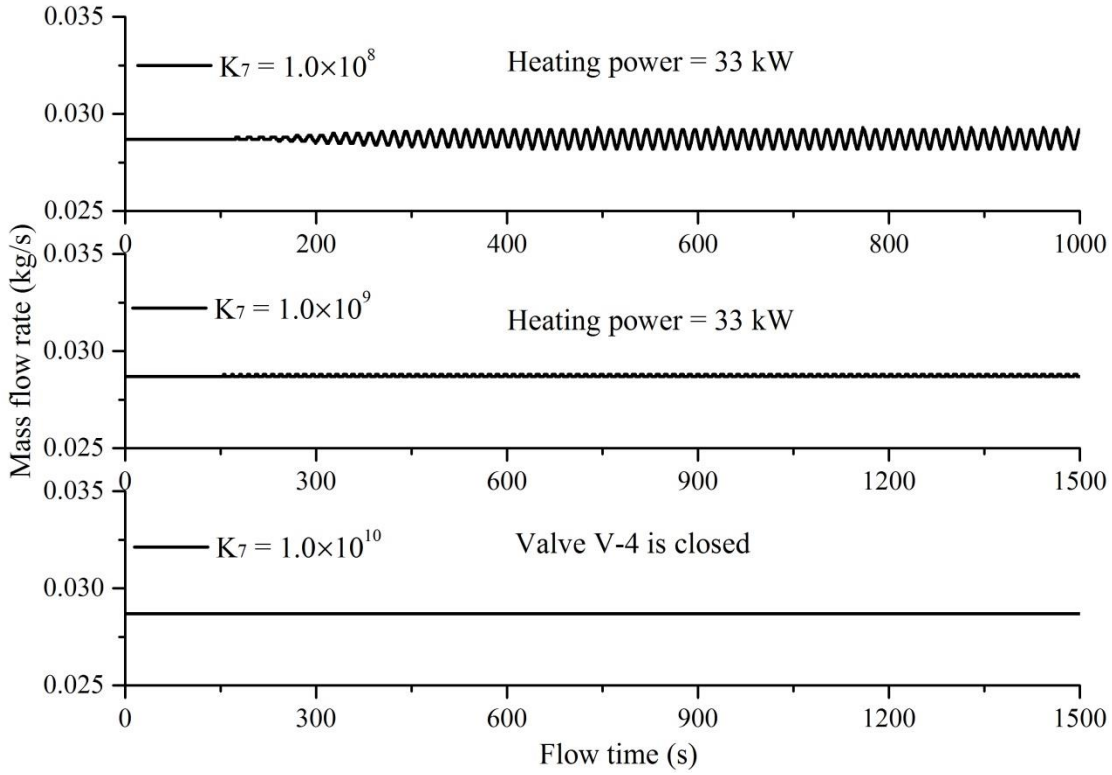

Figure 5.26 Valve effect on flow instability boundary

This is further verified by calculating the case with a relatively higher power at 33 kW. Figure 5.26 shows very small fluctuations of flow rate when the local K factor K_7 is 1.0×10^8. The flow rate is almost constant when the K_7 is 1.0×10^9 which means that the flow instability boundary can be postponed if the valve on the connecting line is throttled to be almost closed. This qualitatively verified the experimental results in section 4.6.

CHAPTER 6

SUMMARY, CONCLUSIONS, AND RECOMMENDATIONS

In this chapter, a summary of current research is presented. Obtained conclusions and recommendations for future work are also listed.

6.1 Summary

An experimental study was conducted to study the flow instability behaviour of supercritical CO_2 in a rectangular natural circulation loop with a horizontal single heated channel at the bottom tier. DC power was added directly to the heated section and heat was removed with a shell & tube heat exchanger. On the secondary side of the heat exchanger, a chiller unit capable of removing 30 kW was utilized and a roof-top unit was used when the outside temperature was low (as low as -20 °C) during winter time so that a better cooling effect could be realized. The inlet CO_2 temperature ranged from 10 to 22 °C. The operating pressures for all the experimental cases were 7.6, 8.0, and 8.6 MPa. Valve throttling effect at the heated channel outlet was also examined. Both steady state characteristics and flow oscillations were recorded during the experimental test. Totally 13 flow instability cases were collected and analyzed. Parametric effects study such as system pressure, inlet temperature, and heated channel outlet local loss were established based on the steady state results of the obtained instability cases. The accumulator effect as well as different loop configurations on flow instability behaviours was also studied.

To get a better understanding of the flow behaviours observed in the experiment and gain an insight into the mechanisms of flow instability in a natural circulation loop, a licensed non-linear code CATHENA was applied with supercritical water due to the limitation of current CATHENA version. A numerical analysis of the same experimental loop was performed with the purpose of testing the code's capability in numerical analysis of supercritical water in a natural circulation loop for which no

relevant results were reported in open literature, and checking if similar oscillation behaviours observed in the experiments can be obtained for the same loop. The steady-state solution of the CATHENA code was first validated using the supercritical natural circulation loop of Y.Z. Chen [67], then flow instability of the current experimental loop was numerically studied with two models of an open loop and a loop connected with accumulator (reservoir). For both models, this numerical study did not consider the wall structure effects. In addition, the present numerical study explained the possible reasons for the complicated flow oscillation behaviour observed during experiment and tested the effect of the valve on the connecting line. Factors that affect the predictions of the steady state results with CATHENA code were also discussed.

6.2 Conclusions

Present work performed both experimental and numerical study of supercritical flow instability in a natural circulation system. Relevant conclusions were drawn and presented as follows with two parts.

6.2.1 Experimental Study

Totally 13 flow instability cases were collected which somehow enriches the extremely lacking of experimental flow instability data in this filed and may be helpful for future numerical code validation.

Steady state flow-power curve with flow instability boundary points in the experimental study clearly showed that all the typical loop instabilities found in this experiment were on the negative slope. This is believed due to the effect of wall heat. As was expected, increase of the system pressure made the system more stable. Increase of outlet K factors always destabilized the system. By isolating the accumulator, flow oscillations disappeared. The flow oscillation returned when the accumulator was reconnected.

Experiments with various geometrically different loop configurations were systematically tested and compared, which helped gain more insights into the flow instability phenomenon within a supercritical natural circulation loop. A further test of the valve on the connecting line provides a plausible way of suppressing or even diminishing the flow instabilities in real applications.

Instability was not found with the closed loop configuration (C1) at the given power range which means the accumulator (pressurizer) is an indispensable part in supercritical natural circulation flow instability studies.

Two different flow oscillations were identified with distinct different periods. The short period flow fluctuation was found when the loop was connected with the rigid settling tank and may be due to the Helmholtz resonance effect between the settling tank and the loop. The second flow oscillation occurred with the accumulator connected and was typical loop instability with the important parameters oscillating in a similar manner.

By throttling the valve in the connecting line between the bladder type accumulator and the loop, the loop instability boundary didn't change much, whereas the short period oscillations could be postponed or even eliminated if more local resistance was added in the pipeline between the settling tank and the loop. And the introduction of accumulator together with the settling tank could not absorb the short period fluctuations.

Comparison of the steady state flow-power curves showed that the typical loop instabilities were found to be on the negative slope while the short period oscillations were observed to occur on the positive slope which was near the peak region. The short period oscillations occurred when heated channel outlet temperature was around the pseudo-critical temperature. Increase in inlet temperatures would cause the system to be more unstable. For the typical loop instability, increase of inlet temperature (10 ~ 22 °C) also destabilized the system.

6.2.2 Numerical Modeling

The CATHENA code is capable of capturing flow instability in a natural circulation loop under supercritical conditions with supercritical H_2O.

Test of the local loss K factors showed that the local loss K factor on the hot side had a more evident effect on the steady state mass flow rate results than the local loss K factor on the cold side. Increase the local K factor on the cold side shifted the steady state curve to the right and decrease the local K factor on the hot side also shifted the steady state curve to the right. It also could be seen that increase of pipe roughness decreased the predicted mass flow rate and shifted the peak of the flow rate to the left.

The accumulator contributed to the diversity behaviour of the flow oscillations, but it didn't affect the flow instability boundary when the valve on the connecting line was fully open, which agreed with the experimental findings.

Test of the valve on the connecting line showed that fully closing the valve stabilized the system. The throttling of valve could only be effective in postponing the flow instability boundary when it was almost closed (local K factor around or larger than 10^8), which also agreed with the experimental findings qualitatively.

6.3 Recommendations for Future Work

6.3.1 Experimental Study

The current experimental loop can be modified with constant area of piping, so the uncertainties in calculation of the local resistance will decrease, which will be better for numerical comparisons.

The current flow meter for measuring the flow rate of liquid CO_2 is a turbine flow meter. The CO_2 flow rate being measured is actually at the bottom 30% measurement range of the flow meter, which causes an underestimate (about 3%) of the flow rate. In this case, a new flow-meter with a smaller measurement range can be used to replace the current one. It is also applicable to increase the vertical height of the loop to improve the driving head in the loop so a larger flow rate can be achieved.

6.3.2 Numerical Modeling

Since the current version of CATHENA code only supports the modeling of supercritical water, the direct comparison of supercritical CO_2 results between the experiment and numerical work is still not available. When the code version is updated, the input file of current numerical work should be modified for supercritical CO_2 study and comparison with the experimental results.

Both Debrah, S.K. et al. [71] and Sharma et al. [61] pointed out the thermal capacity of the heater wall can have a big effect on natural circulation flow instability boundary and must be carefully studied. Thus, the future work should be mainly focused on a more realistic model with heater wall structure. To be specific, both full and reduced heat capacity of heater wall should be modeled by reducing the wall thickness to see its effect on flow instability behaviours as well as the boundary. And the effect of heat transfer correlations should also be tested.

REFERENCE

[1] IPCC, 2014: Climate Change 2014: Synthesis Report. Contribution of Working Groups I, II and III to the Fifth Assessment Report of the Intergovernmental Panel on Climate Change [Core Writing Team, R.K. Pachauri and L.A. Meyer (eds.)]. IPCC, Geneva, Switzerland, 151 pp.

[2] Adoption of the Paris Agreement, Resolution FCCC/CP/2015/L.9/Rev.1, United Nations Framework Convention on Climate Change, Bonn (2015).

[3] International Atomic Energy Agency (IAEA), 2017. PRIS database online available at: https://www.iaea.org/PRIS/WorldStatistics/OperationalByAge.aspx (Accessed 2017).

[4] Stephen M. Goldberg and Robert Rosner, Nuclear Reactors: Generation to Generation, American Academy of Arts and Sciences (2011).

[5] GEN IV International Forum (GIF), 2017. Online available at: https://www.gen-4.org/gif/jcms/c_9260/public (Accessed 2017).

[6] Technology Roadmap Update for Generation IV Nuclear Energy Systems, Issued by the OECD Nuclear Energy Agency for the GEN IV International Forum (2014).

[7] Schulenberg, T., L.K.H. Leung, and Y. Oka, Review of R&D for supercritical water cooled reactors. Progress in Nuclear Energy, 2014. 77: p. 282-299.

[8] Duffey, R., THE DEVELOPMENT AND FUTURE OF THE SUPERCRITICAL WATER REACTOR. CNL Nuclear Review, 2016. 5(2): p. 181-188.

[9] Ruchi Shukla1, K.S., M. Raisul Islam, An Experimental Study on a Density Driven Solar Water Heating System Using Supercritical CO_2 as Working Fluid. International Journal of Environment and Resource, 2014. 3(2): p. 13-22.

[10] Okazaki, T. and Y. Seshimo, Cooling System Using Natural Circulation for Air Conditioning. Vol. 25. 2011. 239-251.

[11] Greif, R., Natural Circulation Loops. Journal of Heat Transfer, 1988. 110(4b): p. 1243-1258.

[12] Khartabil, H.F., Review and Status of the Gen-IV CANDU-SCWR Passive Moderator Core Cooling System. 2008(48175): p. 429-434.

[13] AGENCY, I.A.E., Passive Safety Systems in Advanced Water Cooled Reactors (AWCRs): Case Studies. IAEA TECDOC Series. 2013, Vienna: INTERNATIONAL ATOMIC ENERGY AGENCY.

[14] Yetisir, M., et al., CANADIAN SUPERCRITICAL WATER-COOLED REACTOR CORE CONCEPT AND SAFETY FEATURES. CNL Nuclear Review, 2016. 5(2): p. 189-202.

[15] E.W. Lemmon, M.O.M.a.D.G.F., "Thermophysical Properties of Fluid Systems" in NIST Chemistry WebBook, NIST Standard Reference Database Number 69, Eds. P.J. Linstrom and W.G. Mallard, National Institute of Standards and Technology, Gaithersburg MD. 2017.

[16] Knez, Ž. et al., Industrial applications of supercritical fluids: A review. Energy, 2014. 77(Supplement C): p. 235-243.

[17] Ambrosini, W. and M. Sharabi, Dimensionless parameters in stability analysis of heated channels with fluids at supercritical pressures. Nuclear Engineering and Design, 2008. 238(8): p. 1917-1929.

[18] Vijayan, P.K., Introduction to instabilities in natural circulation systems. 2014, Global Centre for Nuclear Energy Partnership: India.

[19] Boure, J.A., A.E. Bergles, and L.S. Tong, Review of two-phase flow instability. Nuclear Engineering and Design, 1973. 25(2): p. 165-192.

[20] Fukuda, K. and T. Kobori, Classification of Two-Phase Flow Instability by Density Wave Oscillation Model. Journal of Nuclear Science and Technology, 1979. 16(2): p. 95-108.

[21] Kakac, S. and B. Bon, A Review of two-phase flow dynamic instabilities in tube boiling systems. International Journal of Heat and Mass Transfer, 2008. 51(3-4): p. 399-433.

[22] Jiyun, Z., A Pradip, Saha, A Mujid. Stability of supercritical water-cooled reactor during steady-state and sliding pressure start-up conditions. in 11th international topical meeting on nuclear reactor thermal hydraulics (Nureth 11). 2005. France.

[23] Ambrosini, W., On the analogies in the dynamic behaviour of heated channels with boiling and supercritical fluids. Nuclear Engineering and Design, 2007. 237(11): p. 1164-1174.

[24] Sarkar, M.K.S., A.K. Tilak, and D.N. Basu, A state-of-the-art review of recent advances in supercritical natural circulation loops for nuclear applications. Annals of Nuclear Energy, 2014. 73(0): p. 250-263.

[25] Chatoorgoon, V., A. Voodi, and P. Upadhye, The stability boundary for supercritical flow in natural-convection loops: Part II: CO_2 and H2. Nuclear Engineering and Design, 2005. 235(24): p. 2581-2593.

[26] Tummalapalli, S.K.V.B., Supercritical flow experimental facility. 2007, University of Manitoba.

[27] Hanna, B.N., CATHENA: A thermalhydraulic code for CANDU analysis. Nuclear Engineering and Design, 1998. 180(2): p. 113-131.

[28] Zuber, N., An analysis of thermally induced flow oscillations in the near-critical and super-critical thermodynamic region, in Final Report Nas8-11422. 1966.

[29] Yi, T.T., S. KOSHIZUKA, and Y. OKA, A Linear Stability Analysis of Supercritical Water Reactors, (I) Thermal-Hydraulic Stability. Journal of Nuclear Science and Technology, 2004. 41(12): p. 10.

[30] Gómez, T.O., et al., Stability analysis of a uniformly heated channel with supercritical water. Nuclear Engineering and Design, 2008. 238(8): p. 1930-1939.

[31] Ambrosini, W., Discussion on the stability of heated channels with different fluids at supercritical pressures. Nuclear Engineering and Design, 2009. 239(12): p. 2952-2963.

[32] Ambrosini, W., Assessment of flow stability boundaries in a heated channel with different fluids at supercritical pressure. Annals of Nuclear Energy, 2011. 38(2-3): p. 615-627.

[33] T'Joen, C., L. Gilli, and M. Rohde, Sensitivity analysis of numerically determined linear stability boundaries of a supercritical heated channel. Nuclear Engineering and Design, 2011.

[34] Tian, X., et al., Flow instability analysis of supercritical water-cooled reactor CSR1000 based on frequency domain. Annals of Nuclear Energy, 2012. 49: p. 70-80.

[35] Chatoorgoon, V., Non-dimensional parameters for static instability in supercritical heated channels. International Journal of Heat and Mass Transfer, 2013. 64: p. 145-154.

[36] Zhang, Y., et al., A new model for studying the density wave instabilities of supercritical water flows in tubes. Applied Thermal Engineering, 2015. 75: p. 397-409.

[37] Sharabi, M.B., W. Ambrosini, and S. He, Prediction of unstable behaviour in a heated channel with water at supercritical pressure by CFD models. Annals of Nuclear Energy, 2007. 35(5): p. 767-782.

[38] Sharabi, M., et al., Transient Three-Dimensional Stability Analysis of Supercritical Water Reactor Rod Bundle Subchannels by a Computatonal Fluid Dynamics Code. Journal of Engineering for Gas Turbines and Power, 2009. 131(2): p. 022903.

[39] Ampomah-Amoako, E., et al., Analysis of flow stability in nuclear reactor subchannels with water at supercritical pressures. Annals of Nuclear Energy, 2013. 60: p. 396-405.

[40] Ampomah-Amoako, E., et al., CFD analysis of the dynamic behaviour of a fuel rod subchannel in a supercritical water reactor with point kinetics. Annals of Nuclear Energy, 2013. 59: p. 211-223.

[41] Ampomah-Amoako, E. and W. Ambrosini, Developing a CFD methodology for the analysis of flow stability in heated channels with fluids at supercritical pressures. Annals of Nuclear Energy, 2013. 54: p. 251-262.

[42] Dutta, G., et al., Numerical models to predict steady and unsteady thermal-hydraulic behaviour of supercritical water flow in circular tubes. Nuclear Engineering and Design, 2015. 289(Supplement C): p. 155-165.

[43] Ebrahimnia, E., V. Chatoorgoon, and S.J. Ormiston, Numerical stability analyses of upward flow of supercritical water in a vertical pipe. International Journal of Heat and Mass Transfer, 2016. 97(Supplement C): p. 828-841.

[44] Chatoorgoon, V., SPORTS - A simple non-linear thermalhydraulic stability code. Nuclear Engineering and Design, 1986. 93(1): p. 51-67.

[45] Chatoorgoon, V., Supercritical flow stability in horizontal channels. Nuclear Engineering and Design, 2008. 238(8): p. 1940-1946.

[46] Hou, D., et al., Stability analysis of parallel-channel systems with forced flows under supercritical pressure. Annals of Nuclear Energy, 2011. 38(11): p. 2386-2396.

[47] Liu, P., et al., Stability analysis of parallel-channel systems under supercritical pressure with heat exchanging. Annals of Nuclear Energy, 2014. 69(0): p. 267-277.

[48] Xiong, T., et al., Experimental study on flow instability in parallel channels with supercritical water. Annals of Nuclear Energy, 2012. 48: p. 60-67.

[49] Xiong, T., et al., Modeling and analysis of supercritical flow instability in parallel channels. International Journal of Heat and Mass Transfer, 2013. 57(2): p. 549-557.

[50] Xi, X., et al., Numerical simulation of the flow instability between two heated parallel channels with supercritical water. Annals of Nuclear Energy, 2014. 64: p. 57-66.

[51] Li, S., V. Chatoorgoon, and S.J. Ormiston, Numerical study of oscillatory flow instability in upward flow of supercritical water in two heated parallel channels. International Journal of Heat and Mass Transfer, 2018. 116(Supplement C): p. 16-29.

[52] Xi, X., et al., An experimental investigation of flow instability between two heated parallel channels with supercritical water. Nuclear Engineering and Design, 2014. 278(0): p. 171-181.

[53] Dutta, G., C. Zhang, and J. Jiang, Analysis of flow induced density wave oscillations in the CANDU supercritical water reactor. Nuclear Engineering and Design, 2015. 286: p. 150-162.

[54] Zhang, L., et al., Experimental investigations on flow characteristics of two parallel channels in a forced circulation loop with supercritical water. Applied Thermal Engineering, 2016. 106: p. 98-108.

[55] Chatoorgoon, V., Stability of supercritical fluid flow in a single-channel natural-convection loop. International Journal of Heat and Mass Transfer, 2001. 44(10): p. 1963-1972.

[56] Chatoorgoon, V., A. Voodi, and D. Fraser, The stability boundary for supercritical flow in natural convection loops: Part I: H_2O studies. Nuclear Engineering and Design, 2005. 235(24): p. 2570-2580.

[57] Lomperski, S., et al., Stability of a Natural Circulation Loop with a Fluid Heated Through the Thermodynamic Pseudo-critical Point. 2004. Medium: X; Size: page(s) 1736-1741.

[58] R. Jain, M.L.C., A Linear Stability Analysis for Natural-Circulation Loops Under Supercritical Conditions. Nuclear Technology, 2006. 155(3): p. 312-323.

[59] Jain, P.K. and u. Rizwan, Numerical analysis of supercritical flow instabilities in a natural circulation loop. Nuclear Engineering and Design, 2008. 238(8): p. 1947-1957.

[60] Sharma, M., et al., Steady state and linear stability analysis of a supercritical water natural circulation loop. Nuclear Engineering and Design, 2010. 240(3): p. 588-597.

[61] Sharma, M., et al., Steady state and stability characteristics of natural circulation loops operating with carbon dioxide at supercritical pressures for open and closed loop boundary conditions. Nuclear Engineering and Design, 2013. 265: p. 737-754.

[62] Sharma, M., et al., Natural convective flow and heat transfer studies for supercritical water in a rectangular circulation loop. Nuclear Engineering and Design, 2014. 273(0): p. 304-320.

[63] Chen, L., et al., Effect of heat transfer on the instabilities and transitions of supercritical CO_2 flow in a natural circulation loop. International Journal of Heat and Mass Transfer, 2010. 53(19-20): p. 4101-4111.

[64] Chen, L., et al., Thermal and hydrodynamic characteristics of supercritical CO_2 natural circulation in closed loops. Nuclear Engineering and Design, 2013. 257(Supplement C): p. 21-30.

[65] Chen, L., B.-L. Deng, and X.-R. Zhang, Experimental study of trans-critical and supercritical CO_2 natural circulation flow in a closed loop. Applied Thermal Engineering, 2013. 59(1-2): p. 1-13.

[66] T'Joen, C. and M. Rohde, Experimental study of the coupled thermo-hydraulic–neutronic stability of a natural circulation HPLWR. Nuclear Engineering and Design, 2012. 242: p. 221-232.

[67] Chen Yuzhou, Z.M., Yang Chunsheng, Bi Keming, Du Kaiwen. An experiment on flow and heat transfer characteristics in natural circulation of supercritical water. in The 3rd China-Canada Joint Workshop on Supercritical-Water-Cooled Reactors, CCSC-2012. 2012. Xi'an, China.

[68] Chen Yuzhou, Z.M., Yang Chunsheng, Bi Keming, Du Kaiwen. Experiment of heat transfer of supercritical water in natural circulation with different diameters of heated tubes. in The 6th International Symposium on Supercritical Water-Cooled Reactors ISSCWR-6. 2013. Shenzhen, Guangdong, China.

[69] Swapnalee, B.T. and P.K. Vijayan, A generalized flow equation for single phase natural circulation loops obeying multiple friction laws. International Journal of Heat and Mass Transfer, 2011. 54(11–12): p. 2618-2629.

[70] Debrah, S.K., W. Ambrosini, and Y. Chen, Discussion on the stability of natural circulation loops with supercritical pressure fluids. Annals of Nuclear Energy, 2013. 54(0): p. 47-57.

[71] Debrah, S.K., W. Ambrosini, and Y. Chen, Assessment of a new model for the linear and nonlinear stability analysis of natural circulation loops with supercritical fluids. Annals of Nuclear Energy, 2013. 58: p. 272-285.

[72] Mahmoudi, J., Experimental thermal-hydraulic study of a supercritical CO_2 natural circulation loop. 2014, University of Manitoba.

[73] Tilak, A.K. and D.N. Basu, Computational investigation of the dynamic response of a supercritical natural circulation loop to aperiodic and periodic excitations. Nuclear Engineering and Design, 2015. 284(0): p. 251-263.

[74] Archana, V., A.M. Vaidya, and P.K. Vijayan, Numerical modeling of supercritical CO_2 natural circulation loop. Nuclear Engineering and Design, 2015. 293: p. 330-345.

[75] Misale, M., et al., Analysis of single-phase natural circulation experiments by system codes. International Journal of Thermal Sciences, 1999. 38(11): p. 977-983.

[76] Naveen, K., et al., Investigations on single-phase natural circulation loop dynamics. Part 3: Role of expansion tank. Progress in Nuclear Energy, 2015. 78(Supplement C): p. 65-79.

[77] Kevin Keener, Small Meat Processing Plants: Selection and Maintenance of Temperature Measurement Devices (FS-25-W). 2007, PURDUE EXTENTION

[78] Stewart E., Stewart P., Watson A., 1973, Thermo-acoustic oscillations in forced convection heat transfer to supercritical pressure water, International Journal of Heat and Mass Transfer, Volume 16, Issue 2, 257–270.

[79] Joe Wolf, 2005, online at: https://newt.phys.unsw.edu.au/jw/Helmholtz.html, School of Physics, The University of New South Wales (accessed 2017)

[80] Hanna, B.N., CATHENA Simulation of supercritical heat transfer in a tube (INIS-XA--10E0105). 2010: International Atomic Energy Agency (IAEA).

[81] Beuthe, T.G., CATHENA MOD-3.5d Abstract. 2005, Atomic Energy of Canada Limited Report.

[82] Hanna, T.G.B.a.B.N., CATHENA MOD-3.5D THEORY MANUAL. 2013, Atomic Energy of Canada Limited Report.

[83] Dittus, F.W., & Boelter, L. M. K., Heat transfer in automobile radiators of the tubular type. Berkeley, Calif: University of California Press, 1930.

[84] Claxton, K.T., et al., H.T.F.S. correlations for two-phase pressure drop and void fraction in tubes. 1972, Harwell [England]: Heat Transfer and Fluid Flow Service.

[85] Colebrook, C.F., Turbulent flow in pipes, with particular reference to the transition region between the smooth and rough pipe laws. Journal of the Institution of Civil Engineers, 1939. 11(4): p. 133-156.

[86] Idel'chik, I.E. and M.O. Steinberg, Handbook of hydraulic resistance. 1993, Boca Raton, FL: CRC Press : Begell House.

APPENDIX I

EXPERIMENTAL TEST FACILITY

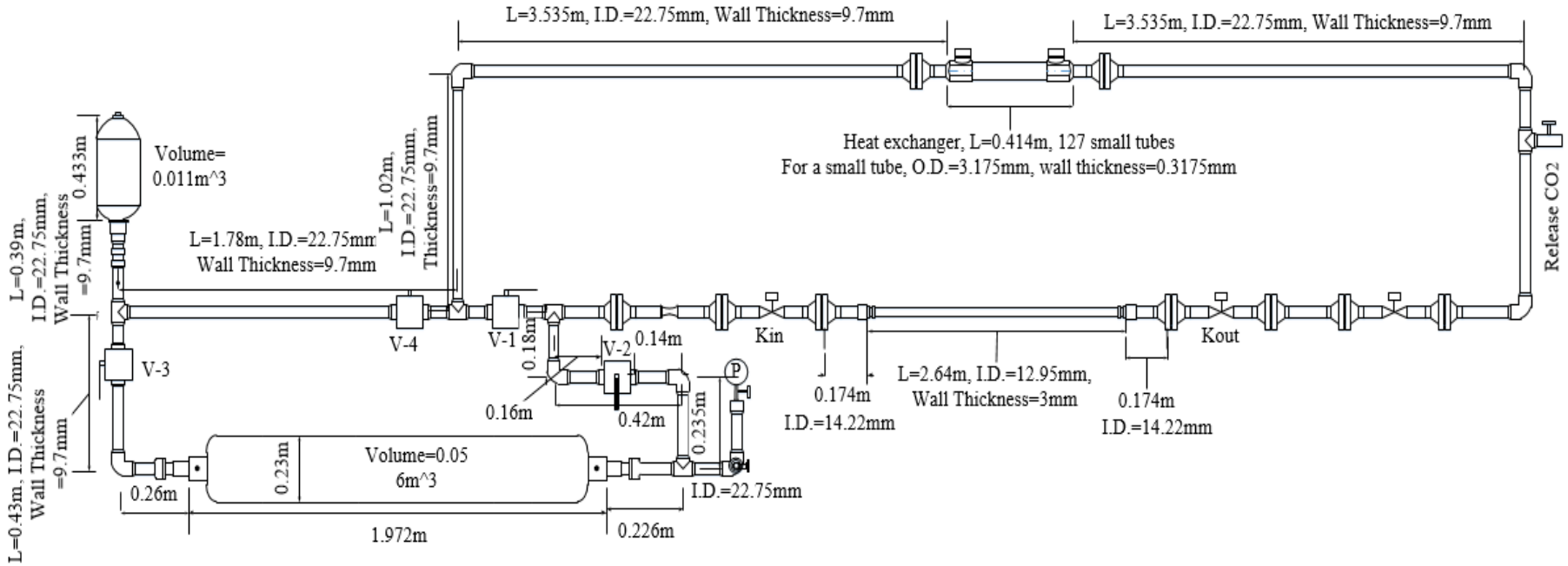

Figure A I. 1 Experimental test facility

APPENDIX II

CALCULATION OF LOCAL LOSS COEFFICIENTS

Main area changes of the experimental loop are the horizontal bottom parts that connecting with the pneumatic valves. The horizontal bottom part of the loop model is shown in Figure A II. 1. Local pressure loss K factors induced by these area changes were calculated based on [86].

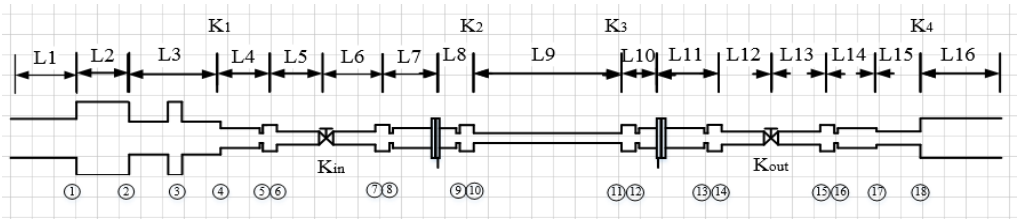

Figure A II. 1 Horizontal bottom part of the experimental loop

Calculation of Reynolds Number

A typical Reynolds number for CO_2 side is a system pressure of 8 MPa, inlet temperature of 20°C and maximum flow rate about 0.06kg/s.

$$\mathrm{Re}=\frac{wD_h}{\nu}=\frac{MD_h}{\mu A}=\frac{0.06\times 10.414\times 10^{-3}}{7.5717\times 10^{-5}\times\pi\left(10.414\times 10^{-3}\right)^2/4}=9.688\times 10^4<10^5,$$

where w (m/s) is the mean velocity of the stream at the smallest cross section of the pipe, D_h (m) is the hydraulic diameter, M (kg/s) is the mass flow rate of CO_2, A (m^2) is the smallest cross section area of the pipe. ν (m^2/s) and μ (Pa·s) are the kinetic and dynamic viscosity, respectively.

Calculation of pressure drop local loss coefficient K

Section 1:

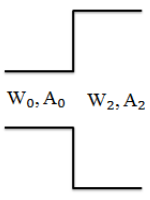

Figure A II. 2 Area enlargement of tubes

This is an area enlargement of pipe connected with a flexible hose.

For circular tube with sudden expansion, $\mathrm{Re} > 3.5\times10^3$

$K_1 = \frac{1}{n^2} + 2 - \frac{2.66}{n}$, where $n = \frac{A_2}{A_0} = \frac{\pi D_2{}^2/4}{\pi D_0{}^0/4} = \left(\frac{D_2}{D_0}\right)^2$

$D_2 = 25.4mm$, $D_0 = 22.7584mm$, so $K_1 = 0.51$

Section 2:

This is an area contraction of flexible hose connected with Swagelok tube.

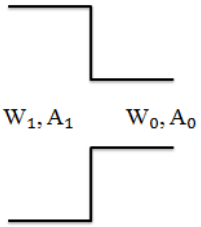

Figure A II. 3 Area contraction of tubes

For $\mathrm{Re} < 10^5$ (approximately):

$K = K_\varphi + K_0^{\mathrm{Re}} \cdot K_0$, where φ is velocity coefficient at discharge from a sharp-edged orifice, depending on the Reynolds number Re and the area ratio $\frac{A_0}{A_2}$. K_0^{Re} is coefficient depending on Re.

$\frac{A_0}{A_2} = 1$, so $K_\varphi = 0$. For $\mathrm{Re} \approx 10^5$, $K_0^{\mathrm{Re}} \approx 0.9$

$$K_0 = 0.5\left(1 - \frac{A_0}{A_1}\right) + \left(1 - \frac{A_0}{A_2}\right)^2 + \tau\sqrt{1 - \frac{A_0}{A_1}}\left(1 - \frac{A_0}{A_2}\right)$$

$\tau = 0$ and $A_0 = A_2$, so $K_2 = K_0^{\mathrm{Re}} \cdot K_0 = 0.9\times0.5\left(1 - \frac{A_0}{A_1}\right) = 0.45\left[1 - \left(\frac{D_0}{D_1}\right)^2\right] = 0.137$

Section 3:

Section 3 is the area changes at both ends of turbine flow meter which is similar to section 1 (flow expansion) and section 2 (flow contraction). K_3 is calculated to be $K_3 = 0.767$.

Section 4:

This is an area expansion of Swagelok tube connected with flanges. Similar to section 1, the local loss $K_4$is calculated to be $K_4 = 0.25$.

Section 5:

This part is the small annular chamber which can be treated as an orifice.

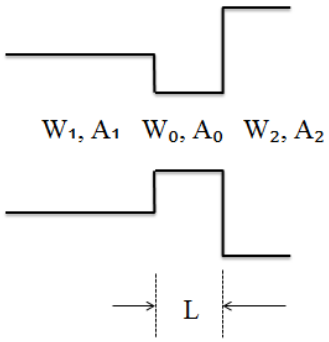

Figure A II. 4 Annular chamber

For $\mathrm{Re} \approx 10^5$, $K_0^{\mathrm{Re}} \approx 0.9$. $\frac{A_0}{A_2} = \left(\frac{D_0}{D_2}\right)^2 = 0.343$, so $K_\varphi \approx 0.04$, $\frac{A_0}{A_1} = \left(\frac{D_0}{D_1}\right)^2 = 0.536$.

$K_0 = 0.5\left(1-\frac{A_0}{A_1}\right)+\left(1-\frac{A_0}{A_2}\right)^2+\tau\sqrt{1-\frac{A_0}{A_1}}\left(1-\frac{A_0}{A_2}\right)$ where $\tau = 1.22$ based on $\frac{l}{D_0} \approx 0.2$.

So $K_5 = K_\varphi + K_0^{\mathrm{Re}} K_0 = 0.04 + 0.9K_0 \approx 1.13$

Similar to sections 1 ~ 5, the rest of the sections are calculated and listed as following:

$K_6 = 0.22$, $K_7 = 0.9$, $K_8 = 0.9$, $K_9 = 1.13$, $K_{10} = 0.21$, $K_{11} = 0.87$, $K_{12} = 0.9$,

$K_{13} = 1.13$, $K_{14} = 0.22$, $K_{15} = 0.9$, $K_{16} = 0.9$, $K_{17} = 0.09$, $K_{18} = 1.27$

So, $K_{cold} = K_1 + K_2 + ... + K_{10} = 6.16$, $K_{hot} = K_{11} + K_{12} + ... + K_{18} = 6.28$

The K factors for heat exchanger inlet and outlet are from J. Mahmoudi [72], which were calculated based on experimental cases with various Reynolds number.

$K_{HX-in} = 2.0$, $K_{HX-out} = 2.7$

APPENDIX III

RAW AND PROCESSED DATA FROM THE EXPERIMENTAL STUDY

Table A III. 1 Averaged values of measured signals during experiment for each data point (Case 1)

No.	Pressure (MPa)	Heating power (kW)	Mass flow rate (kg/s)	CO_2 inlet temperature (°C)	CO_2 outlet temperature (°C)	Water inlet temperature (°C)	Water outlet temperature (°C)	Water flow rate (kg/s)	Pressure drop across outlet valve (Pa)	Pressure drop across heat exchanger (Pa)
1	7.617	1.1337	0.0265	20.6	29.3	19.2	19.5	1.0261	390.04	41.66
2	7.607	1.9032	0.0339	19.6	31.2	16.8	17.2	1.0237	620.14	52.18
3	7.612	2.8484	0.0399	19.4	32.1	15.6	16.3	1.0232	930.87	66.32
4	7.606	3.7899	0.0439	18.9	32.4	13.8	14.8	1.0223	1254.67	79.40
5	7.596	4.7300	0.0462	18.7	32.6	12.9	14.0	1.0205	1570.24	91.69
6	7.602	5.6682	0.0474	18.4	32.9	11.7	13.1	1.0204	1874.15	103.22
7	7.607	6.6182	0.0477	18.3	34.3	10.8	12.4	1.0200	2197.70	114.59
8	7.607	7.0825	0.0473	18.1	35.2	10.1	11.9	1.0199	2368.76	118.27
9	7.606	7.5566	0.0466	18.0	37.1	9.8	11.6	1.0198	2546.03	124.00
10	7.617	8.0323	0.0460	18.0	40.2	9.4	11.3	1.0192	2739.97	129.59
11	7.609	8.4950	0.0453	17.9	43.4	9.1	11.1	1.0187	2906.79	133.15
12	7.613	8.9710	0.0449	17.7	47.5	8.5	10.6	1.0191	3088.48	136.20
13	7.608	9.4342	0.0440	18.3	54.4	8.8	10.9	1.0186	3236.49	138.70

Table A III. 2 Averaged values of measured wall surface temperature during experiment for each data point (Case1)

No.	TS21T (°C)	TS21B (°C)	TS22T (°C)	TS22B (°C)	TS23T (°C)	TS23B (°C)	TS24T (°C)	TS24B (°C)	TS25T (°C)	TS25B (°C)	TS26T (°C)	TS26B (°C)
1	32.3	29.8	34.5	31.3	36.1	31.9	38.0	32.8	39.7	34.2	39.8	35.0
2	36.9	33.6	40.0	35.3	42.2	35.4	44.6	35.8	47.7	37.2	48.4	38.3
3	43.0	37.3	47.7	39.6	50.3	39.5	55.2	39.7	58.1	41.8	59.4	43.3
4	51.1	41.6	57.7	45.1	59.1	44.2	66.8	44.0	70.8	46.9	71.5	48.9
5	62.3	47.7	69.7	52.2	72.6	49.8	80.3	49.0	86.1	52.9	85.7	56.1
6	75.4	55.5	82.8	60.4	86.2	55.9	95.0	54.6	100.9	59.8	101.9	65.8
7	90.7	65.9	98.0	70.3	99.8	62.6	110.9	61.0	117.9	68.8	122.2	79.7
8	96.7	71.0	104.5	75.4	103.9	66.0	118.1	64.3	127.0	74.4	134.2	88.8
9	102.8	76.7	111.8	80.3	107.8	69.0	124.9	68.2	137.4	81.6	147.9	99.8
10	111.5	83.2	115.3	83.0	112.1	72.0	134.3	73.5	150.1	91.1	163.7	113.2
11	121.0	89.9	120.7	87.0	116.9	75.1	144.1	79.0	162.7	101.1	179.3	127.3
12	130.6	97.0	122.2	89.3	120.3	78.3	156.0	86.1	177.1	112.8	196.9	143.6
13	133.1	101.3	121.3	91.1	124.2	82.2	172.5	94.3	192.3	125.5	214.8	160.3

Table A III. 3 Averaged values of measured signals during experiment for each data point (Case 2)

No.	Pressure (MPa)	Heating power (kW)	Mass flow rate (kg/s)	CO_2 inlet temperature (°C)	CO_2 outlet temperature (°C)	Water inlet temperature (°C)	Water outlet temperature (°C)	Water flow rate (kg/s)	Pressure drop across outlet valve (Pa)	Pressure drop across heat exchanger (Pa)
1	7.994	1.5251	0.0291	20.5	31.2	18.9	19.2	1.0255	541.66	48.96
2	8.017	1.9055	0.0327	19.9	32.1	17.4	17.9	1.0244	673.17	52.22
3	7.999	2.8518	0.0384	19.4	33.7	15.4	16.1	1.0224	1009.85	65.34
4	8.024	3.7906	0.0420	19.1	34.0	14.6	15.5	1.0216	1345.88	76.95
5	8.002	4.7322	0.0443	18.9	34.4	13.5	14.6	1.0211	1709.64	89.72
6	8.009	5.6730	0.0457	18.3	35.4	11.7	13.1	1.0204	2077.25	99.84
7	8.021	6.6121	0.0455	18.2	36.8	11.0	12.6	1.0190	2427.73	108.85
8	8.016	7.5630	0.0447	18.0	41.2	9.8	11.7	1.0175	2856.14	125.31
9	8.025	8.5045	0.0433	17.7	48.4	8.6	10.6	1.0162	3249.80	132.50
10	8.020	8.9690	0.0427	17.7	53.0	8.6	10.7	1.0173	3402.93	135.78
11	8.020	9.4444	0.0418	17.6	58.8	8.1	10.3	1.0172	3579.28	139.51

Table A III. 4 Averaged values of measured wall surface temperature during experiment for each data point (Case2)

No.	TS21T (°C)	TS21B (°C)	TS22T (°C)	TS22B (°C)	TS23T (°C)	TS23B (°C)	TS24T (°C)	TS24B (°C)	TS25T (°C)	TS25B (°C)	TS26T (°C)	TS26B (°C)
1	35.9	32.6	38.3	34.2	40.9	35.1	44.6	35.9	45.9	37.5	46.7	38.7
2	38.3	34.4	40.3	36.1	43.9	37.0	48.6	37.5	49.9	39.4	51.3	40.6
3	44.0	38.6	47.1	40.4	51.5	40.9	59.1	41.1	60.5	43.6	61.9	45.5
4	51.6	42.8	57.9	45.5	61.6	45.8	71.5	46.0	73.7	48.6	75.8	52.2
5	62.1	48.2	69.7	51.9	75.1	51.4	86.3	51.2	90.8	55.8	91.3	60.1
6	74.9	55.4	82.7	59.9	89.0	57.7	103.1	57.4	106.8	63.7	108.3	70.8
7	89.5	64.9	98.3	70.0	100.5	64.9	118.3	64.3	124.4	74.1	129.5	86.7
8	101.9	75.8	111.9	79.5	107.8	70.3	130.7	71.7	144.6	88.7	157.1	108.6
9	118.3	88.4	119.7	84.6	118.3	77.1	153.1	83.2	171.5	108.5	189.8	137.0
10	128.3	95.6	124.5	87.9	121.7	80.3	163.2	90.0	185.9	120.7	207.4	153.5
11	131.9	100.4	123.6	89.4	125.4	84.3	178.2	99.1	202.3	134.8	226.7	171.5

Table A III. 5 Averaged values of measured signals during experiment for each data point (Case 3)

No.	Pressure (MPa)	Heating power (kW)	Mass flow rate (kg/s)	CO_2 inlet temperature (°C)	CO_2 outlet temperature (°C)	Water inlet temperature (°C)	Water outlet temperature (°C)	Water flow rate (kg/s)	Pressure drop across outlet valve (Pa)	Pressure drop across heat exchange (Pa)
1	8.002	1.9065	0.0311	20.3	32.2	18.1	18.5	1.0249	806.96	54.24
2	8.003	2.8426	0.0368	19.4	33.2	16.0	16.6	1.0219	1216.20	67.45
3	8.000	3.7877	0.0404	18.8	33.8	13.9	14.8	1.0201	1658.40	80.34
4	8.013	4.7321	0.0424	18.4	34.9	12.4	13.6	1.0184	2106.11	91.90
5	7.998	5.6752	0.0430	18.1	36.1	11.1	12.5	1.0181	2554.89	100.96
6	8.008	6.6168	0.0421	18.2	39.0	10.5	12.0	1.0178	2989.51	112.29
7	8.010	7.5583	0.0410	17.9	44.3	9.4	11.2	1.0171	3475.41	122.71
8	8.018	8.5005	0.0391	17.6	53.9	8.4	10.4	1.0162	3903.37	131.73
9	8.010	8.9657	0.0380	17.8	60.7	8.4	10.5	1.0151	4084.56	137.38

Table A III. 6 Averaged values of measured wall surface temperature during experiment for each data point (Case3)

No.	TS21T (°C)	TS21B (°C)	TS22T (°C)	TS22B (°C)	TS23T (°C)	TS23B (°C)	TS24T (°C)	TS24B (°C)	TS25T (°C)	TS25B (°C)	TS26T (°C)	TS26B (°C)
1	38.9	35.0	40.7	36.7	45.0	37.4	50.5	37.9	50.7	39.4	51.8	40.8
2	44.7	39.0	49.6	40.9	54.0	41.4	60.5	41.3	62.3	44.1	63.8	45.9
3	53.0	43.2	60.3	46.4	64.2	46.4	74.0	46.3	75.8	48.3	77.7	52.8
4	64.1	49.2	73.5	53.5	78.4	52.3	90.0	52.2	94.0	56.6	94.6	61.7
5	78.6	57.3	88.0	62.6	93.5	59.5	107.9	58.8	111.1	65.9	113.4	74.3
6	92.9	67.9	105.5	74.0	102.9	66.4	120.5	65.7	130.2	78.3	138.3	93.8
7	108.9	80.4	116.5	81.2	111.7	72.2	136.6	75.0	154.7	96.3	170.2	120.0
8	126.2	94.0	125.2	87.3	121.7	79.3	162.0	89.4	186.5	122.2	209.0	156.1
9	126.3	97.2	122.5	87.9	125.7	83.5	177.7	99.9	204.5	138.2	230.1	176.0

Table A III. 7 Averaged values of measured signals during experiment for each data point (Case 4)

No.	Pressure (MPa)	Heating power (kW)	Mass flow rate (kg/s)	CO_2 inlet temperature (°C)	CO_2 outlet temperature (°C)	Water inlet temperature (°C)	Water outlet temperature (°C)	Water flow rate (kg/s)	Pressure drop across outlet valve (Pa)	Pressure drop across heat exchange (Pa)
1	7.610	1.9073	0.0321	20.0	31.6	17.1	17.6	1.0226	1030.48	53.91
2	7.611	2.8429	0.0368	19.2	31.8	15.1	15.8	1.0199	1519.11	67.04
3	7.595	3.8780	0.0398	18.8	31.8	13.6	14.6	1.0190	2065.31	81.07
4	7.586	4.7339	0.0407	18.7	32.8	12.4	13.6	1.0169	2541.42	91.30
5	7.607	5.6743	0.0402	18.3	34.8	11.0	12.5	1.0159	3083.24	101.98
6	7.603	6.6153	0.0391	18.3	40.2	10.0	11.6	1.0156	3631.27	111.02
7	7.611	7.5565	0.0365	18.1	49.2	9.0	10.8	1.0154	4142.08	119.27

Table A III. 8 Averaged values of measured wall surface temperature during experiment for each data point (Case4)

No.	TS21T (°C)	TS21B (°C)	TS22T (°C)	TS22B (°C)	TS23T (°C)	TS23B (°C)	TS24T (°C)	TS24B (°C)	TS25T (°C)	TS25B (°C)	TS26T (°C)	TS26B (°C)
1	37.6	34.2	40.8	35.4	44.3	35.9	48.6	36.2	50.2	37.7	49.5	38.6
2	44.4	37.9	51.0	40.0	54.8	40.2	61.4	40.2	62.0	41.7	61.3	43.9
3	55.9	43.9	64.5	47.0	68.7	46.4	76.9	45.9	79.3	48.8	77.8	51.7
4	68.9	51.1	78.5	54.9	81.5	52.5	90.6	51.2	94.0	56.0	94.0	60.6
5	82.1	60.7	95.0	65.5	92.7	59.8	104.3	57.2	111.7	66.0	116.7	76.3
6	98.9	73.4	110.5	75.6	102.6	65.8	120.0	65.4	135.3	82.0	147.8	101.4
7	118.1	87.8	121.6	82.3	115.9	73.3	145.2	79.1	167.8	107.3	187.8	138.0

Table A III. 9 Averaged values of measured signals during experiment for each data point (Case 5)

No.	Pressure (MPa)	Heating power (kW)	Mass flow rate (kg/s)	CO_2 inlet temperature (°C)	CO_2 outlet temperature (°C)	Water inlet temperature (°C)	Water outlet temperature (°C)	Water flow rate (kg/s)	Pressure drop across outlet valve (Pa)	Pressure drop across heat exchange (Pa)
1	8.610	1.9081	0.0323	19.9	33.6	17.6	18.1	1.0200	580.28	57.14
2	8.598	2.8453	0.0384	19.1	35.4	15.1	15.8	1.0174	857.22	68.46
3	8.597	3.7899	0.0423	18.8	36.7	14.2	15.1	1.0168	1149.48	80.33
4	8.604	4.7349	0.0449	18.5	37.3	13.2	14.3	1.0162	1455.54	90.59
5	8.607	5.6781	0.0463	18.4	38.4	12.2	13.5	1.0161	1770.67	99.88
6	8.607	6.6205	0.0472	18.0	40.5	10.5	12.1	1.0150	2084.97	108.11
7	8.603	7.5642	0.0473	18.0	43.3	9.8	11.7	1.0132	2416.21	120.30
8	8.616	8.4951	0.0465	17.9	48.9	8.9	11.0	1.0131	2765.93	120.97
9	8.613	10.3876	0.0434	17.6	65.8	7.3	9.8	1.0130	3418.46	161.70

Table A III. 10 Averaged values of measured wall surface temperature during experiment for each data point (Case5)

No.	TS21T (°C)	TS21B (°C)	TS22T (°C)	TS22B (°C)	TS23T (°C)	TS23B (°C)	TS24T (°C)	TS24B (°C)	TS25T (°C)	TS25B (°C)	TS26T (°C)	TS26B (°C)
1	39.0	35.1	42.8	37.8	45.8	38.3	49.5	39.4	52.3	41.9	52.3	43.4
2	44.8	39.9	49.5	43.2	52.8	42.9	58.9	43.6	62.7	46.5	63.8	48.4
3	51.3	44.1	58.4	47.8	61.6	47.4	69.9	47.7	75.4	51.7	78.0	54.5
4	59.6	48.6	70.0	53.9	73.6	52.5	83.8	53.1	91.1	57.3	93.3	62.7
5	70.6	54.5	82.2	61.1	87.7	58.5	101.1	59.3	108.3	65.8	110.2	73.0
6	83.8	62.0	95.7	69.9	101.1	65.1	116.5	65.7	124.3	75.0	128.2	85.8
7	96.4	71.3	109.9	80.2	106.6	70.9	123.7	70.7	139.7	85.7	150.8	102.7
8	108.0	81.4	121.5	87.5	114.8	76.3	139.8	79.6	161.4	101.2	178.5	125.7
9	138.4	106.5	134.9	100.0	137.1	92.6	188.2	108.9	220.6	149.3	246.4	188.2

Table A III. 11 Averaged values of measured signals during experiment for each data point (Case 6)

No.	Pressure (MPa)	Heating power (kW)	Mass flow rate (kg/s)	CO_2 inlet temperature (°C)	CO_2 outlet temperature (°C)	Water inlet temperature (°C)	Water outlet temperature (°C)	Water flow rate (kg/s)	Pressure drop across outlet valve (Pa)	Pressure drop across heat exchange (Pa)
1	8.003	1.8991	0.0282	19.8	31.9	17.0	17.5	1.0171	1117.06	48.03
2	8.002	2.8475	0.0336	19.3	33.2	15.4	16.0	1.0168	1723.76	62.29
3	7.997	3.9276	0.0368	18.4	33.8	12.0	13.2	1.0155	2415.74	75.93
4	8.001	4.7290	0.0376	18.4	35.1	10.7	12.1	1.0137	2934.65	85.55
5	8.003	5.6737	0.0372	18.1	37.4	9.9	11.5	1.0129	3541.94	94.71
6	8.013	6.6161	0.0350	18.0	43.8	8.7	10.5	1.0127	4184.05	103.9
7	8.017	7.5599	0.0310	17.6	52.1	8.2	10.0	1.0125	4775.29	111.00

Table A III. 12 Averaged values of measured wall surface temperature during experiment for each data point (Case6)

No.	TS21T (°C)	TS21B (°C)	TS22T (°C)	TS22B (°C)	TS23T (°C)	TS23B (°C)	TS24T (°C)	TS24B (°C)	TS25T (°C)	TS25B (°C)	TS26T (°C)	TS26B (°C)
1	39.5	35.4	43.5	37.3	47.3	37.7	50.8	38.6	52.2	39.9	52.3	41.5
2	46.5	39.6	54.9	42.3	57.1	42.1	61.9	41.6	65.8	45.2	66.5	46.4
3	58.0	45.2	71.3	49.7	72.5	48.6	80.3	48.7	84.7	51.6	85.7	56.5
4	69.8	51.7	86.2	57.6	87.9	55.0	94.9	54.9	101.8	60.1	103.0	67.0
5	87.0	62.0	105.2	69.2	105.4	64.0	114.6	63.2	122.6	72.1	127.7	86.1
6	103.9	74.9	123.8	81.8	115.0	70.8	129.2	72.1	148.1	91.1	162.5	115.2
7	121.1	89.2	133.9	88.1	127.4	78.0	155.4	88.3	185.6	123.9	210.0	159.6

Table A III. 13 Averaged values of measured signals during experiment for each data point (Case 7)

No.	Pressure (MPa)	Heating power (kW)	Mass flow rate (kg/s)	CO_2 inlet temperature (°C)	CO_2 outlet temperature (°C)	Water inlet temperature (°C)	Water outlet temperature (°C)	Water flow rate (kg/s)	Pressure drop across outlet valve (Pa)	Pressure drop across heat exchange (Pa)
1	7.980	1.6186	0.0285	18.1	30.3	15.9	16.3	1.0205	674.55	33.65
2	7.957	2.1887	0.0329	17.7	32.0	14.5	15.0	1.0192	921.42	42.17
3	8.007	2.8465	0.0366	17.4	33.2	13.6	14.2	1.0172	1207.19	52.04
4	7.981	3.7926	0.0405	16.9	33.6	11.9	12.8	1.0163	1645.54	64.48
5	7.996	4.7386	0.0427	16.6	34.1	10.5	11.7	1.0143	2079.66	75.12
6	8.017	5.6716	0.0438	16.4	35.4	9.5	10.9	1.0134	2531.36	84.20
7	7.988	6.6159	0.0434	16.1	37.4	8.1	9.8	1.0130	3054.40	102.73
8	7.982	7.5599	0.0420	15.9	41.8	7.2	9.0	1.0104	3510.17	114.86
9	8.017	8.5036	0.0396	15.6	50.9	6.0	8.0	1.0095	3974.69	faulty
10	8.005	9.4426	0.0376	15.5	54.4	5.8	7.9	1.0100	4319.75	124.78

Table A III. 14 Averaged values of measured wall surface temperature during experiment for each data point (Case7)

No.	TS21T (°C)	TS21B (°C)	TS22T (°C)	TS22B (°C)	TS23T (°C)	TS23B (°C)	TS24T (°C)	TS24B (°C)	TS25T (°C)	TS25B (°C)	TS26T (°C)	TS26B (°C)
1	35.3	31.7	39.8	34.0	42.0	34.9	44.9	35.8	47.3	37.9	46.7	39.0
2	39.1	34.9	44.0	37.2	46.9	37.8	50.8	38.4	54.0	39.8	54.2	42.4
3	43.3	38.1	50.6	40.5	53.4	40.7	57.9	41.6	62.5	44.1	62.4	44.8
4	50.6	41.9	62.1	45.6	63.3	45.6	70.9	45.8	75.2	48.2	76.9	51.9
5	61.1	47.4	75.6	52.6	77.8	51.7	86.3	51.9	93.7	56.2	93.8	60.5
6	74.6	54.8	90.9	61.4	92.8	58.7	102.6	58.5	110.4	64.9	111.8	71.7
7	83.9	63.5	109.7	73.2	100.2	65.3	110.1	63.1	123.4	75.4	134.9	91.0
8	89.3	71.0	126.0	83.7	109.5	70.7	126.1	71.7	147.5	91.8	164.7	114.6
9	118.3	89.6	138.0	89.4	116.8	77.4	141.2	83.0	179.3	116.6	203.4	149.4
10	138.2	104.2	148.4	97.2	133.1	87.0	176.5	103.9	214.4	145.6	241.6	185.5

Table A III. 15 Averaged values of measured signals during experiment for each data point (Case 8)

No.	Pressure (MPa)	Heating power (kW)	Mass flow rate (kg/s)	CO_2 inlet temperature (°C)	CO_2 outlet temperature (°C)	Water inlet temperature (°C)	Water outlet temperature (°C)	Water flow rate (kg/s)	Pressure drop across outlet valve (Pa)	Pressure drop across heat exchange (Pa)
1	7.993	3.4592	0.0385	21.9	33.8	17.6	18.4	1.0182	1681.69	80.64
2	8.005	4.2167	0.0401	21.7	34.3	16.4	17.4	1.0163	2054.26	89.30
3	7.971	4.7297	0.0405	21.6	35.6	15.6	16.8	1.0162	2344.68	96.28
4	7.998	4.9184	0.0406	21.6	35.6	15.5	16.7	1.0161	2401.80	93.59
5	8.005	5.6750	0.0404	21.3	37.7	14.4	15.7	1.0154	2766.23	100.32
6	7.986	6.6197	0.0396	21.0	42.7	13.0	14.7	1.0133	3261.26	113.51
7	8.012	7.5622	0.0379	20.7	51.8	12.0	13.8	1.0129	3726.23	120.08
8	8.002	8.4956	0.0366	20.8	64.7	11.3	13.4	1.0113	3697.98	125.08
9	8.015	9.4376	0.0332	20.5	68.6	10.7	12.8	1.0103	4352.24	faulty

Table A III. 16 Averaged values of measured wall surface temperature during experiment for each data point (Case8)

No.	TS21T (°C)	TS21B (°C)	TS22T (°C)	TS22B (°C)	TS23T (°C)	TS23B (°C)	TS24T (°C)	TS24B (°C)	TS25T (°C)	TS25B (°C)	TS26T (°C)	TS26B (°C)
1	53.0	43.5	63.2	46.7	62.7	45.8	67.4	45.6	72.5	48.2	73.8	51.3
2	62.3	48.5	74.4	52.6	74.1	50.6	79.7	50.3	86.8	54.6	88.1	59.1
3	69.6	52.6	82.4	57.2	81.7	54.0	88.3	53.5	96.0	59.2	98.4	65.4
4	72.5	54.4	85.9	59.2	84.9	55.6	91.6	55.0	99.7	61.3	102.4	68.2
5	84.8	62.2	98.8	67.2	94.0	61.5	104.3	60.8	115.2	70.2	121.3	81.8
6	99.5	73.9	106.4	74.3	101.1	67.0	118.6	69.1	138.5	86.5	152.2	106.8
7	103.4	81.3	113.3	79.7	115.9	75.8	144.9	83.5	169.0	110.1	188.9	140.1
8	118.9	92.9	140.8	93.6	135.2	87.0	172.2	101.9	200.9	138.4	228.0	176.7
9	128.1	100.7	156.3	100.4	148.4	96.1	205.3	129.1	241.1	175.3	273.6	221.9

Table A III. 17 Averaged values of measured signals during experiment for each data point (Case 9)

No.	Pressure (MPa)	Heating power (kW)	Mass flow rate (kg/s)	CO_2 inlet temperature (°C)	CO_2 outlet temperature (°C)	Water inlet temperature (°C)	Water outlet temperature (°C)	Water flow rate (kg/s)	Pressure drop across outlet valve (Pa)	Pressure drop across heat exchange (Pa)
1	8.022	2.3796	0.0331	21.7	33.4	17.0	19.1	0.2827	1121.30	42.17
2	8.029	2.8476	0.0350	22.4	34.2	17.8	20.2	0.2816	1384.39	51.76
3	7.975	3.7951	0.0381	22.0	34.9	16.9	17.8	1.0340	2041.45	62.38
4	7.973	4.7304	0.0392	21.6	35.6	15.4	16.5	1.0338	2531.14	71.30
5	8.005	5.6743	0.0387	21.4	38.9	14.3	15.6	1.0352	3042.16	79.20
6	8.012	6.6203	0.0371	21.2	44.7	12.9	14.4	1.0342	3551.90	faulty
7	8.010	7.5574	0.0360	21.0	55.1	11.9	13.7	1.0332	3983.89	84.16
8	8.020	8.0206	0.0353	21.0	61.0	11.7	13.5	1.0327	4145.56	88.39
9	8.023	8.4919	0.0341	20.8	62.9	11.6	13.4	1.0329	4279.07	faulty
10	8.025	9.6281	0.0302	20.5	87.2	10.1	12.3	1.0321	4726.45	94.86

Table A III. 18 Averaged values of measured wall surface temperature during experiment for each data point (Case9)

No.	TS21T (°C)	TS21B (°C)	TS22T (°C)	TS22B (°C)	TS23T (°C)	TS23B (°C)	TS24T (°C)	TS24B (°C)	TS25T (°C)	TS25B (°C)	TS26T (°C)	TS26B (°C)
1	43.1	38.3	48.8	39.9	50.7	40.2	54.5	41.1	57.6	42.2	58.1	44.5
2	47.7	40.8	55.3	42.7	55.9	42.8	60.7	42.5	64.5	45.5	65.5	46.8
3	57.7	45.9	69.0	49.0	69.1	48.0	74.6	47.1	79.5	50.7	80.9	55.0
4	71.3	53.5	84.7	57.4	84.1	54.8	90.8	54.3	97.8	59.9	100.7	67.1
5	87.1	63.6	102.0	67.8	97.4	62.7	108.3	62.5	118.9	72.4	125.7	85.6
6	101.7	75.5	110.0	74.8	105.5	68.5	124.8	72.3	144.2	90.4	158.9	113.1
7	114.9	87.1	128.4	85.6	124.4	79.5	152.3	87.2	173.8	114.9	196.0	147.3
8	119.2	91.8	132.5	88.7	129.7	84.3	164.2	97.2	191.8	131.4	218.2	168.6
9	125.6	97.4	142.8	93.9	139.3	90.8	177.3	108.7	210.4	148.2	239.8	189.6
10	146.6	113.6	173.9	109.4	173.2	110.3	227.2	144.9	263.3	196.5	299.6	248.1

Table A III. 19 Averaged values of measured signals during experiment for each data point (Case 10)

No.	Pressure (MPa)	Heating power (kW)	Mass flow rate (kg/s)	CO_2 inlet temperature (°C)	CO_2 outlet temperature (°C)	Water inlet temperature (°C)	Water outlet temperature (°C)	Windshield washer fluid flow rate (GPM)	Pressure drop across outlet valve (Pa)	Pressure drop across heat exchange (Pa)
1	7.587	2.3060	0.0330	10.2	30.2	6.2	7.7	7.3420	786.42	45.61
2	7.611	2.9399	0.0379	10.0	31.6	5.2	7.7	5.4118	1007.66	54.75
3	7.595	3.4355	0.0407	10.1	31.8	4.5	7.4	5.3338	1191.69	61.99
4	7.605	3.9726	0.0435	10.0	32.1	2.7	7.8	3.4840	1402.12	70.95
5	7.607	4.7024	0.0465	10.2	32.6	3.1	6.2	7.1287	1720.69	80.87
6	7.612	5.5923	0.0485	10.0	32.9	0.2	6.1	4.4190	2086.31	92.58
7	7.590	6.5859	0.0493	10.2	33.5	-0.6	5.2	5.2216	2527.18	103.35
8	7.615	7.6541	0.0488	10.1	36.7	-1.9	4.0	5.9297	3032.82	111.46
9	7.614	8.4992	0.0473	10.1	42.3	-3.0	3.3	6.3479	3429.92	115.45
10	7.605	9.4350	0.0431	10.2	53.3	-4.1	2.1	7.1320	3890.23	faulty
11	7.610	10.0648	0.0421	9.9	59.8	-5.4	1.5	6.2962	4103.45	120.03
12	7.612	10.7405	0.0403	10.2	69.5	-5.6	1.4	6.4861	4312.29	121.88

Table A III. 20 Averaged values of measured wall surface temperature during experiment for each data point (Case10)

No.	TS21T (°C)	TS21B (°C)	TS22T (°C)	TS22B (°C)	TS23T (°C)	TS23B (°C)	TS24T (°C)	TS24B (°C)	TS25T (°C)	TS25B (°C)	TS26T (°C)	TS26B (°C)
1	31.0	30.5	45.0	33.5	44.2	39.6	51.5	35.5	57.3	34.7	57.5	37.9
2	33.3	33.9	51.7	36.5	49.9	43.5	59.0	38.5	66.1	37.4	63.9	41.5
3	36.8	36.3	58.1	38.5	56.2	46.5	64.9	40.3	71.8	39.8	70.2	45.2
4	40.2	38.7	65.3	41.8	62.4	49.8	72.0	42.7	78.5	43.0	76.2	48.6
5	45.8	42.4	74.9	47.4	70.5	54.2	81.8	47.2	88.8	47.8	85.3	52.5
6	57.2	49.2	89.3	55.3	83.3	61.6	94.2	53.6	101.7	54.2	99.2	58.5
7	72.6	59.9	108.2	66.2	98.6	73.1	109.7	60.8	117.7	62.1	116.9	66.2
8	91.1	74.7	132.1	79.7	117.0	94.3	128.9	69.0	138.5	71.1	144.0	78.8
9	99.2	86.0	151.6	91.7	127.4	117.7	145.4	76.9	160.0	78.3	171.1	93.7
10	106.6	97.5	166.9	99.0	135.0	157.0	161.6	89.9	191.3	84.0	212.6	121.5
11	119.6	109.1	183.7	107.3	149.8	181.0	183.2	102.9	212.3	91.4	236.9	140.9
12	135.0	122.3	187.6	108.9	151.3	214.1	202.8	121.4	241.3	96.9	270.0	168.6

Table A III. 21 Averaged values of measured signals during experiment for each data point (Case 11)

No.	Pressure (MPa)	Heating power (kW)	Mass flow rate (kg/s)	CO_2 inlet temperature (°C)	CO_2 outlet temperature (°C)	Water inlet temperature (°C)	Water outlet temperature (°C)	Windshield washer fluid flow rate (GPM)	Pressure drop across outlet valve (Pa)	Pressure drop across heat exchange (Pa)
1	7.588	5.0299	0.0458	13.3	32.7	5.5	9.0	6.511	2119.29	94.74
2	7.601	5.7350	0.0468	13.1	33.4	3.7	7.9	6.495	2458.40	103.96
3	7.615	6.4386	0.0467	13.1	34.8	2.8	7.7	6.165	2781.06	111.01
4	7.596	7.1778	0.0459	13.1	37.7	2.1	7.0	6.696	3147.68	117.35
5	7.611	7.8816	0.0429	13.1	44.1	1.3	6.2	7.299	3545.36	123.19
6	7.619	8.4357	0.0420	12.8	46.5	0.7	5.6	7.291	3773.07	118.42
7	7.623	8.8637	0.0410	13.3	51.5	0.7	5.7	7.522	3951.05	127.61
8	7.623	9.3091	0.0398	13.2	57.7	0.0	5.3	7.515	4130.07	137.07

Table A III. 22 Averaged values of measured wall surface temperature during experiment for each data point (Case11)

No.	TS21T (°C)	TS21B (°C)	TS22T (°C)	TS22B (°C)	TS23T (°C)	TS23B (°C)	TS24T (°C)	TS24B (°C)	TS25T (°C)	TS25B (°C)	TS26T (°C)	TS26B (°C)
1	55.2	48.6	84.7	52.5	77.7	59.0	86.2	51.6	93.5	51.5	90.6	55.7
2	66.7	55.2	96.9	59.9	88.7	67.0	97.2	56.0	105.5	57.0	104.9	61.3
3	77.4	63.4	111.3	68.1	99.5	78.1	109.1	60.9	119.3	62.6	120.7	68.2
4	86.1	73.1	128.8	77.5	108.3	94.9	119.9	66.4	134.1	68.3	141.6	78.6
5	94.1	82.5	140.8	84.3	113.4	119.1	129.8	73.6	153.8	72.1	168.9	94.3
6	102.6	89.8	150.4	87.8	120.6	138.4	141.6	81.2	171.2	76.7	188.6	108.4
7	114.1	98.3	158.7	92.5	128.6	156.4	154.8	89.4	186.7	80.7	207.9	122.0
8	120.3	105.7	162.0	94.8	131.6	176.9	168.5	100.0	205.9	84.8	229.6	137.9

Table A III. 23 Averaged values of measured signals during experiment for each data point (Case 12)

No.	Pressure (MPa)	Heating power (kW)	Mass flow rate (kg/s)	CO_2 inlet temperature (°C)	CO_2 outlet temperature (°C)	Water inlet temperature (°C)	Water outlet temperature (°C)	Windshield washer fluid flow rate (GPM)	Pressure drop across outlet valve (Pa)	Pressure drop across heat exchange (Pa)
1	7.576	2.038	0.0322	16.1	31.2	13.5	13.9	16.570	917.92	44.57
2	7.596	2.528	0.0357	16.2	31.9	13.1	13.7	16.561	1118.72	52.51
3	7.587	3.086	0.0388	16.1	32.1	12.5	13.1	16.538	1375.85	61.24
4	7.598	3.704	0.0412	16.1	32.3	12.0	12.8	16.522	1663.00	70.34
5	7.575	4.539	0.0431	16.2	32.3	11.1	12.2	16.514	2104.19	81.65
6	7.571	5.393	0.0437	16.2	32.8	10.4	11.7	16.512	2539.69	93.32
7	7.608	6.327	0.0442	16.2	34.6	9.5	11.0	16.464	2767.96	102.62
8	7.628	6.994	0.0439	16.1	37.7	8.9	10.6	16.479	3070.18	109.93
9	7.621	7.559	0.0431	16.4	42.6	8.6	10.5	16.455	3375.70	113.91
10	7.603	8.215	0.0418	16.0	50.5	7.8	9.8	16.451	3708.15	122.31
11	7.604	8.969	0.0400	16.1	60.9	7.6	9.6	16.444	4002.24	127.87

Table A III. 24 Averaged values of measured wall surface temperature during experiment for each data point (Case12)

No.	TS21T (°C)	TS21B (°C)	TS22T (°C)	TS22B (°C)	TS23T (°C)	TS23B (°C)	TS24T (°C)	TS24B (°C)	TS25T (°C)	TS25B (°C)	TS26T (°C)	TS26B (°C)
1	37.1	32.9	42.1	35.2	44.9	35.7	48.5	35.8	51.7	38.2	50.7	39.0
2	40.0	35.3	47.0	37.4	49.9	37.8	54.5	38.2	57.5	40.2	55.5	41.8
3	44.2	37.4	53.4	40.4	56.1	40.6	60.9	40.6	65.8	42.7	62.2	44.1
4	50.2	40.5	61.4	44.4	63.7	44.2	69.7	44.2	75.9	47.0	71.4	47.3
5	61.3	46.5	73.9	51.3	75.4	49.9	81.6	49.3	88.2	53.0	84.8	54.8
6	75.6	54.8	88.6	60.3	87.4	56.5	94.0	54.8	102.4	60.2	101.1	65.0
7	89.3	64.4	102.5	69.9	100.0	63.8	109.2	61.0	118.5	69.1	120.5	80.3
8	96.0	71.6	115.5	77.5	105.0	67.6	115.6	65.5	131.8	78.5	139.6	94.1
9	107.4	80.2	121.0	81.1	108.8	70.6	124.7	71.3	147.6	90.5	161.5	113.0
10	123.4	91.3	130.2	87.0	118.6	75.9	142.8	80.9	169.5	107.6	188.2	137.6
11	129.7	99.3	133.6	90.4	126.7	83.0	165.4	96.4	197.5	131.8	221.4	169.0

Table A III. 25 Averaged values of measured signals during experiment for each data point (Case 13)

No.	Pressure (MPa)	Heating power (kW)	Mass flow rate (kg/s)	CO_2 inlet temperature (°C)	CO_2 outlet temperature (°C)	Water inlet temperature (°C)	Water outlet temperature (°C)	Windshield washer fluid flow rate (GPM)	Pressure drop across outlet valve (Pa)	Pressure drop across heat exchange (Pa)
1	7.587	2.4689	0.0339	19.4	31.7	15.2	18.3	2.839	956.84	67.48
2	7.598	3.1453	0.0391	19.1	32.2	13.9	16.3	5.344	1306.38	82.67
3	7.594	3.8629	0.0426	19.1	32.4	12.6	15.6	5.579	1620.27	94.14
4	7.613	4.7330	0.0444	19.1	33.2	10.7	15.3	4.464	1990.64	106.79
5	7.616	5.6259	0.0437	19.2	35.2	9.7	14.0	5.658	2445.62	115.91
6	7.619	6.5151	0.0427	19.2	40.4	7.8	12.9	5.884	2851.58	124.41
7	7.615	7.3892	0.0411	19.0	46.6	7.3	12.0	6.662	3203.22	faulty
8	7.620	8.1163	0.0401	19.1	51.6	6.8	11.8	6.592	3381.54	127.40
9	7.634	8.6998	0.0394	19.1	55.3	6.9	11.6	7.190	3462.35	faulty

Table A III. 26 Averaged values of measured wall surface temperature during experiment for each data point (Case13)

No.	TS21T (°C)	TS21B (°C)	TS22T (°C)	TS22B (°C)	TS23T (°C)	TS23B (°C)	TS24T (°C)	TS24B (°C)	TS25T (°C)	TS25B (°C)	TS26T (°C)	TS26B (°C)
1	36.4	36.2	53.9	37.2	51.1	41.7	55.5	38.6	59.7	38.0	57.1	40.9
2	41.7	39.6	61.2	41.3	56.9	45.1	61.4	41.4	66.0	41.6	63.5	44.1
3	49.1	44.1	71.0	46.4	64.8	50.5	69.7	45.2	75.4	45.7	73.7	48.4
4	58.9	51.6	85.4	53.9	75.4	60.1	82.0	50.6	89.5	51.2	89.1	55.3
5	72.8	62.0	104.1	63.0	89.7	75.4	96.8	57.0	106.3	57.7	111.2	65.7
6	85.5	72.2	112.8	69.8	96.2	96.8	111.4	65.0	128.2	63.6	139.3	79.3
7	86.2	79.3	121.6	74.7	108.5	124.7	131.9	77.3	154.0	70.8	170.4	99.2
8	90.3	85.3	142.6	84.4	128.5	151.1	153.0	89.9	177.7	80.3	197.5	118.6
9	104.8	97.0	166.5	96.4	141.8	165.4	164.5	98.8	191.4	86.7	210.6	130.8